The MINOS Detectors
Technical Design Report

Version 1.0

October 1998

The MINOS Collaboration

Argonne - Caltech - Dubna - Fermilab - Harvard - IHEP-Beijing
Indiana - ITEP-Moscow - Lebedev - Livermore - UC-London
Minnesota - Oxford - Protvino - Rutherford - Stanford - Sussex
Texas A&M - Texas-Austin - Tufts - Western Washington

The MINOS Collaboration
Main Injector Neutrino Oscillation Search

September 1998

P. Adamson[17], K.V. Alexandrov[9], W.W.M. Allison[13], G.J. Alner[15], I. Ambats[1],
B. Anderson[11], D.F. Anderson[4], Yu. Antipov[14], C. Arroyo[16], D.S. Ayres[1], B. Baller[4],
B. Barish[2], P.D. Barnes Jr.[10], W.L. Barrett[21], R. H. Bernstein[4], R.E. Blair[1], V. Bocean[4],
D.J. Boehnlein[4], D. Bogert[4], P.M. Border[12], C. Bower[7], J. Byrne[17], T. Chase[12],
S. Chernichenko[14], S. Childress[4], B.C. Choudhary[2], J.H. Cobb[13], J.D. Cossairt[4],
H. Courant[12], P. Cushman[12], J.W. Dawson[1], A. Denisov[14], P.J. Dervan[11], N. Diaczenko[18],
G. Drake[1], M. Drew[18], A. Durum[14], R. Edgecock[15], V.K. Ermilova[9], O. Eroshin[14],
R. Fahrutdinov[14], G.J. Feldman[5], T.H. Fields[4], D. Fujino[10], H.R. Gallagher[13],
M. Gebhard[7], Yu. Gilitsky[14], M.C. Goodman[1], Yu. Gorin[14], Yu. Gornushkin[3],
M. Graham[12], N. Grossman[4], V.J. Guarino[1], Yu. Gutnikov[14], R. Halsall[15], J. Hanson[2],
P.G. Harris[17], E. Hartouni[10], R. Hatcher[16], R. Heinz[7], K. Heller[12], N. Hill[1], T. Hu[6],
Y. Huang[2], J. Hylen[4], M. Ignatenko[3], G. Irwin[16], C. James[4], T. Joffe-Minor[1], T. Kafka[20],
T. Kirichenko[19], J. Kilmer[4], H. Kim[2], V. Kochetkov[14], G. Koizumi[4], Z. Krumstein[3],
N.N. Kundu[13], A. Ladran[10], Y.F. Lai[6], K. Lang[19], C. Laughton[4], P.J. Litchfield[15],
N.P. Longley[2], P. Lucas[4], S. Madani[15], V. Makeev[14], W.A. Mann[20], H.S. Mao[6],
M.L. Marshak[12], D. Maxam[12], E.N. May[1], J.R. Meier[12], E. Melnikov[14], G.I. Merzon[9],
D.G. Michael[2], R.H. Milburn[20], L. Miller[7], W.H. Miller[12], S.J. Mishra[5], J. Morfin[4],
L. Mualem[12], S. Mufson[7], J. Musser[7], A. Napier[20], J.K. Nelson[12], H. Newman[2],
A. Nozdrin[3], S. O'Day[4], W. Oliver[20], A. Olshevski[3], V. Onuchin[14], A. Para[4], G.F. Pearce[15],
C.W. Peck[2], C. Perry[13], E.A. Peterson[12], A. Petruhin[14], D.A. Petyt[15], R.K Plunkett[4],
L.E. Price[1], M. Proga[19], D.R. Pushka[4], R.A. Rameika[4], A.L. Read[4], K. Ruddick[12],
R. Rusack[12], V.A. Ryabov[9], A. Sadovski[3], M. Sanchez[20], J. Schneps[20], P.V. Schoessow[1],
R. Schwienhorst[12], V. Semenov[14], B.W. Shen[6], P.D. Shield[13], R. Shivane[12], A. Sisakian[3],
W. Smart[4], V. Smirnitsky[8], V. Smotriaev[8], T. Soesbe[19], A. Soldatov[14], R. Soltz[10],
N.I. Starkov[9], R. Talaga[1], J. Thomas[11], J.L. Thron[1], D. Tovee[11], J. Trevor[2], I. Trostin[8],
V.A. Tsarev[9], L.R. Turner[1], N. Tyurin[14], M. Vakili[18], L. Wai[16], D. Wall[20], R.C. Webb[18],
A. Wehmann[4], N. West[13], R.F. White[17], S.G. Wojcicki[16†], D. Wright[10], X.M. Xia[6],
W.G. Yan[6], and J.C. Yun[4].
† **Spokesman**

Argonne[1] - Caltech[2] - Dubna[3] - Fermilab[4] - Harvard[5] - IHEP-Beijing[6] -
Indiana[7] - ITEP-Moscow[8] - Lebedev[9] - Livermore[10] - UC-London[11] -
Minnesota[12] - Oxford[13] - Protvino[14] - Rutherford[15] - Stanford[16] - Sussex[17] -
Texas A&M[18] - Texas-Austin[19] - Tufts[20] - Western Washington[21]

Contents

Executive summary

The MINOS (Main Injector Neutrino Oscillation Search) experiment is designed to search for neutrino oscillations with a sensitivity significantly greater than has been achieved to date. The phenomenon of neutrino oscillations, whose existence has so far not been proven convincingly, allows neutrinos of one "flavor" (type) to slowly transform themselves into another flavor, and then back again to the original flavor, as they propagate through space or matter. The MINOS experiment is optimized to explore the region of neutrino oscillation "parameter space" (values of the Δm^2 and $\sin^2(2\theta)$ parameters) suggested by previous investigations of atmospheric neutrinos: the Kamiokande, IMB, Super-Kamiokande and Soudan 2 experiments. The study of oscillations in this region with a neutrino beam from the Main Injector requires measurements of the beam after a very long flight path. This in turn requires an intense neutrino beam and a massive detector in order to have an adequate event rate at a great distance from the source.

If neutrinos do oscillate, as is suggested by some experimental results and by theoretical extensions of the Standard Model of particle physics, then they will change their flavor as they move through space or matter. Different flavors of neutrinos (electron, muon, tau or sterile) can be identified by the distinctively different patterns of secondary particles they produce when they interact with matter in a massive neutrino detector. Thus an optimum, and most sensitive, way to detect such oscillations is to compare the patterns of their interactions (characterized by topology and energy deposition) at two widely separated locations in a neutrino beam. This technique requires, first, that the beam flavor composition and other characteristics are very similar at these two detector sites, in the absence of oscillations (accelerator neutrino beams consist mainly of muon neutrinos). Second, the two detectors must be identical in their important features. If these two conditions are met, then systematic effects will be minimized by comparing the patterns of interactions in the two detectors, and maximum sensitivity will be achieved. The MINOS experiment design is based on this technique; the technical challenge for the experiment is to build an appropriate neutrino beam and appropriate detectors.

The neutrino beam line proposed for the MINOS experiment will be constructed as part of the Fermilab NuMI Project, which is described in Reference [1]. It relies on the 120 GeV proton beam from the Main Injector, which produces pions and kaons which are then allowed to decay in flight along a 675 m long decay pipe. The neutrinos which constitute the MINOS beam are produced when these pions and kaons decay. The two MINOS detectors are located at Fermilab (the "near detector") and in the Soudan mine in Soudan, Minnesota, 730 km away (the "far detector"). The existing Soudan cavern will be supplemented by a new, adjoining, cavern to be excavated as part of the NuMI Project; the new cavern will house the MINOS far detector. The work associated with the new cavern excavation and outfitting is described in Reference [2].

The proposed MINOS detectors are iron-scintillator sandwich calorimeters, with toroidal magnetic fields in their thin steel planes. The combination of alternating active detector planes and magnetized steel absorber planes has been used in a number of previous neutrino experiments. The MINOS innovation is to use scintillator with sufficiently fine transverse

granularity (4-cm wide strips), so that it provides both calorimetry (energy deposition) and tracking (topology) information. The 5,400 metric ton MINOS far detector is also much more massive, and potentially more expensive, than previous experiments. Recent advances in extruded scintillator technology and in pixelated photomultipliers have made such a detector feasible and affordable for the first time.

This Technical Design Report describes the main components of the MINOS detectors: the toroidal magnet, the scintillator strips, and the readout electronics, as well as the installation procedures at the Fermilab and Soudan sites. Section 3.2 summarizes the physics goals of the experiment and the properties of the detectors we have designed to reach those goals. The baseline detector design is the basis for the experiment cost estimate and schedule presented in Reference [3]. Since the design of MINOS allows for potential future modifications, in response to developments in neutrino physics and detector technology, we also describe briefly some of these possibilities even though they are not included in the current scope of the project. The capability of the NuMI facility and the MINOS detector to respond to new results from other oscillation experiments is addressed in Reference [4].

Environmental, Safety and Health issues for the Project at the Fermilab and Soudan experimental sites are described in detail in References [5] and [6].

The MINOS experiment described in this TDR is based on a far detector composed of two identical 2,700 metric ton supermodules. The scope of the baseline detector has been defined to be compatible with the funds currently believed to be available for its construction. It is possible that funds from the project scope reserve and from the present contingency pool may become available as the uncertainty in the cost estimate is reduced in the future. It is also possible that additional funds from overseas collaborators could become available. If this should turn out to be the case, it may be possible to construct an additional supermodule (the Soudan cavern dimensions have been chosen to allow for this possibility) or some alternative augmentation of the experiment (such as an emulsion detector at Soudan). This decision about the best use of any such funds would of course take into account current knowledge of neutrino oscillation physics, detector technology and more reliable detector cost estimates.

Bibliography

[1] The Fermilab NuMI Group, "NuMI Facility Technical Design Report," October 1998, Fermilab report NuMI-346.

[2] The University of Minnesota, CNA Consulting Engineers, Ericksen-Ellison Associates, Inc., and Miller-Dunwiddie, Inc., "MINOS Far Detector Laboratory Technical Design Report (Including Basis of Estimate & WBS) for Cavern Construction, Cavern Outfitting & Detector Outfitting," October 1998, Fermilab report NuMI-L-263.

[3] The Fermilab NuMI Project Staff, "NuMI Project Cost and Schedule Plan," October 1998, Fermilab report NuMI-362.

[4] The MINOS Collaboration, "Neutrino Oscillation Physics at Fermilab: The NuMI-MINOS Project," May 11, 1998, Fermilab report NuMI-L-375.

[5] The Fermilab NuMI Project Staff, "NuMI Project at Fermilab: Preliminary Safety Assessment Document," October 1998, Fermilab report NuMI-361.

[6] The University of Minnesota, CNA Consulting Engineers, Ericksen-Ellison Associates, Inc., and Miller-Dunwiddie, Inc., "MINOS Far Detector Laboratory Project, Preliminary Hazard Assessment Report," October 1998, Fermilab report NuMI-L-419.

Chapter 1

Introduction

1.1 Historical overview

From the time of the initial conception of the Main Injector it has been realized that the high proton intensity, coupled with the medium-high energy of this accelerator, could provide a source of neutrinos that would be unique in the world. This idea was first seriously discussed in a workshop on Fixed Target Physics with the New Main Injector held at Fermilab in May 1989. In the same time frame there was also a growing realization in the high energy physics community that the search for neutrino oscillations could be one of the most productive ways to test the hypothesis of neutrinos as dark matter and to look for departures from the Standard Model of particle physics. This model required massless neutrinos and thus could not accommodate neutrino oscillations. On the other hand the concept of nonzero mass neutrinos was quite attractive theoretically[1]. In addition there were experimental hints that neutrino oscillations might indeed be occurring in nature. Neutrino oscillations could explain both the solar neutrino deficit and the atmospheric neutrino anomaly.

In 1990 three proposals for Main Injector neutrino oscillation experiments were submitted to Fermilab: a short-baseline proposal, P-803 (COSMOS), to look at the mass region of cosmological interest, and two long-baseline proposals to look at the region suggested by the atmospheric anomaly; these were P-805, which proposed to send the neutrino beam 570 kilometers to the IMB water Cerenkov detector in Ohio, and P-822, which proposed to send it 730 kilometers to the 1 kiloton Soudan 2 detector in northern Minnesota. These ideas were further developed and elaborated on in a workshop on Neutrino Long-Baseline experiments held at Fermilab in November 1991[2]. Eventually P-805 was withdrawn because of the accident which caused the shutdown of the IMB detector. The PAC encouraged P-822 but made it clear that a more ambitious effort, involving an order of magnitude more massive detector, was required to make a statistically significant search.

It was in this environment that the Fermilab management issued a call for Letters of Intent (LOIs) for long-baseline neutrino experiments, with a deadline of May 16, 1994. Three LOIs were received in response to this call. The 1994 workshop on Particle and Nuclear Astrophysics and Cosmology in the Next Millennium[3] in Snowmass, Colorado, sponsored by the American Physical Society, provided a good forum for the proponents of these LOIs, as well as other interested parties, to meet and discuss issues of common interest.

As a result of these discussions, and of the recommendations from the summer 1994 Fermilab PAC meeting, a more focused meeting was held at Fermilab in late summer 1994 to consider forming a single collaboration to study long-baseline neutrino oscillations.

Such a Collaboration was indeed formed in the fall of 1994 and a decision was made to focus the effort on an experiment with a magnetic detector of roughly 10 to 15 metric kilotons (kt), to be located in the Soudan mine in Minnesota. At the first meeting of the Collaboration, a formal "constitution" was adopted and management and policy-setting groups were established. Stanley Wojcicki from Stanford University was chosen as the first Spokesperson of the Collaboration. The Collaboration adopted MINOS, an acronym for Main Injector Neutrino Oscillation Search, as the name for its experiment.

The Collaboration immediately initiated an effort on detector R&D with the goal of obtaining the information necessary to design an optimum detector, which could be built at reasonable cost, to characterize the interactions of neutrinos produced by the Main Injector. Unfortunately the level of the R&D had to be rather limited, both in 1995 and in the subsequent two years, because of serious funding constraints. In parallel, the Collaboration started work on a formal proposal to the Fermilab management which defined the scope of physics interest, the general method proposed to address this physics, and a "Reference Detector". The Reference Detector concept was devised by the Collaboration as a design which could address the relevant physics satisfactorily, did not require any new or unproven technology, and could be costed reliably. The Collaboration recognized from the beginning, however, that the results of the planned R&D program could lead eventually to an alternate design. The Collaboration chose the summer of 1997 as the deadline for specifying the basic parameters and technologies of the MINOS detectors.

The MINOS Proposal[4] was submitted to Fermilab management in early 1995 for consideration at its February 17-19, 1995, meeting. In response to specific questions formulated by the PAC at this meeting, the Collaboration prepared an Addendum[5] to elaborate on a number of physics and technical issues. At the next meeting of the Fermilab PAC, on April 28-30 of the same year, the Committee recommended that Stage I approval be granted to the Collaboration and Director John Peoples accepted this recommendation.

Fermilab was not the only location under consideration by the U.S. HEP community for a possible long-baseline neutrino oscillation experiment. Somewhat before the MINOS Proposal, another proposal was submitted to the Brookhaven National Laboratory management for an experiment utilizing the BNL AGS accelerator as the source of neutrinos. This proposal was approved by the BNL directorate and in subsequent months the proposal was further refined[6].

The large scale of these proposed efforts implied that the U.S. HEP program could not afford to mount both experiments. Accordingly, the Director of DOE's Office of Energy Research, Dr. Martha Krebs, requested the High Energy Physics Advisory Panel (HEPAP) to form a Subpanel with the following charge[7]:

> *Evaluate the existing evidence for neutrino oscillations, and consider the feasibility of testing this phenomenon in experiments at U.S. accelerator facilities. Review the status and discovery potential of ongoing and proposed experiments at accelerators in the U.S. and abroad. Conduct an indepth review of the neutrino oscillation experiments proposed at U.S. accelerators, and compare them on the*

*basis of scientific merit, discovery potential, and likelihood of achieving a defini-
tive result. Also, for each of these proposals, comment on the reliability of its
cost and schedule estimates, and the impact on the host laboratory. Consider the
priority of these experiments in the context of the U.S. accelerator-based High En-
ergy Physics Program. If appropriate, recommend to the Department of Energy
a cost-effective plan for pursuing this physics.*

The creation of a Subpanel with such a charge was unprecedented in the history of U.S.
high energy physics and its peer review process. Never before had there been conducted a
national level peer review of experiments approved at two different laboratories with a goal
of performing only the one with a higher physics potential.

Stanley Wojcicki, chair of HEPAP at that time, being one of the principals in the MINOS
effort at Fermilab, recused himself from all deliberations on this issue including the discus-
sions on Subpanel formation. Dr. Piermaria Oddone, from Lawrence Berkeley National
Laboratory, was designated by DOE to be the Acting HEPAP Chair for the Consideration
of Neutrino Oscillation Experiments. He acted as chair in the activities of HEPAP con-
nected with the Subpanel formation, its deliberations, and the eventual consideration of the
Subpanel's recommendations by HEPAP. Prof. Frank Sciulli from Columbia University was
selected as the chair of the Subpanel. There were also appointed eleven additional members
of the Subpanel, all of them active members of the U.S. HEP community with extensive
knowledge of neutrino physics.

The Subpanel held a number of meetings, the first one on March 22-24, 1995 in Bethesda,
Maryland. Separate three day meetings were held at the two proponent laboratories: at
Fermilab on June 13-15, 1995, and at Brookhaven on June 20-22, 1995. Together with the
evaluation of the physics capability of each experiment, a parallel review was conducted of
their estimated costs with the help of a specially appointed Cost Review Subcommittee. The
Subpanel generated a list of additional questions to the proponents and the two laboratories,
answers to which were provided to the Subpanel before its last meeting[8].

The Subpanel concluded its deliberations, formulated recommendations, and wrote its
report at its final meeting held in Denver, Colorado on July 24-28, 1995. The Subpanel
stated in its report[9]:

*The discovery of neutrino oscillations, and consequently the discovery of neutrino
mass, would constitute a major breakthrough in particle physics and the first
evidence of physics beyond the minimal Standard Model.*

Its four recommendations were:

1. *The search for neutrino oscillations with accelerator experiments, including
   a single long-baseline beam, should form an important segment of the U.S.
   high energy physics program.*

2. *The MINOS experiment at Fermilab should be supported; the E-889 experi-
   ment at Brookhaven should not be supported.*

3. *The COSMOS experiment at Fermilab should be supported.*

4. *The Fermilab program should remain flexible to react to new information.*

Subsequently, at its September 18-19, 1995 meeting in Washington, D.C., the full HEPAP considered the Subpanel report. After extensive discussion, HEPAP unanimously supported the report. In its transmittal letter to Dr. Martha Krebs, Acting HEPAP Chair Oddone wrote[10]:

> *We believe that the program of neutrino oscillations, to be carried out at FNAL as recommended by the subpanel, is an important component of the future national program .... Discovery of neutrino oscillations accessible to accelerator experiments would revolutionize particle physics.*

In the time since the HEPAP recommendations, the MINOS Collaboration grew in size by attracting additional collaborating institutions: Dubna and IHEP-Protvino from Russia, IHEP-Beijing from China, University College London from Great Britain, and the University of Texas at Austin and Harvard University from the U.S. During that same period, Oak Ridge National Laboratory and Columbia University have withdrawn from the MINOS Collaboration. The detector-oriented R&D program during that time focused on the simulations of physics reactions of interest and the development of associated software, the experimental investigation of different active detector technologies, and the examination of different methods of constructing the large steel absorber planes. Four different active detector technologies were investigated: resistive plate counters, proportional gas chambers, liquid scintillator and solid scintillator. Considerations in the ultimate selection were based on cost estimates, simulations of physics performance, laboratory bench tests, test beam results, and experience of HEP experimental groups around the world.

A specific steel plane design was chosen in the fall of 1996. In September 1997 the Collaboration decided on solid scintillator as the active detector technology. These choices form the basis for the design of the detector described in this Technical Design Report.

The Fermilab PAC reviewed the project at its June 1997 meeting and made the following recommendations, which provide part of the motivation for the present baseline design with a 5.4 metric kt far detector:

> 1. *The collaboration should proceed as quickly as possible with a smaller detector (e.g. 5 kton) focussing on the CC/Total method. The reduced mass would still allow the experiment to cover the atmospheric neutrino region and save a substantial portion of the requested funds.*
>
> 2. *The collaboration should prepare for a future upgrade using the funds saved by reducing the detector mass. An upgrade might be vital in addressing future developments in the field, where improved electron or τ identification could be necessary.*

In February 1998 the HEPAP Subpanel on Planning for the Future of U.S. High Energy Physics (the Gilman Subpanel)[11] reiterated HEPAP's endorsement of the Fermilab long-baseline program, but noted that new experimental results on neutrino oscillations made this an appropriate time for Fermilab to reexamine the configuration of the NuMI-MINOS facility. Such a review is consistent with the fourth recommendation of the 1995 HEPAP Subpanel. In response to this, a special MINOS Subcommittee of the Fermilab PAC was appointed, with

Prof. Charles Baltay as chair, to review the physics goals and the scientific capability of the NuMI-MINOS project; the review was held in May 1998. The MINOS Collaboration input on the issues considered by the Subcommittee is discussed in detail in Reference [12]. The Subcommittee concluded[13] that "there now appears to be a respectable body of evidence indicating the existence of neutrino oscillations," and expressed the feeling that "it is more desirable than it was even a few years ago to go ahead with a strong long-baseline neutrino oscillation program at Fermilab." The Subcommittee's report was strongly endorsed by the Fermilab PAC at its June 1998 meeting. The PAC added its own recommendations to those of the Subcommittee:

> *The compelling evidence for ν oscillations that has developed over the past year, primarily from the Super-Kamiokande experiment, makes a confirmation and study of this phenomenon an important and exciting area of research. Fermilab is well-positioned to take a leading role in this effort, and the NuMI/MINOS program should be pursued with high priority. The Committee believes the MINOS priority should be second only to Run II at this time. . . .*
>
> *The high priority is based on the goals of observing the oscillation signal, ascertaining whether the observed oscillations are $\nu_\mu \to \nu_\tau$ or $\nu_\mu \to \nu_s$, measuring precisely the values of Δm^2 and $\sin^2(2\theta)$ and measuring the $\nu_\mu \to \nu_e$ component of the oscillations.*

1.2   Organization of the report

As the Technical Design Report for the MINOS detector, this document naturally emphasizes the technical descriptions of the design and construction methods we propose to use for the far and near MINOS detectors (located at Soudan, Minnesota and Fermilab, respectively). We want it to be, however, a relatively self-contained document and thus we have included, in abbreviated form, some additional material which provides the background for the experiment and its physics motivation.

The organization of the report is as follows. Following the brief historical introduction of the present Chapter, Chapter 2 presents the physics motivation for the experiment. Chapter 3 gives a general overview of the experiment: the experimental layout, the physics capabilities of the baseline design and possible future directions.

The next five chapters give technical descriptions of the components of the MINOS baseline detectors. Each of these chapters treats a Level 2 task of the MINOS Work Breakdown Structure (WBS). The first three, Chapters 4, 5 and 6, describe the three main technical components of MINOS: the magnet steel and coils, the active detector elements, and the electronics and data acquisition systems, respectively. The next two, Chapters 7 and 8, deal with the installation of the detectors and their associated infrastructure at the far (Soudan) and near (Fermilab) sites. All five of these Chapters follow the same general organization:

- an overview, intended as a self-contained summary of the task,

- a statement of the task's technical requirements and performance criteria,

- a definition of the scope of the task in terms of interfaces with other tasks,

- a detailed description of WBS elements, as a guide to the cost estimate[14],

- a brief description of the remaining optimization and engineering work.

The following three chapters deal with topics which are, strictly speaking, outside the scope of the formal NuMI/MINOS Project, in that they do not involve any Project costs. Chapter 9 discusses the existing software and its likely future evolution, as well as the computing and data storage requirements of the experiment. Chapter 10 gives a brief description of the existing Soudan 2 detector, which is an integral part of the Fermilab long-baseline neutrino oscillation program. Chapter 11 deals with a possible MINOS upgrade in the form of a hybrid emulsion detector, which appears today to be the most interesting option for expanding MINOS capabilities in the future.

Chapter 12 gives a brief description of the ES&H issues, on both the Fermilab and Minnesota sites. Chapter 13 summarizes the costs and schedules for the baseline near and far detectors, which are given in much greater detail in Reference [14]. Appendix A is a glossary of the specialized terms and acronyms used throughout this report.

Chapter 1 References

[1] H. Harari, "Proceedings of Neutrino '88," p. 574, World Scientific (1988), and Phys. Lett. **B216**, 413 (1989).

[2] "Proceedings of the Workshop on Long-Baseline Neutrino Oscillations," Fermilab, Nov. 17-21, 1991, ed. M. Goodman (unpublished).

[3] "Proceedings of the 1994 Snowmass Summer Study, Particle and Nuclear Astrophysics and Cosmology in the Next Millennium," eds. E.W. Kolb and R.D. Peccei, World Scientific Publishing Co.

[4] The MINOS Collaboration, "P-875: A Long-baseline Neutrino Oscillation Experiment at Fermilab," Fermilab, February 1995, Fermilab report NuMI-L-63.

[5] The MINOS Collaboration, "Addendum to P-875, A Long-baseline Neutrino Oscillation Experiment at Fermilab," April 21, 1995, Fermilab report NuMI-L-79.

[6] The E-889 Collaboration, "Long Baseline Neutrino Oscillation Experiment, Long Island, New York," April 1995, Physics Design Report, BNL No. 52459.

[7] Letter from Martha A. Krebs to Stanley G. Wojcicki, January 3, 1995, appended to Ref.[9].

[8] The MINOS Collaboration, "MINOS Answers to HEPAP Subpanel Questions," June 9, 1995, Fermilab report NuMI-L-96; The Fermilab NuMI Group and the MINOS Collaboration, "Fermilab Answers to HEPAP Subpanel Supplemental Questions," July 14, 1995, Fermilab report NuMI-L-100.

[9] "Report of the HEPAP Subpanel on Accelerator-Based Neutrino Oscillation Experiments," September 1995, DOE Office of Scientific and Technical Information Report No. DOE/ER-0662.

[10] Letter from P.J. Oddone to Martha A. Krebs, October 3, 1995, appended to Ref.[9].

[11] "HEPAP Subpanel Report on Planning for the Future of U.S. High Energy Physics," February 1998, DOE Office of Scientific and Technical Information Report No. DOE/ER-0718.

[12] The MINOS Collaboration, "Neutrino Oscillation Physics at Fermilab: The NuMI-MINOS Project," May 11, 1998, Fermilab report NuMI-L-375.

[13] C. Baltay *et al.*, "Report of the MINOS Subcommittee of the Fermilab Physics Advisory Committee, May 26-27, 1998," June 1998, Fermilab report NuMI-L-389.

[14] The Fermilab NuMI Project Staff, "NuMI Project Cost and Schedule Plan," October 1998, Fermilab report NuMI-362.

Chapter 2

Physics motivation

2.1 Current knowledge of neutrinos

The existence of the neutrino was postulated in 1930 by W. Pauli[1] to explain the apparent energy nonconservation in nuclear weak decays. It was another 23 years before this bold theoretical proposal was verified experimentally in a reactor experiment performed by C. Cowan and F. Reines[2]. The most fundamental properties of the neutrino were verified during the subsequent decade. The neutrino was shown to be left handed in an ingenious experiment by Goldhaber, Grodzins and Sunyar[3] in 1957. The distinct nature of ν_e and ν_μ was demonstrated in 1962 in a pioneering accelerator neutrino experiment at Brookhaven by Danby *et al.*[4].

The following years saw remarkable progress in neutrino experiments, especially those utilizing accelerators as their sources. Increases in available accelerator energies and intensities, advances in neutrino beam technology, and more sophisticated and more massive neutrino detectors were all instrumental in our ability to perform ever more precise neutrino experiments. The focus of those experiments, however, was until very recently mainly on using neutrinos as a probe in only two areas. First, together with experiments utilizing electrons and muons, the worldwide neutrino program played a key role in measuring the nucleon structure functions. Second, along with a variety of other efforts (especially e^+e^- annihilations, inelastic electron scattering), neutrino experiments played a key role in establishing the validity of the Standard Model, through the discovery of neutral currents[5], measurements of the neutral-current to charged-current ratio[6], and measurements of the neutrino lepton scattering cross sections[7].

We are entering now a new era in experimental neutrino physics whose main thrust will likely be twofold: better understanding of the nature of the neutrino, i.e., a study of the neutrino properties, and use of the neutrino in astrophysics and cosmology as an alternative window on the universe, to supplement investigations with electromagnetic radiation. The MINOS experiment, which addresses the subject of neutrino oscillations, will make important contributions to the first part of this program.

Neutrinos are among the fundamental constituents in nature. The space around us is permeated with neutrinos which are relics of the Big Bang, with about 110 ν's/cm^3 for every neutrino flavor. But our knowledge of the neutrino's properties lags far behind our knowledge

of other elementary constituents, for example, the charged leptons. A few examples will illustrate this point, where we quote the lepton values from the latest compendium by the Particle Data Group[8]:

- We do not know whether neutrinos have mass; our current information gives us only upper limits ranging from a few eV for ν_e to some 20 MeV for ν_τ. We can contrast that with a fractional mass error of about 3×10^{-7} for the electron and muon and about 2×10^{-4} for the tau.

- We do not know if neutrinos are stable or decay, either into neutrinos of other flavors or into some new, as yet undiscovered, particles. In contrast, we know that the electron is stable, and we know the muon lifetime with a fractional error of 2×10^{-5} and the tau lifetime at the level of 0.5%.

- Finally, we do not know if the neutrinos have electromagnetic structure, for example a magnetic moment. The electron magnetic moment is known with a precision of about one part in 10^{11}, and the magnetic moment of the muon to one part in 10^8.

These are only a few examples of our ignorance of the basic nature of neutrinos, but they are sufficient to demonstrate that almost half a century after their discovery, neutrinos are still poorly understood. Because of their fundamental nature, we cannot profess to understand our universe without understanding neutrinos.

2.2   Neutrino masses and oscillations

The study of neutrino oscillations offers us potentially the most sensitive means to search for and to measure neutrino masses (or, to be precise, neutrino mass-squared differences). Observation of a nonzero neutrino mass, which would follow directly from the observation of neutrino oscillations, would be a clear example of a breakdown of the Standard Model and thus an indication of physics beyond it. Many of the popular extensions of the Standard Model do indeed predict nonzero neutrino masses and the existence of neutrino oscillations[9]. Furthermore, neutrino oscillations are more than just an attractive theoretical concept: the existence of the phenomenon is strongly suggested by several experimental observations:

a) The need for dark (i.e., non-shining) matter[10], is based mainly on three phenomena: the motion of galaxies within clusters of galaxies, the flat rotational curves for stars in spiral galaxies, and the successes of inflationary Big Bang cosmology which predicts that the density of the universe equals the so-called critical density. Neutrinos, since they are present in abundance everywhere, could account for at least a part of the dark matter if they have finite mass.

b) The solar neutrino deficit, i.e., the observation of fewer sun-originated neutrinos on earth than is expected from the known solar luminosity[11].

c) The atmospheric neutrino anomaly[12], i.e., a measured ν_μ/ν_e ratio for neutrinos from cosmic ray interactions in our atmosphere which is significantly smaller than predicted.

The hypothesis that this anomaly is caused by neutrino oscillations is strongly supported by the recent observation of an up-down asymmetry in the atmospheric ν_μ flux by the Super-Kamiokande Collaboration[13], as well as by their studies of upward going muons.

d) The apparent observation of $\overline{\nu}_e$ in an almost pure $\overline{\nu}_\mu$ beam in the Los Alamos LSND experiment[14].

The MINOS experiment can explore a large region in oscillation parameter space. Furthermore, it can confront directly and conclusively the atmospheric neutrino anomaly and should be able to check the validity of the oscillation interpretation for the LSND effect. In the discussion in Section 2.3, which describes these hints in more detail, we shall emphasize the current status of the atmospheric neutrino anomaly. But first we shall describe briefly the standard neutrino oscillation formalism.

The underlying principle behind neutrino oscillations[15] is the fact that, if neutrinos have mass, then a generalized neutrino state can be expressed either as a superposition of different mass eigenstates or of different flavor eigenstates. This is mainly a restatement of a well known quantum mechanics theorem that, in general, several different basis vector representations are possible, with the different representations being connected by a unitary transformation. Other well known examples of this principle in particle physics are the $K^\circ/\overline{K}^\circ$ system (strong interaction and weak interaction eigenstates) and the quark system (weak interaction and flavor eigenstates connected by the CKM matrix).

From the study of e^+e^- annihilations at the Z° peak[16], we know that there are only three light neutrino flavor eigenstates. Accordingly, the most likely situation is that we have three mass eigenstates and that the connecting unitary matrix is a 3×3 matrix. This is not rigorously required since we could have states with $m_\nu > m_Z/2$ or flavor states that do not couple[17] to the Z°. Even though such possibilities appear *a priori* unaesthetic, there has recently been significant theoretical effort to see whether such mechanisms could explain some of the anomalous effects seen in neutrino experiments.

Thus, for the 3-flavor case, the weak eigenstates $|\nu_a\rangle = \nu_e, \nu_\mu, \nu_\tau$ and the mass eigenstates $|\nu_i\rangle = \nu_1, \nu_2, \nu_3$ are related by

$$
\begin{bmatrix} \nu_e \\ \nu_\mu \\ \nu_\tau \end{bmatrix} = [U] \begin{bmatrix} \nu_1 \\ \nu_2 \\ \nu_3 \end{bmatrix}
\tag{2.1}
$$

i.e., $\nu_\alpha = U\nu_i$, where U is the unitary matrix that can be parametrized as (in analogy with the CKM matrix):

$$
U = \begin{bmatrix} C_{12}C_{13} & S_{12}C_{13} & S_{13} \\ -S_{12}C_{23} - C_{12}S_{23}S_{13} & C_{12}C_{23} - S_{12}S_{23}S_{13} & S_{23}C_{13} \\ S_{12}S_{23} - C_{12}C_{23}S_{13} & -C_{12}S_{23} - S_{12}C_{23}S_{13} & C_{23}C_{13} \end{bmatrix}
\tag{2.2}
$$

where $C_{ij} = \cos\theta_{ij}$ and $S_{ij} = \sin\theta_{ij}$ and for simplicity we have taken the phase $\delta = 0$, i.e., assumed CP conservation.

The probability, then, that a state, which is pure ν_α at t = 0, is transformed into another flavor β at a time t later (or distance L further), is

$$P_{\alpha\beta} = \delta_{\alpha\beta} - 4 \sum_{j>i} U_{\alpha i} U_{\beta i} U_{\alpha j} U_{\beta j} \sin^2 \left(\frac{\Delta m_{ij}^2 L}{2E} \right), \tag{2.3}$$

with E being the energy of the neutrino and

$$\Delta m_{ij}^2 = m^2(\nu_i) - m^2(\nu_j). \tag{2.4}$$

Thus (assuming CP invariance) we have five independent parameters: three angles, θ_{12}, θ_{23}, and θ_{13} and two Δm_{ij}^2 (the third Δm_{ij}^2 must be linearly related to the first two). All of the neutrino oscillation data must then be capable of being described in terms of these five parameters. Furthermore, if at least two neutrinos have nondegenerate, nonzero masses and if the mixing angles are nonzero, neutrino oscillations must exist.

Clearly, the above expression is complicated and the relationship of experimental results to the five basic parameters somewhat obscure. It also could be that Nature has arranged itself in such a way that this full 3 × 3 formalism is not required, at least to explain the currently available data, and that a two flavor approximation is adequate.

As a minimum such a two-flavor representation provides a much easier way to parametrize the existing and expected future data. In addition, it would be a good approximation if the matrix U has similar structure to the CKM matrix (i.e., is almost diagonal). In this formalism it is customary to represent the results of a single experiment in terms of oscillation between two flavors and involving only two mass eigenstates, hence only one Δm_{ij}^2. The two possible representations of a given neutrino state are then related by

$$\begin{bmatrix} \nu_\alpha \\ \nu_\beta \end{bmatrix} = \begin{bmatrix} \cos\theta & \sin\theta \\ -\sin\theta & \cos\theta \end{bmatrix} \begin{bmatrix} \nu_1 \\ \nu_2 \end{bmatrix}. \tag{2.5}$$

This approximation yields the well known transition probability equation

$$P(\nu_\alpha \to \nu_\beta) = \sin^2 2\theta \; \sin^2 \left(1.27 \Delta m^2 \frac{L}{E} \right), \tag{2.6}$$

giving the probability of conversion of a neutrino of energy E and flavor α into a neutrino of flavor β after traversing a distance L, where L is in km (m), E in GeV (MeV), and $\Delta m^2 = m_1^2 - m_2^2$ in eV^2. This expression is obviously much simpler than the one for the three flavor case and the results of any experiment, within the framework of this formalism, can be easily displayed on a two-dimensional plot since only two physics parameters, θ and Δm^2, are involved.

2.3 Hints for neutrino oscillations

In Section 2.2 we enumerated briefly the current hints for neutrino oscillations. In the present Section we shall elaborate on this topic in more detail, emphasizing especially the results of atmospheric neutrino measurements, since it is these results that are most germane to MINOS. Figure 2.1 summarizes the current picture of positive evidence for neutrino oscillations. In this plot, we take at face value the exclusive limits presented by the relevant experiments with negative results.
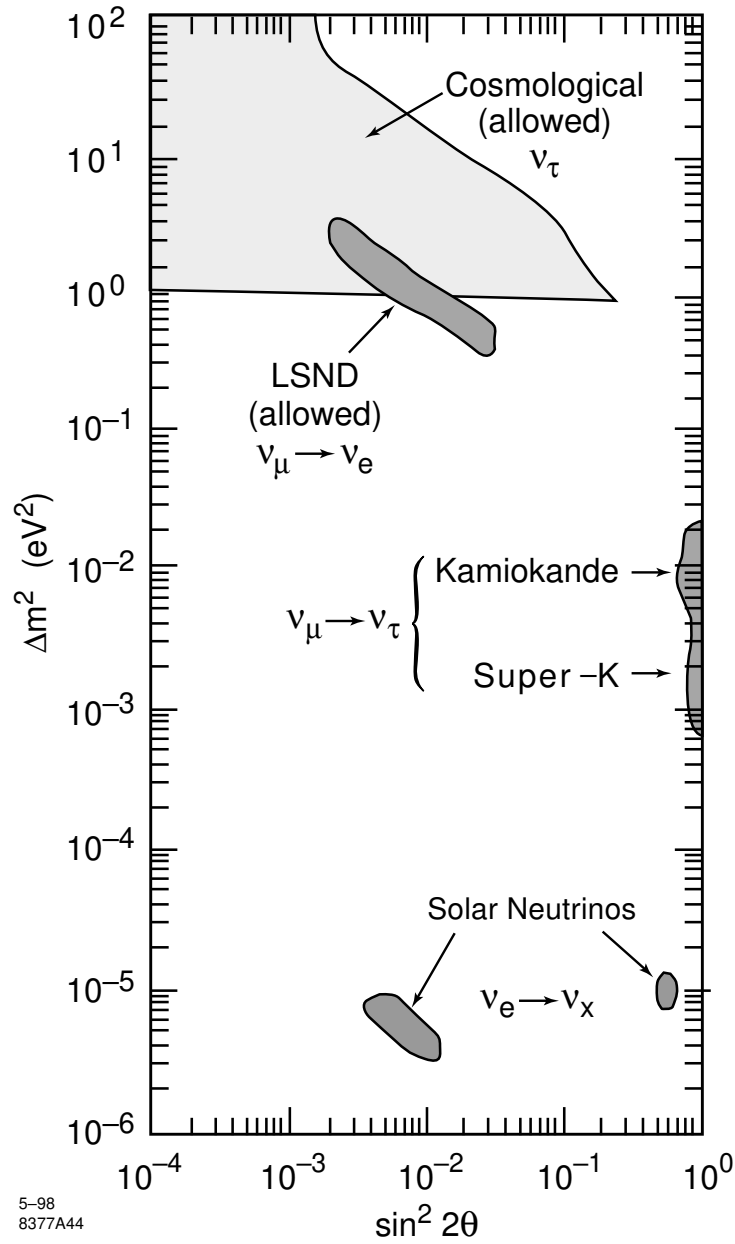
Figure 2.1: Regions of neutrino oscillation parameter space in which positive experimental evidence exists for neutrino oscillations.

We can make several observations about Figure 2.1. First of all, the three sets of experimental results (solar neutrino deficit, atmospheric neutrino anomaly, LSND effect) indicate three different mass-squared scales: approximately 10^{-5}, 10^{-3} to 10^{-2} and 1 eV^2, respectively. As mentioned in Section 2.2, this is incompatible with the conventional picture of three species of neutrinos. One can resolve this difficulty by invoking a fourth, sterile neutrino. Alternatively, at least one of the three sets of data would have to be wrong or require an explanation outside of the area of neutrino oscillations.

The next observation concerns the atmospheric neutrino anomaly. The contour plots shown indicate the best currently available analyses of all the data on zenith angle distributions and the ν_μ/ν_e ratio, from both Kamiokande and Super-Kamiokande. The results of the two experiments give only a small region of overlap in parameter space.

The third point has to do with the LSND effect. The Figure shows only that small part of the LSND-suggested parameter space which is not incompatible with the results of other, negative result, experiments.

Finally, the region in Figure 2.1 indicated by dark matter evidence is somewhat arbitrary and not directly comparable to the three sets of experimental data. The missing dark matter arguments give indications of possible masses of neutrinos, not of their mass squared differences. But if the idea of neutrino mass hierarchy is valid, then this comparison is justified. In general, cosmological mass arguments suggest neutrino masses in the range of a few to a few tens of eV, and do not say anything about mixing angle. Thus, very conservatively, we indicate the suggested region as above 1 eV^2 and cut off the large $\sin^2(2\theta)$ region on the right using the limits from the most recent $\nu_\mu \to \nu_\tau$ oscillation laboratory experiments.

We proceed now to discuss these four pieces of evidence in more detail.

2.3.1   The dark matter issue

The dark matter topic is complex, from both theoretical and observational points of view, and we can give only a very brief discussion of the subject in this document. In addition, it is unlikely that the MINOS experiment will confront this particular area of the physics of neutrino masses. That possibility is not completely excluded, however: if two mass states are relatively heavy (in the few eV range) but almost degenerate, i.e., Δm^2 in the 10^{-3} to 10^{-1} eV^2 range, then MINOS would be sensitive to oscillations between these two massive states. In this Section we limit ourselves to just a brief summary of the most pertinent facts and ideas.

Probably the most significant piece of relevant evidence in this area comes from the measurements of rotation velocities of stars in spiral galaxies, which indicate that these velocities stay constant out to very large distances. From simple mechanics, this implies the existence of mass at large radii in amounts significantly larger than accountable by the observed "shining" matter. There are many candidates for this dark matter: their mass spectrum extends from some 10^{-5} eV for the axion hypothesis to about 10^4 solar masses for the black hole hypothesis – a range of masses of some 75 orders of magnitude. Clearly, this topic is still quite speculative[18].

Cosmological models in which neutrinos provide all the missing mass needed to close the universe call for a neutrino mass of about 30 eV. Aside from other problems with these

models, such neutrinos could not account for all the dark matter in spiral galaxies because the Pauli exclusion principle limits their number and thus requires a mass exceeding 80 eV[18, 19]. The currently favored view is that dark matter is composed of a number of different components, massive neutrinos possibly being one of them.

This cosmological dark-matter motivation for nonzero mass neutrinos has led to the initiation of a short baseline neutrino oscillation search program at CERN, aimed at detection of ν_τ, with two experiments, CHORUS and NOMAD. The data taking phase has been completed (possibly NOMAD may run one more year) and initial results from the analyses have already been reported[20, 21]. The best limits on $\sin^2(2\theta)$ for massive ν_τ (responsible for the cutoff of the cosmologically interesting region on the right in Figure 2.1) come from these experiments.

2.3.2 LSND effect

The LSND Collaboration has published evidence for a $\overline{\nu}_\mu \to \overline{\nu}_e$ transition from an experiment at LAMPF[22]. The data were taken in an experiment where π^+'s produced in a water target by the 800 MeV primary protons were stopped in a downstream copper beam stop. The resulting neutrinos, both from π^+ and μ^+ decays, were then detected in a large liquid scintillator tank. Experimental conditions were such that neutrinos from π^- and μ^- (and hence any primary $\overline{\nu}_e$ component) were suppressed by more than a factor of 10^3.

The experimental signature of a $\overline{\nu}_e$ reaction:

$$\overline{\nu}_e + p \to e^+ + n$$

was correlated signals, in space and time, from the primary positron and the delayed gamma ray from subsequent neutron capture. Cosmic ray background was measured with data taken during the beam off part of the machine cycle. The published analysis yielded 22 candidate events with the expected background of 4.6 ± 0.6. The measured oscillation probability for $\overline{\nu}_\mu \to \overline{\nu}_e$ was P = $(0.31 \pm 0.12 \pm 0.05)\%$.

The resulting contours in oscillation parameter space, at both 90% and 99% confidence levels, are shown in Figure 2.2. Also shown are the excluded regions from the negative results of several other experiments, which apparently rule out a large fraction of the LSND-suggested region. The CCFR[23] and, more recently, NOMAD[21] experiments exclude most of the high mass region, KARMEN[24] and BNL E-776[25] the intermediate region, and the Bugey reactor[26] experiment the lowest Δm^2 region. The LSND "sliver" shown in Figure 2.1 represents that part of the LSND region which is compatible with all of those experiments. The LSND data cannot be used to determine a unique set of oscillation parameters for this allowed region because the L/E range is not very large and its value is not determined very precisely on an event by event basis.

The LSND collaboration is continuing to take data, and with the new data they should be able to improve their statistics with somewhat different systematics. In addition, the Collaboration has analyzed the decay-in-flight data, which are sensitive to $\nu_\mu \to \nu_e$ oscillations with the ν_μ from π decay in flight[27]. Their analysis of these data is consistent with the published results but the significance is weaker and one is not able to determine the oscillation parameters any better.
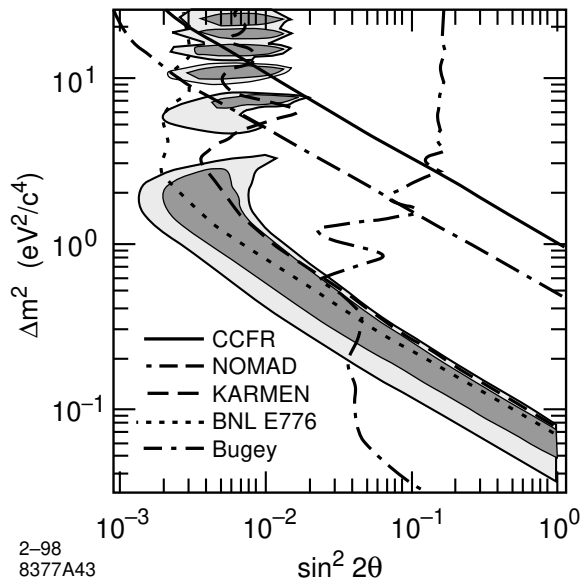
Figure 2.2: Regions of neutrino oscillation parameter space in which $\overline{\nu}_\mu \rightarrow \overline{\nu}_e$ oscillations are suggested by the LSND experiment.

The experiment which is able to confront the LSND results most directly is KARMEN[24], which uses neutrinos from the spallation source ISIS at the Rutherford Appleton Laboratory. This experiment is very similar to LSND in the reaction studied, the source of neutrinos, and the general method of detection. Its sensitivity is lower by a factor of 2 to 3 because of its higher backgrounds, smaller detector mass and the shorter source to detector distance. However the fine grained segmentation of their detector and the excellent L/E determination (2 to 3%) for each event partially offsets the more negative features. KARMEN is just commencing a new run, with a much better shielding arrangement which has significantly reduced the background from cosmic-muon produced neutrons. It was those neutrons which limited the sensitivity of the original run. Indications from the initial data taken under the changed conditions are that the improved shielding works as well as expected and that the experiment should be able to cover the LSND region completely[28].

Recently a new proposal, MiniBooNE[29], has been submitted to Fermilab with a goal of investigating the LSND effect with a new detector, similar to LSND, exposed to neutrinos from the Fermilab 8-GeV Booster. Their sensitivity, based on Monte Carlo calculations, is claimed to be roughly a factor of 3 to 5 better than LSND. The MiniBooNE proposal has been given Stage I approval by the Fermilab Director following the May 1998 Fermilab PAC meeting.

2.3.3 The atmospheric neutrino anomaly

It is this specific neutrino puzzle that MINOS can confront most directly and thus the situation here is most relevant to the potential physics of the MINOS experiment. Accordingly we shall give a more detailed description of the current status of this anomaly.

The cosmic rays (protons or heavier nuclei), which impinge on our atmosphere from

above, will generally interact in its first 100 g or so, i.e., in the top 10% of the atmosphere. These interactions will ordinarily produce a number of π's and K's, which subsequently will either interact themselves, thus continuing the hadronic cascade, or decay. These first few interactions, which produce most of the secondary hadrons, generally occur far enough from the earth's surface that most of the muons resulting from π or K decay will themselves decay before hitting the earth. The net effect is that the ratio of ν_μ's to ν_e's arriving at the earth, in the 1 GeV range and below, will be close to a factor of 2 (one of each flavor from muon decay, and one ν_μ from hadron decay).

There are now a number of theoretical calculations which attempt to perform rather detailed and realistic calculations of this ratio as a function of neutrino energy, putting in all that is known about the relevant physical phenomena: cosmic ray composition and spectra, the evolution of hadronic cascades, geomagnetic field effects, and the exact nature of pion, kaon, and muon decays[30]. These calculations predict both the absolute values of the fluxes and the ratio of neutrino flavors. They tend to reproduce very closely the result of the above simple argument and find that, even though there is an uncertainty of about $\pm 20\%$ in the absolute normalization of the neutrino flux, the flavor ratio calculation is good to better than $\pm 5\%$.

Several experiments have now studied this ratio and generally find a deficiency of muon neutrinos, the so called "atmospheric neutrino anomaly". The experiments can be conveniently classified into two categories: those that use large water Cerenkov counters and those that use solid media instrumented with gas chambers. The purely experimental systematics in these two sets of detectors should be quite different. We discuss the results from these two sets of experiments in the next two Sections.

2.3.3.1   The results from water Cerenkov counters

The initial studies of atmospheric neutrinos were performed by the IMB (Irvine-Michigan-Brookhaven) Collaboration[31] and the Kamiokande Collaboration[32]. Both detectors were located deep underground; both were initially motivated by the search for proton decay; both used ultra pure water as a neutrino target material and as the Cerenkov radiator. The photomultipliers viewed the volume from the inner surface of the detector. The Kamiokande experiment had the capability to veto cosmic ray muons by means of an optically isolated outer layer of water viewed by an independent set of photomultipliers. The IMB analysis relied on vetoing the throughgoing muons in software. It was the pattern of hits in the photomultipliers which allowed these detectors to distinguish between charged current ν_μ and ν_e interactions. The fact that this method works in the GeV range and below was verified by exposure of similar detector configurations at KEK to muon and electron beams from the KEK accelerator. The identification was shown to be good at the level of 99%[33].

Water Cerenkov experiments can make reasonably good estimates of electron neutrino energies from the total numbers of hits observed. On the other hand, for ν_μ's the events have to be classified into "fully contained events," where the muon stops in the detector, and the "partially contained, multi-GeV events," where the muon exits the detector. The total energy can be determined only for the fully contained events. The data are generally analyzed separately for the sub-GeV sample (low energy ν_e's and ν_μ's, namely those with $E_{vis} < 1.33$ GeV) and the multi-GeV sample (high energy ν_e's and ν_μ's, and exiting muon

events). To eliminate the uncertainty in the absolute flux normalization, it is conventional to evaluate and present a ratio of ratios, R, defined by:

$$R = \frac{(\nu_\mu/\nu_e)_{data}}{(\nu_\mu/\nu_e)_{MC}}.$$

In addition, one can try to obtain some information about the L/E value of the observed events. To a good approximation one can deduce the value of L (flight path of the neutrino) from the measured zenith angle. However the correlation is such that for zenith angles of the order of 90°, a small error in the angle measurement gives a large error in the value of L. Furthermore, as mentioned above, one does not measure energy for all the events. Thus it is conventional to look at the flavor ratio and at the individual ν_μ and ν_e rates as functions of zenith angle for the two sets of events. Because of measurement errors, Fermi motion, and the finite momentum carried off by the unseen low energy particles, the zenith angle measurement improves at higher energies.

Both IMB and Kamiokande reported deficits of muon neutrinos, i.e., values of R below unity. In addition, the Kamiokande data showed a zenith angle dependence of the R value for the multi-GeV data set[34]. This effect, even though not statistically compelling, was in the direction which would be expected from the neutrino oscillation hypothesis, i.e., larger depletion of ν_μ's for the upward going direction. This angular dependence allowed one to set an upper limit of about 0.1 eV^2 on Δm^2. The sub-GeV data sample was consistent with no angular dependence[32, 34]. Neither of these experiments could provide any significant information on the neutrino oscillation mode, i.e., $\nu_\mu \leftrightarrow \nu_e$ vs $\nu_\mu \leftrightarrow \nu_\tau$ or $\nu_\mu \leftrightarrow \nu_{sterile}$.

Recently[13], the Super-Kamiokande Collaboration reported their analysis of the first 535 days of data taking from their new detector. Like the original Kamiokande detector, the new detector is also located in the Mozumi mine in Japan and is also a cylindrical water Cerenkov detector with an optically separated outer region used for anti-coincidence to eliminate cosmic ray muon background. The primary difference is the much larger fiducial mass of the Super-Kamiokande detector: 22.5 kt, about 20 times larger than Kamiokande or IMB. In addition to increasing the rate of atmospheric neutrino interactions in proportion to the fiducial volume increase, this larger size increases the fraction of contained ν_μ events.

At the present time the Super-Kamiokande detector has collected 33.0 kt-years of analyzed atmospheric neutrino data[13]. The global R values for both the sub-GeV and multi-GeV data sets are consistent with the Kamiokande values, as can be seen from Table 2.1.

Detector	Sub-GeV		Multi-GeV	
	Observed	Expected	Observed	Expected
Kamiokande	0.60±0.06±0.05	1.00	0.57±0.08±0.07	1.00
Super-Kamiokande	0.63±0.03±0.05	1.00	0.65±0.05±0.08	1.00

Table 2.1: Comparison of the Kamiokande[34] and Super-Kamiokande[13] R-value results. The ratios are calculated based on the Honda *et al.*[30] flux model. The first error shown for each ratio is from statistics and the second is from systematics.

In addition, there is a pronounced and statistically significant variation of the ν_μ rate as a function of the zenith angle, as shown in Figure 2.3(a), with the upward going ν_μ events being significantly depleted. This effect increases as the neutrino energy increases. In contrast, the ν_e distribution appears to be consistent with the Monte Carlo prediction if one allows for a 20% flux normalization uncertainty.

All of the available Super-Kamiokande data have been analyzed with programs similar to those used for the Kamiokande analysis[35]. The results of these analyses, for the $\nu_\mu \rightarrow \nu_\tau$ hypothesis, are shown in Figure 2.3(b). Based on these data, the Super-Kamiokande Collaboration has concluded that the data give evidence for neutrino oscillations in the modes $\nu_\mu \rightarrow \nu_\tau$ or $\nu_\mu \rightarrow \nu_{sterile}$, with $10^{-3} < \Delta m^2 < 10^{-2}$ eV^2 and $\sin^2(2\theta) > 0.8$.

2.3.3.2   Results from the solid gas-chamber detectors

The fine grained gas calorimeters which have contributed data relevant to the question of the atmospheric neutrino anomaly were also originally constructed to search for proton decay. Hence they were also located underground so as to provide adequate shielding against cosmic rays. The results from the first two of these detectors, Frejus[36] and NUSEX[37] indicated that the value of R is consistent with unity, i.e., no anomaly, even though the errors on these measurements were quite large. Accordingly, there was a question for some time whether the Kamiokande-IMB result could be caused by some instrumental effect. More specifically, some of the possible differences in the experimental setups that could be responsible for the difference in the results between water Cerenkov and iron calorimeter detectors are: difference in neutrino interactions in water and iron, different detection technique, different energy and spatial resolution, different methods of neutrino flavor determination, and different depths and hence different cosmic ray muon rates.

The importance of the Soudan 2 experiment is that it is able to confront these specific questions. Soudan 2 is a 1 kt iron TPC which produces event pictures of close to heavy-liquid bubble-chamber quality. Thus it is easy to distinguish track-like and shower-like events. At atmospheric neutrino energies, about two thirds of the events are quasi-elastic, containing only a single lepton plus a recoil proton. In Soudan 2 almost half of the recoil protons are visible as short low energy tracks whereas in water Cerenkov detectors most of the recoil protons are below Cerenkov threshold and hence invisible. The tracks and showers can be reconstructed in three dimensions. An ionization measurement is also obtained and, together with a Coulomb scattering measurement, allows one to to separate protons from muons.

Based on analysis of the current data, which corresponds to an exposure of 3.9 kt years[38, 39], the Soudan 2 Collaboration has reported a value of R of 0.64 $\pm$ 0.11 $\pm$ 0.06. This result is completely compatible with, and hence confirms the existence of, the atmospheric neutrino anomaly first seen by the water Cerenkov experiments. The Soudan 2 data can provide a better determination of the L/E values for individual events because the detector measures recoil protons in some quasi-elastic interactions. The preliminary results of this analysis[39] favor values of Δm^2 somewhat higher than those suggested by Super-Kamiokande.
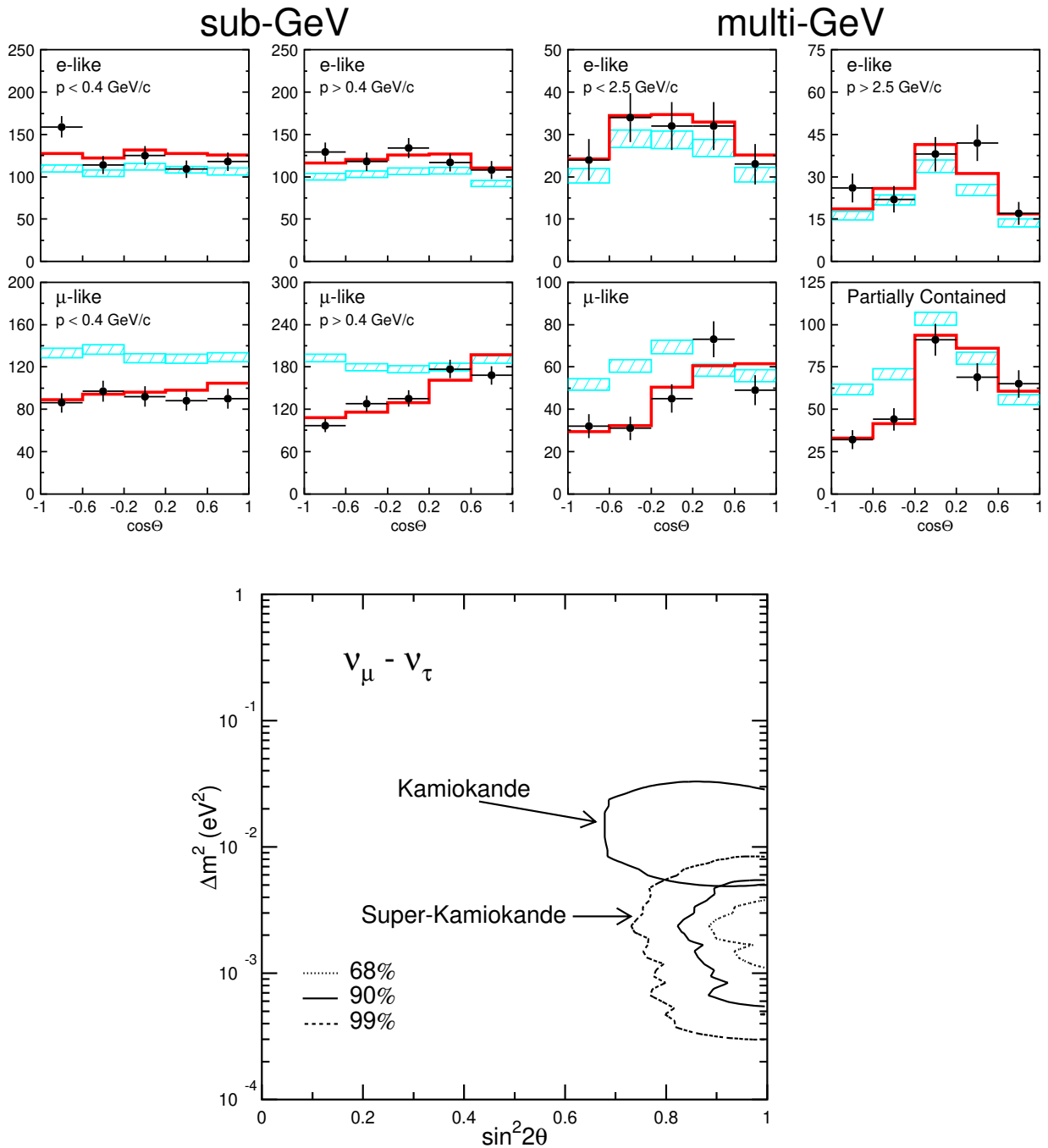
Figure 2.3: Recent results from the Super-Kamiokande experiment and final results from the Kamiokande experiment. Upper (a): Expected and observed zenith angle distributions for Super-Kamiokande sub-GeV and multi-GeV events (shaded bars are the no-oscillation predictions, histograms are the best-fit distributions with oscillations, and points with error bars are the data). Lower (b): Regions of neutrino oscillation parameter space allowed by atmospheric neutrino data from the Super-Kamiokande and Kamiokande experiments.

2.3.3.3 Upward-going muons

In addition to interacting within the fiducial mass of a detector, neutrinos can interact in the rock surrounding the detector. If a rock interaction occurs close enough to the detector, muons resulting from ν_μ charged-current processes can penetrate to the detector and be measured there. Generally, only muons from upward-going neutrinos can be identified as originating from that source, since the flux of muons from downward-going neutrinos is very much smaller than the flux of direct muons (from pion decay in the atmosphere) which penetrates the rock overburden of an underground detector.

The existence of oscillations will affect the results of upward-going muon measurements because oscillations can deplete the ν_μ flux as a function of L/E, and hence of zenith angle. Thus, any discrepancies between predictions and measurements of the rate and zenith angle distribution of upward-going muons can provide information about neutrino oscillation parameters. Detectors to date have not been able to measure the energies of muons unless they stop in the detectors. The ratio of stopping to through-going muons can also be sensitive to the values of oscillation parameters.

The early measurements of upward-going muons performed in the Baksan[40] and IMB[41] detectors showed no evidence of anomalies, but were handicapped by the relatively small sizes of these detectors. More recently, MACRO[42], Kamiokande[43] and Super-Kamiokande[44] have all reported deviations from the predictions, in both the rates and zenith angle distributions. The rate deviations provide less information because the comparison with predictions relies heavily on the knowledge of the absolute normalization of the atmospheric neutrino flux. The zenith angle distributions can provide information which is less sensitive to uncertainties in the theoretical models. The results of all three of these experiments can be explained by neutrino oscillations with the parameters derived from observations of atmospheric neutrino interactions occurring within the detectors themselves, as discussed above.

2.3.3.4 Overview of the ν_{atm} situation

The currently available results on the atmospheric neutrino R-value anomaly are summarized in Figure 2.4. It appears that there is a trend to convergence on a value of R $\sim$ 0.6. The best estimate of the magnitude of the error on this quantity, due mainly to uncertainties in neutrino flux calculations, is about 0.05. Thus the effect appears to be real. In addition, the observed zenith angle dependence of the ν_μ rate favors the oscillation hypothesis as the explanation of this anomaly.

To date, no accelerator experiments have been able to confront these results. On the other hand, two reactor experiments, near Chooz, France, and in Palo Verde, Arizona, have been constructed to test the hypothesis that this anomaly is due to $\nu_\mu \leftrightarrow \nu_e$ oscillations. The CHOOZ experiment has already reported highly significant results[45]: they find no evidence for $\nu_\mu \rightarrow \nu_e$ oscillations with large values of $\sin^2(2\theta)$ and are able to set a 90% CL limit on Δm^2 of 9×10^{-4} eV^2 at $\sin^2(2\theta) = 1$. The result rules out almost all of the Super-Kamiokande suggested region when their data are interpreted under the $\nu_\mu \leftrightarrow \nu_e$ hypothesis.

The situation on the determination of oscillation parameters (assuming the oscillation hypothesis is the correct one) from the zenith angle and L/E distributions, the R-value data and upward going muon results, is still murky. Kamiokande and Super-Kamiokande results
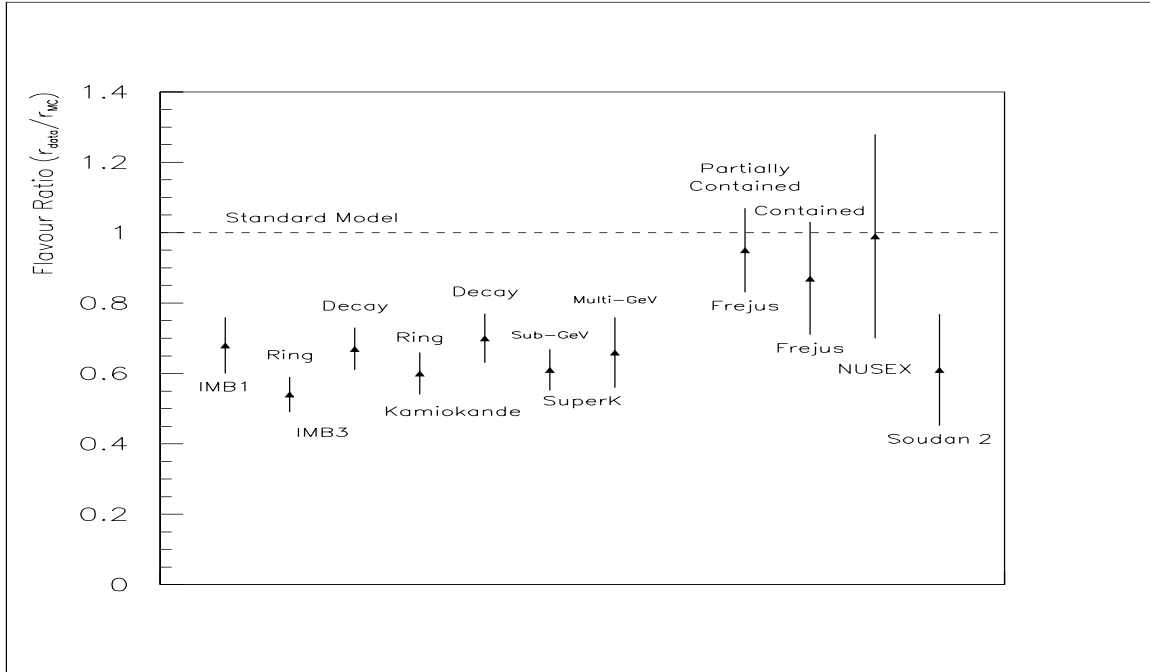
Figure 2.4: Comparison of experimental results for the atmospheric neutrino flavor ratio R. Results from water Cerenkov detectors are on the left and those from solid gas-chamber detectors are on the right.

appear to favor somewhat different values of Δm^2 although they both require values of $\sin^2(2\theta)$ close to unity. The preliminary results reported on this issue by the Soudan 2 Collaboration favor the region of Δm^2 around 10^{-2} eV^2. The recent results from the MACRO, Kamiokande and Super-Kamiokande experiments on upward-going muons are consistent with this full range of Δm^2 values. It is our (conservative) view that a reasonable conclusion from all the data would be

$$\log_{10}(\Delta m^2) = -2.5 \pm 0.5$$

(where Δm^2 is in eV^2) if it is neutrino oscillations which cause the atmospheric neutrino anomaly. Furthermore, the results from CHOOZ and Super-Kamiokande favor $\nu_\mu \to \nu_\tau$ or $\nu_\mu \to \nu_{sterile}$ (or a mixture of the two) as the most likely mode.

2.3.4   The solar neutrino deficit

Because it is unlikely that MINOS can confront directly the question of the solar neutrino deficit, we shall discuss the situation here only very briefly. We know that the nuclear fusion reaction of protons into helium, that is responsible for the production of most of the solar energy, must also generate electron neutrinos, specifically 2 ν's for every helium nucleus made. Thus from the amount of total solar energy generated we can predict the total number of neutrinos created and thus the neutrino flux that should reach the earth.

To obtain the spectrum of these neutrinos, one has to understand the details of the reactions that compose this fusion cycle, as well as the less important CNO cycle. The

conventional belief is that the Standard Solar Model[46] is reliable enough that the spectra are understood at the level of a few percent.

The last three and a half decades have seen an extensive experimental effort to detect solar neutrinos and measure their flux. Four major experiments have been mounted and obtained results: Homestake[47], Kamiokande[48], GALLEX[49], and SAGE[50]. They all measure a smaller flux of neutrinos than predicted. Furthermore, because the neutrino energy threshold for detection is quite different in these experiments (except GALLEX and SAGE, which use similar techniques and hence have the same threshold), quantitative analysis of the discrepancies allows one to draw conclusions about any possible energy dependence of the deficit. It appears that the observed depletion does have an energy dependence. Such an effect would be very difficult to generate by a variation of the parameters in the solar model. Hence, one is led to searching for an explanation in the area of particle physics; one of the possibilities would be neutrino oscillations.

There has been an extensive theoretical effort to see how well one can explain the solar neutrino deficiency through the mechanism of neutrino oscillations. A very important contribution in this general area has been by Mikheyev and Smirnov[51] and Wolfenstein[52], who first showed that the different interaction cross sections of the three neutrino species in matter can effectively contribute to neutrino oscillations. These so called "matter oscillations" are able to explain the observed neutrino flux deficit. Two general regions, shown in Figure 2.1 with Δm^2 around 10^{-5} eV^2, appear to fit all of the available data[53]. In addition there is a pure vacuum oscillation solution[54] with a much lower value of Δm^2 (off scale in the Figure) of around 10^{-11} eV^2.

It is unlikely that the solar neutrino anomaly will be illuminated significantly by any terrestrial experiment, except possibly by the proposed KamLAND experiment in Japan, which relies on a very large reactor neutrino detector in the former Kamiokande cavern. The next generation of solar neutrino detectors, e.g., SNO (with its ability to measure the neutral current reaction rate), Super-Kamiokande (with its ability to measure the high energy portion of the flux as well as temporal variations) and Borexino (with its ability to measure the energy spectrum of low energy neutrinos in real time) should, however, be able to shed some new light on this situation.

2.4   New results expected before 2002

We expect that there will be some new experimental information by the year 2002 which will be relevant to the question of possible neutrino oscillations. On the other hand, it is unlikely that definitive answers will exist by that time. We elaborate next on what new information will be available in each of the four areas corresponding to different "hints."

Regarding "dark-matter" neutrinos, it is possible that CHORUS and/or NOMAD will find convincing ν_τ events. On the other hand, their future reach, beyond what is known today, is considerably less than an order of magnitude. Thus it is not clear how convincing the signal would be if they observe the few events that would be allowed by the present limits. In any case, such an observation would not be able to determine the value of Δm^2.

The LSND result should be confirmed or contradicted by 2002. The current LSND run in 1998, if it gives results consistent with the past ones, should determine somewhat better

the parameter space of the LSND effect. Equally or even more important is the KARMEN experiment, where an order of magnitude improvement in sensitivity over the past experiment is expected. KARMEN results, which should be available in a year or two, should provide a very strong check on the LSND results.

Several new experimental results will undoubtedly shed some light on the solar neutrino puzzle by 2002. The biggest impact should come from the SNO, Borexino and Super-Kamiokande data. The SNO experiment will be able to measure the neutral current cross section of the solar neutrinos and thus determine the absolute value of the solar neutrino flux. It is a very hard measurement but the initial results should be available by 2002. In addition, they can obtain good total energy measurements for the inverse beta decay events. Super-Kamiokande has the ability to measure the energy spectrum of the neutrinos above 6 MeV and to look for the diurnal and semi-annual variations in the observed interaction rate. Borexino can measure the energy of low energy neutrino interactions as well as the time dependence of the energy spectrum. All of these measurements can provide crucial information that will be able to test the validity of various models attempting to explain the solar neutrino deficit. It is unlikely, in our opinion, that other experiments currently in the planning or construction phase, i.e., ICARUS, the Iodine experiment at the Homestake mine, or the helium detector experiments, will have any significant results by 2002.

As far as the atmospheric neutrino anomaly is concerned, new results are expected in three areas:

a) Both Super-Kamiokande and Soudan 2 will continue their investigations of atmospheric neutrinos. The Super-Kamiokande R value measurements are already beginning to be limited by systematics. Thus additional data will not contribute significantly to a better value of this parameter. The zenith angle distributions, however, will become more informative with a larger data sample.

   The Soudan 2 experiment can make an independent contribution towards understanding the zenith angle distribution and its impact on the estimate of Δm^2. At low energies (below 1 GeV), the major problem in the L/E analysis is not statistical but the smearing of both L and E by the fact that one has to use the outgoing particles to obtain the energy and angle of the interacting neutrino. Both the Fermi motion of the struck nucleon and the presence of unobserved particles smear the calculations of L (from the angle) and of E. Soudan 2 has a potentially significant advantage here over Super-Kamiokande in that recoil protons and low energy charged pions can be observed and measured, thus substantially reducing smearing. The improved L/E resolution of Soudan 2 might well compensate for the poorer statistics. Thus Soudan 2 should be able to test in the future the angular distribution of the interacting neutrinos.

b) The CHOOZ experiment should complete their analysis and the Palo Verde experiment should soon be able to either confirm or cast doubt on the CHOOZ result. Together these experiments should be able to convincingly demonstrate the absence (or otherwise) of $\nu_e \rightarrow \nu_\mu$ oscillations down to values of Δm^2 somewhat below 10^{-3} eV^2 for large mixing.

c) Most important, the K2K experiment[55], which observes neutrinos from KEK with the Super-Kamiokande detector, will be the first accelerator experiment to test the

hypothesis that the atmospheric neutrino anomaly is due to $\nu_\mu \to \nu_\tau$ or $\nu_\mu \to \nu_{sterile}$. Their calculated sensitivity, expected to be achieved by 2002, for both $\nu_\mu \to \nu_\tau$ and $\nu_\mu \to \nu_e$ oscillations, is shown in Figure 2.5.
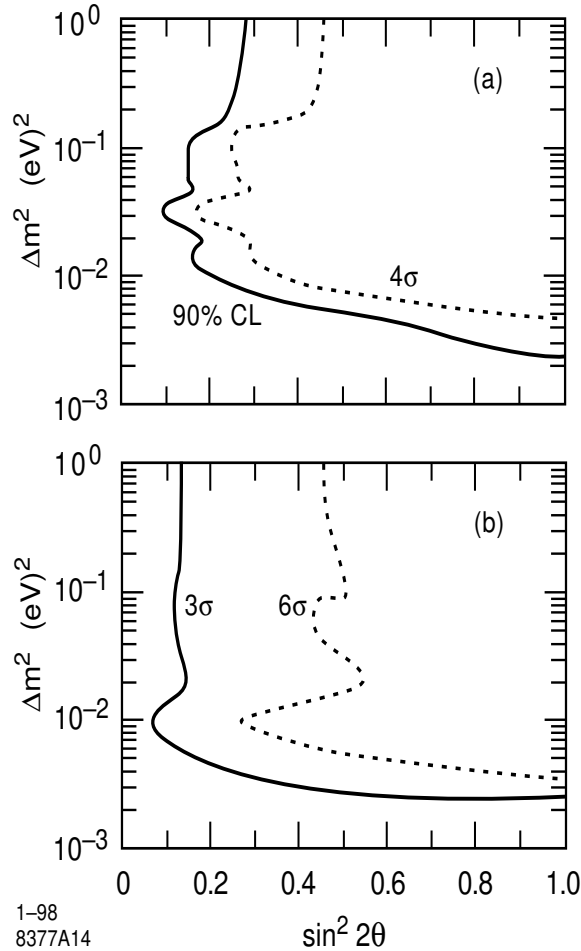
Figure 2.5: Predicted sensitivity of the K2K experiment by the year 2002. Limits on neutrino oscillation parameters are shown for (a) $\nu_\mu \to \nu_x$ (disappearance) and (b) $\nu_\mu \to \nu_e$ (appearance), for the case of no oscillation signal. Note the linear scale in $\sin^2(2\theta)$.

In summary, we list some possible resolutions of the atmospheric neutrino anomaly:

a) The process responsible is $\nu_\mu \to \nu_\tau$ oscillations with Δm^2 in the range 2×10^{-3} to 10^{-2} eV^2. This is the most likely hypothesis if all the relevant existing data are taken at face value. If this is indeed the correct explanation, and Δm^2 is in the upper range, then the results of the K2K experiment should go a long way towards establishing the validity of this hypothesis. In addition, the Soudan 2 L/E distributions and Super-Kamiokande zenith angle measurements would be able to support such a conclusion.

b) The process responsible is $\nu_\mu \to \nu_{sterile}$ with Δm^2 in the range 2×10^{-3} to 10^{-2} eV^2. The existing data do not distinguish between this hypothesis and hypothesis (a) above,

but theoretical prejudice has been that (a) is the less radical conjecture. The K2K experiment will provide only very limited information which could discriminate between these two hypotheses.

c) The process responsible is $\nu_\mu \rightarrow \nu_\tau$ or $\nu_\mu \rightarrow \nu_{sterile}$ oscillations with $\Delta m^2 = 2 \times 10^{-3}$ eV^2 or lower. This possibility appears less likely than the two above when one considers all the available data. If this hypothesis is correct, then we would not expect to see any significant signal from reactor or accelerator experiments until MINOS begins taking data.

Of course, the complete oscillation picture could be more complex. The actual physical situation probably includes contributions from several oscillation modes with different strengths. For completeness, we should also include two other possibilities, even though they do not appear very likely today:

d) The atmospheric neutrino anomaly exists but is unrelated to neutrino oscillations. So far, no satisfactory alternative hypothesis has been put forth to explain the effect, but this does not necessarily exclude this dark-horse possibility.

e) There is no atmospheric neutrino anomaly – the observed effects are either instrumental and/or explainable by modifications of the cosmic ray shower models. Unlikely as this possibility may seem in light of the convergence of most recent results on R = 0.6 and the observation of an up-down asymmetry in atmospheric ν_μ's by Super-Kamiokande, it must be kept in mind if a self-consistent picture for other alternatives cannot be formulated.

Chapter 2 References

[1] W. Pauli's bold suggestion of the existence of a new particle, the neutrino, was never published. The idea was put forth in a letter dated December 4, 1930, to the attendees of a conference in Tubingen. It was addressed to "Dear Radioactive Ladies and Gentlemen." Pauli himself was not able to participate in the meeting because of a prior commitment to attend a ball in Zurich. The letter has been reproduced in a number of places, e.g., N. Solomey, "The Elusive Neutrino" (Scientific American Library, 1997), pp. 16-17.

[2] F. Reines and C.L. Cowan., Phys. Rev. **92**, 830 (L), (1953).

[3] M. Goldhaber, L. Grodzins and A.W. Sunyar, Phys. Rev. **109**, 1015 (L), (1958).

[4] G. Danby *et al.*, Phys. Rev. Lett. **9**, 36 (1962).

[5] Some of the key early papers are: F.J. Hasert *et al.*, Phys. Lett. **B46**, 121 (1973); F.J. Hasert *et al.*, Phys. Lett. **B46**, 138 (1973); A. Benvenuti *et al.*, Phys. Rev. Lett. **32**, 800 (1974); B.C. Barish *et al.*, Phys. Rev. Lett. **34**, 538 (1975).

[6] Some of the early papers are: B. Aubert *et al.*, Phys. Rev. Lett. **32**, 1457 (1974); B.C. Barish *et al.*[5]; D. Cline *et al.*, Phys. Rev. Lett. **37**, 252 (1976); F.A. Harris *et al.*, Phys. Rev. Lett. **39**, 437 (1977).

[7] F. Reines *et al.*, Phys. Rev. Lett. **37**, 315 (1976); A.M. Cnops *et al.*, Phys. Rev. Lett. **41**, 357 (1978).

[8] C. Caso *et al.* (Particle Data Group), Eur. Phys. J. **C3**, 1 (1998).

[9] For a comprehensive review of the subject of neutrino masses see S.M. Bilenky and S.T. Petcov, Rev. Mod. Phys. **59**, 671 (1987).

[10] F. Zwicky, Helv. Phys. Acta **6**, 110 (1933); V.C. Rubin and W.K. Ford, Astrophys. J. **159**, 379 (1970); T.S. van Albada *et al.*, Astrophys. J. **295**, 305 (1985).

[11] The first experimental paper on the subject was by R. Davis, Jr., Phys. Rev. Lett. **12**, 303 (1964); for a recent review see A.Y. Smirnov, in Proceedings of the 17th International Conference on Neutrino Physics and Astrophysics (Neutrino '96), edited by K. Enqvist, K. Huitu and J. Maalampi (World Scientific, 1997), pp. 3855; for a review of solar models see J.N. Bahcall and M.H. Pinsonneault, Rev. Mod. Phys. **67**, 1 (1995); for a nonconventional point of view, arguing that the solar neutrino data are consistent with solar models if all the uncertainties are taken into account, see A. Dar and G. Shaviv, Astrophys. J. **468**, 933 (1996).

[12] The initial evidence came from K.S. Hirata *et al.*, Phys. Lett. **B280**, 146 (1992); Y. Fukuda *et al.*, Phys. Lett. **B335**, 237 (1994); R. Becker-Szendy *et al.*, Phys. Rev. **D46**, 3720 (1992).

[13] Y. Fukuda *et al.*, Phys. Rev. Lett. **81**, 1562 (1998).

[14] C. Athanassopoulos *et al.*, Phys. Rev. Lett. **75**, 2650 (1995); but see also J.E. Hill, Phys. Rev. Lett. **75**, 2654 (1995). See also References[22, 27].

[15] The possibility of neutrino oscillations was first suggested by B. Pontecorvo, Zh. Eksp. Theor. Fiz. **33**, 549 (1957) and **34**, 247 (1958).

[16] G.S. Abrams *et al.*, Phys. Rev. Lett. **63**, 2173 (1989) for the SLC results; J.R. Carter in Proceedings of the Joint International Lepton-Photon Symposium and Europhysics Conference on High Energy Physics, edited by S. Hegarty, K. Potter and E. Quercigh (World Scientific, 1992), pp. 1-26, for a summary of LEP results from Z line shape; for a recent compendium of the latest CERN results using other methods see S.C.C. Ting, Phys. Rep. **279**, 204 (1997).

[17] For a recent review of various possible schemes see A.Yu. Smirnov, in Proceedings of the 28th International Conference on High Energy Physics, edited by Z. Ajduk and A.K. Wroblewski (World Scientific, 1997), pp. 288-306.

[18] For a comprehensive review see e.g., K. Griest in "Particle and Nuclear Astrophysics and Cosmology in the Next Millenium," edited by E.W. Kolb and R.D. Peccei (World Scientific, 1994), pp. 21-28; M. Fich and S. Tremaine, Ann. Rev. Astron. Astrophys., **29**, 409 (1991).

[19] J.E. Gunn and S. Tremaine, Phys. Rev. Lett. **42**, 407 (1979).

[20] E. Eskut *et al.* (CHORUS Collaboration), Phys. Lett. **B424**, 202 (1998) and **B434**, 205 (1998).

[21] J. Altegoer *et al.* (NOMAD Collaboration), Phys. Lett. **B431**, 219 (1998).

[22] C. Athanassopoulos *et al.*, Phys. Rev. Lett. **77**, 3082 (1996) and Phys. Rev. **C55**, 2079 (1997).

[23] K.S. McFarland *et al.*, Phys. Rev. Lett. **75**, 3993 (1995); A. Romosan *et al.*, Phys. Rev. Lett. **78**, 2912 (1997).

[24] J. Kleinfeller *et al.*, in "Proceedings of the 17th International Conference on Neutrino Physics and Astrophysics," edited by K. Enqvist, K. Huitu, and J. Maalampi (World Scientific, 1997), pp. 193-202.

[25] L. Borodovsky *et al.*, Phys. Rev. Lett. **68**, 274 (1992).

[26] B. Achkar *et al.*, Nucl. Phys. **B434**, 503 (1995).

[27] C. Athanassopoulos *et al.*, Phys. Rev. Lett. **81**, 1774 (1998).

[28] G. Drexlin *et al.*, Prog. Part. Phys. **40**, 193 (1998).

[29] BooNE Collaboration, Proposal submitted to Fermilab National Laboratory, Janet Conrad and William C. Louis III, spokespersons.

[30] G. Barr, T.K. Gaisser, and T. Stanev, Phys. Rev. **D39**, 1140 (1993); M. Honda *et al.*, Phys. Lett. **B248**, 193 (1990); H. Lee and Y.S. Koh, Nuovo Cimento **105B**, 883 (1990).

[31] R. Becker-Szendy *et al.*, Phys. Rev. **D46**, 3720 (1992).

[32] K.S. Hirata *et al.*, Phys. Lett. **B280**, 146 (1992).

[33] S. Kasuga *et al.*, Phys. Lett. **B374**, 238 (1996).

[34] Y. Fukuda *et al.*, Phys. Lett. **B335**, 237 (1994).

[35] Performed by Kenji Kaneyuki, Tokyo Institute of Technology, Super-Kamiokande Collaboration.

[36] Ch. Berger *et al.*, Phys. Lett. **B227**, 489 (1989).

[37] M. Aglietta *et al.*, Europhys. Lett. **8**, 611 (1989).

[38] W.W.M. Allison *et al.*, Phys. Lett. **B391**, 491 (1997) and "Updated measurement of atmospheric neutrino flavor ratio in Soudan 2," draft in preparation, to be submitted for publication.

[39] H.R. Gallagher, "Atmospheric neutrinos in Soudan 2," talk presented at the ICHEP 98 Conference, Vancouver, July 1998.

[40] M.M. Bolier *et al.*, Proceedings of the 24th International Cosmic Ray Conference, Rome, 1995, Vol. 1, p. 722.

[41] R. Becker-Szendy *et al.*, Phys. Rev. Lett. **69**, 1010 (1992).

[42] M. Ambrosio *et al.*, Phys. Lett. **B434**, 451 (1998).

[43] S. Hatakeyama *et al.*, Phys. Rev. Lett. **81**, 2016 (1998).

[44] T. Kajita, "Atmospheric neutrino results from Super-Kamiokande and Kamiokande – Evidence for neutrino oscillations," talk presented at the Neutrino 98 Conference, Takayama, Japan, June 1998.

[45] M. Apollonio *et al.*, Phys. Lett. **B420**, 397 (1998).

[46] J.N. Bahcall and M.H. Pinsonneault, Rev. Mod. Phys. **67**, 1 (1995).

[47] R. Davis, Jr., D.S. Harmer and K.C. Hoffman, Phys. Rev. Lett. **20**, 1205 (1968); B.Cleveland *et al.*, Nucl. Phys. **B38**, 47 (1995).

[48] K.S. Hirata *et al.*, Phys. Rev. **D44**, 2241 (1991).

[49] P. Anselmann *et al.*, Phys. Lett. **B327**, 377 (1994) and Phys. Lett. **B342**, 440 (1995).

[50] A.I. Abazov *et al.*, Phys. Rev. Lett. **67**, 3332 (1991).

[51] S.P. Mikheyev and A.Yu. Smirnov, Sov. J. Nucl. Phys. **42**, 913 (1985) and Sov. Phys. JETP **64**, 4 (1986) and Prog. Part. Nucl. Phys. **23**, 41 (1989).

[52] L. Wolfenstein, Phys. Rev. **D17**, 2369 (1978).

[53] See for example N. Hata and P. Langacker, Phys. Rev. **D50**, 632 (1994).

[54] P. Krastev and S.T. Petcov, Phys. Rev. Lett. **72**, 1960 (1994).

[55] KEK Proposal E-362; also Y. Suzuki in "Proceedings of the 17th International Conference on Neutrino Physics and Astrophysics," edited by K. Enqvist, K. Huitu and J. Maalampi (World Scientific, 1997), pp. 237-241.

Chapter 3

Overview of the experiment

3.1   Guiding design principles

Historically, neutrino oscillation experiments have turned out to be quite difficult. Evidence for neutrino oscillations has been tentatively reported on several occasions only to be retracted or modified later. The skepticism that exists, at least in some circles, regarding the definitiveness of the LSND results[1] illustrates the point that the standards for a convincing experiment in this area are very high.

In designing the MINOS experiment we have paid close attention to these factors[2, 3]. Accordingly, our goal is to be able to perform several independent and parallel measurements, each one of which by itself is capable of addressing the question of neutrino oscillations. Thus we should be able to obtain internal verification of any effect that we might observe. That is, to be believable, our experiment should yield several independent measurements which give a consistent picture of the oscillation scenario.

Very briefly, the physics goals of MINOS are:

a) If Nature has chosen not to have neutrino oscillations in the parameter space accessible to MINOS, we want to be able to demonstrate this fact convincingly over as large an area in oscillation parameter space as possible.

b) If oscillations do exist in the space accessible to MINOS, we want to convincingly demonstrate their existence, measure the oscillation parameters with high precision, and determine the oscillation modes. Specifically, we want to ensure that we can cover the full region of parameter space suggested by the Super-Kamiokande experiment.

These broad physics goals determine the general design of the experiment. To reduce systematic uncertainties as much as possible, we believe that it is necessary to have two detectors: one close to the neutrino source, i.e. on the Fermilab site, and the other one far away, so that the oscillations have sufficient time to develop, even for low Δm^2. The neutrino beam spectra at the two locations should be as nearly identical as possible and their difference should be well understood and independently verifiable. Similarly, the two detectors should be as similar as possible in their important parameters, namely the nature of the active detector, the steel thickness, and the magnetic field configuration in the neutrino interaction

regions. The beam and detector similarities should minimize the systematic errors in the comparison of results from the two detectors. Because the statistical significance of the results will be determined by the event rate in the far detector, we can sacrifice statistics at the near detector to make the conditions there as similar as possible to those at the far detector.

Neutrino oscillations can cause changes in the neutrino event rate in the far detector, as extrapolated from observations in the near detector; oscillations can also cause differences in the characteristics of the events observed in the two detectors. The systematics of these two kinds of measurements will be quite different. Thus, following our goal of having as diverse a set of measurements as possible, we plan to compare both the rates and the characteristics of events in the two detectors.

An additional experimental feature we have incorporated into the design of MINOS is the ability to change experimental conditions in response to the initial results from the experiment. Results obtained in the modified experiment should be different in a way that is predictable from the hypothesis purporting to explain the initial results. Thus, for example, we can change the tune and/or the arrangement of the wide-band beam horn system in order to change the neutrino energy spectrum. Alternatively, we might switch to the narrow-band beam mode in response to the initial results, so as to increase or decrease the size of the observed effect in a predictable way.

Finally, we want to be responsive to the fourth recommendation of the Sciulli Subpanel[4], namely to maintain as much flexibility as feasible to respond to future physics and technology developments[5]. In that spirit, we have recently developed alternative beam configurations which shift the neutrino spectra to lower energies. Such beams could be more appropriate for investigating oscillations with Δm^2 around 10^{-3} eV^2. Our detector design has also been chosen with the goal of maintaining flexibility; for example, the scintillator active detector and the relatively thin steel absorber planes allow us to extend our sensitivity for detecting and identifying oscillations down to relatively low energies[6]. This detector design will also allow us to perform independent atmospheric neutrino flux measurements. Such measurements might be quite topical even 5 to 10 years from now if the results from accelerator neutrinos and atmospheric neutrinos do not appear to have a single self-consistent explanation. We are also proceeding in parallel on an R&D effort for a possible emulsion detector (see Chapter 11) in the ECC (emulsion cloud chamber) mode, to be used as a potential complementary τ-lepton detector.

3.2 Summary of experiment goals and requirements

This Section gives a brief summary of the specific physics goals of the MINOS experiment and the properties of the detectors which we have designed to reach these goals. The physics goals and the rationale for them are discussed in more detail in Section 3.7 and in Reference [3].

As discussed in the preceding Section, the general goals of the experiment are to extend the search for neutrino oscillations into previously unexplored regions of Δm^2 and $\sin^2(2\theta)$ parameter space. If oscillations are found, the experiment should be able to measure the parameters and to identify the oscillation modes. The basic experimental parameters have been chosen to have maximum sensitivity to $\nu_\mu \rightarrow \nu_\tau$ and $\nu_\mu \rightarrow \nu_e$ oscillations in the region

of parameter space suggested by the atmospheric neutrino anomaly observed by Super-Kamiokande and other experiments. The determination of oscillation parameters can be made with a precision comparable to the limits achieved by ν_e disappearance experiments at reactors. If one oscillation mode (e.g., $\nu_\mu \to \nu_\tau$) is dominant, a limit on the admixture of the other mode (e.g., $\nu_\mu \to \nu_e$) can be set at better than 10% to provide a good test of models which predict equal oscillation strengths. The ability to identify τ lepton decays explicitly should give a statistically compelling signal if the atmospheric neutrino anomaly is caused by $\nu_\mu \to \nu_\tau$ oscillations, as suggested by Super-Kamiokande results. Table 3.1 gives a quantitative summary of the physics goals which are achieved by the MINOS baseline design.

Measurement	Sensitivity (90% CL)
$\nu_\mu \to \nu_\tau$ limit, high Δm^2	$\sin^2(2\theta) > 1.9 \times 10^{-2}$ (NC/CC test)
$\nu_\mu \to \nu_\tau$ limit, $\sin^2(2\theta) = 1$, high energy beam	$\Delta m^2 > 2 \times 10^{-3}$ eV^2 (NC/CC test)
$\nu_\mu \to \nu_\tau$ limit, $\sin^2(2\theta) = 1$, low energy beam	$\Delta m^2 > 6 \times 10^{-4}$ eV^2 (ν_μ disappearance)
$\nu_\mu \to \nu_\tau$ limit, $\sin^2(2\theta) = 1$, τ identification	$\Delta m^2 > 1.7 \times 10^{-3}$ eV^2 (ν_τ CC events)
$\nu_\mu \to \nu_e$ limit, high Δm^2	$\sin^2(2\theta) > 2 \times 10^{-3}$ (ν_e appearance test)
$\nu_\mu \to \nu_e$ limit, $\sin^2(2\theta) = 1$	$\Delta m^2 > 3 \times 10^{-4}$ eV^2 (ν_e appearance test)
Δm^2 measurement precision	1×10^{-3} eV^2 for $\Delta m^2 = 10^{-2}$ eV^2
$\sin^2(2\theta)$ measurement precision	1×10^{-1} for $\Delta m^2 = 10^{-2}$ eV^2
Limit on admixture of $\nu_\mu \to \nu_e$, $\nu_\mu \to \nu_\tau$	$\sin^2(2\theta) < 0.06$ for $\Delta m^2 = 10^{-2}$ eV^2

Table 3.1: MINOS physics goals. The baseline detector described in this report will achieve these sensitivities in a two year run. The high energy wide-band (PH2) beam is assumed unless otherwise indicated. A beam optimized for lower energy neutrinos extends these sensitivities to lower values of Δm^2. If oscillations are not found, the 90% confidence level limits shown will be achieved. If oscillations are observed with $\Delta m^2 = 10^{-2}$ eV^2, the parameters and modes will be determined with the indicated precisions.

The goals discussed above were used to determine the detector and neutrino beam parameters of our baseline design. The high energy configuration of the wide band beam is well above threshold for charged current ν_τ interactions; this energy, together with the far detector distance and mass, gives Δm^2 and $\sin^2(2\theta)$ sensitivities over a large fraction of the region suggested by the atmospheric neutrino anomaly. The lower end of the region suggested by the Super-Kamiokande experiment can be explored with the low energy beam option. The most sensitive limits on the occurrence of $\nu_\mu \to \nu_\tau$ oscillations are set by comparing the ratio of charged current to neutral current events in the near and far detectors. Thus the beam spectra should be as similar as possible at the two detectors and the detectors themselves should be very similar. The statistical limits on sensitivity to oscillations are set by the far detector mass. The steel must be thin enough to give good efficiency for neutral current events with small visible hadronic energies. The near detector must be located far enough downstream from the decay pipe that the beam energy spectrum is as close as possible to that at the far detector. The active detector technology needs to be effective for both detectors, i.e., appropriate for both the large neutrino flux at the near detector and also for the much lower flux at the far detector.

If oscillations occur, the experiment must be able to measure the parameters and distinguish between different oscillation modes. This requires good energy resolution for hadrons, muons and electrons, and the ability to distinguish the topologies of ν_μ, ν_e, and ν_τ interactions. These requirements determine the transverse and longitudinal granularities and the magnetic field strength; however, sensitivities depend rather weakly on these parameters. Calibration of the relative energy scales of the near and far detectors is important for the determination of Δm^2. Good hadronic energy resolution is also important for this measurement; good electromagnetic energy resolution is needed for ν_e identification and parameter measurement if $\nu_\mu \to \nu_e$ oscillations occur. The explicit identification of the decays of τ leptons from ν_τ charged current interactions, via statistical analyses, puts stringent demands on several detector parameters: longitudinal and transverse granularities, π^o/electron identification and the tails of the calorimetric energy response. The baseline design has compromised on these τ-identification requirements somewhat in order to maintain a high far detector mass (for oscillation search sensitivity) while conforming to overall cost guidelines. However, our design is quite conservative with regard to Δm^2 sensitivity: we have chosen detector parameters which will retain good event identification and measurement capabilities should it turn out to be advisable, for physics reasons, to run at lower beam energies than the high-energy wide-band beam. Table 3.2 summarizes the experimental parameters of the MINOS baseline design.

Parameter	Value
Near detector mass	0.98 (metric) kt total, 0.1 kt fiducial
Far detector mass (2 supermodules)	5.4 (metric) kt total, 3.3 kt fiducial
Steel planes (far detector)	8-m wide, 2.54-cm thick octagons
Magnetic field (far detector)	Toroidal, 1.5 T at 2 m radius
Active detector planes	Extruded polystyrene scintillator strips
Active detector strips	4.1-cm wide, 1-cm thick, $\sim$8-m long
Near detector distance from decay pipe	290 m
Far detector distance from decay pipe	730 km
Cosmic ray rates	270 Hz in near det., 1 Hz in far det.
Neutrino energy range (3 configurations)	1 to 25 GeV
Detector energy scale calibration	5% absolute, 2% near-far
Detector EM energy resolution	$23\%/\sqrt{E}$ ($<$5% constant term)
Detector hadron energy resolution	$60\%/\sqrt{E}$ ($<$7% constant term)
Detector muon energy resolution	$<$12% (from curvature or range)
NC-CC event separation	Efficiency $>$90%, correctable to 99.5%
Electron/π separation	Hadron rejection $\sim 10^3$ for ϵ_e $\sim$20%
Far det. ν event rate (high-energy beam)	3000 ν_μ CC events/kt/yr (no oscillations)
Near det. ν event rate (high-energy beam)	20 events/spill in target region
Near-far relative rate uncertainty	2%

Table 3.2: MINOS experimental parameters with the wide-band (PH2) beam.

3.3 Geographical layout of the experiment

The "map" of the experiment is illustrated in Figure 3.1. The neutrino beam is produced by the 120 GeV protons from the Fermilab Main Injector and is aimed at the Soudan mine in northern Minnesota, some 730 km away. Because of the earth's curvature the parent hadron beam has to be pointed downward at an angle of 57 mrad.
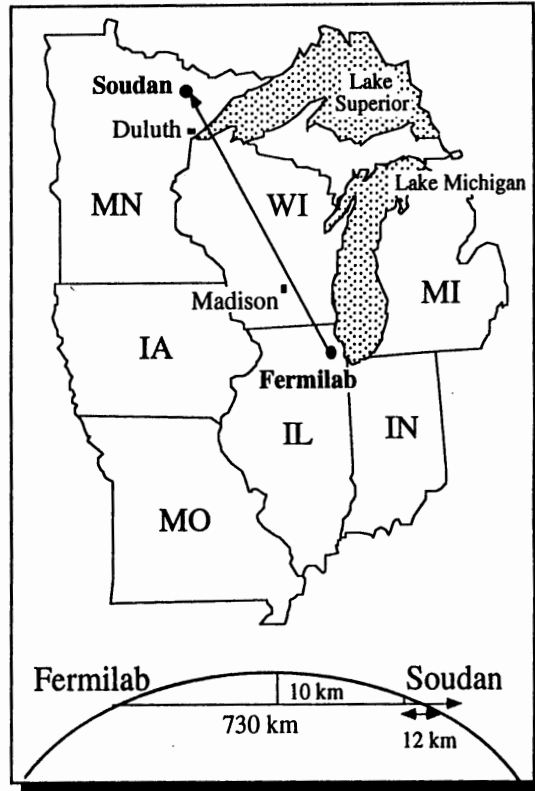
Figure 3.1: The trajectory of the MINOS neutrino beam between Fermilab and Soudan. The beam must be aimed into the earth at an angle of 57 mrad to reach Minnesota.

The hadron beam decay pipe will be 675 m long, a compromise between our desire to obtain the maximum number of π and K decays and the cost of the civil construction. The near detector is located 290 m downstream of the hadron beam absorber. This location is also a compromise between the desire to have the neutrino spectrum be as similar as possible at the two locations (arguing for a large distance) and the need to keep the construction costs low (arguing for a short distance, mainly because of the cost of constructing the near-detector cavern deep underground). The proposed layout of the MINOS experiment on the Fermilab site is shown in Figure 3.2.

The far detector will be located in the Soudan mine in northern Minnesota. This historic iron mine no longer supports active mining, but was converted some time ago into a Minnesota State Park. The MINOS detector will be constructed 710 m below ground level, in a new cavern to be excavated during 1999-2000. The axis of the MINOS cavern will point toward Fermilab; the new cavern will be constructed next to the existing underground laboratory which houses the operating Soudan 2 detector[7].
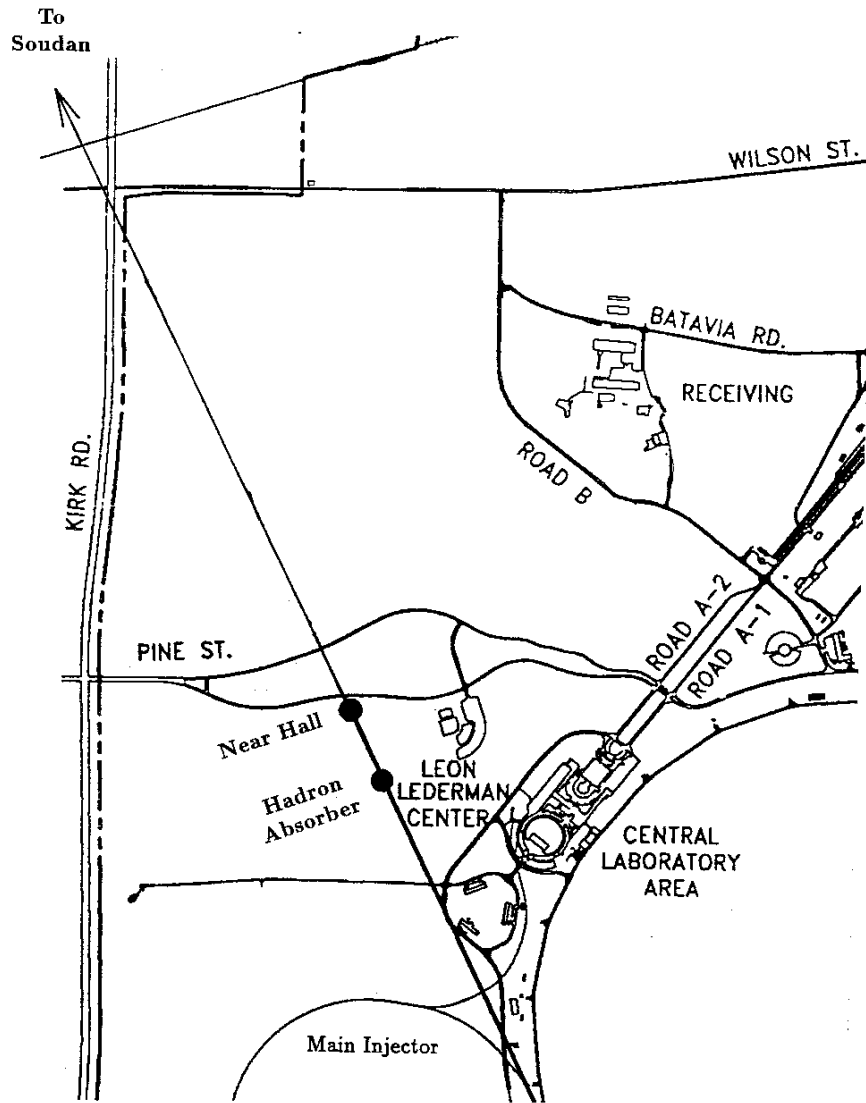
Figure 3.2: Map of the Fermilab site, showing the NuMI beamline and the approximate locations of the hadron absorber and the MINOS near hall.

Several arguments led us to the choice of the Soudan location for the MINOS far detector:

a) 730 km is a reasonable compromise between sensitivity in $\sin^2(2\theta)$, which improves as the distance L between the two detectors decreases (because of the higher event rate), and the sensitivity in Δm^2, which improves with the larger L (because low Δm^2 oscillations have more time to develop). At this distance, we can achieve sensitivities below 0.001 eV^2 in Δm^2 (with the low energy beam option) and 0.01 in $\sin^2(2\theta)$.

b) The existing infrastructure in the Soudan mine (because of its continuing use as a State Park) and the record of excellent collaboration with the state of Minnesota in carrying out the Soudan 1 and Soudan 2 experiments, has convinced us that the conditions for the MINOS experiment at Soudan will be very favorable.

c) The existing Soudan 2 detector, currently operating in the Soudan underground laboratory, will provide an additional, very fine grained, 1 kt detector whose systematics will be significantly different from those of the principal MINOS detector.

d) A distance much longer than 730 km would necessitate a steeper tunnel resulting in a higher civil construction cost at Fermilab.

e) The NuMI neutrino beamline pointing towards Soudan can be readily accommodated on the Fermilab site.

f) There are significant advantages to locating the far detector underground. These have mainly to do with a lower cosmic ray background rate and the ability to perform additional nonaccelerator measurements such as the study of high energy atmospheric neutrinos.

3.4   The neutrino beam

The NuMI neutrino beam has been described in some detail already[8, 9]. Accordingly, we focus here only on its salient features which are most relevant to the physics capabilities of the MINOS experiment.

The primary 120 GeV protons are extracted from the Main Injector using the standard resonant extraction technique over a time period of 1 msec. They are subsequently transported to the downstream target hall and aimed downwards at 3.3° so as to point at the MINOS far detector on the lowest level of the Soudan mine. By 2002 the Main Injector is expected to deliver about 4×10^{13} protons per pulse on target.

The target design optimizes neutrino yield but also takes into account the need to have a conservative design that can withstand the proton beam intensities contemplated. The target is a small diameter (matched to the transverse size of the proton beam) segmented graphite or beryllium cylinder about 160 cm long. The gaps between the segments allow most of the produced pions and kaons to leave the target before interacting. A 0° targeting angle will be used for the wide-band beam (WBB) configurations considered here.

The resulting hadron beam is subsequently sign selected and focused by specially designed focusing elements and then transported through an evacuated decay pipe, 1 m in radius and

675 m long, before striking a secondary hadron absorber downstream. Including the 50 m distance between the production target and the decay pipe, the total decay length is 725 m. The dolomite between the hadron absorber and the first MINOS detector provides sufficient shielding to range out all the muons produced by π and K decays in the beam pipe.

Our original beam design (referred to as H66) used three magnetic horns as focusing elements. The design maximized the total neutrino event rate in the far detector by optimizing the acceptance for neutrinos in the range of 8 to 25 GeV. The recent Super-Kamiokande results indicate the potential importance of achieving good sensitivity for investigation of the low Δm^2 region, necessitating a low energy beam option. With that in mind, we have developed an alternative wide-band beam design (generically referred to as PH2)[9] with two movable parabolic horns which can be configured to provide much higher fluxes at low energies than the original H66 beam. Beams optimized for investigations of different ranges of Δm^2 (and hence having maximum neutrino flux at different energies) can be obtained by varying the currents and locations of the two horns. The high energy configuration of the PH2 beam gives an energy spectrum comparable to that of the H66 beam with only slightly lower neutrino flux.

Figure 3.3 displays the calculated performance of this parabolic horn NuMI beam. The upper curve, corresponding to perfect focus and a 675 m long decay pipe, shows the maximum neutrino flux theoretically available, given the Main Injector proton intensity and the proposed NuMI target. The lower three curves show the event rate as a function of energy for three different configurations of the beam. About 3000 ν_μ CC events/kt/year are expected in the MINOS far detector for the highest energy configuration.

We have also studied the design of a narrow-band beam (NBB) for MINOS. An NBB accepts only a narrow hadron energy band and thus yields a relatively narrow energy spectrum of neutrinos, at the expense of total flux. Oscillation effects could then be easily varied by altering the choice of the central energy. In addition, such an NBB would allow identification of $\tau \to \mu\nu\nu$ decays on an event by event basis, by observation of the missing energy which is carried off by the two decay neutrinos. The design work to date gives us confidence that a beam of such a design could be constructed within the constraints imposed by the NuMI civil construction baseline design[9], although the NBB option is not included in the scope of this baseline design.

3.5   The near detector

The primary function of the near detector is to serve as a reference for the principal MINOS (far) detector in the Soudan mine. Our philosophy is to obtain a direct measurement of the rates and characteristics of the neutrino interactions before the neutrinos have had a chance to oscillate. The measurements can then be compared with the equivalent measurements at the far detector to see if oscillations have occurred. The dependence on Monte Carlo calculations is greatly reduced by comparing far detector data to near detector data instead of making comparisons to Monte Carlo predictions. For such a comparison to be most useful, the beam and detector characteristics at the two locations, as well as the experimental environment, have to be as similar as possible and their differences well understood.

There are several differences, however, that cannot be eliminated:
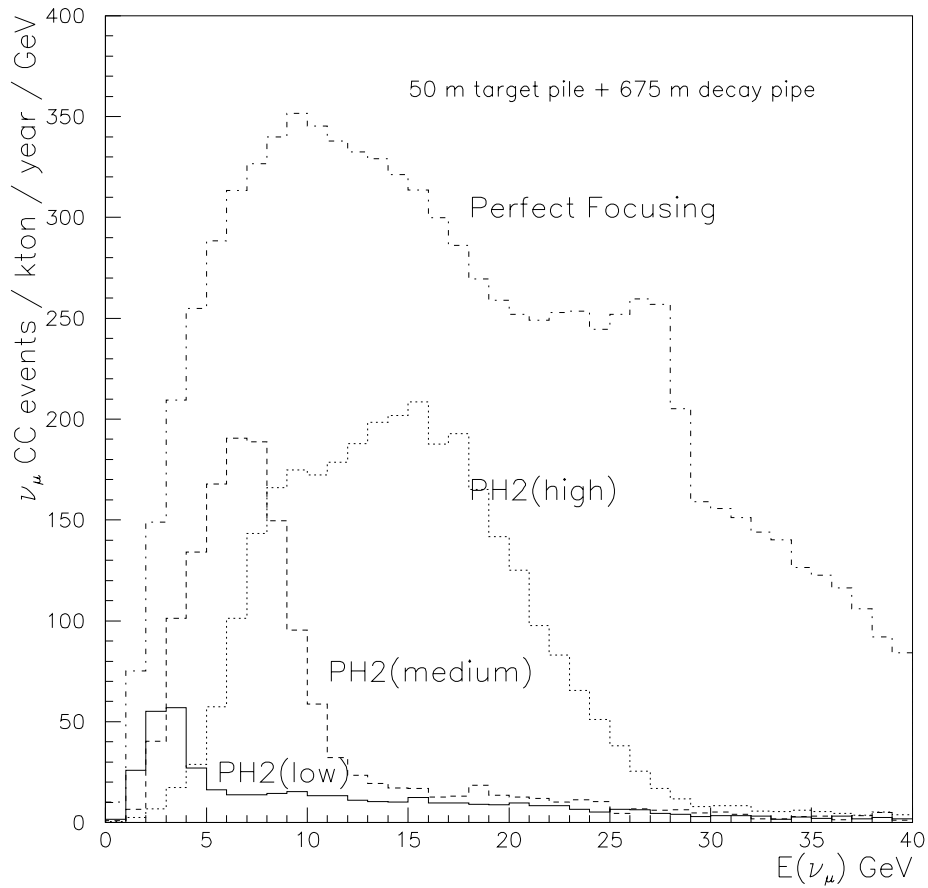
Figure 3.3: Neutrino interaction energy spectra predicted for different beam focusing conditions. 'Perfect Focusing' assumes all secondary charged particles (with the proper sign) from the target are focused into a pencil beam with no divergence. 'PH2(high),' 'PH2(medium)' and 'PH2(low)' are the high, medium and low energy configurations of the parabolic horn beam.

a) The neutrino energy spectrum at the two locations will be somewhat different. This is due to the finite length of the neutrino source. This length is comparable to the distance between a typical π or K decay point and the near detector.

b) The neutrino flux is significantly higher at the near detector.

c) The near detector is at a shallower depth than the far detector.

The beam spectra differences are due to π and K decay kinematics (a neutrino emitted at a larger angle has lower energy) and the fact that lower energy neutrinos tend to be produced further upstream (due to shorter parent lifetime). Thus the differences are easily understood. In addition, if we use neutrino events from only the central beam region of the near detector (we plan to use r < 25 cm), the differences are minimized.

Flux differences at the two locations are not a problem if pileup and overlap rates are kept low, as is the case in our experiment (see Chapter 6).

Finally, the near and far detectors have different cosmic ray rates because of their different depths. Although the ratio of rates is quite large, the absolute rates at both locations are still quite low ($1.8 \times 10^{-3}/m^2/s$ at Soudan and 1.6 /m^2/s in the near detector cavern). The low beam duty cycle, $<10^{-3}$, reduces the impact of cosmic rays even further and allows a very accurate measurement of the effect of any residual cosmic ray background.

The design of the near detector attempts to emulate that of the far detector in all relevant properties: the nature and thickness of absorber planes, the nature and granularity of the active detector, and the strength of the magnetic field. The basic near-detector shape is an elongated octagon, 3.8 m high and 4.8 m wide, as shown in Figure 3.4. The coil hole is placed off center horizontally, and the detector itself is positioned so that the central part of the neutrino beam is about 1 m away from the hole. This geometry was chosen to minimize the amount of steel used while still providing a sufficient steel plane area with an adequate magnetic field in the neutrino interaction region.

In the longitudinal dimension, the detector is composed of four functionally different components. Starting from the upstream end, they are:

a) **Veto part.** This is the upstream part of the detector whose neutrino interactions are not used, because of possible end effects and the need to assure that there is no background from neutron interactions. The veto part also assures that the following target region has no anomalous end effects. This part has a thickness of 0.5 m of steel.

b) **Target part.** Neutrino interactions in this part are used for the near/far comparison. It has a thickness of 1.0 m of steel.

c) **Hadron shower part.** This part has to be long enough to contain the full showers of all neutrino interactions occurring in the target part. It has a thickness of 1.5 m of steel.

d) **Muon spectrometer part.** This part is used to range out muons and/or measure their momentum by curvature. The length is determined by the momentum accuracy needed to match that of the far detector; 4 m of steel is sufficient for this.
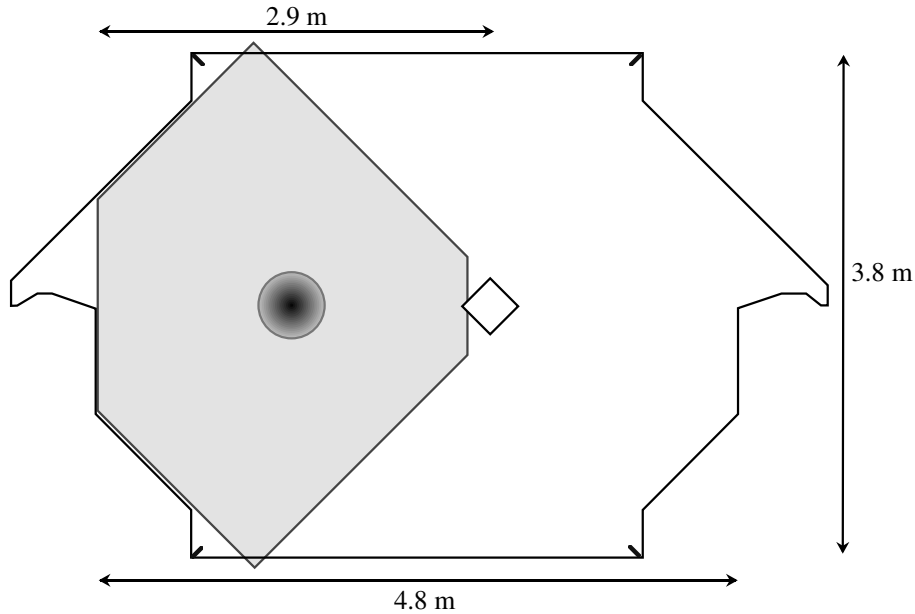
Figure 3.4: Sketch of a partially instrumented near detector plane in one of the three up-stream sections, showing the area instrumented with scintillator strips. The central square represents the magnet coil hole and the circle shows the 25 cm radius central beam region. The shaded area is covered with scintillator strips and the rest of the steel plate is uncovered. Each strip is read out from its outer end only.

Figure 3.5 shows a schematic of the layout of the near detector in the longitudinal direction. The first three parts, although functionally different, are identical in the active detector technology used and their transverse and longitudinal granularities. They are also identical to the far detector in these respects. Because the accuracy of muon measurement by curvature is determined by Coulomb scattering in steel (for sufficiently long traversals, as is the case here), the requirements on the detector elements in the muon spectrometer are less stringent than in the three upstream parts. We therefore use active detectors only on every fourth plane of steel in this part.

As mentioned above, we plan to use only the central part of the neutrino beam (r < 25 cm) for the near/far comparison. Because the transverse spread of a hadronic shower is about half a meter at our energies and in our detector, we need to instrument only a part of the area of the upstream sections of the near detector. In order to measure the neutrino spectrum out to about 1 m from the axis, we will instrument an area of 2.8 m by 2.8 m in this region. In addition, every fifth scintillator plane in the first three sections will have a larger instrumented area to indicate the presence of tracks and interactions outside the central beam area.

The instrumentation of the near detector is very similar to that of the far detector; the basic detector elements are 4-cm wide scintillator strips with a wavelength shifting fiber imbedded in them (see Chapter 5). Because of the higher rates and the smaller number of channels, we will read out each scintillator strip in the three upstream sections separately, without the multiplexing scheme used in the far detector (see Section 3.6 below). Most

3-11

Schematic of the Near Detector
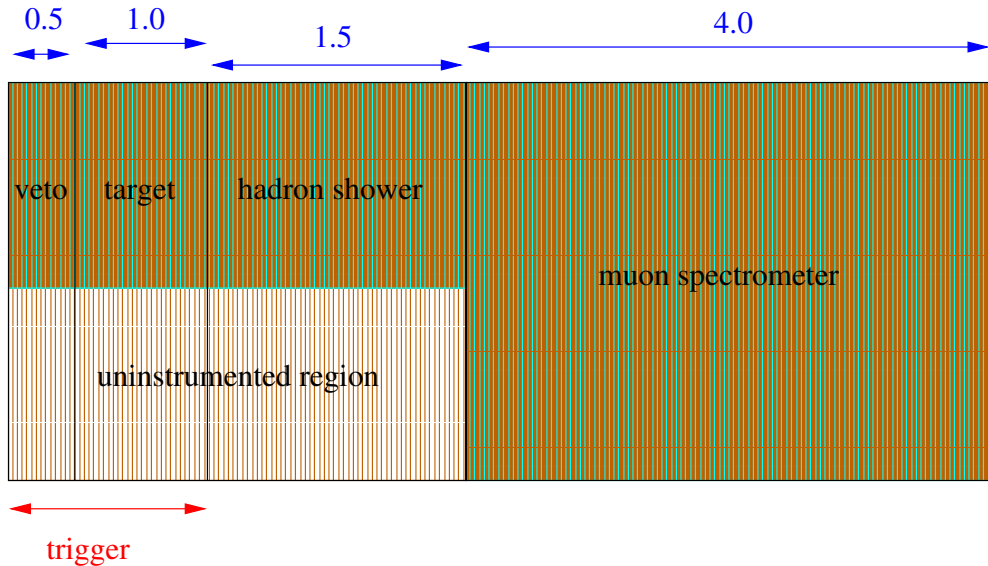
Figure 3.5: Schematic representation of the four functional parts of the MINOS near detector. The thicknesses shown (in meters) are only for the steel planes, and do not include the space occupied by detector planes. The beam enters from the left and is centered on the shaded region. Shading is used to indicate instrumented regions of the detector.

scintillator planes in the upstream part of the detector cover only about one quarter of the steel plane area, as indicated in Figure 3.4. The length of the strips is variable, corresponding to the shape of the iron, and ranges from 1.5 to 2.7 m in length. In the muon spectrometer part, the full area of the steel planes is covered with scintillator and $4\times$ multiplexed readout is used. All near detector strips are read out from only one end and the orientation of strips alternates in successive planes.

Although the rates in the near detector are considerably higher than in the far detector, they do not introduce any significant dead time, pileup, or event overlap problems (see Chapter 6). The singles rate in the detector comes mainly from the neutrino interactions in the detector and from the muons produced by the neutrinos interacting in the earth shield upstream. The neutrino event rate in the detector is shown in Figure 3.6, and the rate of muons from both sources in Figure 3.7. The contribution from hadrons and electromagnetic showers generated in neutrino interactions is shown in Figure 3.8. Because of the high probability of having more than one hit per strip from the same interaction, we plot the last rate as number of strips hit/plane/spill. From these rates we can see that even with a very conservative resolution time of 50 ns, the event overlap probability, as well as the random occupancy probability of any single strip, is considerably less than 10^{-3}.
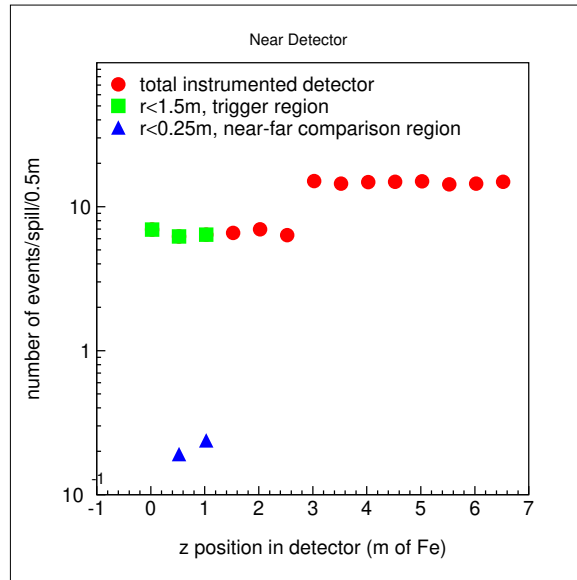
Figure 3.6: Neutrino interaction event rate in the MINOS near detector.
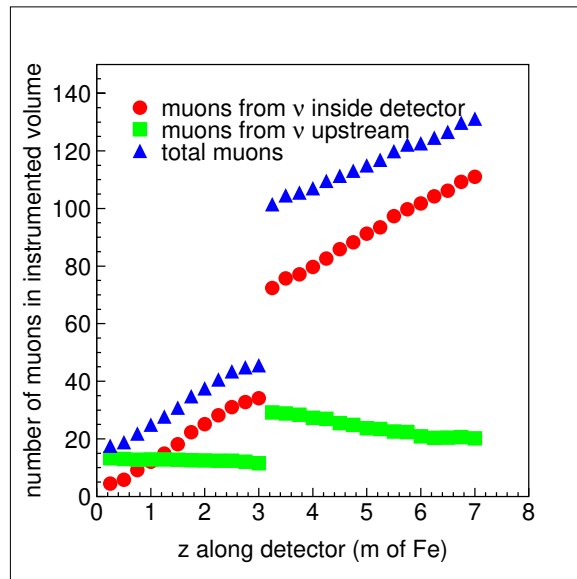
Figure 3.7: Number of muons per spill in the near detector.
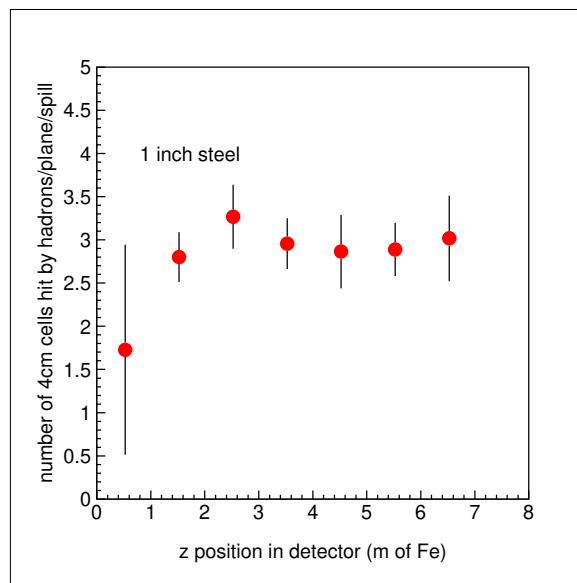
Figure 3.8: Rate contributions from hadron and electromagnetic showers in the MINOS near detector.

3.6 The far detector

The MINOS far detector is a 5.4 metric kt magnetized iron calorimeter with scintillator as the active detector. The basic module is an 8 m diameter, 1-inch thick steel plane (Chapter 4), followed by a scintillator plane (Chapter 5). A MINOS supermodule is made up of 242 of these modules (a supermodule has steel planes on both ends, so each has 242 scintillator planes and 243 steel planes); two supermodules compose the baseline MINOS far detector. Each supermodule is energized independently by current in a 15 kA-turn coil so as to provide a magnetic field in the iron averaging about 1.5 T (Chapter 4). An artist's sketch of the far detector is shown in Figure 3.9.

MINOS (Main Injector Neutrino Oscillation Search)
Far Detector

Fermilab

25,800 m^2 Active Detector Planes
4 cm wide solid scintillator strips
WLS fiber readout

$\vec{B}$

31 m
(2 sections 15 m long)

8m

Magnetized Fe Plates
486 Layers x 2.54 cm Fe
5.4 kT Total Mass

Magnet coil
<B>=1.5 T
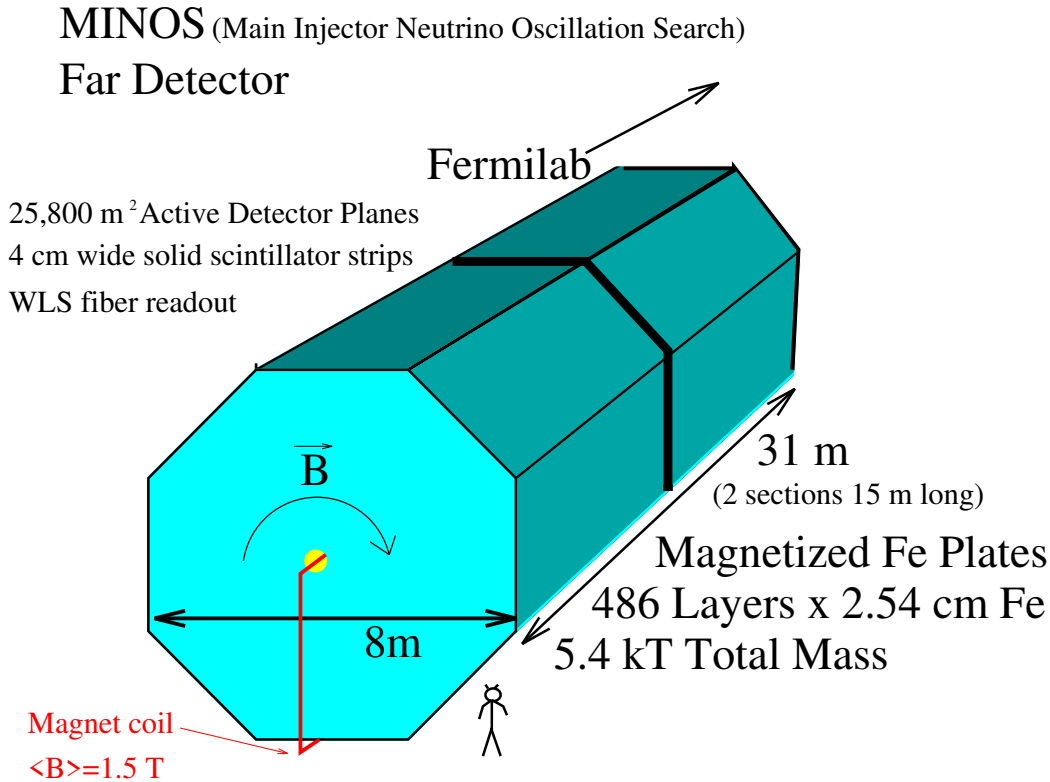
Figure 3.9: Sketch of the MINOS far detector.

Each scintillator plane is made up of 192 strips, each one 4 cm wide and up to 8 m long, depending on their location in the plane. The orientation of the strips alternates by $\pm 90°$ in successive planes. Each scintillator strip has a wavelength shifting fiber imbedded in it to capture, wavelength shift, and transport the light to the two ends. Both ends of each fiber are coupled through clear fibers and multiplexing boxes to multipixel photomultiplier tubes. Eight different fibers, from eight strips spaced roughly 1 m apart on the detector, are coupled to each pixel. The resultant 8-fold ambiguity can be resolved in software by utilizing the fact that the exact arrangement of which fiber is coupled to which pixel is somewhat different at the two strip ends. In addition, we will use timing and pulse height information from adjoining planes to provide independent ambiguity resolution.

The MINOS far detector will be located in a new cavern, to be excavated in 1999-2000, next to the cavern where the Soudan 2 detector is already operating. The MINOS cavern will

be oriented so that its axis points toward Fermilab. A perspective view of the two caverns and their access shafts and corridors is shown in Figure 3.10.
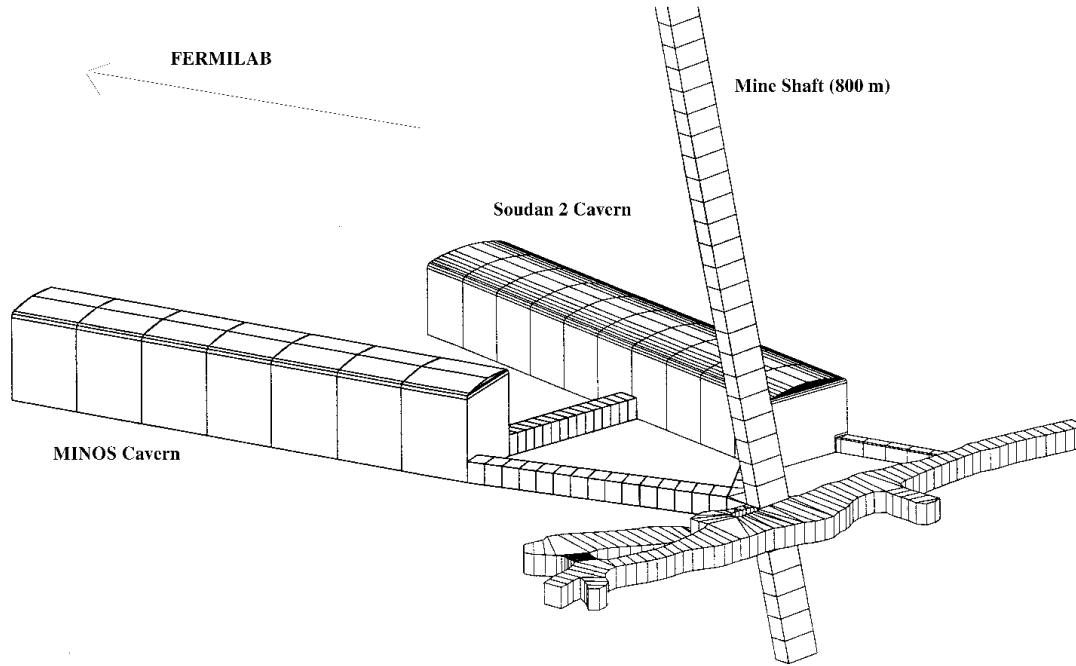
Figure 3.10: Sketch of the MINOS and Soudan 2 caverns in the Soudan Underground Mine State Park in northern Minnesota.

The MINOS Collaboration has adopted a baseline design of the far detector based on the results of three years of highly focused R&D work[10]. This development program has included extensive laboratory tests of different active detector technologies, test beam work, Monte Carlo simulations of reactions of interest to MINOS, and evaluation of the costs of various options. We believe that this baseline design represents the best experimental approach, in light of the current knowledge of neutrino oscillation physics, and also offers a high probability of being able to react effectively to potential future physics developments.

The existing Soudan 2 detector, described in Chapter 10, is viewed by the Collaboration as an integral part of the MINOS experiment. At the beginning of the run it will provide us with an opportunity to study neutrino interactions in Minnesota with a well understood detector. Results from that detector will be available immediately, in real time. Subsequently, Soudan 2 will offer complementary capabilities to the main MINOS far detector: very fine granularity, but lower mass. Soudan 2 should be able to identify examples of exclusive neutrino interaction channels, for example quasi-elastic τ-lepton production and its subsequent

decay through the $\tau \to e\nu\nu$ mode.

The baseline design of the MINOS detector has two supermodules with a total mass of 5.4 kt. We believe that the rather generous contingency allowed, together with our scope reserve, may permit us eventually to enlarge the detector while remaining within the financial constraints imposed on the total MINOS detector cost. This issue should be reexamined roughly two years from now when the costs are better understood. If financial considerations allow it, we might then build another supermodule or augment the detector with alternative instrumentation. The actual course of action would be influenced by future developments in physics and technology. One especially interesting option is a hybrid emulsion detector with a mass of a few hundred tons which would detect τ's by their decay kinks on an event by event basis. We are currently in the midst of an active R&D program to investigate this option, as is described in Chapter 11. This option is not a part of the present baseline design; its only impact on our current planning is that we plan to leave open the upstream 10 m of the MINOS cavern, reserving that space for the subsequent addition of a possible emulsion detector to complement MINOS.

3.7 MINOS physics capabilities

The combination of the NuMI beam and the MINOS detectors, whose characteristics are summarized in the previous three sections, has been designed to provide an optimum tool to search for and to study neutrino oscillations. But the design has also been guided by our belief that nonaccelerator issues will still be of great interest in 2002 when MINOS becomes operational. This dual capability of MINOS is described in the next two Sections.

3.7.1 Accelerator neutrino physics

In this Section we shall describe MINOS physics capabilities using Main Injector neutrinos. The potential measurements can be divided into three groups: statistical measurements, $\nu_\mu \to \nu_e$ identification, and study of exclusive τ decay channels. They all provide information about neutrino oscillations and will give us complementary and mutually reinforcing information should a positive signal be observed.

The statistical measurements can be viewed as providing four independent quantities, namely the rates and energy spectra for both neutral current (NC) and charged current (CC) reactions. In practice, the event identification for this study is actually made by classifying events as either "short" or "long," but we use the NC/CC nomenclature as being roughly equivalent. Both rate and energy measurements of CC events yield results which are independent of the mode of oscillation. Any mode of ν_μ oscillations will result in the depletion of ν_μ CC events, and the CC energy spectrum can be used to measure the oscillation parameters. Comparison of CC energy spectra at the near and far detectors allows us to determine the relative fraction and the energy spectrum of the "missing" events. The size of the depletion is related to $\sin^2(2\theta)$ and their mean energy provides a measure of Δm^2. Figure 3.11 displays this effect for two different sets of the oscillation parameters.

As the third statistical measurement, we choose to use the ratio NC/CC, rather than the rate of the NC events themselves. This ratio has the advantage that it does not require
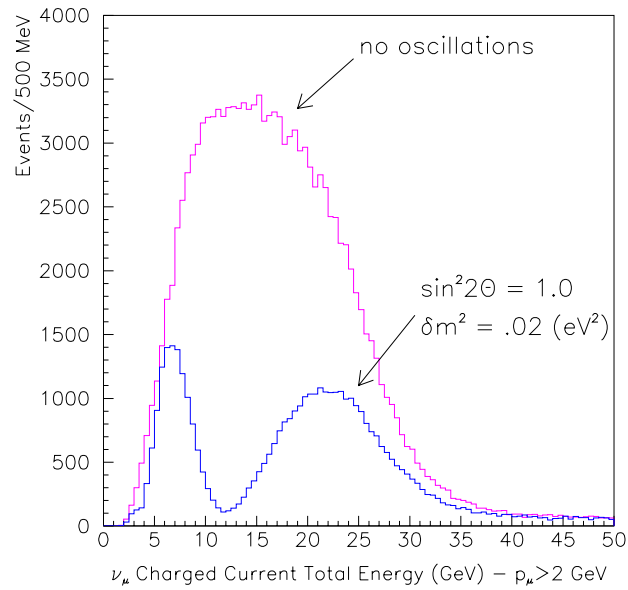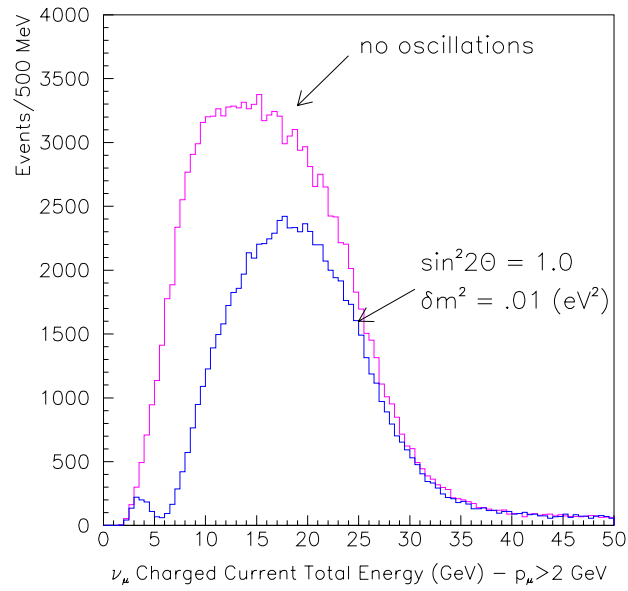
Figure 3.11: Energy spectrum of reconstructed ν_μ^{CC} events in the MINOS far detector in the case of no oscillations, compared to the spectra obtained for oscillations with $\Delta m^2 = 0.01$ eV^2 (top) and $\Delta m^2 = 0.02$ eV^2 (bottom). The high-energy WBB has been assumed, and the spectra have been smeared by expected detector resolution.

understanding of the relative fluxes at the near and far detectors and thus is less subject to systematic errors. It is quite sensitive to oscillations because, not only are the CC events depleted, but the NC events are enhanced, since most of the ν_τ and all of the ν_e events created through oscillations will add to the NC category.

The NC energy spectrum is also quite sensitive to oscillations. Whereas the true NC events will give a spectrum peaked at low energies, both ν_e and ν_τ CC events will tend to populate preferentially the higher energy region. This effect is illustrated in Figure 3.12. The power of the NC-event rate and energy spectrum measurement has been demonstrated by the CCFR experiment[11], which has been able to set a limit on $\sin^2(2\theta)$ of 2.7×10^{-3} (1.9×10^{-3}) for $\nu_\mu \rightarrow \nu_\tau$ $(\nu_\mu \rightarrow \nu_e)$ oscillations in the region of Δm^2 corresponding to their maximum sensitivity. The NC measurements, when combined with the CC measurements, are able to identify the relative contributions of the different oscillation modes.
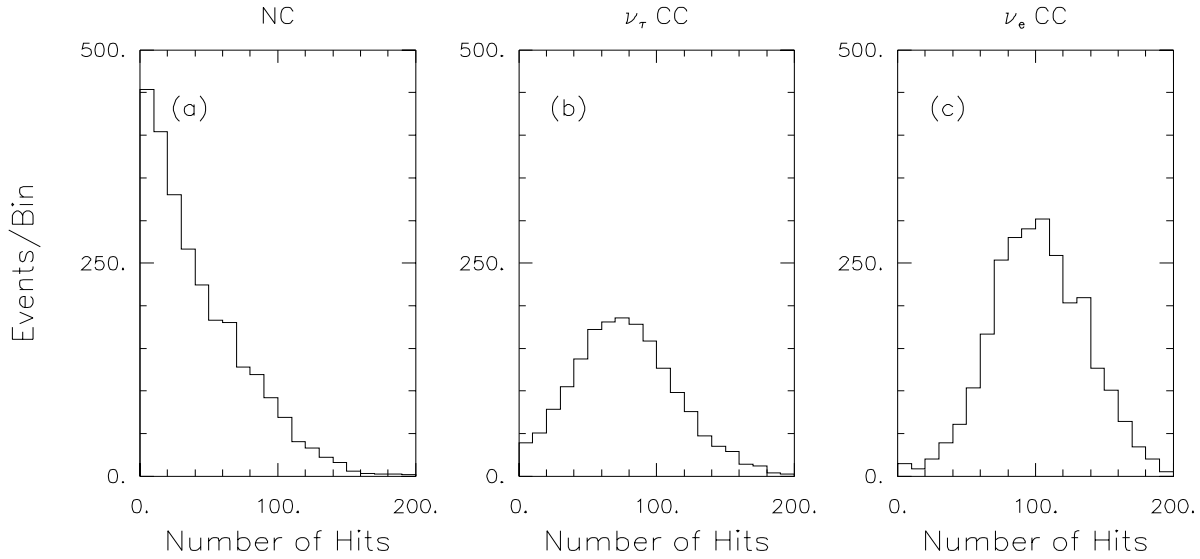
Figure 3.12: Effect of neutrino oscillations on the energy spectra of events with neutral current topologies in the MINOS far detector. The simulation used a 10 kt-year exposure with the high-energy beam in a detector with 2-cm thick steel planes and 2-cm wide scintillator strips. NC events were selected with a 20-plane length cut. The number of hit strips is used as a measure of event energy. The spectrum for true NC events is shown in (a). Oscillations with $\Delta m^2 = 0.01$ eV^2 and $\sin^2(2\theta) = 1.0$ for $\nu_\mu \rightarrow \nu_\tau$ and $\nu_\mu \rightarrow \nu_e$ produce the spectra (from ν_τ and ν_e CC events) shown in (b) and (c) respectively.

MINOS has excellent capability to distinguish ν_μ and ν_e CC events from NC events based on the shapes of hadronic and electromagnetic showers. The ν_e CC events will deposit most of their energy early in the shower, and the transverse width of the shower will be significantly narrower than for the hadronic shower of the NC events, which constitute the main background. The CCFR experiment[12] has already demonstrated that at high energies one can identify the ν_e CC events by the longitudinal shape alone, even with 10 cm thick iron plates. Our sensitivity to $\nu_\mu \rightarrow \nu_e$ oscillations using this method will be limited mainly by the statistical fluctuations in the number of ν_e CC events expected in the far detector

due to the ν_e component in the beam.

The MINOS sensitivities obtained by different methods, at the 90% confidence level, for both $\nu_\mu \rightarrow \nu_\tau$ and $\nu_\mu \rightarrow \nu_e$ are shown in Figure 3.13. The limit curves shown correspond to a 10 kt-yr (before fiducial cuts) exposure of the far detector in the high-energy wide-band beam, using realistic fiducial volume cuts. The assumed 1% systematic error limits the sensitivity of the near-far rate comparison test.
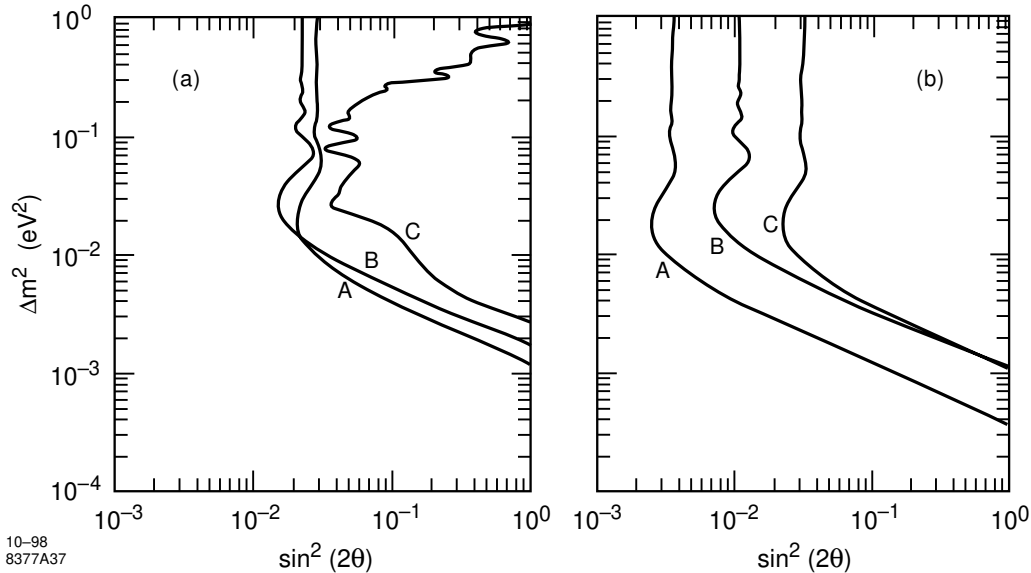
Figure 3.13: 90% confidence level limits on neutrino oscillation parameters which would be established by MINOS with 10 kt-years in the absence of oscillations, using the high energy wide band beam. The A, B and C curves show limits obtained from different oscillation tests. (a) $\nu_\mu \rightarrow \nu_\tau$ limits, where curve A is for the near-far event rate comparison, B is for the NC/CC ratio test, and C is for the CC-event energy test. (b) $\nu_\mu \rightarrow \nu_e$ limits, where curve A is for the electron appearance test, B is for the NC/CC ratio test, and C is for the near-far event rate comparison.

Our studies to date indicate that we should be able to identify, with a signal to noise ratio of better than 1:1, several τ exclusive decay modes. For example, for the parameters $\Delta m^2 = 0.01$ eV^2 and $\sin^2(2\theta) = 1.0$ we would obtain a 7 σ effect for the $\tau \rightarrow \pi(K)\nu$ mode. For the modes $\tau \rightarrow e\nu\nu$ and $\tau \rightarrow$ hadrons(s) $+ \pi^\circ$(s) we can do even better, but there is some confusion in these channels with the ν_e CC interactions, and thus there is a mode ambiguity. Our capability for tau identification has been summarized in an internal report prepared for the Fermilab PAC[13].

The reach of MINOS can be extended to lower values of Δm^2 by using the lower energy PH2(medium) and PH2(low) beam configurations. Our sensitivity using the PH2(low) beam and the CC ν_μ disappearance test is shown in Figure 3.14.

In addition, we can perform a number of independent measurements with the Soudan 2 detector. Those have been described in detail in the original MINOS proposal[2] and are summarized in Chapter 10.

Finally, if our initial physics results justify it, MINOS has the capability of additional

running in the NBB configuration. These studies would provide a number of independent measurements on such issues as the existence of oscillations, the values of oscillation parameters, and the relative contributions of different oscillation modes. The quality of these results would be comparable to those obtained from the WBB running, but the systematics would be very different.
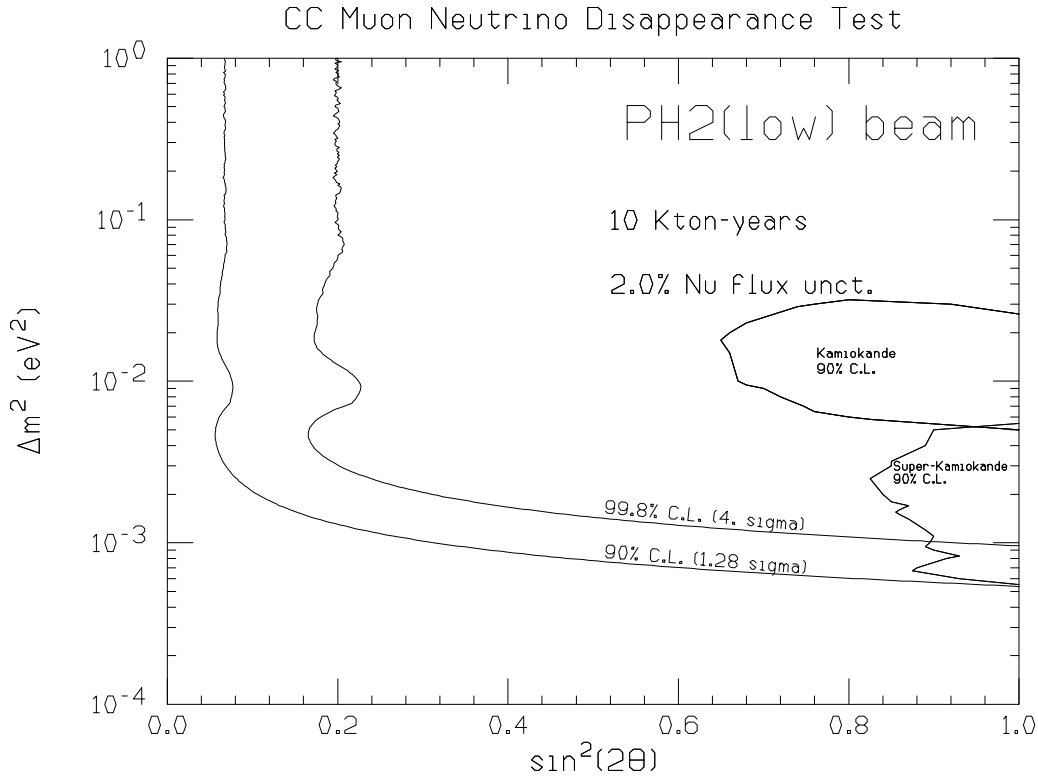
Figure 3.14: Sensitivity of the ν_μ disappearance test (90% CL limits and 4σ contour) for a 10 kt-yr exposure in the low energy PH2(low) neutrino beam.

3.7.2   Nonaccelerator phenomena

The MINOS detector will be the first large underground detector with a magnetic field. Thus it will be able to provide new information on a variety of nonaccelerator physics issues even though it will follow several years after other big underground detectors, notably Super-Kamiokande and MACRO[14].

The issue of atmospheric neutrinos is one where MINOS could make significant contributions. At the present time the two sets of measurements from Super-Kamiokande that are relevant to the neutrino oscillation hypothesis, namely the μ/e ratio-of-ratios R (Section 2.3.3.1) and the L/E distribution, are on the verge of being inconsistent with each other; the R value appears to require a higher value of Δm^2 than the L/E distribution. Furthermore the parameter region indicated by the Super-Kamiokande data is barely consistent with that derived from Kamiokande data analysis. The ability of MINOS to measure the energy of the muon, and hence of the neutrino initiating a CC event, will allow us to under-

stand the behaviors of L/E and the R value (as a function of energy) in more detail than is possible today. In addition, MINOS will provide complementary information about the sign of the muon. The ability to study atmospheric neutrinos should allow MINOS to extend its Δm^2 reach to values near 10^{-4} eV^2. We are currently studying the potential capabilities of our detector in this area.

Another area where there is a lack of good understanding today is upward going cosmic ray muons. The conventional explanation for these muons is that they are produced by upward going neutrinos interacting in the earth beneath the detector. Thus their rate and energy spectrum is sensitive to neutrino oscillations. The current status is somewhat murky. The measured rate from MACRO[15] is lower than predicted from the conventional cosmic ray neutrino calculations (as would be expected for $\nu_\mu \rightarrow \nu_e$ or $\nu_\mu \rightarrow \nu_\tau$ oscillations) but the observed zenith angle distribution is anomalous. The data from Super-Kamiokande and Kamiokande[16] on this topic are consistent with the oscillation hypothesis but do not provide any strong constraint on oscillation parameters. There is very little information on the energy or charge distributions of these muons (only the ratio of stopping to through-going muons has been measured). MINOS will provide unique information in both of these areas.

MINOS will also be able to study a number of other astrophysics issues. Some examples are cosmic ray muon studies, searches for point sources and large scale anisotropies, and searches for new exotic particles. Our capabilities in this area are described in more detail in the MINOS Proposal[2] and in its Addendum[17].

3.8 Future MINOS options

The baseline NuMI/MINOS project consists of the parabolic horn neutrino beam (which can be tuned to produce a wide range of neutrino energies), the associated conventional facility construction, the near detector cavern with the MINOS near detector, the new cavern in the Soudan mine, and the 5.4 kt iron calorimeter MINOS far detector. We believe that this combination will allow us to do excellent neutrino physics and to address in a definitive way many of the current unresolved issues in neutrino oscillation physics.

On the other hand, neither physics nor technology will remain stationary during the four year period required to construct the NuMI/MINOS facility. In light of that, and in light of the considerable investment required to construct the experiment, we feel it is appropriate for us to start thinking now about the possible evolution of the program in the future. This is consistent with Recommendation 4 of the Sciulli Subpanel[4] and the advice from the Fermilab PAC. This evolution might suggest future modifications of the baseline design or additions to it. In this final section of the Overview Chapter, we briefly mention some of the possibilities that might become attractive in the future. Several of them have been already alluded to in previous discussion.

A very attractive possibility would be to incorporate in the detector an ability to identify τ's on an event by event basis. The best way to accomplish this with today's technology (or small extrapolations from it) is with a hybrid emulsion detector. Our effort in this area is described in Chapter 11. Should this look feasible, attractive and cost effective, as a result of our R&D effort and other developments around the world, we would propose to build an

emulsion-based detector as an addition to the 5.4 kt calorimeter. We are therefore proposing to reserve space for such an addition in the upstream part of the new Soudan cavern. This location would allow the MINOS detector to be used as a muon spectrometer for the events produced in the emulsion detector.

As described in Section 2.3.3.4, it is quite likely that the atmospheric neutrino anomaly can be explained by $\nu_\mu \rightarrow \nu_\tau$ oscillations. However, in this scenario there is still a large uncertainly in the value of Δm^2 responsible for the oscillations. The zenith angle distributions from Super-Kamiokande suggest that this value could be 10^{-3} eV^2 or even lower. In that case, a lower energy beam would be more effective for studying the oscillations, given the 730 km distance from Fermilab to Soudan. The NuMI beam facility has been designed so that the beam elements can be configured to give much higher fluxes of low energy neutrinos.

Another possible beam alteration is running in the narrow band beam (NBB) configuration. Such a modification would make sense if we knew the oscillation parameters with reasonable certainty. In that case, NBB running would allow us to provide independent confirmation of an oscillation hypothesis and to perform measurements of the oscillation mode and parameters in a different, and perhaps a better, way. The NBB configuration has been designed and the changeover from the baseline beam configuration could be made in a relatively straightforward way if the physics situation should warrant it.

Another potential future modification would be an upgrade of the MINOS far detector by surrounding it with a veto shield. Such a shield would improve the quality of nonaccelerator physics measurements by providing good identification of externally produced muons and a much longer time base to determine the direction of tracks which enter or leave the main MINOS detector. The latter would be important in obtaining a clean sample of upward going muons and would also clarify the nature of events occurring near the edges of the detector.

Chapter 3 References

[1] C. Athanassopoulos *et al.*, Phys. Rev. Lett. **75**, 2650 (1995); J.E. Hill, Phys. Rev. Lett. **75**, 2654 (1995).

[2] The MINOS Collaboration, "P-875: A Long-baseline Neutrino Oscillation Experiment at Fermilab," February 1995, Fermilab report NuMI-L-63.

[3] The MINOS Collaboration, "MINOS Physics Goals and Experimental Requirements," January 1997, Fermilab report NuMI-L-229.

[4] "Report of the HEPAP Subpanel on Accelerator-Based Neutrino Oscillation Experiments," September 1995, DOE Office of Scientific and Technical Information Report No. DOE/ER-0662.

[5] The MINOS Collaboration, "Neutrino Oscillation Physics at Fermilab: The NuMI-MINOS Project," May 11, 1998, Fermilab report NuMI-L-375.

[6] The MINOS Collaboration, "MINOS Progress Report to the Fermilab PAC," October 1997, Fermilab report NuMI-L-300.

[7] W.W.M. Allison *et al.*, Phys. Lett. **391A**, 491 (1997); W.W.M. Allison *et al.*, Nucl. Instrum. and Methods **A376**, 36 (1996) and **A381** 385 (1996); S.M. Kasahara *et al.*, Phys. Rev **D55**, 5282 (1997); H.M. Gallagher, "Neutrino Oscillation Searches with the Soudan 2 Detector," University of Minnesota Ph.D. thesis, 1996.

[8] J. Hylen *et al.*, "Conceptual Design for the Technical Components of the Neutrino Beam for the Main Injector (NuMI)," September 1997, Fermilab-TM-2018.

[9] The Fermilab NuMI Group, "NuMI Facility Technical Design Report," October 1998, Fermilab report NuMI-346.

[10] The MINOS Collaboration, "MINOS Experiment R&D Plan: FY 1996-1998," June 1996, Fermilab report NuMI-L-184.

[11] K.S. McFarland *et al.*, Phys. Rev. Lett. **75**, 3993 (1995).

[12] A. Romosan *et al.*, Phys. Rev. Lett. **78**, 2912 (1997).

[13] The MINOS Collaboration, "Status Report on τ Identification in MINOS," January 1997, Fermilab report NuMI-L-228.

[14] F. Ronga, "Upgoing Muons in MACRO," Proceedings of the 25th International Cosmic ray Conference, Durban, South Africa, July 1997.

[15] S. Ahlen *et al.*, Phys. Lett. **B357**, 481 (1995).

[16] T. Kajita, "Atmospheric neutrino results from Super-Kamiokande and Kamiokande – Evidence for neutrino oscillations," talk presented at the Neutrino 98 Conference, Takayama, Japan, June 1998; S. Hatakeyama *et al.*, Phys. Rev. Lett. **81**, 2016 (1998).

[17] The MINOS Collaboration, "Addendum to P-875: A Long-baseline Neutrino Oscillation Experiment at Fermilab," April 1995, Fermilab report NuMI-L-79.

Chapter 4

Magnet steel and coils

4.1 Overview

This Chapter describes the design and fabrication of the massive steel plane structures of the MINOS near and far detectors. These toroidally magnetized, 1-inch thick steel planes are suspended vertically in large arrays. Each steel plane also provides mechanical support for a plane of scintillator detector modules. The 8-m wide steel planes of the far detector are assembled in the Soudan underground laboratory from 2-m wide plates. The smaller near detector steel planes are made from single steel plates and require no underground assembly work. This task also includes the design and construction of the multi-turn coils, the power supplies and cooling systems used to magnetize the planes, and the instrumentation used to measure the magnetic fields in the planes. The design addresses several important engineering issues, including the mechanical stability and flatness of hanging planes with very large width to thickness ratios, and the effect of the composite plane structure on magnetic field quality. A program is under way at Fermilab to check the design calculations by constructing a number of full-size prototype planes. The first of these planes has been hung and provides initial confirmation of these calculations. This prototype detector plane program includes scintillator and steel integration checks, verification of safe steel handling techniques, and training for the detector assembly crews. The magnet steel and coils task also provides the fixtures for handling steel planes and the near detector support structure.

4.1.1 The far detector

The MINOS far detector will be installed in a new underground laboratory in the Soudan mine. The 5.4 kt structure is assembled from 8-m wide, 1-inch thick octagonal steel planes. The 486 steel planes are arranged as two "supermodules" of 243 planes each, separated by 1.5-m long gaps to allow space for installation of the magnet coils. An 8-m wide octagonal plane of scintillator detector "modules" is attached to each steel plane before it is raised to a vertical orientation and installed in a supermodule. A supermodule contains 242 planes of scintillator detectors and 243 steel planes with a center-to-center spacing of 5.94 cm. Each plane is hung by two "ears," which are extensions of the octagonal plane structure, similar to the hanging files in a file drawer. The scintillator detector is described in Chapter 5 and the installation of the steel and scintillator planes is described in Chapter 7.

Figure 4.1 is a sketch of a hanging steel plane and the detector support structure. Each steel plane is constructed from eight 2-m wide, 0.5-inch thick plates of steel which are welded together in a cross lamination to form the full octagon. A hole at the center of each plane is provided for the magnet coil that carries 15,000 A-turns of current through the center of each supermodule to produce an average toroidal magnetic field of 1.5 T in the steel planes. The return leg of the coil is located in a shallow trench in the floor directly under the axis of the supermodule.
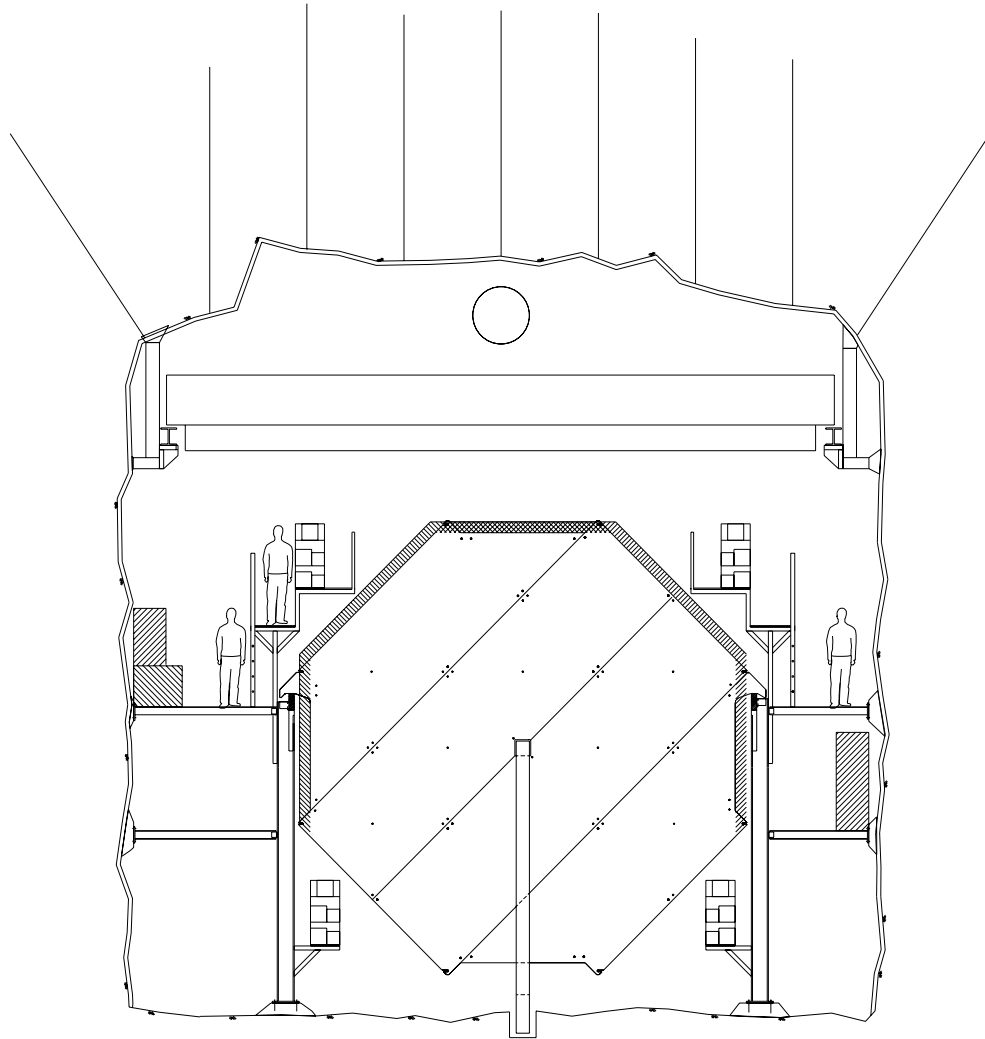
Figure 4.1: Sketch of an 8-m wide MINOS far detector steel plane hanging from the detector support rails. Four of the eight steel plates which make up the plane are visible; the other four plates are behind the first four and are oriented at 90° to them. Also shown are the detector support structure, the side walkways, the racks for photodetectors and electronics, the magnet coil and the overhead bridge crane.

The engineering and fabrication of the detector support structure is part of the MINOS cavern excavation and outfitting task and is described in the MINOS Far Detector Laboratory

Technical Design Report[1]. It is very similar to that for the near detector (described below).

4.1.2 The near detector

The 980 ton MINOS near detector will be installed in the new NuMI near hall at Fermilab[2]. The near detector is essentially a smaller version of one of the far detector supermodules. Because the neutrino beam at the near detector is only about 1 m in diameter, the detector plane geometry is designed to reduce the area (and cost) of the steel planes. A near detector plane and the detector's support structure are shown in Figure 4.2. The "squashed octagon" planes are small enough (6.2 m wide by 3.8 m high) that they can be manufactured as single, 1-inch thick units. They do not have to be assembled from 0.5-inch thick plates as in the far detector. The smaller beam area also allows most of the scintillator detector planes to be much smaller than those in the far detector. As shown in Figure 3.4 in Chapter 3, most of the first (upstream) 120 planes have scintillator modules covering only a 2.8 m × 2.8 m area. The last (downstream) 160 planes have full scintillator coverage only on every fourth steel plane; the remaining three out of four planes in this section do not have scintillator. The scintillator module design is described in Chapter 5 and the installation of the steel and scintillator planes is described in Chapter 8.

A hole is provided in each plate for the magnet coil, offset 0.56 m from the center of the plane. Because of the near detector's squashed-octagon geometry and the offset coil, the near detector coil must carry nearly three times as much current (40,000 A-turns) to achieve a magnetic field of about 1.5 T in the beam region. The return leg of the coil is located near the lower 45° edge of the plane.
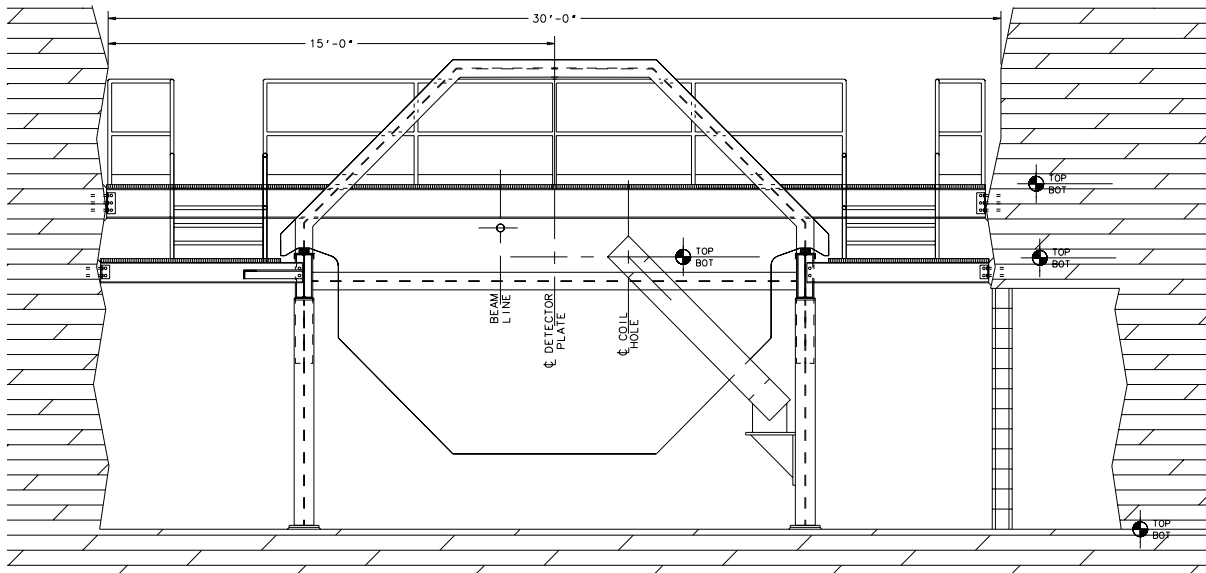
Figure 4.2: Sketch of a MINOS near detector steel plane hanging from the detector support rails. Also shown are the detector support structure, the side walkways, the magnet coil, the magnet support, and the bookend. (Dimensions shown are in feet and inches.)

A preliminary design of the near detector support structure has been completed by Facil-

ities Engineering Services Section (FESS) at Fermilab. This structure conforms to Fermilab engineering standards and to the AISC code for structural steel fabrication[3]. The support includes "bookend" structures which constrain the first plane of each supermodule to be plumb in the vertical orientation and square to the support rails. Then bookends also provide a reference to ensure the flatness and stability of the sequentially installed planes for each supermodule.

4.1.3 The steel planes

4.1.3.1 Steel plate fabrication

Choosing the steel for MINOS planes required some compromises. The carbon content must be high enough to give high tensile strength, but low enough for good magnetic properties[4, 5]. We have chosen steel in the range specified by AISI 1006 low-carbon steel, with the properties summarized in Table 4.1. By requiring the carbon content to be between 0.04% and 0.06% (standard AISI 1006 steel can have carbon content between 0.04% and 0.08%), we can guarantee high magnetic permeability while still maintaining adequate tensile strength. The specification for MINOS steel[6] is the same as that used for the BaBar magnet steel[7].

Property	Specification
Tensile strength:	
Ultimate tensile strength	40,000 psi minimum
Yield strength	20,000 psi minimum
Elongation of 2 inches	22% minimum
Chemical composition (% by weight):	
Carbon	0.04% to 0.06%
Manganese	0.40% (max.)
Silicon	0.40% (max.)
Sulfur	0.01% (max.)
Phosphorous	0.07% (max.)
Nitrogen	0.008% (max.)
Aluminum	0.05% (max.)
Chromium	0.05% (max.)
Copper	0.06% (max.)
Nickel	0.06% (max.)
Molybdenum	0.01% (max.)
Vanadium	0.01% (max.)
Niobium	0.01% (max.)

Table 4.1: Mechanical and chemical specifications for MINOS steel plate material. The chemical composition specifications also include upper limits on the content of possible contaminants such as sulfur, phosphorous and nitrogen.

Dimension	Far detector	Near detector
Plate thickness	12.7	25.4
Thickness tolerance	+0.8, −0.254	+1.8, −0.254
Finished plate width	2000	3810
Finished width tolerance	±0.76	±0.76
Flatness over any 12 ft length	8.0	14.5
Max. number of waves	8 waves per 8 m	4 waves per 4 m

Table 4.2: Dimensional tolerances on steel plates for MINOS far and near detectors. All dimensions are in millimeters.

The specified steel is readily available at low cost from a wide variety of vendors, has a low carbon content for good magnetic properties, and is strong enough for MINOS planes. This steel has very good welding characteristics which is important for the assembly of the far detector planes; two layers of 0.5-inch thick plates are held together by 76 plug welds in each plane.

One of the most important properties is the flatness of the component steel plates. Steel producers and fabricators use an American Society of Testing and Materials (ASTM) Standard number A6, "Standard Specification for General Requirements for Rolled Steel Plates, Shapes, Sheet Piling, and Bars for Structural Use" for making steel plates. Table 4.2 gives the relevant flatness specifications for the MINOS far and near detector plates[8]. These specifications are about half of the ASTM standard values; several local steel vendors we have contacted claim to routinely produce steel plate which meets the flatness requirements in Table 4.2.

It is important to note that the flatness specifications are for single plates lying on a perfectly flat horizontal surface. The far detector planes are composite structures laminated from eight half-thickness plates, and will hang vertically; this may affect their flatness[9]. Prototype studies of full-size hanging steel planes, discussed in Section 4.4.5.1, will determine how the flatness of actual MINOS planes, hanging vertically, compares with the specifications listed in Table 4.2. Initial results from the first full-sized prototype plane show flatness deviations which are consistent with numerical models and within tolerances.

Steel plates must be cut to the proper shapes before they can be used. Many shops in the Midwest can handle plates of this size. The most inexpensive way to cut the plates to MINOS specifications[8] is to use a numerically controlled plasma torch. The plates for the MINOS single-plane test, described in Section 4.4.5.1, were fabricated in that manner. Measurements of the widths of gaps between edges of the plates in the assembled plane are very encouraging; less than 2 m out of the ∼40 m of gap length are more than 1 mm in width, and these gaps are all less than 3 mm wide. An alternative, more precise, way to cut the plates is by machining them. Several shops in the Midwest can machine plates of this size with the required accuracies. Based on these initial results, the baseline MINOS cost estimate[10] assumes cutting with a plasma torch, which is cheaper than machining. If more extensive experience from the four-plane prototype (Section 4.4.5.1) shows that plasma cutting does not provide an edge true enough to give gaps under 1 mm, then machining can
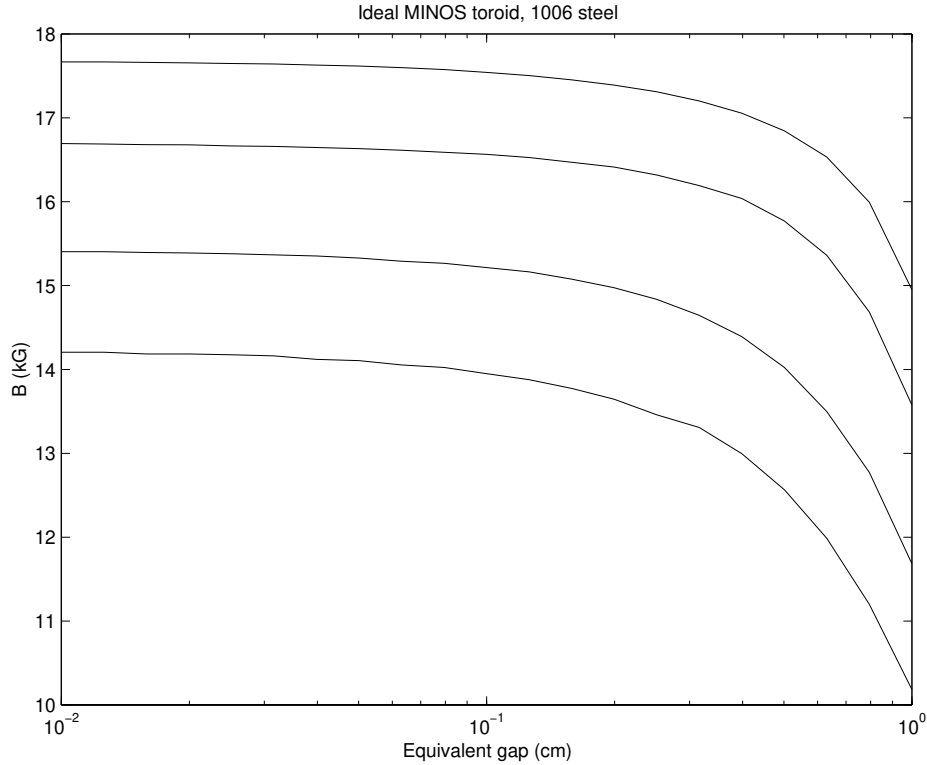
Figure 4.3: B-field *vs* the cumulative gap length at different radii for far detector octagons made from AISI 1006 steel. From top to bottom the curves show the results for R = 50, 100, 200 and 300 cm. For R = 200 cm, a 1 mm rms variation of a 5 mm effective gap results in a 0.1 T spread in the field distribution.

meet that gap requirement, albeit at higher cost.

Calculations show that an edge gap of less than 1 mm between individual plates does not degrade the magnetic field significantly[11]. A Monte Carlo simulation verified that the effect of 1 mm edge gaps on the magnetic field in a plate is small; for a muon passing within a few millimeters of a 1 mm gap, the field distortion contributes a potential directional uncertainty of about the same size as the multiple Coulomb scattering in the plate[12]. However, larger average gaps will require a higher coil current to achieve the average 1.5 T field level. Figure 4.3 shows the cumulative effect of all edge gaps on the average toroidal field at several radii. The field falls significantly for integrated gap widths larger than 5 mm[4].

4.1.3.2 Steel handling procedures

Procedures for handling steel plate sections and assembled MINOS planes are being developed as part of the magnet steel and coils task, and are a major focus of the prototype work described in Section 4.4.5. These optimized procedures will be used for the installation of the MINOS far and near detectors, described in Chapters 7 and 8. The large plates of steel must be handled carefully to avoid permanent deformation. Since standard handling at steel fabricators produces plates within the flatness specifications, similar procedures will be used at the experimental sites.

The far detector plates must fit into the hoist cage[1] at the Soudan site. This requires the 8-m octagons be formed from 2-m wide plates. A new cage has been designed specifically to carry MINOS plates from the surface to the underground laboratory, as described in Chapter 7. That Chapter also describes the monorail system which carries the plates from the shaft to the experimental cavern. Plates are packaged in sets of four (enough to build one of the two layers of a single octagonal plane), to match to the hoist's weight capacity. Additional holes are provided in the steel plates to aid in rigging the packages of plates onto and off of the shaft cage. The steel handling and assembly procedures are described in detail in Chapter 7.

A custom-sized 100-m deep drop shaft is provided near the entrance to the MINOS near detector hall[2]. This shaft allows the near detector planes to be delivered as one-piece plates that require no underground assembly. An overhead crane lowers near detector steel planes onto a cart which transports them down the access tunnel and into the hall. In the hall itself, an overhead crane lowers the planes onto a strongback for scintillator detector mounting. The steel-handling procedure for the near detector is described in more detail in Chapter 8.

4.1.3.3 Steel plane assembly and mounting

The procedures for assembling and mounting the far detector steel planes are being developed as part of the full-size plane prototype studies[13] described in Section 4.4.5. Detailed installation plans based on these procedures are described in Chapters 7 and 8; the current concepts for the plane assembly and mounting procedures are only summarized here.

The far detector planes are constructed using a strongback as the assembly fixture. The steel plates are laminated in a criss-cross pattern where the top plates are at 90° to the bottom plates and are welded together with a series of 1-inch diameter plug welds. The strongback provides a flat surface for plane construction. To minimize the gap between the layers, four movable hydraulic jacks ("the compression rig") force the plates together prior to welding. The strongback also has reference elements to ensure minimal gaps between adjacent plates. Near detector planes are single steel plates and require no welding.

After the plane is laminated, fixtures for mounting scintillator modules and fiber optics cabling are attached to the plane. This is described in detail in Chapters 7 and 8. After the scintillator modules are mounted and tested, restraint clips are installed to hold the plane to the strongback. The strongback is then used as the lifting fixture while the planes are lifted to vertical and transferred to the detector support structure.

4.1.4 Steel support structures

The MINOS steel support structures are critical interfaces to the detector planes. The closest equivalents to these supports in industrial construction are overhead bridge crane rails. The first and most important requirement is that the rails have sufficient bending strength to support the weight of the planes without sagging. Because the steel planes must be mounted sequentially, if there is not enough strength against bending between the vertical columns then the planes will tend to slip down the rails or will hang at an angle with respect to the vertical. The rail strength and column spacing have been chosen to prevent this problem. In addition, the support rails have a structural frame, or bookend, at the upstream end of

each supermodule. The bookend is adjusted to be square to the direction of the rails and plumb with local gravity. The first plane of steel is bolted to the bookend to ensure that the starting plane is correctly mounted. Additional planes are constrained to be parallel to the first by the axial restraint system, described in Section 4.4.1.2.

The second important criterion for the support structure is that the two support rails must be properly aligned, similar to a pair of crane rails. A "guiding" ear on one side of each plane is closely matched in width to its rail ($-0.0/+0.10$ inch). The other ear has a flat surface which allows the second rail to wander by ± 1 inch from the guiding rail. The detector will follow the alignment of the first rail, which could cause problems in alignment of the axial restraints if the guiding rail is not sufficiently straight. The design of the detector support structure includes appropriate tolerances to prevent such problems.

The support structure must also support all of the ancillary equipment needed to operate the scintillator detector planes, as described in Chapters 5, 7 and 8. It is important that the weight of such equipment (e.g., the multiplexing boxes, photodetectors and electronics crates) be carried by the main detector support structure, and not by the steel's ears. Of course, all walkways and service platforms are also held up by the support structure.

The far detector support structure has been designed by CNA Engineering Consultants and is part of the Soudan cavern detector outfitting task[1]. The near detector support structure has been designed by Facilities Engineering Services Section (FESS) at Fermilab and is the responsibility of the magnet steel and coils task.

4.1.5 The magnet coils

The designs of the magnet coils for the MINOS near and far detectors are based on a Fermilab engineering study. The far detector uses a water cooled coil[14] with a total of 15,000 A-turns for each supermodule. The near detector coil (which is about the same length as a far detector supermodule) must carry a 40,000 A-turn current and requires substantially more cooling and a higher current power supply. These coils produce an average toroidal field (at a radius of 2 m) of 1.5 T in the far detector steel planes and a similar field at the position of the neutrino beam in the near detector. As shown in Figure 4.1, the far-detector return coil is routed vertically down from the coil holes on the ends of the detector and runs in a floor trench directly under the central coil. The near detector return coil is routed along the lower 45° face of the uninstrumented flux-return side of the steel plane, as shown in Figure 4.2. These locations minimize interference with photodetectors and electronics.

The far-detector coil-cooling water is provided by a local closed loop system; this is supplied by the MINOS far detector outfitting task[1]. The coil cooling system is connected to the cavern cooling system that carries the heat up the shaft to a heat exchanger on the surface, as described in Section 7.4.1.6. The low conductivity cooling water system for the near detector hall is provided as part of the NuMI project facility.

4.2 Requirements and performance criteria

4.2.1 Goals

The goals of the magnet steel and coils task are:

- To design and fabricate the multi-plane steel structures for both the far and the near detectors, including their assembly fixtures, while optimizing the flatness and magnetic properties of the steel planes.

- To prove the feasibility of the designs and procedures for the manufacture and safe erection of the planes into stable mechanical structures meeting required physical specifications.

- To design and provide the coils, power supplies, cooling and monitoring elements for exciting the magnets to the required field levels and thermal dissipations.

- To design and fabricate the near detector support structure.

- To build and test a succession of prototype structures for optimization of the magnet design details, to enable a demonstration of the integration with active detector elements and electronics into a working system prototype, and to train technical staff for their final manufacture and installation of the detector underground.

4.2.2 Performance criteria

The most critical performance criteria for the magnet steel and coils are:

- **Energy resolution.** The magnetic field in the steel planes must be known and stable to 5% so that the muon momentum resolution does not dominate the overall energy resolution. However, the relative near-far magnetic field calibration must be known to 2% to meet systematic error requirements; this can be achieved using events with stopping muon tracks. (Local mass variations in the steel plane structures must be known to about 10% for good calorimetry, but this should be very easy to achieve.)

- **Fiducial mass.** For the CC disappearance measurement the fiducial masses of the near and far detectors must be known to 1%. The mass of the far detector plates can easily be measured using a digital scale attached to a crane. The fiducial target region in the near detector is limited to a 25-cm radius circle near the center of the plane. The average thickness of the target region must be measured to 0.05 mm precision for the 40 planes of the near detector target.

- **Flatness.** Residual waviness or nonflatness of the steel planes must be within the 1.5 cm tolerance required by the scintillator planes, i.e., each 2.54 cm thick plane must be completely contained within a 4.04 cm thick planar volume to leave enough space for the scintillator planes when adjacent steel planes are pushed together. In particular, the steel planes must not change their flatness outside of this 1.5 cm tolerance during the raising and mounting operation. (The scintillator module mounting is flexible enough that the modules will not be damaged by plane movement within this volume.)

- **Radioactivity.** The steel planes must be free of contamination from radioactive material. Any such contamination should not significantly increase the singles counting rate from photodetector dark current and the room radioactivity counts in the exposed edges of scintillator planes. (Very small amounts of ^{60}Co are occasionally found in commercial steel.)

- **Costs and schedules.** The cost of fabricating, installing and operating the steel and coil system must be minimized in the context of the entire experiment. The present design has resulted from tradeoffs among many interrelated parameters, e.g., expensive plane flatness allows a given detector mass to be installed in a shorter cavern; expensive underground assembly space allows schedule goals to be met and makes more efficient use of manpower; coils with more conductor area cost more to fabricate but save cooling and operating costs.

- **Safety.** The steel planes must be kept stable and safe against structural failure due to mechanical stress at all stages of assembly, mounting and operation.

4.2.3 Tasks

The following tasks are included in the magnet steel and coils WBS element:

- **Steel plane fabrication tasks**

  1. **Steel plane components.** Design, procure and deliver to the Soudan mine and/or Fermilab, as appropriate for far/near detectors and prototypes. These include shaped octagon steel plate components, axial bolts, center bore pieces and ear spacer plates.

- **Near support structure task**

  2. **Near support structure.** Design and procure components for the near detector hanging-file support structures.

- **Steel handling fixture tasks**

  3. **Strongbacks.** Design and procure strongback components for the far and near detectors.

  4. **Near detector transport carts.** Design and procure components for the near detector materials transport carts.

  5. **Far detector compression devices.** Provide devices to mate with the far detector compression rig and force the far detector plates together prior to welding.

  6. **Welding.** Provide systems for automatic submerged arc welding of the far detector plane components into octagonal planes; provide criteria and protocols to ensure the quality of the resulting assemblies.

- **Magnet coil tasks**

7. **Magnet coil design.** Design and provide components for the magnet coils and their supports for both the far and near detectors; this includes design of procedures for the delivery of coil components into the detector caverns, for their assembly on site, for their insertion into the steel bore, and for their final interconnection.

8. **Field calibration and monitoring.** Design and provide fixtures and equipment to measure the magnetic fields within the near and far detectors, directly and by on-line measurement of the excitation current.

9. **Fabrication and installation.** Provide mechanical fixtures for manufacturing the coils on the Fermilab and Soudan sites, for handling their components and for installing them in the detector bores.

10. **Electrical systems.** Specify and procure the power supplies and control systems for the near and far detector magnet coils.

11. **Cooling systems.** Design and provide components for the magnet cooling systems; for the far detector magnets this includes connection to the Soudan cavern cooling system which is supplied as part of the far laboratory detector outfitting task; for the near detector this includes connection to a deionized water cooling system that is supplied as part of the NuMI project facility.

- **Full-scale prototyping tasks**

12. **One-plane prototypes.** Provide a proof of principle that far detector planes can be fabricated, assembled and hung safely. Perform initial measurements of mechanical and magnetic properties.

13. **Four-plane prototype.** Provide a prototype to check all aspects of the design, assembly and performance of the far detector steel and scintillator planes.

14. **Steel-handling prototype.** Provide a simulation of the Soudan hoist cage and shaft stations to demonstrate safe and efficient handling of the far detector plates at Soudan.

15. **Four-plane training prototype.** Construct a prototype of the final detector assembly in order to train the far detector assembly supervisors and crew bosses.

16. **Four-plane near-detector prototype.** Provide a four-plane prototype of the near detector to check the design of the near detector and to train the near detector assembly crews.

4.3 Interfaces with other MINOS systems

4.3.1 Scintillator detector planes

The steel planes interface with the scintillator detector planes by supplying the mechanical support for the detectors, as described in detail in Section 7.4.3.3. Chapter 7 also describes the scintillator plane "clear zone" for getting signal fibers out of the modules. The design

of the steel has allowed for a clear zone (20 cm on the sides, 40 cm on the top and 25 cm on the bottom) around the perimeter of the octagons for signal fibers and for the other hardware which is permanently attached to the scintillator planes. The axial restraint bolts and the ears take up small areas inside the octagons which the scintillator planes must avoid. The scintillator planes must also avoid the axial restraint collars which surround the central coil holes. The design of scintillator modules which satisfy these constraints is described in Chapter 5.

4.3.2 Near and far detector installation

The magnet steel and coils task must be carefully coordinated with the near and far detector installation procedures. An important interface issue is the integration of the steel packaging and shipping with the rigging and storage facilities at the Soudan site. The existing infrastructure at the Fermilab site makes this integration relatively simple for the near detector but the more limited facilities at Soudan make the far detector situation somewhat more difficult.

The new cage for the Soudan-mine hoist has been specifically designed for underground delivery of 5.5-ton "bundles" of pre-sorted steel plates. The preparation of these bundles will be combined with weighing each plate and with quality control measurements. These operations will be performed after delivery of the steel plates to the surface building in Soudan. Storage for one month's worth of steel is provided in the surface building. Additional storage, if needed, will be provided by the steel fabricator.

The assembly of the magnet coils is an interface area where the optimum solutions for the near and far detectors are different. Since the fabrication of the near detector coils can take advantage of existing facilities at Fermilab, the relatively short access shaft has been designed to accommodate the underground delivery of prefabricated, full-length coil sections. The far detector coils, however, must be fabricated underground due to restrictions imposed by the existing shaft. In addition, the coil cooling system at Soudan must interface with a cavern cooling system which is considerably more complex (because of the much greater depth of the far detector cavern) than the corresponding system in the near hall.

To reduce excavation costs both detector halls have been designed to be as small as possible. Because a plane can only be moved with the aid of a strongback, the limited floor space effectively means that planes cannot be removed once they have been mounted on the detector support structure. Although the two most recently installed planes could, in principle, be removed for repairs, this would be time consuming and difficult. This constraint places a high premium on careful quality control during the final checkout of steel and detector planes prior to mounting.

4.3.3 Far detector cavern outfitting

The Far Detector Laboratory Technical Design Report[1] describes the outfitting of the far detector cavern at Soudan and the special equipment required for the installation and operation of MINOS detector systems. The operation of these systems is described in Chapter 7. The following systems are included in the "detector outfitting" task:

- The cavern cooling system and associated electrical systems.

- The MINOS detector electrical and fire suppression systems.

- The detector support structure, including electronics platforms.

- The 3-deck shaft cage for moving detector components underground.

- The underground monorail systems for moving heavy steel and scintillator components.

- The steel plate storage carts and 2-ton rolling gantry cranes.

- The mezzanine storage and testing area in the Soudan 2 cavern.

- The pedestals and compression rigs for steel plane assembly.

The far detector support structure is shown schematically in Figure 4.4. The steel and coil task includes detector plane prototyping and careful testing of the steel handling systems and procedures before underground detector installation begins.

4.3.4   Near detector hall

The near detector support structure has been designed by the Facilities Engineering Services Section at Fermilab in coordination with the design of the near detector hall by the NuMI civil construction task. In addition to supporting the detector planes, this structure also provides walkways which give access to the near detector instrumentation and to the DAQ room. The downstream access shaft and the downstream surface building have been designed to accommodate the installation of the near detector coil components[2].
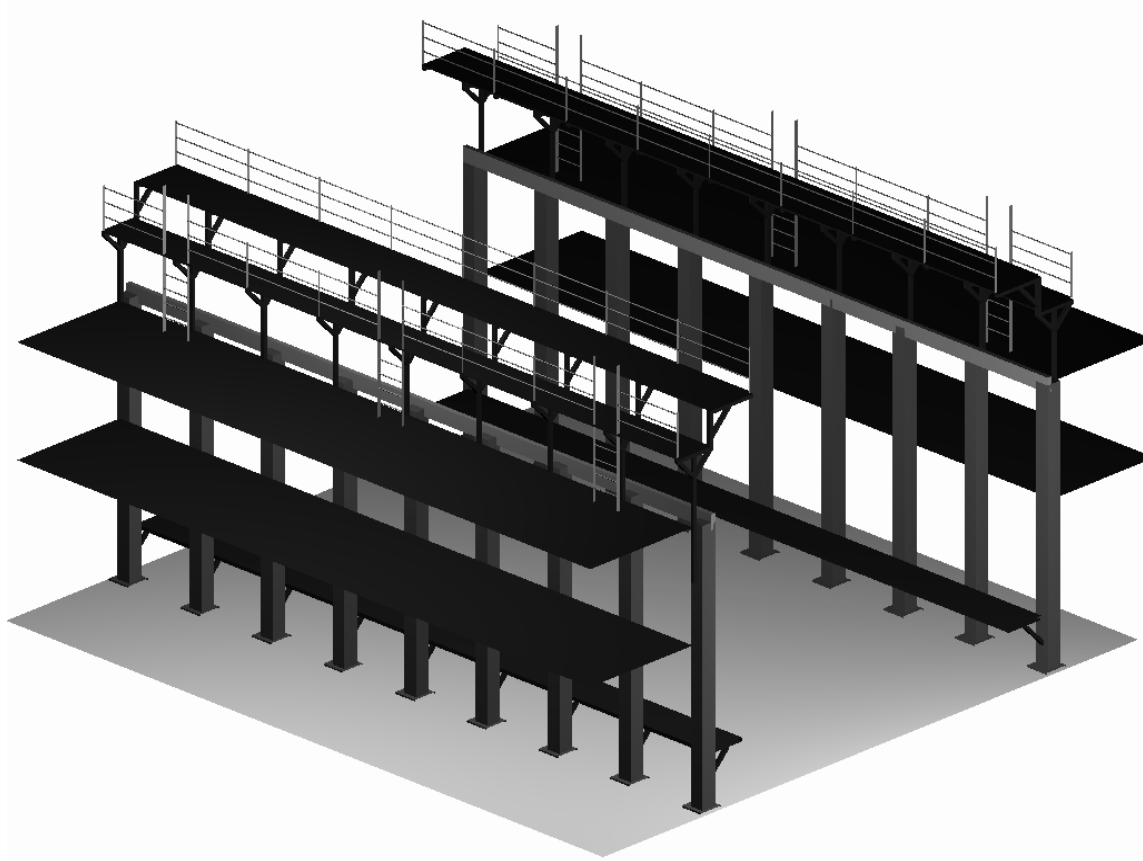
Figure 4.4: Sketch of the far detector steel support structure. The steel plane support rails are the horizontal members at the top of the vertical columns. The upper electronics platforms and personnel access ladders are located above the rails; the lower electronics platforms are cantilevered from the vertical columns.

4.4 Description of WBS elements

This Section describes the magnet steel and coil activities included in each WBS-2.1 Level 3 task. The associated EDIA activities are included in the individual tasks at Level 4, and in the detector plane prototype program within this task (Section 4.4.5).

4.4.1 Steel plane fabrication (WBS 2.1.1)

4.4.1.1 Steel planes

This WBS element includes the purchase of all of the steel plates for the two far detector supermodules and the near detector. The basic requirements on the mechanical and magnetic properties of MINOS steel have already been discussed in Section 4.1.3.1 above.

In order to widen the base of potential vendors, bids for the steel will be requested both from integrated producers (who supply and fabricate steel plate) and also from specialized suppliers (who either make plate or only process it)[15]. Bid requests will also include all axial restraint bolts, center bore pieces, and ear spacer plates. The far detector steel plates will be purchased in a few large orders, whose optimum size will depend on tradeoffs among a number of factors: the uniformity of steel composition and dimensions within large batches, the reduction in unit costs for large production orders (which may depend on individual vendor facilities), and the cost of storage at the vendor.

The magnetic specifications for MINOS steel plates are essentially identical to those used to purchase the plates for the BaBar magnet return yoke[7]. In addition to specifying carbon content between 0.04% and 0.06%, good magnetic properties also require that the plate be hot rolled, with cold processing kept to a minimum. U.S. steel producers generally will not accept direct specification of magnetic properties. The large BaBar steel order was produced in Japan, and consisted of three separate melts. Their measurements of sample magnetization curves indicate that magnetic uniformity of better than $\pm 10\%$ can be expected, which is adequate for MINOS provided that the plate-to-plate variations are measured and included in the experiment's database.

The operation of MINOS scintillator detectors is quite sensitive to any radioactive contamination of the steel planes, which could significantly increase the singles counting rates of the photodetectors. Steel producers use a ^{60}Co tracer in their ceramic furnace linings to indicate when the linings have become thin enough to require replacement. Thus, very low levels of ^{60}Co contamination are relatively common in steel samples. The MINOS specification of less than 0.15 gammas/kg/sec above 0.5 MeV is the same as that used for the steel plates of the Soudan 2 detector. The Soudan 2 experience with 1000 tons of steel calorimeter plates has shown that there is a very low likelihood of significant radioactive contamination (no steel was ever rejected for this reason), so this is not expected to be a serious problem for MINOS. However, it will be necessary to measure the radioactivity of each steel melt, and to have an agreement with the steel producer about how to proceed if a problem is detected.

The 8-m diameter far detector steel planes, shown in Figure 4.1, are assembled at the Soudan detector site from two layers of 2 m wide plates which are plug welded together to form a very strong, flat structure, as described in Section 4.4.2.3 below.

The much smaller near detector steel planes are fabricated from single plates by a com-
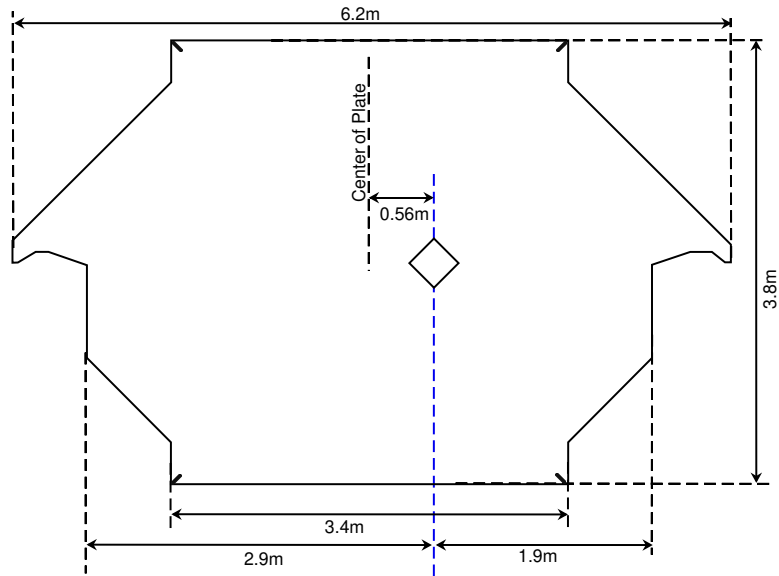
Figure 4.5: Drawing of a near detector steel plane. The beam is centered halfway between the central coil hole and the left vertical edge of the plane.

mercial manufacturer and require no underground assembly work except to attach the scintillator modules. Figure 4.5 shows a drawing of the "squashed octagon" shape of a near detector steel plane. The criterion for the shape of the steel was to provide an adequate magnetic field in the beam region with as little steel as possible for the magnetic flux return path. The planes are made from the same low carbon, hot rolled steel as the far detector. Reducing the amount of steel in the near detector reduces the cost of the steel by about 45% compared to a 6-m wide regular octagon with the same instrumented area. Each plane is made as a single 1-inch thick piece.

The flatness tolerance for the single-piece near detector steel planes may be somewhat harder to to achieve than for the laminated far detector planes. In order to meet the required tolerance of 1.5 cm the manufacturer must provide plate with a flatness of 50% of the allowance in the ASTM A6 standard. This is similar to flatness specifications which are routinely achieved by plate manufacturers. In contrast, in the far detector the laminating process can remove residual bowing in the plates.

It should be noted that the cost estimate does not include preservatives for the steel. Our design study shows this step to be unnecessary, so we have removed it to save the cost of paint and the labor to apply it.

4.4.1.2 Axial restraints

There are three kinds of axial restraints used to stabilize the detector planes, as mounted, for both near and far MINOS detectors. The first restraint consists of "axial bolts" at the eight corners of each octagon; these attach each plane to the previous one as it is installed. The planes are constructed with slots near each of the eight corners which are large enough to accommodate cutting tolerances. Axial bolts also attach the first plane to the bookend. This ensures that the array of planes starts out plumb and square, and remains so. The present

design of the bolt is shown in Figure 4.6. The design is expected to evolve as experience is gained with the flatness achievable in actual welded and erected planes during prototype tests (see Section 4.5.2).
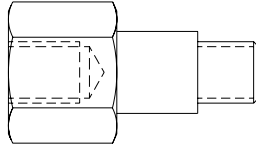
Figure 4.6: Sketch of an axial bolt which is used to restrain the eight corners of each MINOS steel plane. The 3-inch long bolt has threads on both ends to attach to the bolts for adjacent planes. The 1-inch long, 1-inch diameter center section fits into a hole in the steel plane.

The second axial restraint is the collar around the magnet coil hole in each plane. This restraint serves two functions. It sets the spacing in the center of the planes to give the correct gap between planes, and it provides a smooth bore through which the magnet coil can be inserted. The coil hole in each steel plane is deliberately made slightly larger than required for the coil and collar. The collar then allows the centers of the planes to be aligned laterally by taking up all of the tolerance differences caused by the oversize holes, imperfections in the plane assembly, and any misalignment of support rails. These axial restraints do not need to hold against large forces because the bookend is strong enough to stabilize the plates vertically through the axial bolts. Precautions will be taken to minimize the cumulative buildup of forces during the assembly of far detector supermodules and the near detector (see Section 4.5.2). Figure 4.7 is a sketch of the coil collar design. The dotted annulus in the face-on view indicates the allowance for adjusting the position of the collar relative to the 30-cm × 30-cm square hole in the steel plane. Each coil collar bolts to the previously installed collar, and has eight threaded holes to accept the bolts from the collar on the next plane to be installed.

The third axial restraint consists of spacers with the exact shape of the ears, which are welded to the ears. This restraint also serves to fill the gap between adjacent planes so that the ears cannot tip out of a vertical plane. The spacers also supply additional bearing area for the weight of the plane; however, our safety analysis does not make any allowance for this in order to be as conservative as possible.

4.4.1.3 Stability of hanging planes

The stability of the MINOS planes when they are hanging is a difficult engineering problem. Study of this problem was begun at Livermore and continued at Fermilab[16, 17]. All of the analysis has been done for one plane (the single plane test) hanging on the rails with no supports or other engineering aids. In the final detectors, the array of planes bolted to each other and to a bookend is more stable than a single plane. Engineering a stable single plane is an approach that produces a very conservative design for the full detector.

Analyses at both Livermore and Fermilab showed that the planes do not fail from over-stressing the ears. Static hanging planes with no tilt or out-of-plane forces produce stresses

4-17
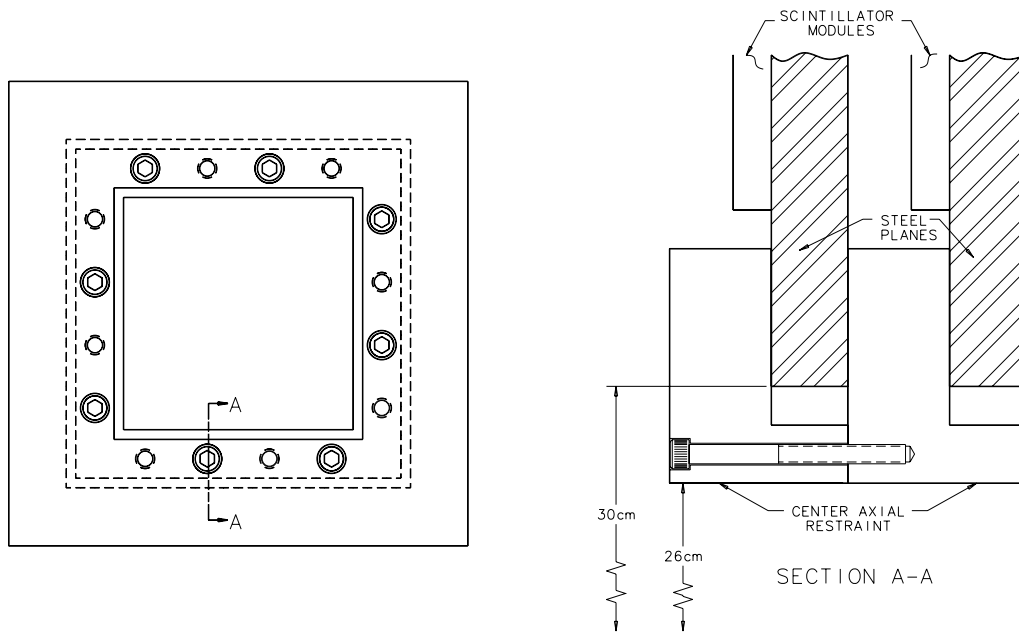
Figure 4.7: Two views of a steel plane coil collar. The face-on view (left) shows the bolt pattern and adjustment allowance (space between the dotted lines). The section view (right) shows how adjacent collars bolt together. The coil hole in the center of the collar is 26 cm × 26 cm.

in the ears of 4500 psi. This stress does not count the bearing area which the ear spacer plates would add. Clearly, this is well below the minimum yield stress of AISI 1006 steel which is 20,000 psi, giving a safety factor of 4.4. The finite element diagrams of the stress show that this is also very localized at the stress riser of the corners of the rails, and would gradually be reduced by local yielding of the metal. The bulk of the planes and much of the ears show stresses far less than even the 4500 psi. Solutions for this static case were obtained using Pro/Mechanica at Livermore and ANSYS at Fermilab; the results agreed within 10%.

Much of our engineering design work to date has focused on the possibility of failure by buckling. Buckling can take on many forms for hanging planes. The planes can fail if they are allowed to rest on the rails at some angle off the vertical. They can also fail by application of a force in the center of the plane which causes bending at the middle, thus pulling the ears off the rails. This bending has many modes, much like the modes a drumhead can take when oscillating. Most of the higher order modes do not appear to cause catastrophic failure but do distort the plane within its flatness allowance.

In order to understand better the buckling characteristics of a hanging plane, engineering analyses were performed at both Livermore and Fermilab. At Livermore, linear eigenvalue theory was used to determine the buckling safety factors for the plane with a variety of constraints and at small angles. Fermilab repeated these calculations to calibrate the models, and then analyzed the problem again. The results were in good agreement. The Fermilab solution showed that for a 0.75-inch thick plane the buckling safety factor is 1.68, and for the 1-inch thick plane the safety factor is 2.99.

Fermilab conducted analyses using nonlinear large deflections to study the post-buckling

behavior of the steel plane. It was shown that, after the initial buckling, the plane warps and tilts to one side, but it is still stable; there is no instantaneous failure of the plane. The analysis showed that the warping and tilt increase as the load on a plane increases.

Preliminary test results using a scale model tend to confirm these conclusions:

1. The plane itself will not buckle if it is kept vertical.

2. The plane will be stable after buckling.

The test specimens were 1/10-scale planes with a thickness of 0.032 inch. Dimensional analysis shows that the scaled plane's buckling characteristics are very similar to those expected of the 1-inch thick full-sized plane. Since it is not possible to increase the density of the scaled plane, an additional load was applied by hanging a weight from the plane's center. The specimen began to buckle when an additional load of 4330 grams was added, more than the 3361-gram weight of the specimen itself.

From studies of the steel planes so far, we have shown that a hanging steel plane will not fail by buckling. If the plane is tilted, or if there is an excessive perpendicular load to cause the plane to buckle and tilt, the stress at the ears may exceed the yield stress of the material and the plane may fail by an ear tearing off. The conclusion of the analysis is clear: the system design must never allow the planes to sit on their support rails without axial restraints of some kind.

4.4.2 Steel handling fixtures (WBS 2.1.2)

4.4.2.1 Strongbacks

The design of the strongbacks is one of the most important tasks in the steel project. The strongback must be as light as possible, strong enough to keep the steel and detector planes flat during assembly and mounting, and must conform to both AISC steel construction code and to ANSI B30.20 "Below the Hook Lifting Devices." It must also hold the steel and detector plane assembly securely during the mounting procedure, without interfering with the plane of scintillator modules which completely covers the top surface of each steel plane. The design analysis was performed according to AISC requirements, including all of the bolted connections and all bending and torsion stresses in the members. ANSI B30.20 requires that any lifting fixture be designed with a minimum safety factor of at least three. The prototype far detector strongback shown in Figure 4.8 was designed at Livermore to these standards. The outer rim and cross members are made from 4-inch × 16-inch, rectangular cross-section, structural steel tubing. Two W16 × 40-lb wide-flange I-beams are used for the main lifting members. The prototype strongback was found to be flat to about 1 cm over the entire 50 m² work surface. This prototype strongback has been successfully used in the New Muon Lab at Fermilab to lift and mount the first prototype steel plane. All joints are bolted so that the strongback can be disassembled for moving down the Soudan mine shaft.

The near detector strongback is similar to, but significantly smaller than, the far detector strongback. It is essentially an assembly platform and lifting fixture for the steel and scintillator detector planes. A conceptual design has been completed at Fermilab. The steel planes for the near detector are manufactured as single pieces and do not require welding or a compression rig.
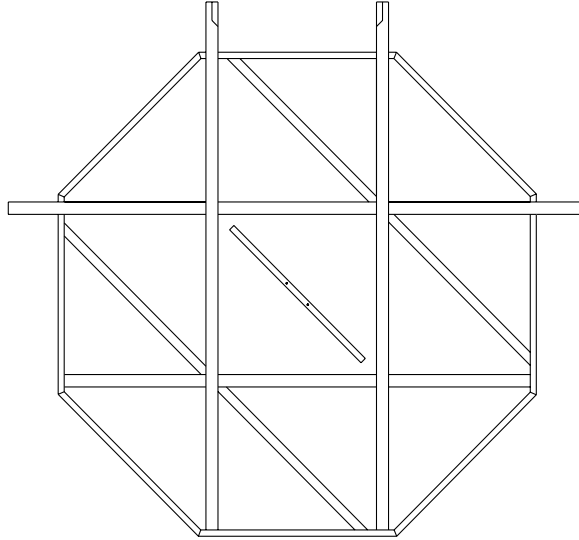
Figure 4.8: Sketch of a MINOS far detector strongback. The diagonal center piece supports the middle of the plane. Its ends are attached to the main structure (not shown in this drawing).

The carts for steel movement in the near detector hall are also included in the magnet steel and coils cost estimate. The near detector carts are similar to the far detector carts that have been designed as part of the Soudan site preparation task[1]. Each near detector cart carries only a single steel plate.

4.4.2.2 Far detector compression devices

The far detector compression rig is designed to force the individual plates together against the strongback during welding to remove any residual waviness; two compression rigs are required for far detector assembly. Calculations using plate theory indicate that a force of 5000 lbs is required to compress two typical plates together to within our specified flatness criteria. The compression rig has four compression devices, 5000-lb hydraulic jacks, that can be individually moved around the plates to supply a total of 20,000 lb of compressive force. The jacks are positioned to flatten the high spots around each weld location and then are reset after the weld is made. The tests described in the next Section have demonstrated the viability of this approach.

The far detector compression rig, shown in Figure 7.3 in Chapter 7, has been designed by CNA and will be constructed as part of the far detector hall detector outfitting task. The design uses a cantilevered jib structure which fits in the limited cavern space. The steel and coil task will provide the eight 5000-lb hydraulic jacks.

We have chosen a specific weld sequence pattern to minimize weld-induced stresses during the assembly of steel plates into octagonal planes. The pattern shown in Figure 4.9 starts the welding at the center of the plates and works to the outside. This pattern flattens the plate from the center and moves towards the edges. As welds are placed at larger radii they

PLUG WELD SEQUENCE

DETAIL A
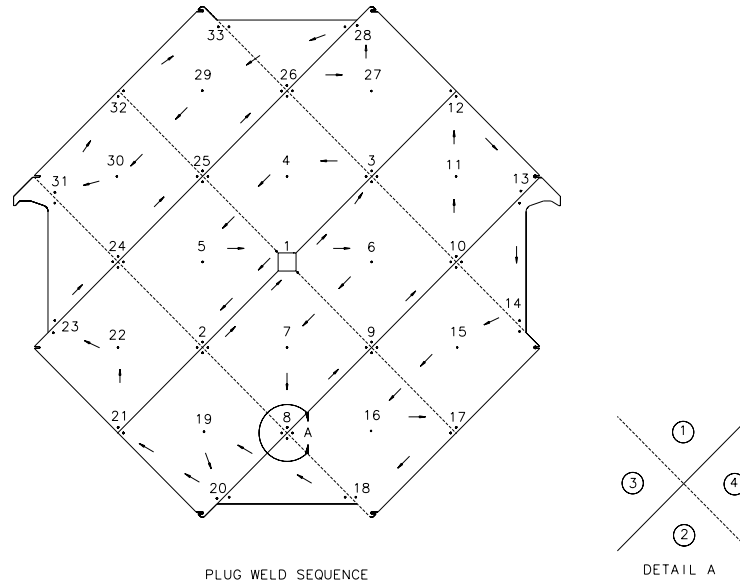
Figure 4.9: Sequence of plug welding operations to assemble an 8-m wide, 1-inch thick octagonal steel plane from eight 2-m wide, 0.5-inch thick plates.

support the flattened areas around the inner sections of the plane.

4.4.2.3 Far detector welding

The plates are welded together to form a plane by 72 one-inch diameter plug welds, as shown in Figure 4.9. Two additional welds are made at each ear to increase their strength. Several different welding processes have been evaluated, including Submerged Arc Welding (SAW), Flux Cored Arc Welding (FCAW), and Gas Metal Arc Welding (GMAW). We have chosen the SAW method for the final production process. Livermore built and tested a prototype SAW welding head using components from an existing welding turntable. For MINOS, SAW is a particularly attractive process because it produces the least arc flash and smoke, which is important for assembly in underground enclosures. The SAW process is simple because the only variable is the on-time of the arc. It can be made fully automatic so that uncertified welding technicians are able to operate the system and a professional welder is needed only to perform quality checks. Although the installation plan includes a certified welder who is always on duty, he or she is mainly occupied with tasks other than plug welding.

The Livermore MINOS group did a test with a pair of 1.2 m^2 plates to discover how the flatness of the plates changed during welding. These plates were measured for flatness before any welding and then again after welding. The gaps between the plates were measured at several times during a series of bolting and welding operations. To model the compression rig, the plates were bolted together with nine 1-inch bolts. The top plate had holes drilled in it to measure the gap between the two plates using a depth gauge. Figure 4.10 shows the plates with the features called out. Welds A, B, C, and D were done first. After the bolts were removed then weld E was done.

WELD TESTS CONFIGURATION
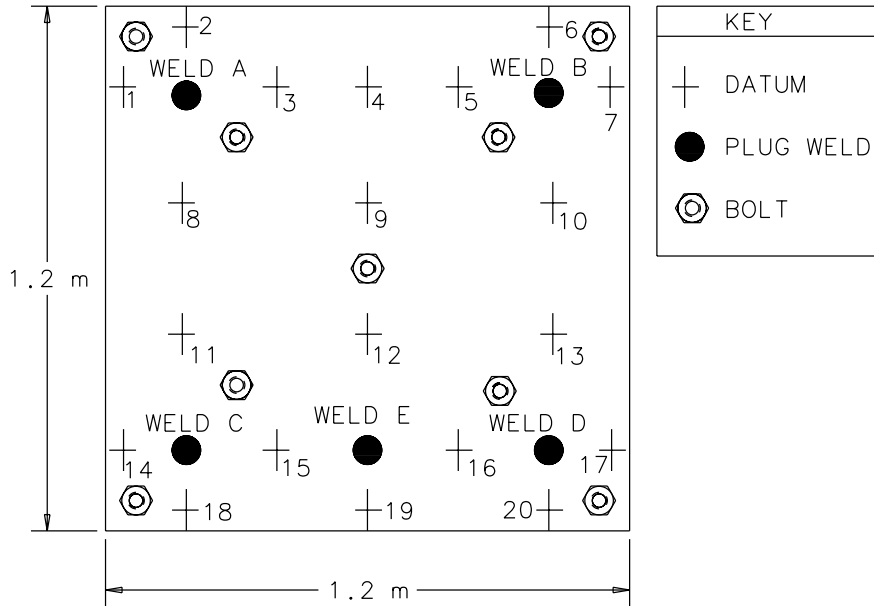
TYPE: ASTM A36 PLATE (1018)
        HOT ROLLED.
SIZE: 1.2m X 1.2m
THICK: 1.9 cm (.750 in)
QTY: TWO PLATES
        A-TOP
        B-BOTTOM

FLATNESS MEASUREMENT
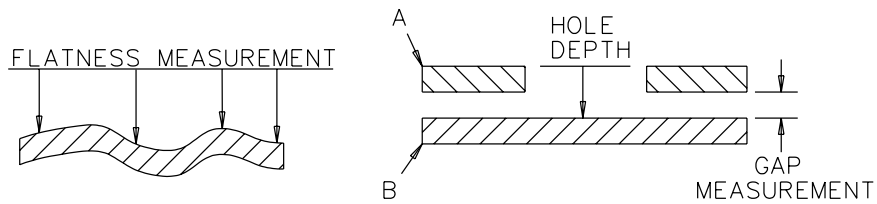
WELD TEST CONFIGURATION FOR TOP PLATE. BOTTOM PLATE
IS NOT SHOWN,BUT ONLY HAS BOLT LOCATIONS DRILLED.

Figure 4.10: Sketch of the Livermore 1.2 m plate plug-welding test setup.

The plates were not pressed against a flat surface, but were only bolted to each other. The plate flatness was measured before and after welding using a Leitz Coordinate Measurement Machine. The finished welded assembly had a flatness around the average of the two individual plates. Although the flatness observed was acceptable, it could have been improved by pressing both plates against a flat platen such as a MINOS strongback.

A summary of the inter-layer gap measurements is shown in Table 4.3. Measurements were taken before the steel was bolted together, after it was bolted, after it was welded, after it was unbolted, and after it was welded at location E. No distortions were seen in the plates at any time during or after the welding.

Measurement	Before bolting	Bolted only	Bolted & welded	Welded only
Median	0.78	0.24	0.25	0.28
RMS	0.68	0.08	0.06	0.09
Max	2.31	0.46	0.41	0.48
Min	0.15	0.13	0.15	0.13

Table 4.3: Gap measurements (in mm) made during the Livermore test of changes in steel plate flatness caused by plug welding. The data represent the spaces between the two plate layers.

Tests of the plug welds were made at Livermore to measure the shear strength of the welds. The results showed that the welds are linear in shear for an applied force of 25,000 lbs. If we assume that all of the welds on a given plate participate uniformly in supporting the plate in shear, then the shear stress is less than 400 psi for any weld, giving a safety factor of around 60. Despite the uncertainty about the uniform loading of the welds, this is a very conservative safety factor. It will also be necessary to do coupon tests for every worker who will operate the welder during detector installation to ensure that the weld quality is adequate; this is much like the procedure used to certify a code welder.

4.4.2.4 Transfer from strongback to rails

The most important restriction in transferring a steel plane from the strongback to the rails is that the ears of the planes cannot support both the weight of the plane and the weight of the strongback. The present design uses a shelf on the bottom edge of the strongback to support the weight of the plane while it is raised to the vertical and carried to the support rails. A sketch of this design is shown in Figure 7.11 of Chapter 7. Clips on the top and at the center only restrain the plane on the strongback from tipping off; these clips support no weight. When the plane is positioned at the proper place on the rails, the clips are removed and the plane is lowered onto the rails. As the strongback is lowered, the plane ears pick up the plane weight and the strongback continues to drop away until it is completely free. The design requires that the "top" layer of each steel plane have edge notches at several locations so that clips can grip the edges of the "bottom" steel layer without touching the scintillator modules.

Included in the cost estimate is a "nudger" mechanism to slide a single plane along the rails for a short distance. This will be needed if the final version of the strongback clips requires some additional space between planes to disengage them. This is a design feature which the 4-plane prototype test is intended to address, as described in Section 4.4.5.2.

Another feature which needs to be verified during the single-plane test (Section 4.4.5.1) is that the design of the strongback permits the safe installation of the axial restraint bolts (see Section 4.4.1.2 below) immediately after a plane has been placed on the rails. As described in Section 4.4.1.3 below, the stability of the planes is such that no part of the assembly and hanging operation should allow a plane to hang alone on the rails without such restraints.

4.4.2.5 Safety

Safety considerations have been included as integral design requirements for all steel handling systems for both the near and far detectors. Safety issues for all NuMI-MINOS facilities are described in the NuMI Project Preliminary Safety Assessment Document[18].

4.4.3 Near detector support structure (WBS 2.1.3)

An initial design of the near detector support structure has been completed by Facilities Engineering Services Section (FESS) at Fermilab as shown in Figure 4.2. The design is in compliance with the Fermilab ES&H manual and the AISC Manual for Steel Construction[3]. As in the far detector structure design by CNA[1], the critical factors included in the design are the stiffness of the support beams, the alignment of the rails and the requirement that the structure support all ancillary equipment.

The support rails for the planes are similar to industrial crane rails; bending moments are supported by a deep I-beam, and lateral moments are supported by a channel welded to the top of the I-beam. The rail has a 4-inch wide bar on top of the channel for the plane ears to rest on. Lateral support for the structure is provided by beams running from the support columns to the walls of the cavern. The lateral supports also provide the frame for work platform decks and walkways at the elevation of the ears. Longitudinal stabilization is provided by cross braces that are built into the framing under the deck. With this placement, the braces allow access to the bottom of the detector and leave clear egress aisles under the decks on each side of the detector.

4.4.4 Magnet coils (WBS 2.1.4)

4.4.4.1 Design and properties of the coils

There are two identical coils for the far detector, one for each supermodule. The far detector coils provide a total of 15,000 A-turns of current in the 30-cm square central bore of the far detector planes[14]. These coils are designed so that their components can easily be moved down the existing hoist cage and so that they can be assembled underground without significant interruption of the assembly of subsequent detector planes. Due to the asymmetric shape of the near detector steel, the single near detector coil must carry nearly three times as much current as a far detector coil (40,000 A-turns). The different current

requirements and the more convenient access at the Fermilab site have led to substantially different optimizations of the near and far detector coils.

Each far-detector coil is fabricated from 163 turns of 1/0 gauge stranded copper wire housed inside a 25-cm diameter, water-cooled, copper jacket. The outer jacket is cooled by water flowing through eight copper tubes. Seven additional tubes provide cooling near the center of the coil. A cross section of a far-detector coil is shown in Figure 4.11. Each of these coils carries a current of 92 A. In order to provide more working space under the detector, the return leg of each coil has been routed through a shallow trench in the floor of the cavern.
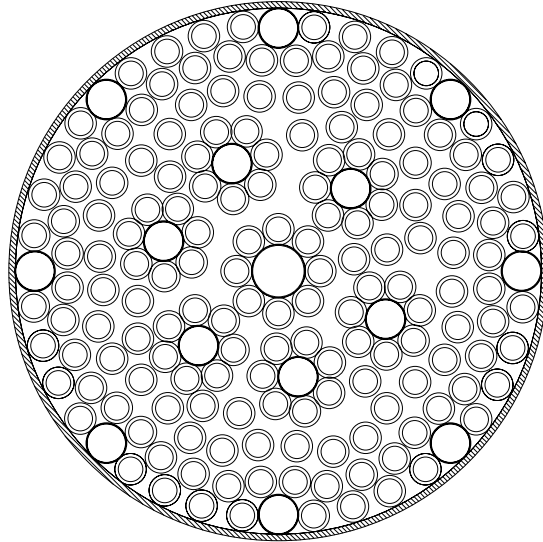
Figure 4.11: Sketch of a cross section of one of the far detector supermodule coils. The larger diameter circles represent the copper cooling tubes and the smaller circles are the 163 turns of 1/0 gauge stranded copper wire. The outline of each of these conductors is a to-scale representation of the insulator thickness. The outer circumference is a copper jacket directly cooled by eight cooling tubes.

Detailed calculations and simulations of the far detector magnetic field configuration have been performed by MINOS groups at Argonne, Fermilab and Livermore for hot-rolled AISI 1006 low carbon steel[5]. Figure 4.12 is a plot of lines of constant field in one of the steel octagons of the far detector. Small variations in these configurations are predicted in the end planes (due to the return leg of the coil). The small fringe fields from the steel and the coil can affect photodetectors and produce mechanical stresses that must be accommodated. Initial calculations indicate the fringe fields will be small in the region of the photodetectors.

The thermal properties of this coil design have been evaluated at Fermilab using ANSYS calculations[19]. The outer jacket of the coil will have a maximum increase in temperature of less than 2°C. To gain greater confidence in these FEA calculations, they have been tested in a 1-m long by 5-cm diameter coil. The measured temperature increase in the center of the model coil, as a function of current, agreed with model calculations to better than 5%.

far detector -- contours of constant B-modulus
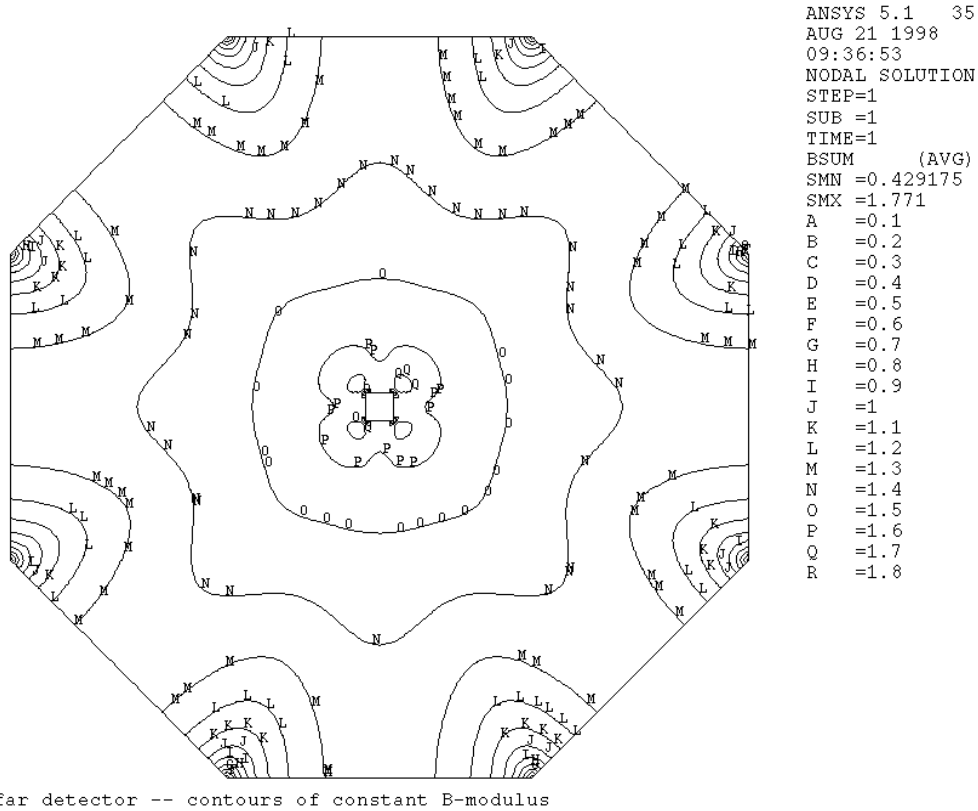
Figure 4.12: Contours of constant B-field magnitude in one of the far detector steel octagons for a 15,000 A-turn excitation. This two dimensional calculation was for a solid steel plane (with no gaps between plates) made of AISI 1006 steel, with a 0.3 m × 0.3 m square hole.
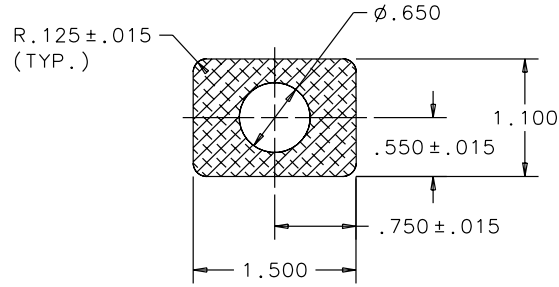
Figure 4.13: Sketch of cross section of one of the 48 conductors in the near detector coil. (All dimensions are in inches.) The conductor is cooled by flowing low conductivity water through the center channel of the conductor.

The relatively high current in the near detector coil requires significantly more cooling than is needed for the far detector coils. Each turn of the near coil is formed from 1.1-in×1.5-in rectangular-cross section aluminum conductors[20] with a 0.65-inch diameter water-cooling channel through its center. The cross section of the one of these conductors is shown in Figure 4.13. The coil has 48 turns where the conductors are arranged in a 6 by 8 rectangular pattern. Each near-detector conductor carries 833 A for a total of 40,000 A-turns.

The near-detector coil produces a toroidal magnetic field averaging about 1.5 Tesla in the target region of the near detector. Figure 4.14 shows the magnetic field contours for a near detector plane. In the near detector there are no photodetectors or electronics on the flux return side of the steel plates so the relatively high magnetic fringe fields on that side do not affect detector operation.

4.4.4.2 Magnetic field calibration and monitoring

The magnetic field must be known accurately in this experiment to achieve the required precision on muon momentum measurements (5% absolute and 2% relative, near to far detector); MINOS energy resolution requirements are explained in Section 5.2. The detailed prediction of the field distribution through the detector relies upon precision simulations using the measured magnetic characteristics of the steel plates as input. Predictions will be verified in field calibration tests during the prototype plane assembly studies described in Section 4.4.5.

The nature of the steel plane fabrication increases the likelihood of errors in prediction of the magnetic field distribution: the large amount of steel required implies that many batches of steel will be needed, each of which can have a different chemistry and hence different permeabilities. The chemistry of individual steel melts will be carefully monitored and controlled and the permeability of plates will be measured after rolling. The plate-to-plate gaps within the composite far detector planes will affect the field, as described above in Section 4.1.3.1. Each assembled plane will have different gaps and thus different reluctances. In order to monitor these various effects each plane will have a pickup coil wound around the toroid to permit measurement of the integrated flux during excitation so that one can compare fields of different planes. Each coil power supply will have a current regulator and precision readout to continuously monitor its current. These systems are included in the cost estimate for the magnet steel and coils task.

ANSYS 5.1   35
AUG 21 1998
08:59:56
NODAL SOLUTION
STEP=1
SUB =1
TIME=1
BSUM   (AVG)
SMN =0.002112
SMX =2.859
A   =0.1
B   =0.25
C   =0.4
D   =0.55
E   =0.7
F   =0.85
G   =1
H   =1.15
I   =1.3
J   =1.45
K   =1.6
L   =1.75
M   =1.9
N   =2.05
O   =2.2
P   =2.35
Q   =2.5
R   =2.65
S   =2.8
T   =2.95
U   =3.1
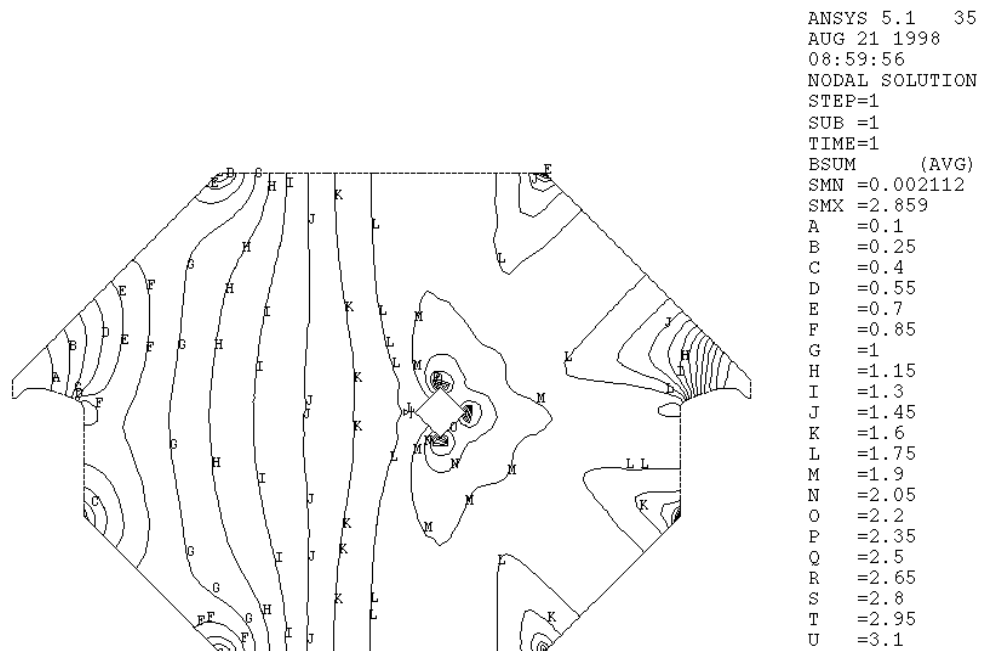
near detector -- contours of constant B-modulus

Figure 4.14: Contours of constant B-field magnitude in one of the near detector steel planes. This two dimensional calculation was for a solid plane made of AISI 1006 hot rolled steel with a 30 cm square coil hole and a current of 40,000 A-turns.

4.4.4.3 Far detector coil fabrication and installation

This process involves close coordination between the present task and the far detector installation tasks described in Chapter 7. The far detector coils have been designed to be assembled underground with minimal labor, fixturing and specialized tools. Coil assembly and installation will cause only a short pause (about two weeks) in the assembly of detector planes after a supermodule is completed. All coil components are packaged to fit easily into the Soudan mine hoist cage.

The components of the far detector coil, the conductor and cooling tubes are delivered to Soudan coiled on reels. The outer jacket is shipped in open sections small enough to fit into the hoist cage. After the last planes of a supermodule are installed, the coil cooling jacket is assembled. The sections are brazed together and the outer cooling tubes are soldered to the inside of the outer shell.

The cooling jacket is then inserted into the completed supermodule. The flexible 1/0 gauge copper wire is pulled through the jacket in single turn lengths and each conductor is labeled. Seven times during the winding of this coil, copper cooling tubes are unrolled and inserted into the coil. After the coil is wound electrical-distribution grade crimp connections are used to connect the separate turns of the coil. Finally, the cooling tubes are plumbed into the cavern cooling system.

One of the advantages of this design is that after the cooling jacket has been inserted into a supermodule, the coil installation and commissioning can proceed in parallel with the assembly of the next supermodule. Another advantage is that, if repairs are needed, faulty turns can be removed and replaced. Further description of the coil installation process is provided in Section 7.4.3.6 of the Far Detector Installation Chapter.

4.4.4.4 Near detector coil fabrication and installation

The design of the near coil takes advantage of the existing above-ground facilities at Fermilab. It is built in half-coil packs in a surface building and then moved to the cavern as two complete units. The drop-shaft into the NuMI near hall tunnel has been designed to allow a full 60-foot long coil segment to be lowered into the cavern.

The aluminum conductor is delivered to Fermilab on spools where it is uncoiled and wrapped with insulation. Lengths of conductor are then bent to an L-shape and bonded together to make one half of the coil pack – either the center bore or the return half. The return half is placed underneath the assembled near detector and the "L" end is lifted at a 45° angle. The center portion is then inserted through the supermodule bore using a special "spreader bar" lifting fixture to support the free end of the conductor assembly as it enters the bore. This fixture is provided by this task. Note that the center segment of the coil assembly weighs about 500 kg, is flexible, and could be easily damaged if overstressed. After the two sections of the coil are mounted in place, electrical and cooling water connections are made. Further description of the coil installation process is provided in Section 8.4 of the Near Detector Installation Chapter.

4.4.4.5 Coil cooling systems

The water cooling system must maintain the magnet coils at 25°C to ensure that scintillator systems are not prematurely aged. Since no current is carried in the cooling tubes in the far-detector coil, the cooling system can operate using ordinary water. This means that the cooling pipes can be directly plumbed into the cavern cooling system. This system transfers heat, via multiple pumping stations, to a surface cooling tower. The far-detector water cooling system will carry about 19 gpm/coil and is designed to carry off as much as 25 kW of heat per far detector supermodule.

The coil cooling system for the near detector will connect to a low-conductivity water (LCW) magnet cooling system provided by the NuMI project facility . The water cooling system will run at about 22 gpm and must carry off the 80 kW of heat generated by the coil.

Both the near and far coils will be instrumented with thermal sensors, electrical sensors, and interlocks to detect possible hot spots in the event of local mechanical or electrical failure.

4.4.4.6 Electrical system

Both the near and far MINOS coils are powered by standard switching supplies. The far detector has two PEI 20 kW Trim switching power supplies, one for each supermodule coil. The input power is 480 V, 3 phase, and the output is 92 A at 190 V. Total power dissipated in the two far detector coils is 37 kW. The high current near detector coil uses a standard Fermilab switching power supply to deliver 833 A at 96 V. All supplies are equipped with input and output filters to reduce electronic noise pickup. The near detector coil power dissipation is 80 kW. All power supplies have remote readout and remote control capabilities.

4.4.5 Detector plane prototypes (WBS 2.1.5)

4.4.5.1 Single plane prototype

A single plane prototype is currently hanging in the New Muon Lab at Fermilab. It consists of an 8-m octagon fabricated from eight steel plates, each 1 cm thick (rather than 1.27 cm thick as planned for the far detector). The main goal of the test is to provide a proof of principle that such planes can be fabricated commercially, assembled, and hung safely. The 2 cm thick prototype plane, which is thinner than the 1-inch thick planes of the baseline design, represents a "worst case" scenario for evaluating the mechanical stability of the detector planes during handling and after erection.

During assembly, measurements were made to judge the flatness of the planes and the gaps between plates. Stresses in the ears were measured as the plane was erected and are consistent with model calculations. The after erection flatness of the plate was also consistent with theoretical expectations. We plan to continue extensive study of the first one-plane prototype and, using the infrastructure in the New Muon Lab, to examine at least one more one-plane prototype. These studies will be designed to evaluate 1-inch thick planes, to study detector plane mounting techniques, to evaluate the effects of loads on the plane, and to perform initial measurements of magnetic fields.

The current infrastructure in the New Muon Lab will be augmented by a second plane-support structure. This new support will allow multiple planes to be raised and lowered, a feature that will allow different scintillator module mounting schemes to be prototyped and tested. The new support will also include a prototype of the final bookend structure.

4.4.5.2 Four plane prototypes

Three 4-plane prototypes will be constructed in the New Muon Lab at Fermilab. The initial 4-plane test will be used to check all aspects of the design, assembly, integration, and performance of the MINOS far detector system. The second prototype will be constructed somewhat later in order to train the far detector assembly supervisors and crew bosses. Finally, a 4-plane prototype of the near detector planes will be constructed to check the design of the near detector and to train the near detector assembly crews.

The first 4-plane prototype will execute the first complete integration of the entire far detector system. It will include four steel planes, three prototype scintillator planes with calibration and diagnostic readout systems, and a magnet coil carrying 15,000 A-turns. It will thus be possible to determine any mechanical interferences of the various components parts during assembly. Necessary design changes can be worked out early in the construction cycle. For the steel system, this will be the first opportunity to see if the design of the strongback will permit a simple and safe installation of the axial restraint bolts. A first fitting of the center-bore restraint system will also be possible. Procedures will be tested for all phases of the mechanical assembly of the final detector.

The initial 4-plane prototype test will be undertaken after extensive studies of the single plane prototype described above. The single-plane studies will be continued with the individual planes of the 4-plane prototype as they are constructed. All mechanical engineering and integration issues will have been resolved by the time the 4-plane device is finally constructed and tested. Integration of the steel planes with the scintillator detector planes and the magnet coil will be a particular focus of the later stages of this work.

After the initial prototype studies are completed, a second 4-plane prototype setup will be used to train the installation crews for the far detector, as described in Chapter 7. Afterwards, a single 4-plane prototype of the simpler near detector planes will be constructed in order to train the near detector installation crews. (Near detector installation is scheduled to begin about a year after the start of installation at Soudan.)

These studies will include detailed measurements of the magnetic properties of the detector. It will be possible to obtain observational data showing the effects of gaps between plane components on the field. Measurements will also determine the heating effects of the magnet coil on the scintillator planes. Fringe magnetic fields will be determined and compared with calculations and measurements of their forces on the planes and on the conductor. The effects of the fringe fields on the photodetectors will also be established.

Alignment procedures for the detector will also be finalized during these studies. These include the methods to determine the positions of the scintillator planes relative to the steel. The procedures and equipment used to measure the actual positions of the scintillator modules on the steel after mounting will be verified. The alignment of the planes on the rails will also be studied.

4.4.5.3 Far detector steel handling

A full-scale mock up of the Soudan shaft and hoist cage will be set up in the New Muon Lab at Fermilab. This structure will be used with the 4-plane prototype steel plates to study steel handling operations to ensure safe, efficient, underground handling of the far detector plates.

4.5 Future optimization and engineering

Many of the future optimization and engineering studies associated with the steel and coils task are summarized in Section 4.4.5. The present Section will concentrate on topics which were not previously discussed in detail.

4.5.1 Steel plane fabrication

Steel plane fabrication techniques for the far detector have been thoroughly studied at several MINOS institutions. The present baseline design was developed by the Livermore group. Their cost estimate includes a number of cost-saving techniques, for example, ordering special long sheets which, when cut in a certain pattern, minimize the amount of scrap. One of the largest remaining uncertainties concerns the gaps between plate edges after assembly. The first single-plane prototype test has already shown that plate to plate gaps are generally less than 1 mm; only about 2 m of the total 40 m length had gaps larger than 1 mm. (These were in the 2 to 3 mm range.) However, if further experiences show that the gaps can not be maintained within specifications, the plate machining option would be a viable alternative procedure for reducing the widths of gaps between steel plates, although it would increase the plate cost somewhat.

If plasma cutting continues to look feasible, the design of the far detector plates will be slightly modified. The central hole in the far detector plates will be changed from the current square hole to a 30-cm circular bore.

4.5.2 Steel handling and mounting fixtures

Testing of the prototype strongback with the 4-plane prototype (Section 4.4.5.2) will indicate what changes must be made before the production strongbacks for both the near and far detectors can be ordered. The present design is well engineered, meets the required flatness specifications, and has successfully hung a bare 8-m steel plate. Experience with fully instrumented planes may require that the plan and the design be changed. It is possible that the clips holding the plane onto the strongback may have to be moved in order to expedite their disengagement. These clips might also have to be moved to accommodate some detailed features on the scintillator planes or their mounting brackets which have yet to be specified. In addition, the detailed design of the strongback for the near detector planes, which have a different size and shape, still remains to be done.

A second important issue is the degree to which the actual planes, as fabricated and erected, contain residual variations in flatness which require variable lengths of axial bolts to serve as stability restraints at the octagon corners. It is an important safety consideration

that mechanical stress energy not be accumulated during the sequential assembly of the multiple planes of the near detector and the far detector supermodules. Bolts of variable lengths, or additional shims or similar devices, may be required to achieve this during detector assembly.

The far detector compression rigs will certainly be able to perform as required. The first welding tests from the one plane prototype, however, indicate that much smaller forces may be sufficient to flatten the steel. In one alternative scheme, the compression could become an inert mass which is moved using the small gantry cranes at each workstation.

4.5.3 Magnet coil installation

A prototype of the far detector coil will be constructed to study the performance of the coil and cooling system and to optimize the installation procedure. Prototype coil studies performed as part of the prototype program described in the previous Section will use these techniques.

The near detector coil installation procedure involves the construction of two monolithic 48-turn L-shaped segments. A large fraction of the installation effort is devoted to connecting the conductor segments to each other, to the power supply and to cooling water system. Prototype studies will also be used to evaluate splicing techniques.

Chapter 4 References

[1] The University of Minnesota, CNA Consulting Engineers, Ericksen-Ellison Associates, Inc., and Miller-Dunwiddie, Inc., "MINOS Far Detector Laboratory Technical Design Report (Including Basis of Estimate & WBS) for Cavern Construction, Cavern Outfitting & Detector Outfitting," October 1998, Fermilab report NuMI-L-263.

[2] The Fermilab NuMI Group, "NuMI Facility Technical Design Report," October 1998, Fermilab report NuMI-346.

[3] Manual of Steel Construction, American Institute of Steel Construction Inc., Ninth Edition, 1989.

[4] P. Schoessow, "MINOS toroid magnetic measurements," February 1998, Fermilab report NuMI-L-347.

[5] P. Schoessow et al., "Comments on MINOS toroid steel properties," May 1998, Fermilab report NuMI-L-378.

[6] J. Kilmer, "Specifications for Carbon Steel Plate for MINOS Detectors," September 1998, Fermilab report NuMI-L-422.

[7] R. Bell, June 1998, private communication.

[8] J. Kilmer, "Specifications for Fabrication of Plates for MINOS Far Detector," September 1998, Fermilab report NuMI-L-424.

[9] T. Ladran *et al.*, "Far Detector Steel Flatness and Gap Tolerances," November 1996, Fermilab report NuMI-L-181.

[10] The Fermilab NuMI Project Staff, "NuMI Project Cost and Schedule Plan," October 1998, Fermilab report NuMI-362.

[11] L. Turner, "Field computation for a neutrino detector magnet: the effect of small gaps in large bodies," September 1996, Fermilab report NuMI-L-209.

[12] E. Hartouni, report at a MINOS Collaboration meeting on the effect of steel plane gaps on muon trajectories (1997).

[13] T. Ladran *et al.*, "MINOS Single Plane Prototype Draft Assembly Procedure," December 1997, Fermilab report NuMI-L-323.

[14] N. Bednar *et al.*, "Basis of Estimate for the MINOS Far Detector Magnet Coils," September 1998, Fermilab report NuMI-L-404.

[15] J. Kilmer, "Advanced Procurement Plane for MINOS Steel," September 1998, Fermilab report NuMI-L-423.

[16] T. Ladran *et al.*, "MINOS Single Plane Prototype Steel Mechanical Analysis," December 1997, Fermilab report NuMI-L-322.

[17] Z. Tang, "MINOS Prototype Steel Plane Buckling Analysis," February 1998, Fermilab report NuMI-L-353.

[18] The Fermilab NuMI Project Staff, "NuMI Project at Fermilab: Preliminary Safety Assessment Document," October 1998, Fermilab report NuMI-361.

[19] Z. Tang, "Thermal analysis of the MINOS far detector magnet coil," September 1998, Fermilab report NuMI-L-413.

[20] J. Kilmer, R.W. Fast, R. Currier, and R. Stanek, "Specifications for Aluminum Conductor," September 1998, Fermilab report NuMI-L-411.

Chapter 5

Scintillator detector fabrication

5.1 Overview

This Chapter describes the MINOS scintillator system. The first Section gives an overview of the baseline design. Section 5.2 sets the performance criteria for the scintillator system and Section 5.3 describes the interfaces of the scintillator system with other MINOS systems. Together, these first three Sections provide a complete overview of the scintillator system. Section 5.4 discusses in detail the elements of the scintillator WBS[1], including components, capital equipment costs, assembly procedures and calibration procedures. Finally, Section 5.5 discusses future engineering and optimization of the design.

5.1.1 Description of the scintillator system

The MINOS detector uses extruded plastic scintillator which is read out by wavelength-shifting (WLS) fibers coupled to multi-pixel photodetectors. This technique provides excellent energy and spatial resolutions. The baseline design relies only on existing technology for which performance measurements have been made. The major components of the scintillator system are:

- **Scintillator strips:** The active detector planes are composed of extruded polystyrene scintillator strips, 1 cm thick and 4.1 cm wide. Each detector plane is an octagonal array of 192 parallel strips. Each scintillator strip is co-extruded with a TiO_2 outer layer for reflectivity and a groove for a wavelength-shifting fiber. Several existing scintillator formulations and producers can meet MINOS specifications.

- **Fibers:** Wavelength-shifting (WLS) fibers are glued into a groove in each scintillator strip. In the far detector the fibers are read out from both ends, while the shorter near detector fibers are read out from only one end. Fibers with acceptable light output and attenuation are produced by Bicron and Kuraray. Figure 5.1 shows a sketch of a single scintillator strip with the fiber readout.

- **Scintillator modules:** The scintillator strips are assembled into either 20-wide or 28-wide (82 cm or 115 cm wide) modules for shipment to the near and far detector sites at Fermilab and Soudan. The shapes of the modules are designed to cover the
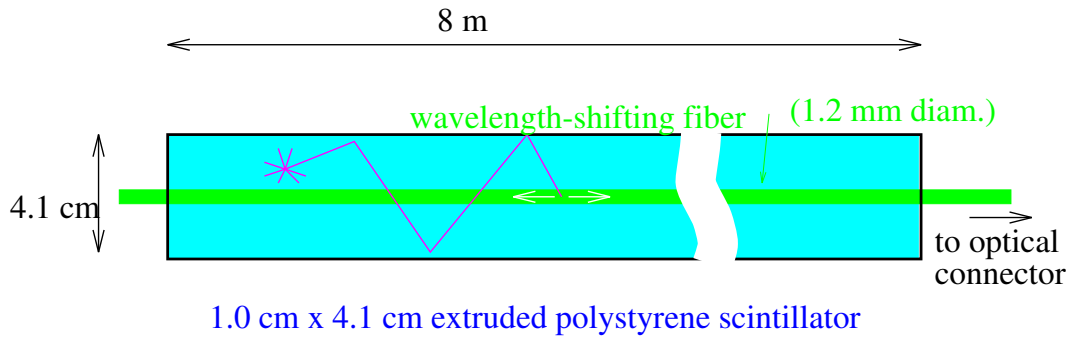
Figure 5.1: Sketch of a single scintillator strip. Light produced by the passage of particles is multiply reflected inside the strip by an outer reflective coating, and eventually may be absorbed inside the WLS fiber. The fiber re-emits light isotropically and some of this light is captured within the fiber and transmitted to the photodetectors.

octagonal steel planes. The strips within a module are glued to a light-tight outer aluminum skin, forming a rigid structure for easy handling and mounting. The ends of the modules have light-tight plastic manifolds which route the WLS fibers to bulk optical connectors.

- **Light guides to photodetectors:** Clear fiber ribbon cables carry light from the detector modules to multiplexing boxes where the photodetectors are mounted. Optical connectors are used for all fiber optics connections. The ribbon cables plug into the front faces of the multiplexing boxes.

- **Multiplexing boxes:** Each detector plane is divided into eight "logical modules." Each logical module consists of 24 adjacent strips (about 100 cm in width). Eight fibers, one from each of eight logical modules, are multiplexed onto a single photodetector pixel and its associated electronics channel. Demultiplexing is straightforward because the local order of fibers on one side of the detector is permuted with respect to the other side, giving unique patterns of light on the two sides. Each box serves two detector planes for one side, i.e., a total of three PMTs resides in a box. The 8-fold multiplexing is practical because of the limited spatial extent of neutrino events within a single detector plane. Figure 5.2 shows a schematic of the readout chain for the scintillator strips. Figure 5.3 shows a schematic of the multiplexing scheme.

- **Photodetectors:** The photodetector is the 16-channel Hamamatsu R5900U-00-M16 photomultiplier. These PMTs are housed in the multiplexer boxes and will couple directly to the front-end electronics. Each pixel of the PMT reads 8 signal fibers from different logical modules. A total of 24 pixels (1.5 photomultipliers) are required to read out each side of a detector plane. Figure 5.4 shows a schematic of how photodetectors are placed in the MUX boxes and interface to the electronics boxes. The assembly is modular and acts as a Faraday cage for the PMTs and electronics.

- **Calibration:** Calibration of the scintillator system is performed regularly using a combination of light injection to give the response curve of the photodetectors, and cosmic ray muons to normalize the response curve to energy. This necessitates an extrapolation over two orders of magnitude in light/energy. A calibration module, which can be placed in a test beam of hadrons and electrons, is used to determine the hadronic energy scale and the EM energy response and resolution. Radioactive sources permit quick checks on scintillator response.

Table 5.1 gives a summary of the scintillator system components.

Item	Each far plane	Each far supermodule	Full far detector	Near detector	Total
Number of scintillator planes	1	242	484	160	644
Area of scintillator [m^2]	53	12,800	25,600	2,400	28,000
Mass of scintillator [kg]	540	130,680	261,360	25,000	286,360
Number of scintillator strips	192	46,464	92,928	12,288	105,216
Length of scintillator strips [m]	1,293	314,200	628,400	60,000	688,400
Length of WLS fiber [m]	1,485	360,900	721,800	65,000	786,800
Number of 28-wide modules	4	968	1,936	224	2160
Number of 20-wide modules	4	968	1,936	320	2256
Number of M16 PMTs	3	726	1,452	588	2,040
Number of M16 PMT pixels	48	11,616	23,232	9,408	32,640
Number of readout channels	48	11,616	23,232	9,408	32,640
Number of MUX boxes	1	242	484	212	696
Number of 8-fold multiplexed pixels	48	11,616	23,232	-	23,232
Number of not-multiplexed pixels	-	-	-	9,216	9,216
Number of 4-fold multiplexed pixels	-	-	-	960	960
Length of (single) clear fiber [m]	1640	397,000	794,000	51,000	845,000

Table 5.1: Summary of basic quantities of the MINOS detector components. The values shown are approximations of exact engineering calculations.

Our choice of two-ended readout of the scintillator strips offers the following advantages:

- Better uniformity in light response from two ends, which may reduce systematic differences between the near and far detectors.

- Higher observed light level than with one-ended readout for the same scintillator light output.

- Redundant trigger capabilities, permitting detailed studies of trigger efficiency across the detector.
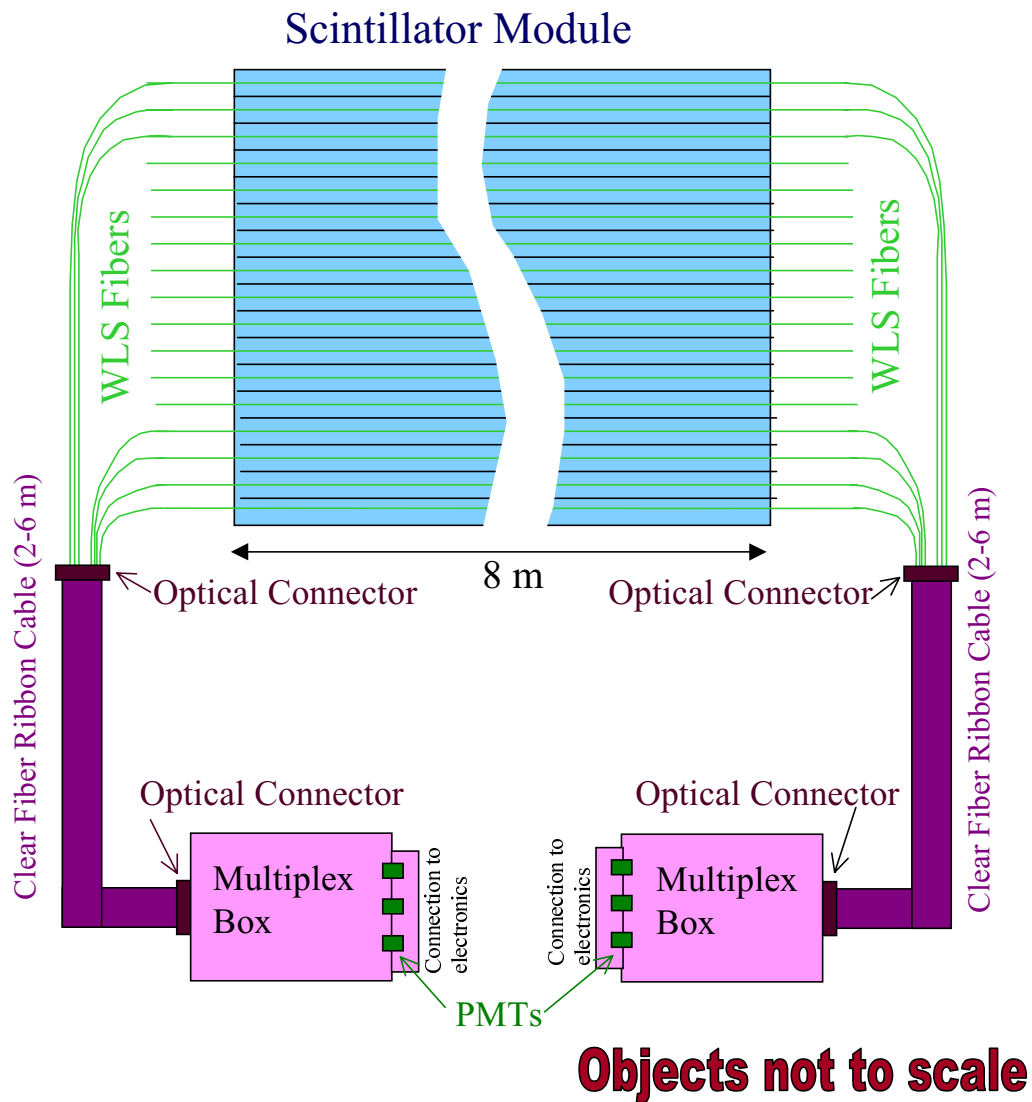
Figure 5.2: Schematic of the scintillator readout system. Modules (of two different widths) have WLS fibers routed to connectors at both ends. From there, light is routed through clear optical-fiber ribbon cables to a central location on each plane where the photodetectors are located. A fiber-routing "Multiplex" box then distributes the light from each scintillator strip to the appropriate photodetector pixel. There are eight modules in each plane of scintillator.
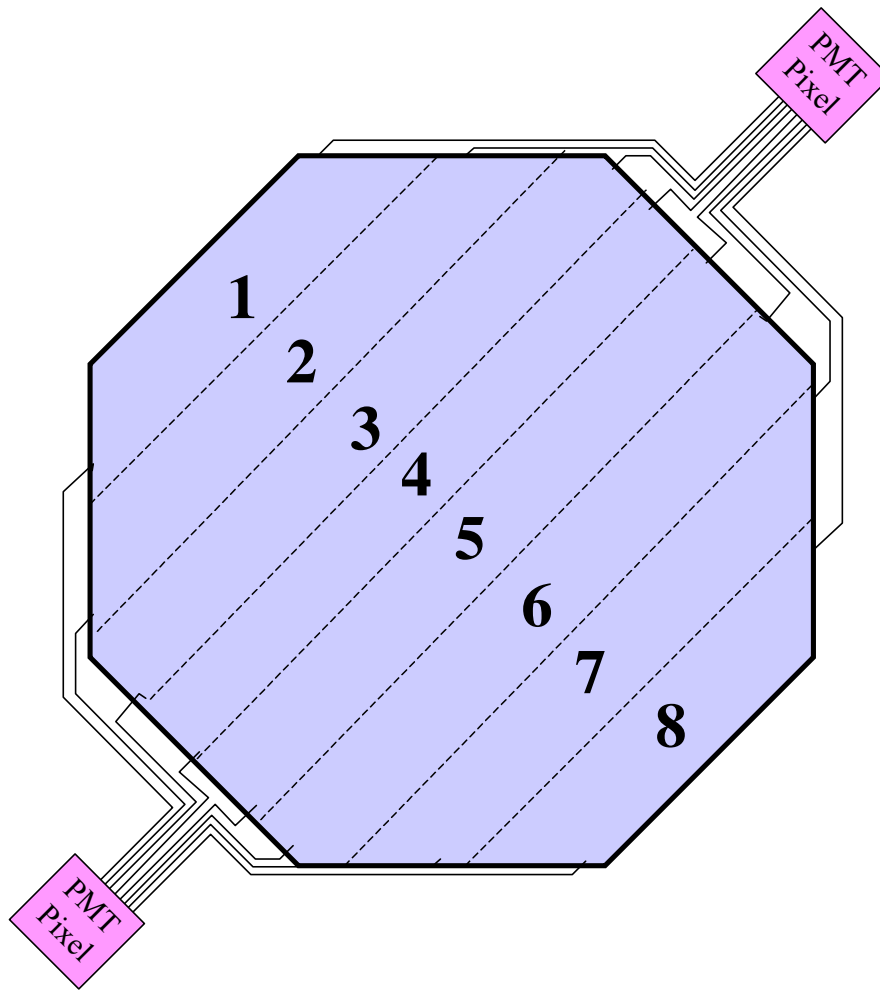
Figure 5.3: The MINOS scintillator system multiplexes eight fibers onto each PMT pixel. The multiplexing scheme combines one fiber from each of eight "logical modules" within a single scintillator plane. The fibers on a single pixel are separated by approximately one meter on the face of the detector. The pixel assignments of fibers on opposite sides of the plane are permuted with respect to the other side to permit demultiplexing in software. Because neutrino events are narrower than the 1 m multiplexing pitch, this approach saves money in PMTs and electronics without degrading sensitivity to neutrino physics.
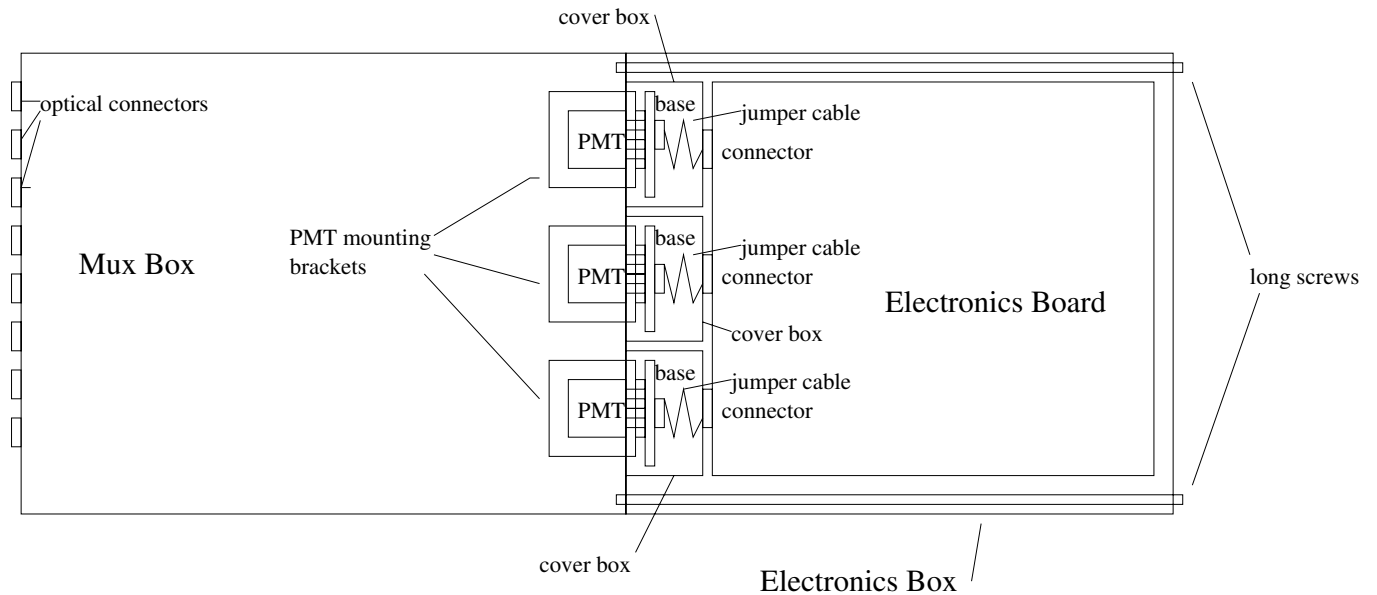
Figure 5.4: Sketch of the layout of a multiplexer box with phototubes and interface to the electronics. Both the multiplexer box and electronics are modular and the phototubes can be removed from the assembly in-situ by removing the electronics board.

5.1.2 Reasons for selection of solid scintillator

Solid scintillator has been used extensively in many particle physics detectors and in particular has frequently been the active detector of choice for sampling calorimeters. Extruded scintillator has already been employed in the D0 upgrade[2, 3]. Some of the features which make solid scintillator attractive are:

- **Good energy resolution:** We expect the energy resolution for 2.54 cm steel plates to be about $23\%/\sqrt{E}$ for EM showers and $53\%/\sqrt{E}$ for hadronic showers (E in GeV).

- **Excellent hermeticity:** There are very small gaps between strips.

- **Good transverse segmentation:** Analyses of simulated events show little improvement in physics measurement capabilities as strip widths are reduced below 4 cm. The baseline design uses 4.1 cm wide strips.

- **Flexibility in readout:** With solid scintillator, it is particularly easy to implement two-ended readout which offers several advantages as described above.

- **Fast timing:** Scintillation detectors have the intrinsic property of permitting nanosecond timing. This has advantages for the study of atmospheric neutrinos and permits a sensitive search for delayed signals in the neutrino beam.

- **Simple and robust construction:** Assembly of solid scintillator strips into detector modules requires little hardware and experience. Techniques for fiber connections have been completely worked out and implemented in major systems for both the D0 and CDF upgrades.

- **Potential for distributed production:** Because of the simplicity, the assembly and testing of complete modules could easily be distributed to multiple sites.

- **Long-term stability:** Our tests of extruded plastic scintillator show no serious aging or crazing problems. Since the stresses on the plastic are small in our design, crazing is not expected to be a problem in any case.

- **Ease of calibration:** A complete scheme for performing calibrations using a test-beam module, muons, laser pulses, radioactive sources and charge injection, has been designed and is described in this document.

- **Low maintenance:** We expect the system to be quite robust and to require little maintenance.

- **Reliability:** There are no catastrophic failure modes for solid scintillator which cannot be externally repaired. A possible long-term decrease in light output can be corrected using calibration data. Because there is little to go wrong, the detector is likely to achieve its intrinsic measurement capabilities.

5.1.3   Scintillator light output, transmission and detection test

In order to demonstrate the feasibility of the scintillator system we have constructed prototypes and measured their light output and uniformity using cosmic rays. All of the components related to the production, transmission and detection of light, which are described in this Chapter, were tested in the following prototype assembly. The setup consisted of two prototype scintillator modules, each with 16 strips. Other features included:

- 8 m long scintillator strips (1 cm × 4.1 cm wide, co-extruded with a reflective coating and with a WLS fiber groove). See Section 5.4.1 for a more detailed description.

- 1.2 mm diameter Kuraray wavelength-shifting fibers[4] were glued in the grooves using an the baseline optical epoxy (Epon resin and TETA hardener).

- End manifolds which route the appropriate lengths of WLS fibers from the strips to bulk optical fiber connectors.

- To simulate a real detector situation the wavelength shifting fibers were extended by 2 m by adding a 1.2 mm diameter clear-fiber ribbon cable running to a box housing the photodetectors. A connector was used on each end of the clear fiber cable.

- The light was routed to the photodetectors through an additional 40 cm of clear fiber inside the photodetector box.

- The photodetectors were 16-pixel Hamamatsu R5900U-00-M16 PMTs.

- The prototype module readout was triggered on cosmic rays by a system of external scintillation counters placed in several locations along the strips.

Figure 5.5 shows the mean effective light yield at each end and for the sum of the signals from both ends, expressed in terms of the number of photoelectrons registered by the Hamamatsu photomultipliers. The events for which the photoelectron yield is plotted were selected to be isolated minimum ionizing cosmic rays. The difference in the light levels on the two sides is due to different WLS fiber lengths extending beyond the ends of the scintillator strips on the two ends of the module. (The end with the longer WLS extensions gives lower light.) We observe that:

- The sum from both ends gives an average of more than 5.5 photoelectrons at all points along the scintillator strip.

- The light yield of the sum has a weak dependence on the distance from the end of the strip (i.e., the distance to a photodetector).

As described in Section 5.2, the observed light yield is adequate for MINOS. Specifically, the light yield is more than twice the minimum amount necessary for physics measurements, as determined by Monte Carlo simulations. This provides contingency for possible variation in, or degradation of, light output which might occur in the construction and operation of the experiment during its lifetime.

5.1.4   Calibration systems

Calibration of the hadronic energy response is of great importance in MINOS. In order to ensure a well-understood calibration at the required level of precision and accuracy, we will employ a combination of several calibration techniques:

- A test-beam calorimeter module for setting the overall energy scale and resolution.

- A combination of a light injection system and cosmic-ray muons for calibration of short-term and long-term variations.

- Radioactive sources for troubleshooting and to cross check other calibration methods.

Measurement of the total hadronic energy of events in MINOS is crucial to a complete set of neutrino oscillation measurements. The ability to measure Δm^2 precisely depends on the absolute calibration of the hadronic energy measurement. In order to reduce systematic limitations, we plan to calibrate the near and far detector hadronic energy responses to about 2% relative and 5% absolute uncertainty. Since it is impossible to illuminate the near and far detectors in-situ with high-energy hadron test beams, we must make careful use of several calibration tools to achieve this goal.

The fundamental calibration of the hadronic energy scale is achieved using a special calibration module for a series of test-beam and other calibration runs. Data are acquired in a test beam for muons, electrons and hadrons. Data from cosmic-ray muons, a radioactive source and light-injection are also collected during the test-beam running to help translate the calibration to the near and far detectors.
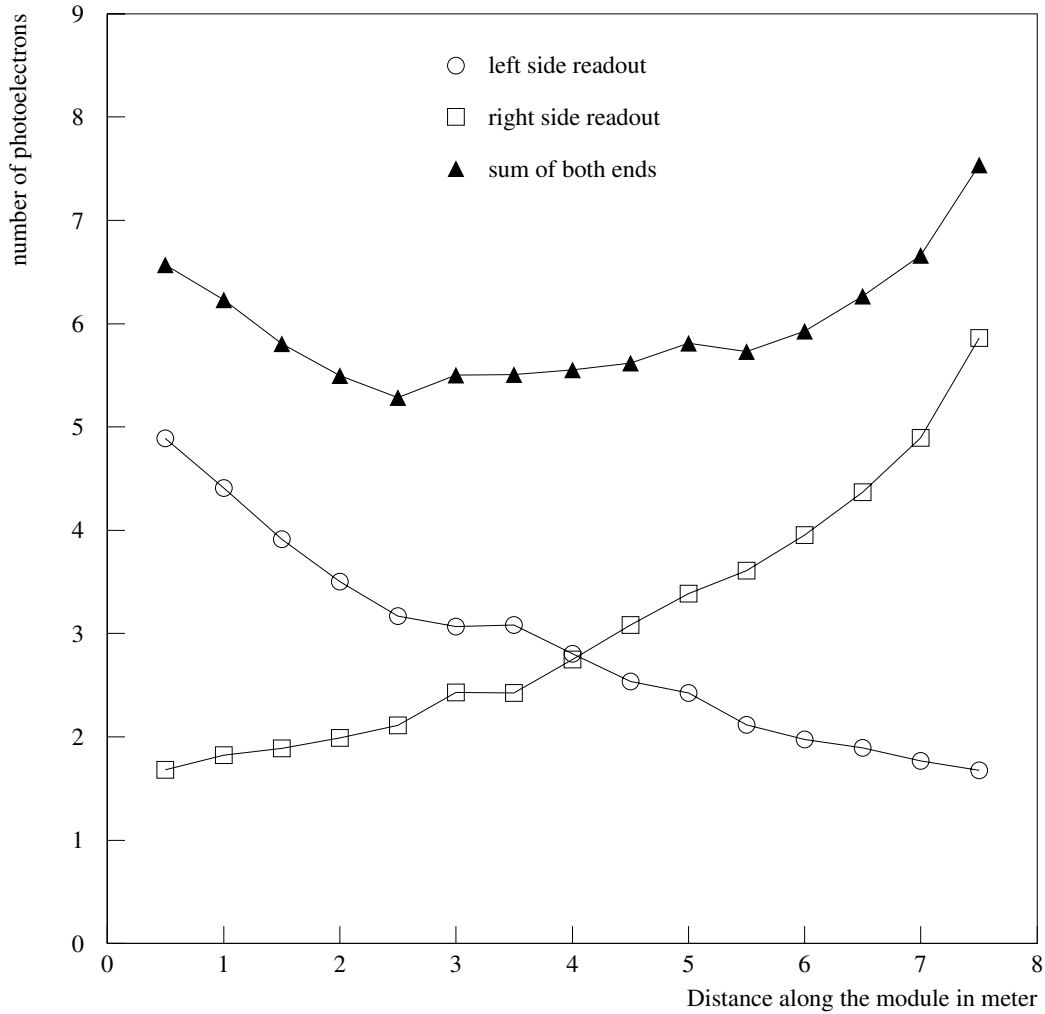
Figure 5.5: Results of photon yield measurements for single cosmic ray muons from a full scale prototype using 1.2 mm diameter fibers. The light measured at each end and the sum of the two ends is shown as a function of position along the strips. The difference in the light from the two ends is due to different lengths of WLS fiber extending beyond the ends of the scintillator strips.

Cosmic-ray muons provide the best means of calibration of the far detector and perhaps the best means of calibration for the near detector as well (although muons from upstream neutrino interactions may play as important a role there). The calibration is obtained by comparing muon energy deposition at different points in the detector with muon energy deposition in the test-beam module and hence with the hadronic energy data from the test beam. Due to differences in muon energies at the different depths of the detector sites, the calibration module could eventually be deployed at each detector site for a direct comparison of cosmic-ray muon data. This would ensure that there is no systematic error in translation of the test-beam calibration. The need to check for systematics of this type will depend on the outcome of neutrino oscillation measurements.

It is important to be able to track short-term variations in the response of the system. Light is injected into the WLS fibers to measure the response of the photodetectors and electronics through the full dynamic range of the system. This is one of the two main functions of the light injection system. The second function is to identify any connector or fiber problems. In addition to the light injection system, the electronics is calibrated by direct charge injection (see Chapter 6).

Muons provide the energy normalization for the light injection system. Because it requires about a month of muon data per strip at the far site (much less time is needed at the near site) to provide an absolute calibration, the light injection system is used to keep the photodetector gains approximately constant during the time over which the muons are recorded.

The responses of all scintillator modules are mapped in detail using a radioactive source during module construction. In addition, a tube which can hold a radioactive source is installed at each end of every scintillator module to permit insertion of a wire source, after the detector plane has been installed, for short-term cross checks on other calibrations and debugging at installation time.

5.1.5 Description of the scintillator factories

Construction of the components for the scintillator system requires a few different types of "factory" operations. Most of these operations are quite compatible with resources and skills available in collaborating laboratories and universities while some require industrial production. Many of the basic components of the system are already available as "catalog" items. Examples include the photodetectors, WLS fiber and clear optical fiber.

Some of the other components require specialized industrial production based on specific requirements for MINOS. Examples of these items include the scintillator strips, the end-manifold and coil bypass components of the scintillator modules, and bulk optical connectors. We have carried out an extensive development program for extruded scintillator over the last year in order to develop an industrial product which meets our light output demands for an acceptable cost. At present, we have a production technique which involves a cooperative effort between MINOS and an industrial extrusion house, Quick Plastics[5]. Since this industry is not experienced in the production of scintillator and the subtleties of measurement of light output, we envision a continued cooperative effort for production of scintillator for MINOS. In addition, two commercial producers of plastic scintillator (Kuraray[4] and Polycast[6]) have been actively pursuing production of extruded scintillator. Kuraray has delivered scintillator of good quality and continues their development program. We are in

close contact with both of these companies to ensure that their products will meet the specifications of the scintillator for MINOS. Because these products are not yet finalized, we assume here that the production will be via a direct cooperative effort of our own technical staff with industrial plastic extruders. However, we expect that Kuraray and Polycast will be able to provide comparable products and we will evaluate bids for production when we are ready to place orders.

The three main systems which must be fabricated "in house" by MINOS are the scintillator modules, assembled clear-fiber ribbon cables (with connectors attached and polished) and multiplexing boxes which house the photodetectors and route light from signal fibers to the appropriate pixels on the photodetectors. The assembly of the scintillator modules requires the most manpower and equipment.

The scintillator modules could be produced at a single production site running two shifts per day. However, we expect that the optimal production scenario will include two factory locations for module production. This permits faster production (or contingency in the schedule) and more efficient use of collaboration resources while keeping costs low. Attractive features of the assembly of plastic scintillator modules are that the cost of specialized assembly equipment is relatively low, the space required for assembly is not particularly large and the level of skill required in the assembly is relatively low. The necessary space, skills and oversight capabilities exist at several collaborating laboratories and universities.

The production of scintillator modules involves the following major steps:

1. Gluing WLS fibers into scintillator grooves.

2. Assembly of strips into 20-wide and 28-wide modules.

3. Routing of fibers through the end manifolds and into the bulk optical connectors.

4. Potting and polishing of optical connectors.

5. Closing the completed assemblies and checking for light leaks.

6. Mapping of modules using radioactive sources.

Specialized machinery and fixtures have been designed to facilitate this work.

The production of optical fiber ribbon cables and boxes to house photodetectors require relatively simple equipment, readily available in most laboratory and university shops. The only specialized equipment needed are assembly jigs and fly cutters for polishing of optical connector faces.

We plan to begin routine production of scintillator components for MINOS detectors in October 2000. The first commercial orders for various components would precede this by several months.

5.2 Requirements and performance criteria

The technical requirements on the scintillator system have been set from a combination of physics studies, general considerations about detector response and practical considerations. They are:

1. **Light output:** The light output must be sufficient so that the hadronic energy resolution is better than $60\%/\sqrt{E}$ and that the efficiency for observation of a muon crossing a strip is greater than 90%. This is expected to be the case as long as the total number of observed photoelectrons per minimum-ionizing particle crossing a scintillator layer is greater than 2.5 with discrimination at the single photoelectron level. A factor of about 2 times more light than this (5.0) is desirable to account for assembly variation and aging of components. The current baseline design meets this requirement. To the extent that higher light output will help with other technical considerations (e.g., noise levels), higher light output will be pursued as long as the overall cost of the detector is not significantly impacted.

2. **Uniformity:** In order to ensure that it is possible to correct for position dependence of showering events, the light output of the scintillator strips should vary by no more than 30% with respect to a nominal response at that location (after correcting for attenuation in the WLS fiber).

3. **Attenuation:** The light observed from the near and far side of a strip (by the detector at the near end) should differ by no more than a factor of 5.

4. **Timing:** The time resolution from the sum of strips within a scintillator plane should be less than 2 ns for 10 pe's and 5 ns for 2 pe's.

5. **Stability:** The light output of the scintillator system should have long-term stability with an expected decay-time of at least 10 years. Short-term variations must be measurable so as to permit relative energy calibration for hadronic showers between the near and far detectors at the level of 2%.

6. **Calibration:** The hadronic energy response should be able to be calibrated to a relative error between the near and far detector of no more than 2% up to at least 30 GeV. An absolute calibration of 5% will be made using a test beam measurement.

7. **Linearity:** The detector response to hadronic showers should be linear to within 5% between 1 GeV and 30 GeV.

8. **Crosstalk:** The crosstalk between scintillator channels should be less than 4%.

9. **Transverse pitch:** The scintillator strips should be 4 cm in width for pattern recognition on EM showers.

10. **Modular construction:** The scintillator strips must be assembled into modules which are easy to handle, relatively rugged and provide light-tight seals.

11. **Cost:** The cost should be as low as possible given the above considerations. The overall cost of the scintillator system should be reviewed with respect to other detector costs prior to final production in order to produce a best overall optimization of physics capability.

5.3   Interfaces to other MINOS systems

Interfaces between the scintillator system and the other MINOS systems have been defined as follows:

- The scintillator fabrication task provides the scintillator modules, clear optical cables, multiplexer boxes, phototubes, HV bases and the various calibration hardware.

- Scintillator modules mount to the steel using mounting bars at the ends and straps attached to plates welded to the steel at intermediate points. The scintillator modules are designed to be mounted on the steel prior to lifting the steel plane into place.

- The interfaces between the scintillator system and electronics system are the mechanical and electrical connectors between the multiplex boxes and the electronics modules. High voltage for the phototubes is provided from these modules by the electronics task.

- Packing and shipping of scintillator modules is part of the scintillator system production responsibility. Handling of the modules at the near and far detector sites is the responsibility of the installation tasks.

- All test and calibration equipment for the scintillator system (including their use during installation) is the responsibility of the scintillator task.

- The cavern outfitting task provides the rack platforms, located along the 45° faces of the octagons, for mounting the scintillator multiplexing (MUX) boxes and electronics racks and modules. The scintillator task is responsible for production and testing of the MUX boxes and the clear fiber cables between the modules and MUX boxes. Installation and in-situ testing of the MUX boxes and cables is the responsibility of the installation tasks.

- The general experiment database system provided by the electronics task is used to manage various construction and calibration information. Data from assembly and testing of scintillator modules are stored in this database for use during installation and analysis. Scintillator modules are marked with bar codes for reading at installation time. The bar-code reader and associated software are supplied by the scintillator task.

5.4   Description of WBS elements

5.4.1   Scintillator strips (WBS 2.2.1)

The recent development of extruded scintillator which can be inexpensively mass produced in very long strips is one of the reasons that solid scintillator can be used in MINOS. The production of extruded scintillator for MINOS has built upon work done by Fermilab in conjunction with the D0 upgrade[2, 3].

CLEAR GROOVE

MN−3202

TiO₂ CAP

POLYSTYRENE
SCINTILLATOR
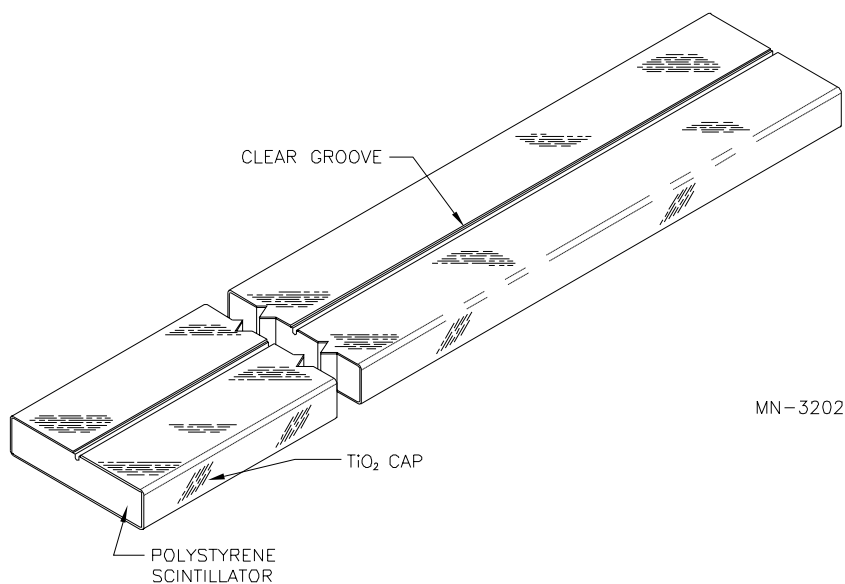
Figure 5.6: Sketch of a scintillator strip with groove and reflective coating.

5.4.1.1 Description of scintillator strips

The scintillator strips are made of polystyrene, infused with the fluors PPO (1%) and POPOP (0.030%). This compound is melted and extruded in the shape of a rectangular bar with a narrow groove along the center of one of the wide sides, as shown in Figure 5.6. The groove is 1.3 mm deep, sufficient to contain a 1.2 mm diameter wavelength-shifting fiber. A thin (0.25 mm thick) reflective jacket, composed of TiO_2 infused in polystyrene, surrounds the entire scintillator bar except for a small region near the groove. Each scintillator strip is 4.1 cm wide, 1.0 cm thick, and up to 8 m long, as shown in Figure 5.7.

Traditionally, the manufacturing of scintillator strips has been accomplished in two steps; first mixing fluors into polystyrene, extruding that mixture and letting it cool and then in a later step re-melting the scintillator mixture to extrude strips of a specified shape. In the last year, we have developed a one-step process where the fluors are infused with raw polystyrene pellets in the same machine which is used to extrude final scintillator strips. In test production, this technique has proven to be reliable and cost effective and we have now specified it as the baseline. We consider the two-step process to be a contingency option in case scaling up the one-step process proves too difficult.

In the one-step or "in-line" production process, fluors are first tumbled with dry polystyrene pellets which have been held under an argon atmosphere for several days prior to extrusion. The PPO and POPOP are pre-measured into convenient packages for addition to a set amount of polystyrene pellets during the mixing process. The mixture of pellets and fluors are fed into an extrusion machine which melts the polystyrene, allowing the fluors to

.020±.010
(0.5±0.25)
TYP.

.055±.006
(1.4±0.15)

FULL R.

R.020
(R0.5)
TYP.

.059±.010
(1.5±0.25)

.394±.020
(10.0±0.5)

MATERIAL:
POLYSTYRENE WITH
WHITE PIGMENTATION

.010
(0.25)
TYP.

.807±.010
(20.5±0.25)

1.614±.030
(41.0±0.8)
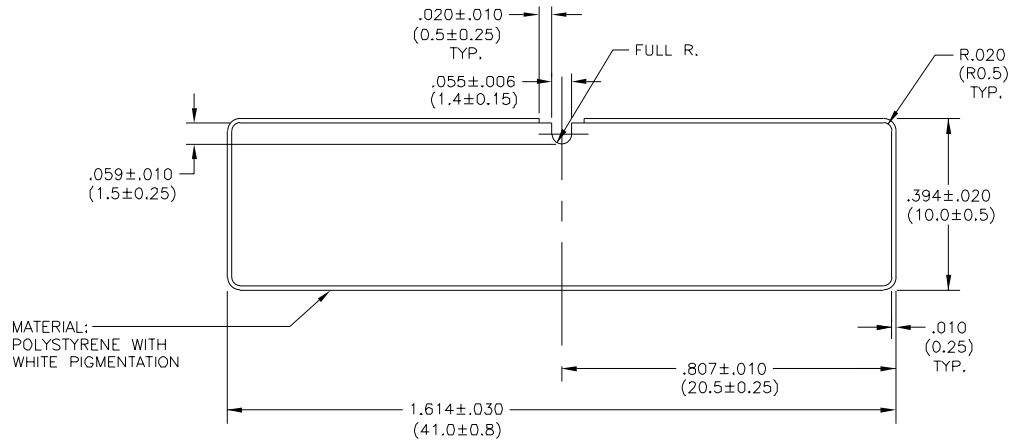
SCINTILLATOR BAR
CRYSTALLINE POLYSTYRENE—CLEAR
AND NOTED

MN−16011A

Figure 5.7: Detailed cross-section of a scintillator strip.

diffuse uniformly. The scintillator mixture is extruded through a die to produce the desired strip cross section. As the scintillator is extruded through the die, the outer reflective coating of polystyrene mixed with TiO_2 (10% by weight) is added through material injected from a second, "satellite" extrusion machine which mixes the polystyrene and TiO_2. As the plastic emerges from the die, it is further formed using vacuum sizing and cooled with air and water. The scintillator is extruded continuously and strips are rough cut to lengths of 8.0 and 11.3 m.

The total weight of plastic scintillator to be installed in the near and far detectors is approximately 630,000 pounds. We estimate that it will require 720,000 pounds of raw polystyrene to produce all of the scintillator strips because of inefficiencies in the extruding and cutting processes. About 42% of the scintillator strips on the far detector are 8 m long. The remainder are between 8 m and 3.3 m long, as the octagonal shape of the detector dictates. By cutting a single 11.3 m long strip into two sections, it is possible to keep the amount of waste material small and still have each strip of exactly the right length for its octagon location. The length of near detector strips ranges from 1.5 m to 4.0 m. Scintillator strips are rough cut at the extruding facility and are cut to the exact lengths required at the module assembly factories.

The commercial production of this quantity of scintillator strips is within the capacity of typical commercial extruders over a 2 year time span. Faster production could be accomplished by having additional extrusion machines operating in parallel. However for our expected needs a single machine is sufficient. We currently have contracts with two extruding

companies, Quick Plastics[5] and Royalite Thermoplastics[6], to produce prototype scintillator strips for MINOS. Kuraray has also expressed interest in the scintillator production for MINOS as has Vladimir Technoplast in Russia.

5.4.1.2 Performance measurements

It is important to understand the light production, collection and uniformity properties of extruded plastic scintillator. These properties will vary with factors such as the shape of the strip, reflective coating and clarity of the material. We must also determine the uniformity which can be achieved during actual mass production of extruded strips.

The TiO_2-loaded co-extruded layer on the strips requires less manpower than wrapping strips with a reflective material such as Tyvek. We have extruded the strips both with and without the TiO_2 coating to measure the reflection efficiency of the coating compared to Tyvek. We found no observable difference in the amount of light collected with the TiO_2 compared to Tyvek, making the co-extrusion an attractive and cost-effective reflector.

We have compared the collection of light from a WLS fiber laid in an extruded groove on the broad side of a scintillator strip with that from a fiber placed in an extruded hole in the center of a scintillator strip. A dry (unglued) fiber in the groove yields about 10% less light than a dry fiber in the hole. However, for our geometry and scintillator material, we find that a fiber glued in the groove yields 1.8 times more light than a dry fiber. Since gluing is much easier in a groove than a hole, we have chosen to glue fibers in grooves for our baseline design.

Our studies of the aspect ratio of scintillator strips (width and thickness) have shown that, for 1-cm thick extrusions, a 2-cm wide strip gives about 1.3 times more light than a 4-cm wide strip. Simulations of neutrino events show that changing from 2-cm to 4-cm strips has very little effect on physics capabilities. The lower light yield of 4-cm strips still meets MINOS requirements, and the cost is lower than for narrower strips. We have therefore chosen 4-cm wide strips for the baseline design. The optimal aspect ratio may be sensitive to the reflectivity of the outer surface and to the clarity of the polystyrene to scintillation light; we are continuing our studies of these effects.

For the baseline scintillator strips, we have measured a number of strips for uniformity in the light output, both along the strip lengths and transverse to their long axes.

1. Longitudinal uniformity

   We have studied the uniformity of the light output of several scintillator strips by measuring photomultiplier tube current while moving a beta source along the strips. The measured light output at each location has been corrected for the fiber attenuation. The results are shown in Figure 5.8 for strips which were intentionally taken from different times of an extrusion production run. The variation in the light collection efficiency of the WLS fiber at different locations is negligible. Hence, the 13% spread in the measurements is probably due to the nonuniformity of the scintillator strips and the variation in optical coupling between fibers and strips.
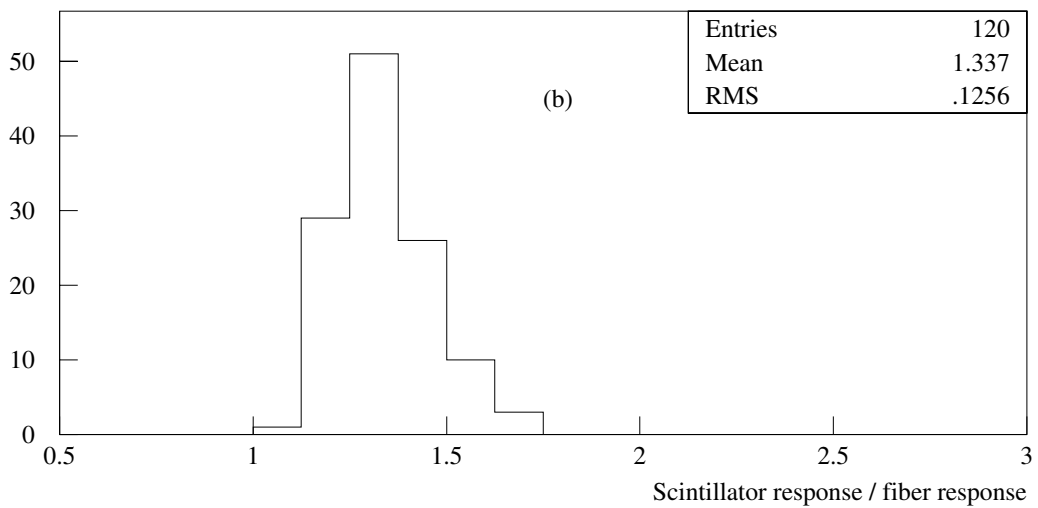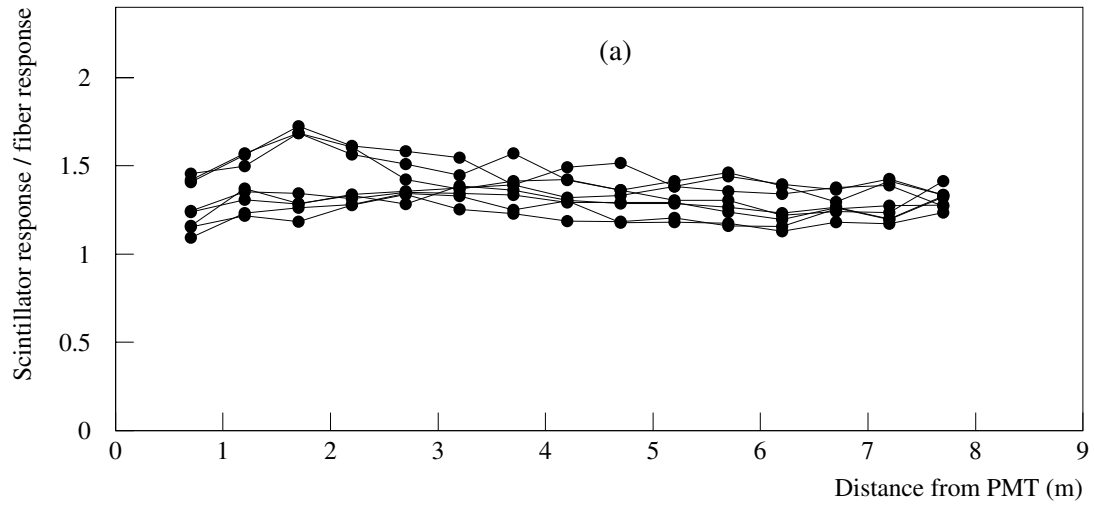
Figure 5.8: Scintillator longitudinal uniformity: Responses of the scintillator strips (arbitrary normalization), corrected for fiber attenuation, are plotted versus the position in (a), and the projection is histogrammed in (b).
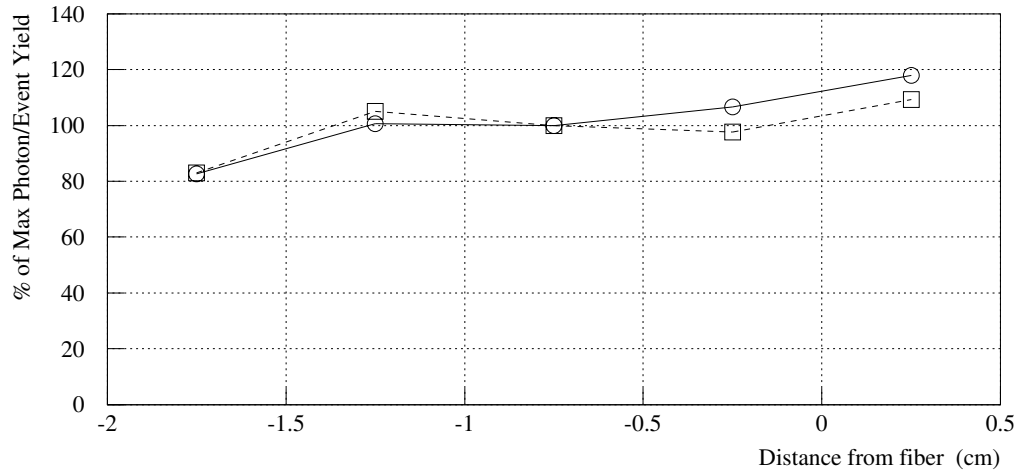
Figure 5.9: Scintillator transverse uniformity.

2. Transverse uniformity

We have measured the uniformity of the light output of scintillator strips transverse to their lengths using cosmic-ray muons. The muon trigger consisted of two narrow scintillators above and below the scintillator strips. Measurements of two strips are shown in Fig. 5.9. The light output decreases by about 20% near the edge, mostly due to the fact that the thickness of the scintillator in these extrusions was slightly smaller near the edge. This was the result of an early production process; all of our commercial extruders have assured us that final scintillator strips will have no such variation. We expect our final strips to have thickness uniformity to better than about 5%.

5.4.2 Fibers (WBS 2.2.2)

5.4.2.1 WLS fibers

The wavelength-shifting (WLS) fibers which shift the blue scintillation light to green are a critical component in the overall light collection scheme. Blue photons produced in the scintillation process make many reflections from the highly reflective outer layer of the co-extrusion. The blue photons eventually hit a fiber where they are absorbed by the WLS Y-11 fluor and re-emitted as green photons. The absorption spectrum of the Y-11 fluor, centered at a wavelength of 420 nm (blue), has only a very slight overlap with the emission spectrum, centered in the green beyond 470 nm, so that self-absorption in the fiber is small. The fibers then act as light guides to channel the green light, through optical connectors and lengths of clear fibers, to the photodetectors. This provides a very efficient means of "focusing" the light into a small-area photodetector, whose cost is roughly proportional to photocathode

area. This is one of the main features which makes scintillator readout practical for MINOS.

Measurements and Monte Carlo calculations have been used to study the various factors affecting light collection: i.e., reflectivity of the outer co-extrusion, and scintillator/fiber sizes and geometry. We have chosen to use 1.2 mm diameter fibers which maximize the use of the available area of photocathode on the PMT and give the required light output with our extruded scintillator strips. The total length of WLS fiber required (including allowance for spares and waste) is about 850 km. The fibers are double-clad to give a maximum trapping fraction for the green light: the inner core containing the WLS fluors is polystyrene (refractive index $n_1 = 1.59$), a thin intermediate layer is acrylic ($n_2 = 1.50$) and the thin outer cladding is a polyfluor ($n_3 = 1.42$). For green light produced on the axis of a fiber, the fraction of light trapped and traveling in one direction is given by $(n_1 - n_3)/2n_1$. This factor is 5.5%. Both experiment and photon-bookkeeping have verified that this simple treatment is correct. (Light produced off-axis has a greater trapping fraction, but these rays are attenuated more rapidly.)

One of the most crucial properties of the WLS fiber for determining the light yield at the photodetector is its effective attenuation length when the source of green light is remote from the photodetector. MINOS requires a very large number of fibers with lengths in excess of 8 m, significantly longer than the requirements of any previous experiment. We have made measurements of many fibers from the two vendors, Bicron[9] in the U.S. and Kuraray[4] in Japan. Performances of some batches of WLS fibers are shown in Figure 5.10. All of the fibers measured from the batches represented here are acceptable for use in MINOS. The results shown here come from three different batches of fiber, two from Bicron and one from Kuraray. The Bicron fibers are all 1 mm diameter BCF91-A while the Kuraray fibers are all 1 mm diameter, double-clad, non-S-type fibers with 150 ppm Y-11 fluor. (Although not shown, we have measured that 1.2 mm diameter fibers have the same attenuation length as 1.0 mm diameter.) The batches of Bicron fibers represent production of about 2000 m of fiber while the Kuraray fiber was from a 100 m sample. Further orders have been placed to study possible variation in larger production batches. The better batch of Bicron fiber represents a newer production of that fiber. We conclude that either of these manufacturers can supply fiber of high quality for MINOS. The Kuraray fibers are somewhat stiffer than the Bicron fibers and require somewhat more space in the end-manifold design.

Aside from the differences in the absolute light output in different batches, all WLS fibers show similar characteristics. The attenuation is approximated quite well by a sum of two exponentials: one with a short attenuation length of less than 1 m and one with a much longer attenuation length of 5 to 6 m, the crucial component for MINOS. The short component is due to self-absorption of the green light in the WLS fiber and the short attenuation length agrees reasonably well with emission and absorption data provided by the manufacturers.

We have found that different batches made months apart can have significantly different values for the longer attenuation lengths. The best long attenuation length that we have measured is 10.5±0.5 m, in fibers from Bicron. This appears to be the best ever produced by that company, and also appears to be the longest attenuation length reported in the literature. It seems likely that this is the best that can be achieved and may represent the limit set by the properties of the polystyrene core of the fibers. The attenuation length of MINOS WLS fibers must be at least 5.0 m.
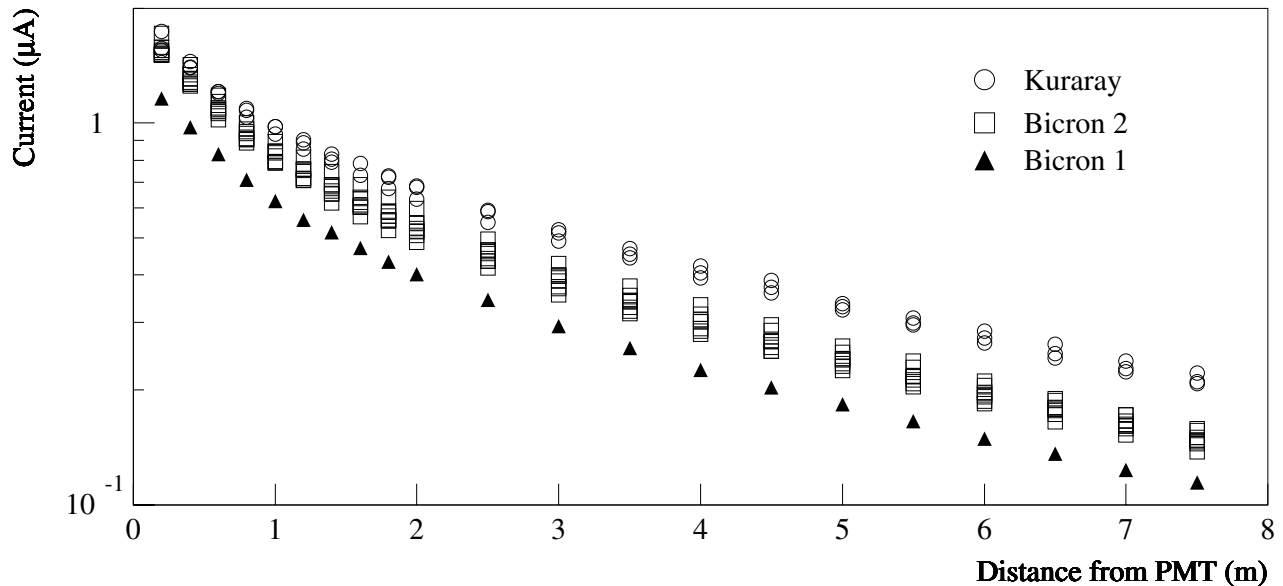
Figure 5.10: Light collection and attenuation in WLS fibers. The current from a phototube is measured as a scintillator is placed at various positions along the length of the fiber. Bicron 1 and Bicron 2 are two batches produced in the summer and fall of 1997 respectively. The Kuraray batch was produced in December of 1997. All results shown here are acceptable for MINOS. See text for additional details.

5.4.2.2 Clear fibers

Clear-fiber ribbon cables are used to transmit light from the WLS fibers to the multiplexing boxes. We plan a similar approach as used for construction of these ribbon cables for the CDF endplug upgrade[10]. MINOS ribbon cables consist of eight or ten clear fibers enclosed in an outer black plastic coating which provides protection and light tightness. Mitsubishi offers a cable of this type and has provided a quotation for production for MINOS purposes. The fibers are 1.2 mm diameter, double-clad polystyrene, manufactured by Kuraray, and are spaced 2.3 mm apart. When coupled to WLS fibers, the clear fiber cables act as extensions of the WLS fibers, but with better attenuation length. (Hence, more light is observed than if a similar length of WLS fiber were used.) The attenuation length of clear-fiber cables has been measured to be 12 m for light which is already collimated (as it is coming from a few meters along a WLS fiber)[11].

The clear fibers are routed along the edges of the steel detector planes, from the scintillator modules to the MUX boxes. The routing for the far detector is shown in Figure 5.11. This routing minimizes the length of clear fiber required while keeping readout isolated be-

tween scintillator planes. The total length of clear fiber required for construction of the ribbon cables for both the near and far detectors is about 1022 km, slightly more than the total length of WLS fiber.
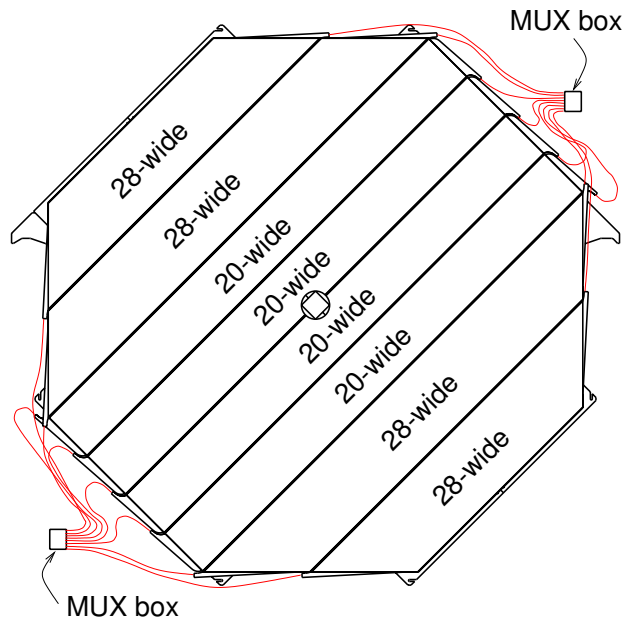
Figure 5.11: Clear fiber routing and scintillator module layout for readout of one view of scintillator modules for the far detector. Each octagon has eight modules with bulk optical connectors at each end.

5.4.3 Scintillator modules (WBS 2.2.3)

5.4.3.1 Design features and requirements

The baseline design simultaneously optimizes several different concerns:

- Gaps between individual strips are kept as small as practical.

- The scintillator fully covers the steel in order to keep the fiducial mass as large as possible.

- Scintillator modules are designed to be light-tight and permit rapid testing.

- Light-fiber connections to the scintillator modules use reliable bulk connectors.

- The mechanical design of the modules gives good light output and long-term stability.

- Assembly work at the near and far detector sites is kept to a minimum in order to permit rapid installation. A modular design of preassembled and pretested strips is ideal for this purpose.

- Total costs for production of scintillator modules are minimized by balancing capital equipment, component, manpower and shipping costs and use of existing resources.

- Assembly operations and equipment are simple, and permit production and testing of modules in both national laboratory and university facilities, staffed by local physicists, students and technicians.

All of these features have been achieved in the design described here. The modules are either 20 or 28 strips wide glued to a thin aluminum skin which provides mechanical strength, light-tightness and fire protection for the polystyrene scintillator. Wavelength-shifting fibers are routed to 28-wide bulk connectors at each end of the module through a simple manifold which curves the fibers through a natural bend radius, protects them from harm and provides a light-tight enclosure. The components have been designed to be rugged and permit easy assembly and handling of the modules. The thin aluminum skin permits mapping of the scintillator modules with radioactive sources to test for any problems in the assembly. Fibers are glued into the scintillator strips to maximize light output. The modules are mounted onto the steel plates using a simple steel-strap technique which permits very narrow gaps between neighboring modules and a minimal gap between steel plates.

5.4.3.2 Overview of module construction

This Section provides an overview of the hardware architecture of a plane of scintillator strips in the far detector. The packaging of scintillator strips into light sealed modules is described first. End manifolds, which route WLS fibers to optical connectors at the end of each module, are discussed next. Hardware used to attach the modules to the steel absorber planes is then described.

Each plane contains a total of 192 scintillator strips. All of these strips have an identical 4.1 cm by 1 cm nominal cross section, as described in Section 5.4.1. However, the lengths vary from 1.5 m to 8 m to match the octagonal shapes of the near and far detector absorber planes.

The scintillator strips are grouped into modules of 20 or 28 strips strips each, yielding a total of 8 modules per plane. The number of strips has been set to permit four 20-wide modules in the center of each octagon and two 28-wide modules on each outer side of the octagon. The layout of the modules on a plane is illustrated in Figure 5.11. The modules are enclosed in aluminum cases to provide a light-tight seal.

A total of four separate module geometries are required for one plane. Two styles of modules have ends angled at 45° to their length. The next module style has perpendicular ends; all strips in this style are 8 m in length. The last style also has perpendicular ends, but requires a bypass at its center to provide clearance for the magnet coil. The same parts are used for the different styles to minimize the number of unique parts required and to maximize assembly efficiency. For example, the two styles having 45° ends differ only in length; both lengths use the same end manifold components.

The parts comprising a module can be subdivided into three functional groups. The first is the scintillator strips themselves. By the time of assembly into a module, the WLS fibers and reflective extrusion groove cover have been glued to the strips, as described in Section 5.4.3.3. Second, a two-piece light seal and structural box is included about the entire

periphery of a module, as described in Section 5.4.3.4. Third, an end manifold assembly routes and protects the WLS fibers extending from the ends of the scintillator strips; the components in the manifolds are described in Section 5.4.3.5.

The innermost two modules have a fourth functional component: the bypass assembly to accommodate the magnet coil. The bypass is described in Section 5.4.3.8.

The scintillator modules are fastened and supported on the steel plane using several techniques, as described in detail in Section 7.4.3.2. Eight meter long modules are fastened to the absorber planes at the end manifolds and at four equally-spaced points along their length. (Some of the shorter modules do not require all four intermediate mounts.) Further support is provided by a shelf positioned at the bottom 45° edge of an absorber plane (shown as the bottom right 45° edge in Figure 5.11). The hardware used to tie the modules to the planes is described in Section 5.4.3.9.

5.4.3.3 Coupling of fibers to scintillator

In prototype tests with extruded scintillator strips, we have found that a significant improvement in light collection is achieved when fibers are glued into the scintillator strip rather than just being placed into a dry groove or hole. For the baseline strips and fibers, we find a consistent factor of 1.8 more light observed at the photodetector for fibers glued into the grooves compared to fibers placed into grooves dry. This is independent of the position along the strip/fiber assembly. Hence, we have decided that in MINOS, fibers will be glued into grooves. It should be noted that in some previous applications of WLS fiber readout of scintillators (tile calorimeters for instance) no significant difference has been observed in the light output when fibers were glued. This is the result of differences in materials and geometry between those detectors and the extruded strips for MINOS.

We have tested several glues which meet MINOS requirements. We have chosen a very cost effective glue which has properties very similar to those of Bicron 600 epoxy (which has been used extensively in other detectors) but at about 1/8 the cost. The baseline glue is Shell Epon 815C resin[12] with triethylenetetramine (TETA) hardener mixed at 100 parts to 13 parts by weight). We have performed assembly and aging tests using this glue and have confidence that it will meet our needs. One concern with use of glue is possible aging and yellowing. Previous aging measurements on BC-600 glue over a 5 year period have shown it to be quite resistant to yellowing, and it does not attack WLS or clear fibers[13]. We have performed our own accelerated aging tests using Bicron 600 and the baseline glue and found them to have very similar performance (with the baseline being slightly better).

1. Optical properties: The index of refraction of the Shell Epon glue is very close to that of polystyrene. This good match ensures minimal loss of light at the scintillator-glue interface, helping to give the factor of 1.8 in increased light collection. The light transmission in the wavelength region of interest is measured and is shown in Figure 5.12. Assuming very conservatively that the light from the scintillator traverses an effective thickness of 500 μm of the glue before reaching the fiber, 1% or less of the light will be absorbed by the glue.

2. Mechanical properties: We have glued several tens of fibers into scintillator strips and have observed no signs of the glue failing to create a good optical bond in normal
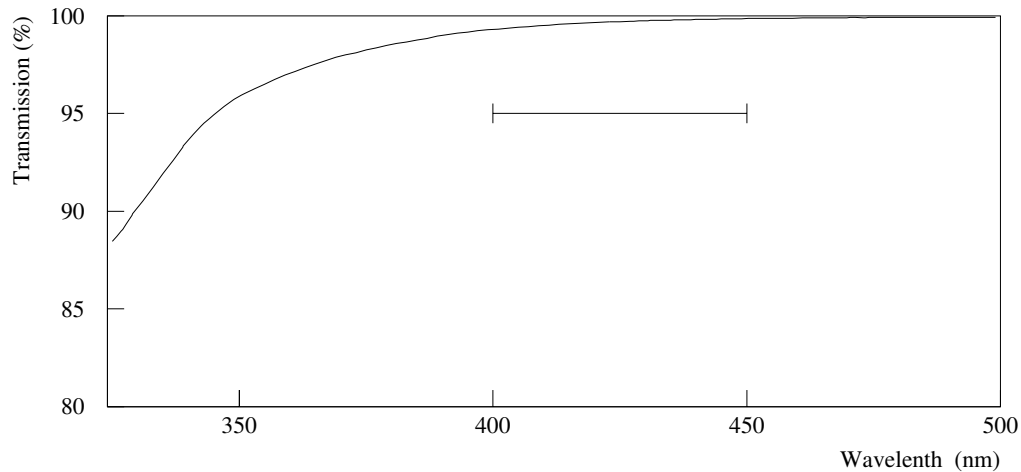
Figure 5.12: Transmission spectrum of 500 μm thick Shell Epon 815C optical cement (with TETA hardener). As a reference, the range of light spectrum emitted by the scintillator and absorbed by the WLS fiber is indicated.

handling. Furthermore, we have subjected some strips to severe mechanical handling and bending with no observed reduction in light collection. We have also subjected some glued strips to repeated severe temperature cycling with no suggestion of the glue releasing from the scintillator.

3. Reflective extrusion groove cover: We have found that aluminized Mylar works very well as a reflective cover above the groove. It can be applied as the fiber is glued in and improves the light collection by about a factor of 1.15 compared with no reflective cover.

5.4.3.4 Light case

Each module is enclosed in a sheet aluminum light case to shield the scintillator from external light and to protect the flammable polystyrene strips from ignition sources. The architecture of the light cases is described here; fabrication and assembly information is provided in Section 5.4.8.3.

The light case is fabricated from 0.5-mm thick 3003H14 aluminum sheet, provided by the manufacturer on a coil. The coil stock is flattened and rolled into shallow U-shaped channel sections (where the bottom of the U is the module width) at each module factory. Two U channels are used to fabricate one case, with the top being slightly narrower than the bottom. The bottom U channel is positioned on the module assembly table and filled with 20 or 28 scintillator strips. The top U channel is positioned over the scintillator strips and nested in the bottom U channel. Figure 5.13 shows a short section of the top and bottom
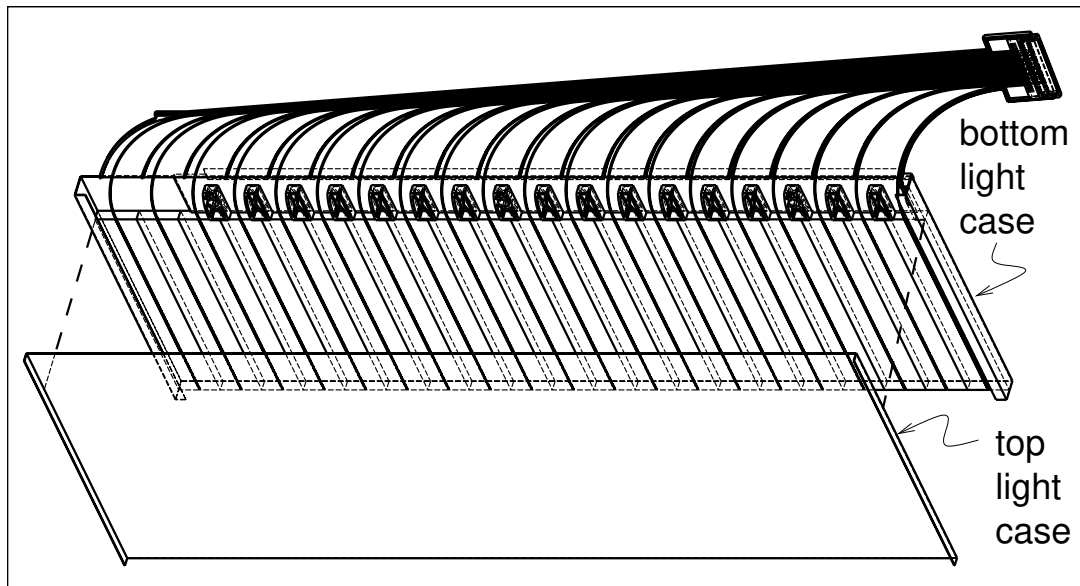
Figure 5.13: Light case assembly, as the top light case is lowered into place onto the bottom light case and strip array, prior to crimping the light case edges.

light cases with scintillator strips in place prior to crimping. The sides of the bottom U channel are bent down 180° to crimp them against the shorter sides of the top U channel. The sides of both the bottom and top U channels are then folded flat against the top of the module.

5.4.3.5 End manifold

The architecture of the end manifolds for perpendicular-ended scintillator modules is described in this Section. These manifolds are functionally identical to those for 45° ended modules. The perpendicular-ended modules have the tightest constraints on fiber bend radius in order to keep the protrusion from the edges of the detector as small as possible. The "snout" design which has been adopted permits all fibers to be routed to one connector while keeping the protrusion from the detector edge as small as possible.

The manifold components of a 20-wide, perpendicular-ended scintillator module are illustrated in Figure 5.14. Optical connectors are mounted on posts on the manifold to join the WLS fibers to the clear-fiber ribbon cables outside the module.

Figure 5.15 shows the detailed design of the end of a 20-wide, perpendicular-ended module. This figure includes the light injection manifold compartment of the optical fiber connector (Section 5.4.3.6), used for strip calibration. Also shown is the mechanical structure (the "integral module mounting bar") which gives rigidity to the manifold and provides a means of attaching the module to brackets on the steel octagon. The bend radii of the WLS fibers are controlled by slots in the base section of the manifold, which guide the fibers into the required paths. The fibers are precut to specific lengths and placed in the slots to produce bend radii of 12 cm, which is the minimum recommended for 1.2 mm diameter Kuraray fibers. All of the end manifold parts are injection molded from optically opaque PVC.

variable width seal

cover

light case

base

variable
width
seal

cover

base

light case
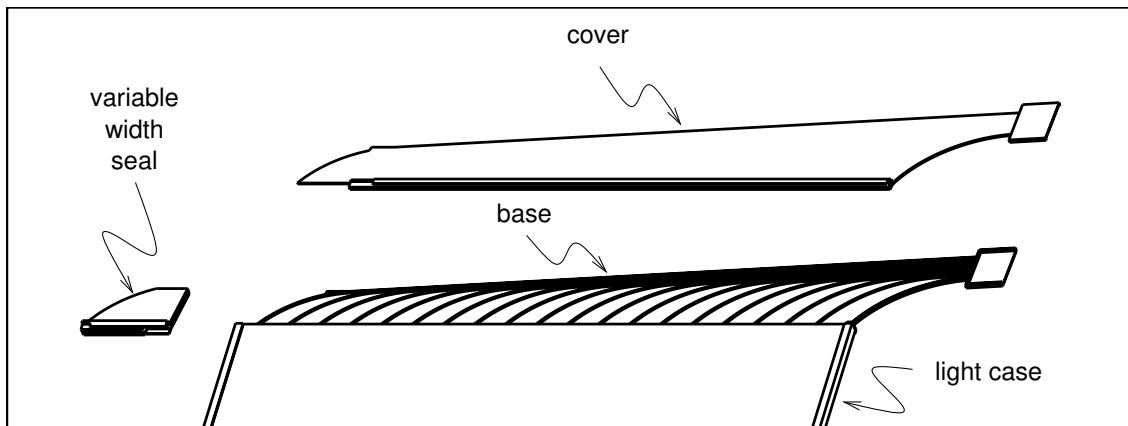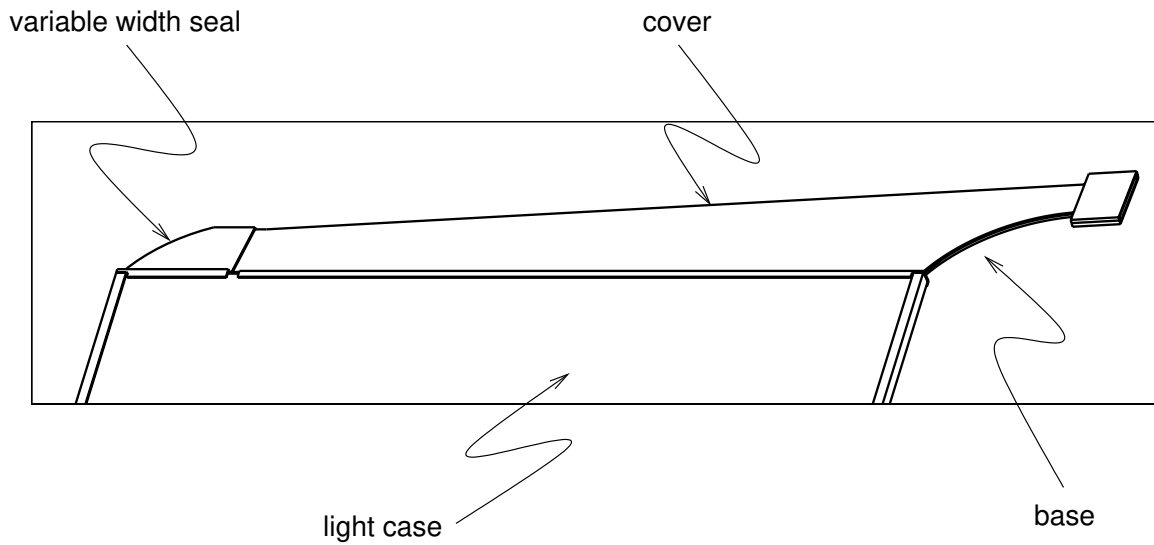
Figure 5.14: Sketches of a 20-wide perpendicular-ended manifold with a right-handed optical connector outlet. The upper drawing shows the assembled manifold and the lower drawing is an exploded view.

WLS fiber #20

base

optical connector

light injection manifold compartment

bottom light case

integral module mounting bar
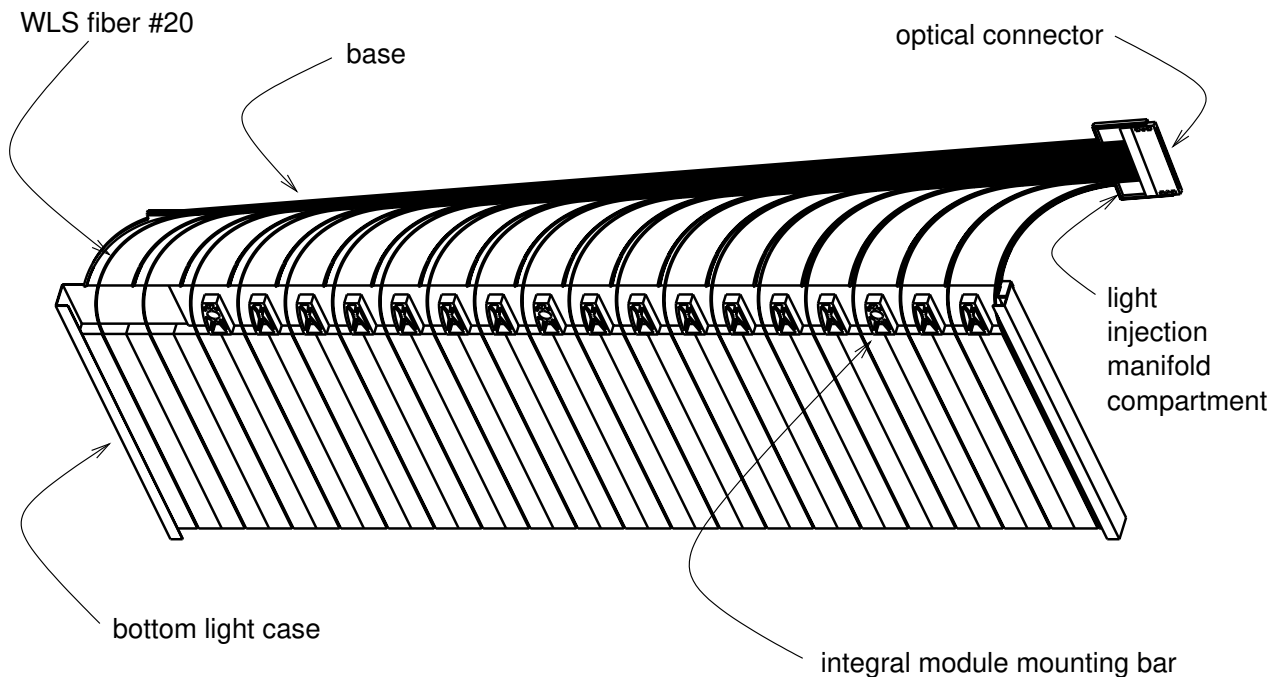
Figure 5.15: Sketch of one end of a partially assembled 20-wide, perpendicular-ended scintillator module, showing the fiber routing and the module mounting bar.

5.4.3.6 Light injection manifold

Light injection manifolds are included in the end manifold assemblies of each module to allow the injection of test pulses of light into groups of WLS fibers. The light injection must be segmented so that only a single fiber will be pulsed on any given PMT pixel at one time (but many pixels can be pulsed simultaneously). This is accomplished by distributing light either to two groups of 10 fibers each for modules which are 20 strips wide, or to three groups of 10, 10 and 8 fibers each for modules which are 28 strips wide. The light injection manifold is an injection-molded block of polystyrene scintillator with 10 parallel grooves on one face and a single hole that enters halfway into the block a few millimeters above the opposite face. Each scintillator module will contain either 2 or 3 of these light injection manifolds depending on the number of scintillator strips contained in the module. Fibers from the laser calibration source are inserted into the holes in each scintillator block, which stop halfway into the block, to illuminate the WLS fibers. The WLS fibers are mounted in the optical connector before they are slipped into the grooves of the light injection manifold. The clear fibers from the laser source distribution system enter each scintillator manifold through a separate optical connector located directly below the optical connector.

5.4.3.7 Module source calibration tube

The source calibration tube assemblies allow small radioactive sources, mounted on piano wire holders, to be moved across the scintillator strips of a module. The tubes are made from 2-mm diameter stainless steel hypodermic tubing and are attached to the aluminum light cases at each end of a module. The tubes are oriented parallel to the strips near the end

manifolds and are curved so that they cross all strips. Each tube is protected by a shield: two pieces of steel wire bent to conform to its shape. The tube and shield are glued to the outside of the light case. The light case is also glued to the scintillator strips in the area underneath the tube to ensure that the tube's position relative to the strips does not change.

5.4.3.8 Coil bypass

A 30-cm wide square hole is provided at the center of each active plane to accommodate the magnet coil. For far detector planes the hole is centered between two perpendicular-ended modules; a semi-circular area is removed from each of these modules. The semi-circular cut extends into the light case and the five scintillator strips at the edge of a module. The WLS fibers for the five cut strips are made long enough so they can be routed around the coil hole.

The semi-circular holes in the affected modules are closed with injection molded plastic bypasses, sealed to the light cases with black adhesive. A bypass is illustrated in Fig. 5.16. The bypass provides a light-tight seal, protects the WLS fibers, maintains the WLS fiber bend radius at more than 12 cm and improves the mechanical integrity of the module in the region of the hole.
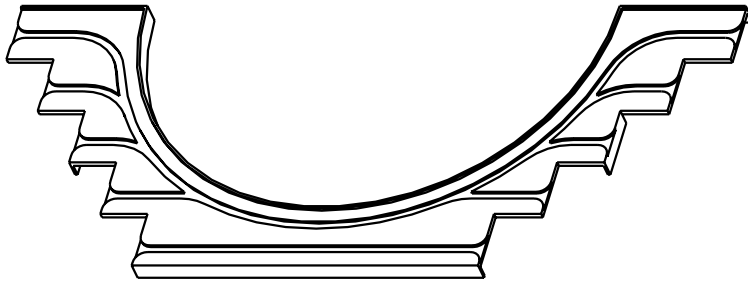
Figure 5.16: Coil bypass.

5.4.3.9 Module mounting hardware

This Section describes the three methods used to attach scintillator modules to the steel detector planes. The actual installation of this hardware is described in Section 7.4.3.2.

The first means of attaching modules to steel detector planes is through the module mounting bars in the end manifolds. Each module mounting bar has a set of holes which penetrate the module and the aluminum light case, as shown in Fig. 5.15. Self tapping screws in these holes are used to attach the both ends of each module to strips of 13 gauge sheet steel which are welded to the edges of the steel detector planes. An elastomeric isolator around the screws cushions the interface between the steel and the modules.

The second means of attachment uses standard 13 mm × 0.5 mm steel packing straps which wrap around the modules and thread through "switchplate" brackets tack welded to the steel plane. These straps prevent the modules from pulling away from the center

of the absorber planes. Wrapping the straps around two modules at a time minimizes the inter-module gaps.

The third means of attachment is a shelf along the lower 45° edge of each plane mounted on the detector. This shelf supports the lower edge of the bottom module, and the weight of the modules in the plane above it. The shelf ensures that the active planes do not sag in the middle; it does not block access to the optical connectors.

5.4.3.10 Differences in near detector modules

The scintillator modules in the near detector share all of the essential features of the far detector. However differences in the size and functional regions of the near detector result in some differences in module construction and layout:

- The modules for the fully instrumented planes, e.g., in the muon-spectrometer section, are similar to those of the far detector except that they are at most 4 m in length and are read out from only one end. Modules in the muon spectrometer section have 4-fold multiplexing to the photodetectors instead of the 8-fold multiplexing used for the far detector.

- The modules in the partially instrumented planes of the target/calorimeter sections are less than 2.7 m long and are also read out from only one end. None of the modules in these forward sections have multiplexed readout, i.e., they have only one fiber per photodetector pixel.

- In order to keep the calorimetric response between the near and far detectors as similar as possible, we plan to modify the design of the near detector modules slightly so that the calorimeter section of the near detector has a one-ended light yield very close to that of the sum of two ends in the far detector. To first order, this occurs naturally since WLS fibers in the near detector are shorter than those in the far detector. However, it may be desirable to include a crude mirror on WLS fibers in the near detector (e.g., white paint on the fiber ends) or to use slightly larger diameter fiber in order to make the best match between the near and far detector light outputs. This will also ensure good efficiency for muons from the spectrometer section of the near detector.

5.4.4 Photodetectors (WBS 2.2.4)

5.4.4.1 Photodetector requirements

MINOS neutrino events produce a wide range of light levels in the scintillator strips. On the low end, muons give at least 1.7 photoelectrons from the lower of a strip's two readout ends (at least 5.5 photoelectrons from the sum of the two ends), and the tails of showers range down to single photoelectrons. On the high end, we want to maintain linear response for showering events with up to 500 photoelectrons per strip on a single pixel. MINOS photodetectors must meet this and other specifications:

1. Linearity over a physics dynamic range of 500.

2. Ability to discriminate at 1/3 of a pe level with acceptably low noise.

3. Shaping times $< 1\mu s$ to avoid pile-up at the near detector.

4. Dark count below 10 Hz/mm^2 of photocathode area.

5. Lifetime of 1 to 3 mC integrated charge and a failure rate of less than 2% per year of operation.

6. Less than 10% effect on gain for up to 10 Gauss magnetic fields.

7. Crosstalk between neighboring pixels $< 4\%$.

8. Quantum efficiency $\times$ collection efficiency such that a muon crossing a strip gives at least 2.5 total pe's observed on average.

9. Pixel-to-pixel nonuniformity of 4:1 or better. Nonuniformity increases the electronics dynamic range requirement.

10. Time resolution of better than 2 ns for signals of $>$10 pe's.

These requirements are met by several commercially available photodetectors, of which multi-pixel photomultipliers are the most attractive for MINOS. We have chosen the Hamamatsu R5900U-00-M16 16-pixel photomultiplier for the MINOS baseline design because of the extensive favorable experience of other experiments with this photodetector.

5.4.4.2   Baseline photodetector

The baseline photodetector for MINOS is a 16-pixel, multi-anode photomultiplier, R5900U-00-M16, manufactured by Hamamatsu Photonics[14]. Our choice of the 16-anode M16 is based on two simple criteria: a) R5900U-00-M16 satisfies all our requirements, and b) among all multi-anode photomultipliers it provides the lowest cost per unit area of the photocathode. The M16 tube behaves like 16 miniature single-channel phototubes. Only a few additional and potentially adverse features, like cross-talk and nonuniformity of pixel response, are introduced through dense packaging. Figure 5.17 and Table 5.2 show the geometry and basic characteristics of the M16. The R5900 family of multi-anode photomultipliers includes tubes with numbers of channels ranging from 1 to 64, with independent anodes and metal-channel dynode structures. Hamamatsu maintains an active R&D program to improve performance of the R5900 series of tubes. The most recent example of this effort is development of an improved bialkali photocathode for the M16 tubes, which gives about a 10% increase in quantum efficiency over previously produced bialkali photocathodes.

The R5900U-00-M16 tube has a wide range of applications. It is used in biomedical imaging as well as in major high energy physics experiments. The HERA-B detector at DESY uses 1500 of these tubes in the central part of the ring-imaging Cerenkov counter readout[15]. The upgraded Plug of the CDF II detector at Fermilab employs about 450 tubes in the readout of the Preshower and Shower Maximum detectors[16].

Several high energy physics groups, including MINOS, have conducted many comprehensive tests on the M16 tubes during the last year[17]. These studies have provided valuable

Parameter	Description/Value
Photocathode material	bialkali
Window material	borosilicate glass
Window thickness	1 mm
Spectral response	300 to 650 nm
Wavelength of maximum quantum efficiency	420 nm
Quantum efficiency at 520 nm	13 %
Dynode type	metal channel structure
Number of stages	12
Anode	an array of 4 × 4 independent pixels
Anode dark current per channel	≤ 1 nA
Pixel size	4 mm × 4 mm square
Maximum high voltage	1000 V
Gain at maximum HV	3.9×10^7
Nominal operating gain for MINOS	10^6
Anode pulse rise time	0.83 ns
Transit time spread per channel (FWHM)	0.3 ns
Pulse linearity per channel ($\pm$ 2 % deviation)	0.5 mA
Cross-talk (4 × 4 mm^2 aperture)	1 %
Pixel-to-pixel gain variation	1:4

Table 5.2: Basic characteristics of the R5900U-00-M16 16-channel photomultiplier produced by Hamamatsu Photonics.

practical experience and allow us to project with high confidence the performance of mass-produced M16 phototubes. Also, the delivery capacity and reliability of the manufacturer is now well established. In this Section we briefly discuss selected features of the M16 tube which are relevant for the MINOS scintillator detector and associated electronics.

- **Quantum efficiency:** The expected light yield for minimum ionizing particles requires that a photodetector be able to clearly separate single photoelectron signals from the pedestal. Since the emission spectrum of the wavelength shifting fibers peaks at about 500 nm, and is further shifted to about 520 nm due to length attenuation, we require high quantum efficiency for photons with wavelengths of about 520 nm.

  Figure 5.18 shows a typical distribution of pulse heights obtained by pulsing a wavelength shifting fiber with a blue LED. Peaks of 1, 2, and 3 photoelectrons can be easily identified. The new M16 tubes have an improved bialkali photocathode with a typical quantum efficiency of about 13% at 520 nm, as shown in Figure 5.19. This constitutes a ∼10% improvement over older tubes of this type.

- **Pixel-to-pixel response uniformity:** Studies by Hamamatsu, HERA-B, and MINOS show that individual pixels of the M16 tube can produce significantly different anode

pulse heights for the same illumination. Figure 5.20 presents an example of response uniformity for one M16 tube. The gain of the inner pixels is typically lower than the gain of the perimeter pixels. About 30% of channels are currently expected to exceed a maximum to minimum response ratio of 2.5. This nonuniformity has no serious adverse effects for MINOS. Its main impact is the increase of the dynamic range requirement on the front-end electronics. For MINOS, Hamamatsu guarantees the ratio to be less than 4.

- **Pixel response uniformity:** Eight 1.2 mm diameter fibers will be multiplexed onto one 4×4 mm^2 pixel. Although there are variations in intra-pixel collection efficiency, our measurements show that these are almost completely averaged out for 1.2 mm diameter fibers. Some pixels have intra-pixel variations in gain for 1.2 mm diameter fibers which are comparable to the inter-pixel gain variations. These intra-pixel gain variations can be directly measured for each fiber using our calibration system, and have the same effects as the inter-pixel gain variations.

- **Fast timing:** We have measured the time resolution of the Hamamatsu M16 tube to be better than 2 ns for greater than 10 observed pe's. Figure 5.21 shows the measured time resolution for the Hamamatsu M16 tube as a function of the number of observed photoelectrons. For these small numbers of pe's, the time resolution is dominated by the decay time of the Y11 fluor in the WLS fiber rather than measurement effects in these photodetectors. This time-of-flight measurement capability will be useful in determining the direction of showering events induced in the MINOS far detector by cosmic-ray neutrinos, and is better than required for determining the direction of high-energy muons traversing the detector.

- **Magnetic field sensitivity:** The M16 tube is a proximity focused photomultiplier with an additional electron focusing grid placed before the first dynode. This architecture assures relatively low sensitivity to magnetic fields. In locations on the MINOS detector in which photodetectors will be installed the expected magnitude of the fringe magnetic field is about 7 Gauss. Unshielded M16 tubes could typically lose about 5 to 10% gain in such a field. However, magnetic fringe fields could have a more serious effect on cross talk between neighboring pixels, particularly for fibers located near pixel edges. To eliminate this effect, a thin soft iron sleeve (2 mm thick transformer laminate) surrounds each MUX box, reducing the field at the photodetector by a factor of five or more.
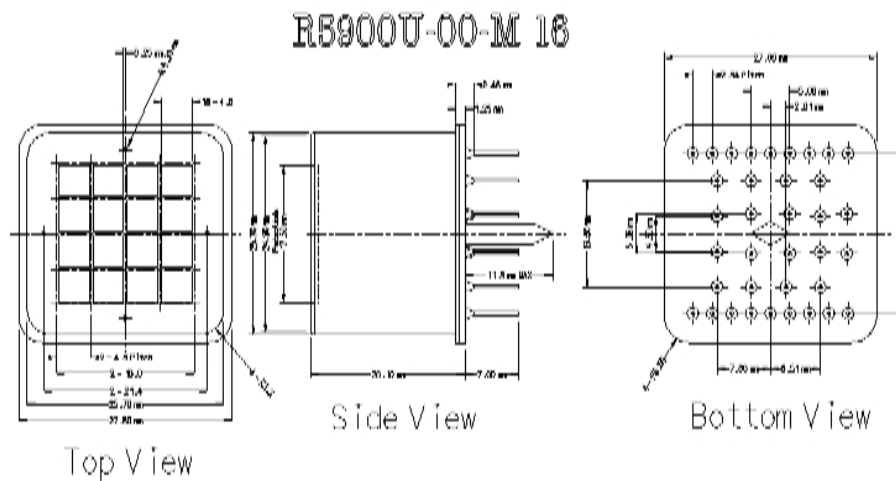
Figure 5.17: Detail drawing of the Hamamatsu R5900U-00-M16 multi-anode photomultiplier.
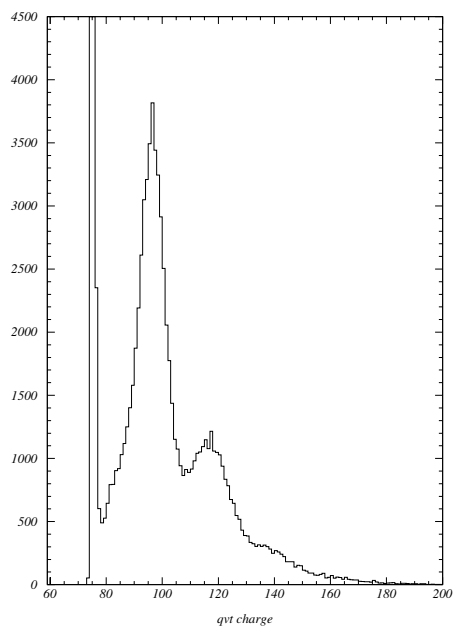
Figure 5.18: A typical pulse height distribution in a pixel of an M16 tube obtained by pulsing a wavelength shifting fiber with a blue LED. Peaks for 1, 2, and 3 photoelectrons are clearly visible.
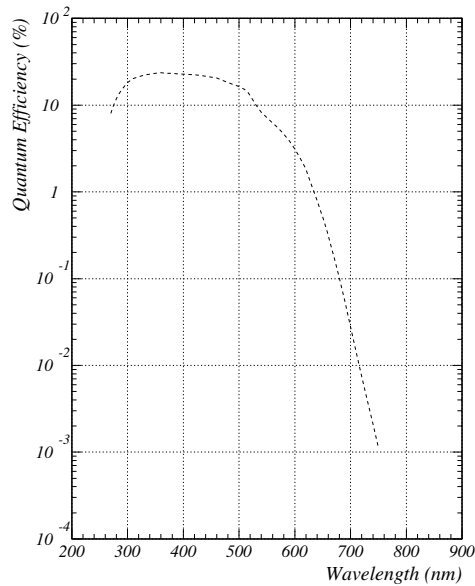
Figure 5.19: A typical spectral response for a Hamamatsu R5900U-00-M16 tube. For MINOS the most important wavelengths are at about 520 nm, the maximum of the emission spectrum of the wavelength shifting fiber.
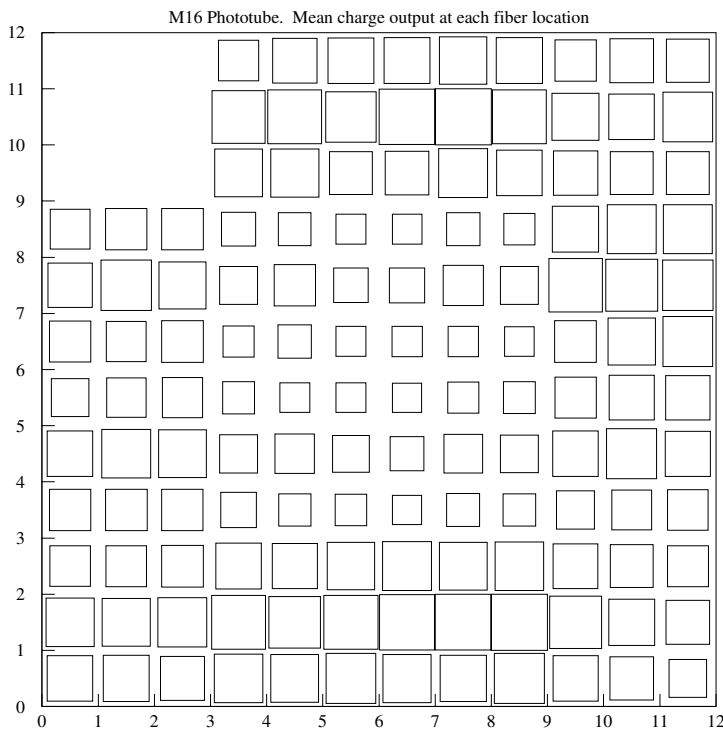
Figure 5.20: A typical response of an M16 phototube. Each pixel was illuminated using a 1 mm diameter wavelength shifting fiber with the same amount of light. On each pixel the fiber was placed in 9 locations in a 3×3 grid. The area of the squares in the plot are proportional to the signal on the anode. A pixel-to-pixel response nonuniformity, and variation within one pixel, are clearly visible. The measurement showed that the observed structure can be attributed mainly to the variation of the effective gain in individual channels rather than quantum efficiency or collection efficiency. One corner pixel was not read out.
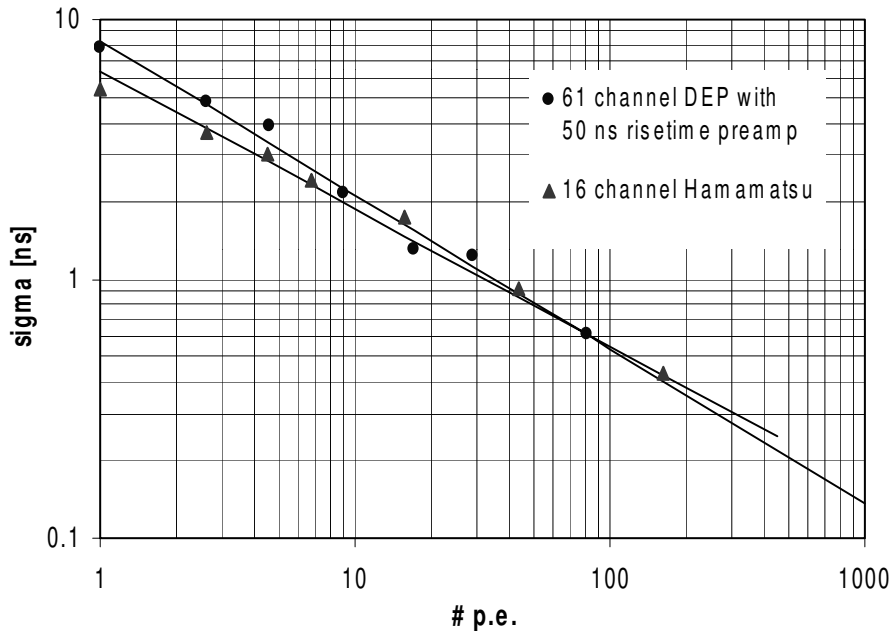
Figure 5.21: Time resolution (σ) measured as a function of the number of observed photo-electrons for the Hamamatsu M16 and DEP HPD reading out WLS fiber. The resolution for small numbers of pe's is dominated by the decay time of the Y11 fluor in the WLS fibers. Of particular interest is the better than 2 ns σ for more than 10 observed pe's which will be useful in determining the direction of showering events.

5.4.5 Connectors and multiplexing boxes (WBS 2.2.5)

5.4.5.1 Fiber connectors

Construction of a modular detector requires efficient and cost-effective fiber-to-fiber connectors. In MINOS, optical fiber connectors are used to couple the WLS fibers coming from the scintillator modules to the clear-fiber ribbon cables and between the ribbon cables and the multiplexer boxes. Such connectors have already been developed for the CDF endplug upgrade (10 fibers), the D0 upgrade (about 100 fibers), and recently for the CMS HCAL (18 fibers). Tests on these connectors have shown similar performance in light transmission. For MINOS, we are planning a custom-designed connector based on one of the previous designs. The MINOS connector will be a 28-wide connector with 2.3 mm pitch for the fibers. (This is most similar to the CMS connector which is 18 wide and with 2.3 mm fiber pitch.) The reason for designing a custom connector rather than just using one of the existing connector designs is cost. To a good approximation, the cost per connector and manpower to assemble it is the same regardless of the design or the number of fibers included (up to some reasonable limit). Furthermore, the cost of clear fiber ribbon cables is much lower if a pitch of about 2 mm is used rather than a pitch of about 1 mm as for previous cables. We are currently evaluating the different connector designs to decide which is optimal for MINOS

needs. We have used both 10-wide CDF connectors and prototype CMS-style connectors in construction of MINOS prototype modules. We find similar results for light transmission from the two types of connectors.

A sketch of a MINOS connector at a 20-wide scintillator module manifold is shown in Figure 5.22. The connector is wide enough to accommodate 28 optical fibers in order to allow just one connector design for all modules. The 8 unused fiber positions are plugged when the connectors are used for 20-wide modules. Appropriately matched connectors are located on the scintillator manifolds, the MUX boxes and each end of clear fiber ribbon cables which connect the two. MINOS ribbon cables are 10 and 8 fibers wide (these are already a custom production so there is no problem specifying these widths). Fibers are glued into the connector housing with epoxy, with a few mm of the fiber left protruding. The protruding fibers are fly cut and polished using a diamond fly cutter. Prototype 28-wide connectors are currently being produced for MINOS.
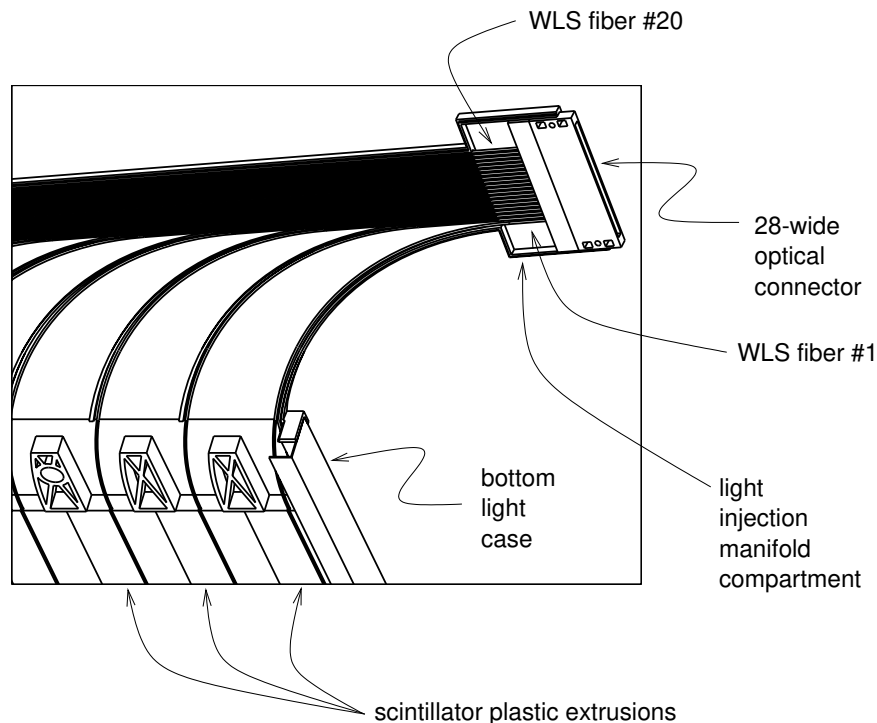
Figure 5.22: Sketch of a MINOS 28-wide optical connector for 1.2 mm diameter fibers, as used on the end manifold of a 20-wide scintillator module.

The CDF connectors were manufactured by the DDK company of Japan[18]. CDF has measured the light transmission across the connector without optical coupling. The mean of the measured light transmission is 83%[10] with small spread. Out of the total light loss of 17%, 10% is expected from the Fresnel reflection. The light loss can be reduced by using optical couplant. The DO collaboration has measured an average light transmission of 90±5% using a diffused light source and 96±3% using a small angle light source[13] for their tracker and preshower detector for the upgrade, but with use of an optical couplant.

CDF has measured the reproducibility of the light transmission for this connector through multiple repetitions of disconnecting and reconnecting. The rms width of the distribution is less than 2%[10]. Our first test results show that MINOS connectors will provide similar performance.

5.4.5.2   Multiplexing boxes

The multiplexing (MUX) box is the link in the readout chain between the signal fibers and the photomultiplier tubes, as shown schematically in Figure 5.4. The mechanical structure of the MUX box is shown in Fig. 5.23. The input signals from the detector are brought to the MUX box by clear optical fibers, bundled into ribbon cables, that plug into bulkhead connectors on the front plate. Inside the MUX box, clear fibers are mated to the signal fibers and then routed to the back plate through an aluminum box chassis. At the back plate, the fibers are laced to three internally mounted cookies that are machined to align precisely with the pixels of three 16-channel PMTs. The MUX box is designed to be light tight and is shielded against magnetic fringe fields.

External to the MUX box on the back plate, the cookies are mated to the PMTs by means of a PMT-cookie assembly. This assembly, shown in Fig. 5.24, allows for the removal/replacement of a PMT without opening the MUX box. In this design, the cookie remains in a fixed position with respect to the cookie holder. To allow for tolerances in the manufacture of its case, the PMT is cemented into an outer jacket. This jacket fits precisely into a holder that permits piston-like motion with respect to the cookie but very little lateral motion. The piston-like motion enables the spring-loaded PMT base to push this assembly into contact with the cookie. The precision alignment of the cookie with the PMT is accomplished by aligning the cookie holder with the PMT holder using a special alignment tool; the alignment procedure takes place in the lab, away from the detector.

The three PMT-cookie assemblies are bolted to the back plate and housed in a light-tight PMT cover box. The electronics are connected to the PMT outputs through the PMT cover box.

There are 484 MUX boxes in the MINOS far detector. The far detector makes use of 8× multiplexing on the PMT pixels while the near detector will make use of 4× multiplexing in the muon spectrometer section and no multiplexing in the target/calorimeter section. However, the same design for both the MUX box and electronics will be used for the near detector. Near detector MUX boxes have fewer connectors on their front plates, fewer fibers to be routed, and special cookies to accommodate the particular number of fibers in each type of box. There are a total of 212 MUX boxes in the near detector.

- **Mechanical construction of the MUX box**

    All MUX box components shown in Fig. 5.23 are stamped and formed from sheet aluminum. The boxes are assembled with stainless steel self-tapping sheet metal screws. Each box is surrounded by a 2 mm thick sleeve of soft iron transformer laminate to shield the photodetectors against magnetic fringe fields (not shown in Fig. 5.23).

    The inputs to each MUX box are 1.2 mm diameter clear polystyrene fibers carrying the signals from two consecutive detector planes with the same stereo view. These 384 signal fibers are bundled in ribbon cables. Each of these ribbon cables terminates in

MINOS Mux Box Assembly

Back Plate

Chassis

Chassis Cover

Front Plate
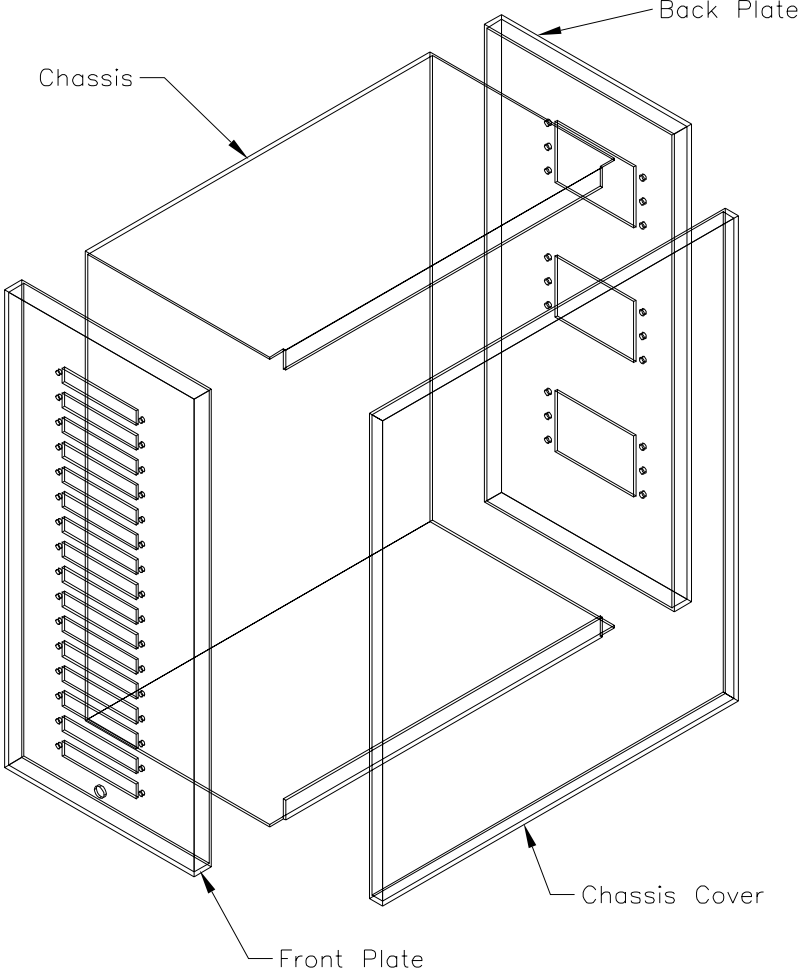
Figure 5.23: MUX box assembly. The external magnetic shield of 2 mm thick soft iron which surrounds the box is not shown.

PMT – Cookie
Assembly

PMT Jacket

PMT Holder

Cookie Holder

Back Plate
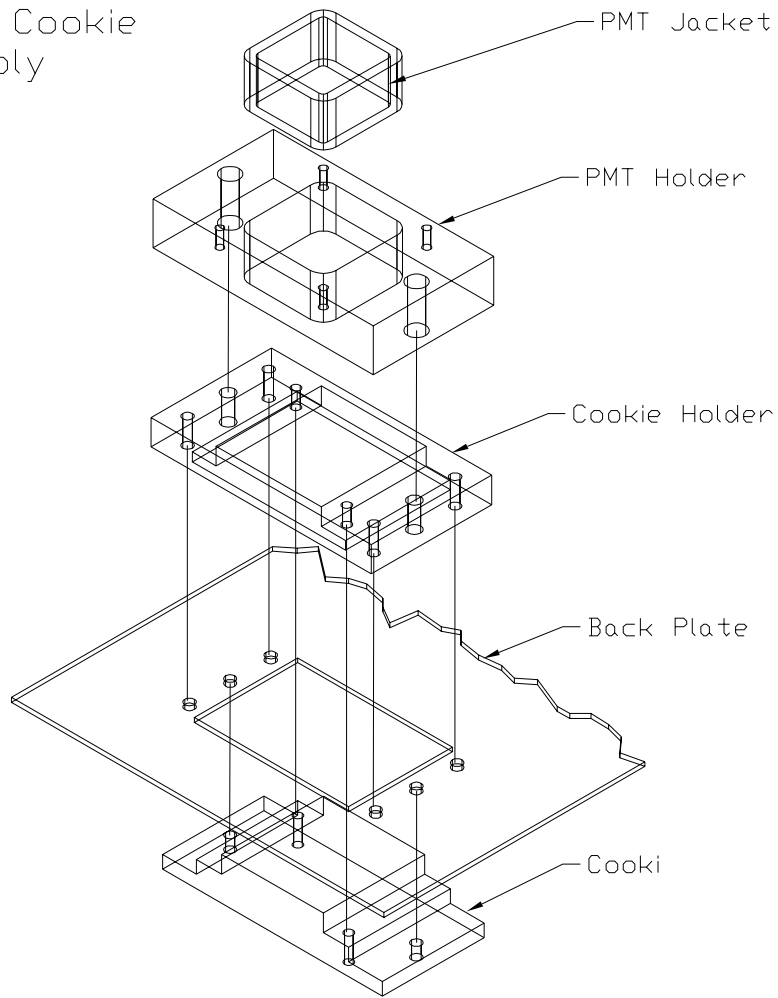
Cooki

IU HEAp

Figure 5.24: PMT-cookie assembly.

a fiber optics connector (see Section 5.4.5.1) that plugs into a double female bulkhead connector mounted on the MUX box front plate. Inside the MUX box, groups of eight clear fibers mate to the signal fibers through the front plate bulkhead connectors. A hole is provided near the bottom of the front plate to mount an LED and diffuser on the inside of the MUX box, as described in Section 5.4.6.2. The internal signal fibers are routed from the front plate, through the box chassis, to the cookie on the back plate. The 25-cm length of the MUX box chassis is set by the requirement that the bend radius of the fibers be greater than 12 cm.

- **Routing and fly cutting fibers**

  The 384 signal fibers are routed to three Hamamatsu M16 multichannel PMTs through precision-machined cookies. Eight fibers are routed to each 4 mm × 4 mm pixel. Two of the PMTs in a far-detector MUX box see 8 × 16 = 128 fibers from single planes; the third PMT sees 8 × 8 = 64 fibers from each plane. The ribbon cable connectors are inserted into the front plate according to a pattern that minimizes fiber lengths within the MUX box.

  The baseline detector has 8-fold multiplexing and 2-ended readout. To resolve ambiguities introduced by the multiplexing, the two strip readout ends will have different routing/lacing schemes. On a single pixel, fibers arrive from each of the eight logical modules within a scintillator plane. The exact scintillator strip location (within the logical module) to pixel location map is permuted within groups of eight fibers. Monte Carlo simulations of neutrino events show that this mapping permits unambiguous identification of the true location of neutrino events for light levels meeting our specifications.

  For cookie assembly, the fibers are first glued into the connectors. Then the connectors for a group of 128 fibers are fixed to a jig and the fibers routed to the cookie according to the appropriate permutation scheme. To facilitate accurate routing to a particular cookie position, the fibers are illuminated with the same programmable LED sources used for quality control checks (see the final bullet in this Section). After gluing the connectors and cookie are fly cut with a commercial fly cutting machine. The procedure for inserting the fibers into the connectors and then lacing the cookie was developed for CDF. However, for MINOS the procedure for routing the fibers to the appropriate cookie hole is more complicated than for CDF. We have begun to optimize this procedure by actual prototype assembly in order to estimate the manpower required.

- **PMT-cookie assembly**

  The PMT-cookie assembly is shown in Fig. 5.24. The cookie is injection molded from grey Noryl and mounted inside the MUX box on the back plate. It has 16 precision holes that accommodate 1.2 mm fibers in a 3-2-3 pattern (three fibers on top and bottom with two fibers in between, arranged in a close-pack array). The cookie holes precisely align with the 16 pixels on the PMT. The cookie mates with a cookie holder outside the MUX box. The cookie holder has a central hole with the exact shape of the cookie and is attached to a PMT holder using slightly over-sized holes. These holes

allow the cookie to be accurately aligned with the pixels on each individual PMT. This alignment is done in the lab using a special clear acrylic 'alignment cookie' with the exact shape of an actual cookie. Both the cookie and the alignment cookie have sockets for two alignment dowels that rigidly fix the cookie and the alignment cookie in the same position relative to the cookie holder to within tolerances of a few thousandths of an inch. The alignment cookie has precision ruled marks that accurately line up with the guide marks on the PMT photocathode. The cookie holder with the alignment cookie is accurately aligned with the PMT holder before they are rigidly fixed to one another.

The PMT is pressed against the cookie, piston-like, by a spring-loaded base. The PMT is glued into an aluminum jacket that allows for the 0.5 mm tolerances on the PMT housing. The outside of the jacket is precisely machined to fit into the PMT holder in a way that allows it to slide without lateral motion. The PMT base is attached to the PMT holder. The cookie holder, PMT holder, PMT, and base assembly are then attached to the cookie. A light-tight housing is placed over the PMT-cookie assembly and bolted to the back plate.

- **QC computer controlled LED array**

  Final checkout of the lacing scheme and the MUX box will be made using a programmable set of LED sources. A set of pattern-generation LED boards is driven by a computer. Clear fibers from the LEDs run to optical connectors which couple to the MUX box connectors. To test the lacing pattern on a cookie: (a) each of the lacing schemes is programmed into the computer; (b) individual fibers are illuminated in such a way that only one fiber in each of the 16 pixel holes on the cookie lights up; simple pattern recognition is performed by eye; (c) the test is then repeated 8 times for each cookie. The completed MUX box will be tested with this computer controlled LED array by flashing attenuated LED signals through each fiber and measuring the PMT output.

  This testing device is also used to facilitate fiber lacing. For this task, the QC computer is programmed to illuminate the 8 fibers that are to be routed from the connectors to a particular pixel hole on the cookie. By plugging and gluing only lighted fibers, fiber routing becomes simpler, more accurate, and less time consuming.

5.4.5.3   PMT bases and mounting

The M16 photomultiplier and its mounting brackets are rigidly attached to the back plate of the MUX box. A square opening in the plate lets the fibers couple to to the photocathode face. The tube is aligned with fibers as described in the preceding Section. The PMT base (voltage divider board) is mounted directly on the pins of the tube. For strain relief this board is also attached to the PMT holder using 4 spacer screws placed in the corners of the board. The entire phototube assembly (i.e., a cookie, a cookie holder, PMT holder, PMT, and the voltage divider card) is housed in a light-tight case sealed to the back plate of the MUX box.

A multi-purpose feed-through D-type connector on the PMT housing supplies HV to the photomultiplier and also carries 16 anode and one common dynode signals. The three

PMT connectors on the MUX box are aligned to mate directly with connectors on the front-end electronics card. The PMT base provides a negative high voltage bias for the dynode structure and also routes the anode signals. "Tapered" resistor values allow a gain of about 10^7, up to 5 mA anode current, and response linearity of $\pm 2\%$ over the entire range of physics and calibration pulses. Heat generated by the divider current (0.4 W for 250 μA at the maximum high voltage of 1000 V) is easily dissipated by the PMT mounting structure and the multiplexing box. This arrangement mechanically decouples the front-end electronics board from the photomultiplier and at the same time provides a short signal path and good noise shielding.

5.4.6 Calibration systems (WBS 2.2.6)

The calibration system provides the means of understanding the calorimetric response of the near and far detector for hadrons and electrons and ensuring that the relative response between the two sites is understood. The goal is to calibrate the hadronic energy response to an absolute level of 5% and a relative level of 2% between the near and far detectors. This requires several different calibration systems as described in the following Sections. Cosmic-ray muons provide an integral part of the system. The calibration plan is discussed in Section 5.4.6.6.

5.4.6.1 Laser light distribution

The baseline design for the MINOS light injection system uses UV laser light sources. The laser light illuminates scintillator blocks surrounding sets of eight or ten WLS fibers. This ensures a good match between the spectrum of light from the calibration system and the scintillation light from real neutrino events. The advantages of a laser system are:

- The laser pulses are extremely short (<5 ns) so that the time profile of the pulse reaching the PMT is dominated by the WLS dyes. This makes calibration pulses very similar to those from a particle.

- Optical filters are used to attenuate the light at well-controlled predefined values.

- With one laser it is possible to illuminate ≈ 5000 WLS fibers at once, so only a small number of lasers is needed.

The far detector requires a single laser coupled to an optical fiber routing network which is used to inject light into the light injection manifolds described earlier. The pulses from the laser can be directed under computer control to distribution points located at the corners of each supermodule as shown in Figure 5.25. The placement of the components is designed to minimize the lengths of fiber in the system. Figure 5.26 shows a schematic for the distribution network. The laser which pulses the system is a N_2 laser which can deliver several hundred micro-joules per pulse at a wavelength of 337 nm. Each laser feeds a distribution system of splitters and fibers allowing it to pulse 1/20 (i.e., one physical light injector module per plane) of each detector block in a given view at a time. This results in only one fiber at a time being pulsed on each photodetector pixel. The laser is equipped with a computer

controlled attenuation wheel, containing neutral density filters, to provide a wide dynamic range for test calibration. A gain-stabilized reference photodetector monitors pulse to pulse variations of the laser output. To ensure the stability of the monitor photodetector, it also views a NaI(Tl) crystal with an imbedded ^{241}Am source. The laser light is transported to the fanouts by quartz fibers, and between the fanouts and the scintillator modules by acrylic fibers. This provides acceptable attenuation at reasonable cost.
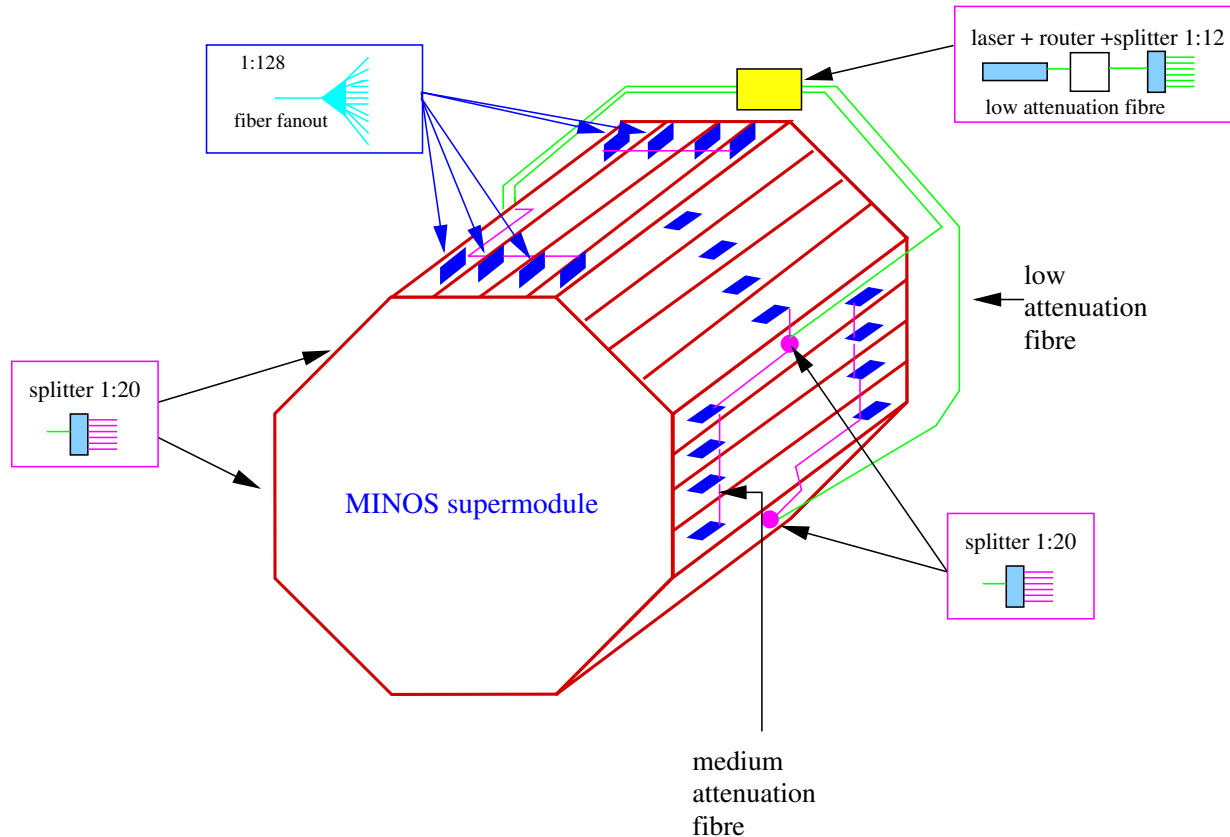
Figure 5.25: Location of components for the laser calibration system.

A similar light-injection system is being implemented as part of the CDF plug upgrade[16]. The CDF laser produces approximately 4.7×10^{14} photons per pulse. The overall light delivery efficiency of the CDF system is $\approx 1.3 \times 10^{-8}$. (This includes coupling to the fiber from the laser, light loss in transmission, light loss in the primary distribution to the splitter boxes, loss of light inside the splitter boxes, laser light dumped in a scintillator block, scintillation light coupling to WLS fibers, and light coupling to the PMTs.) In the system we are planning, we have essentially the same set of steps in our light delivery system except for the losses of light due to transmission in acrylic fibers instead of glass fibers. Both CDF and MINOS use the same Hamamatsu PMT. In CDF, there are 6.2×10^6 photons reaching the photocathodes through approximately 1000 fibers. Folding in a 10% QE in the PMT and dividing out the fiber count, results in 6.2×10^2 pe's per fiber, which will be enough light for the high energy end of the calibration.
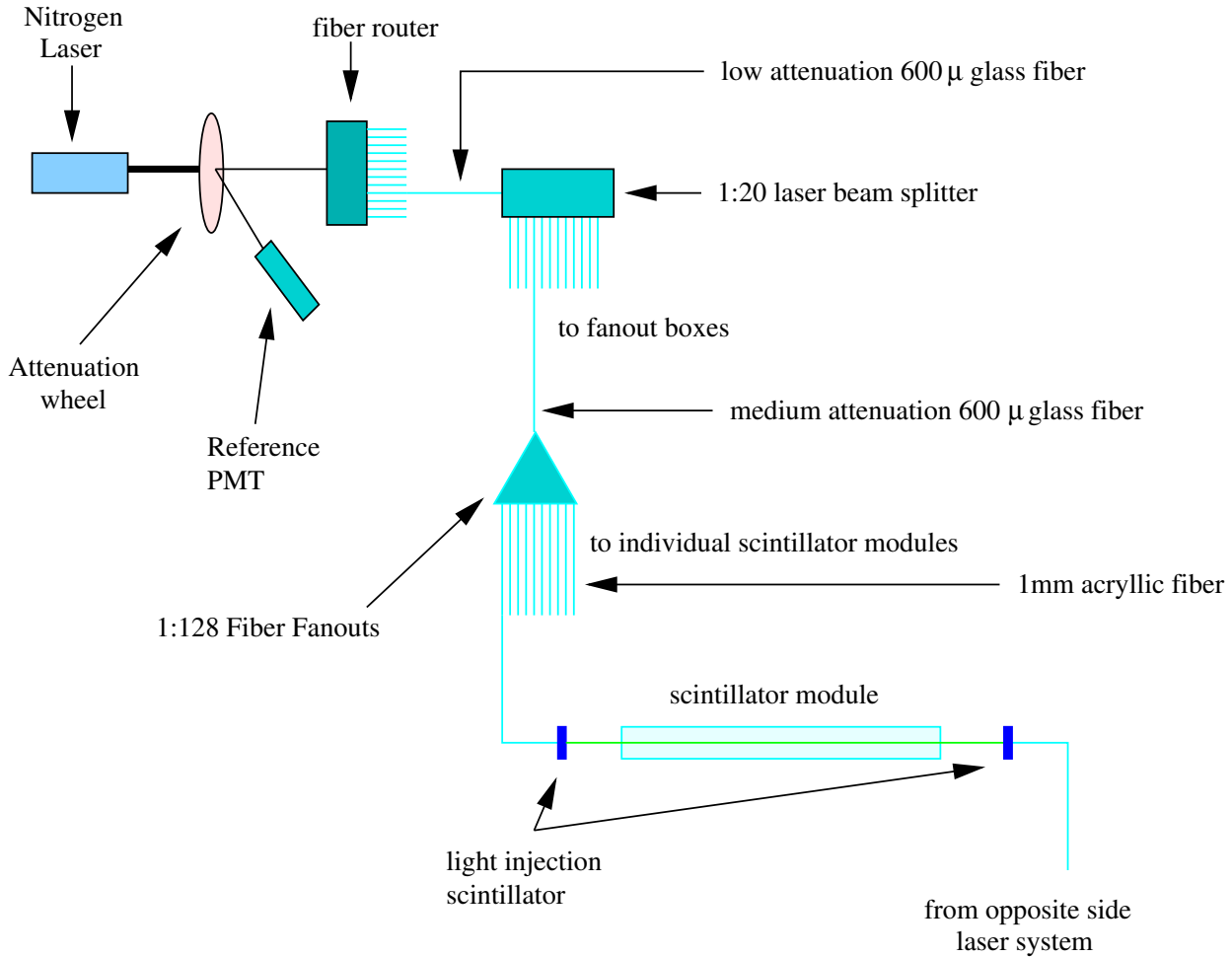
Figure 5.26: Schematic of the distribution network for the laser calibration system.

It is not necessary to have complete uniformity in the light injection system as long as the illumination is constant over time. Differences in intensity of up to 30% are acceptable across the WLS fibers within a manifold. Differences of up to a factor of two are acceptable for the amount of light arriving at completely different photodetectors. (More light settings are then required to get a complete calibration.)

5.4.6.2 Light injection to photodetectors

A green (505 nm) ultra-bright LED is installed in each MUX box to help isolate light transmission problems in the readout chain. The LED is pulsed at a low voltage level to check the response from all pixels of the three photodetectors simultaneously.

5.4.6.3 Radioactive source system

The purpose of the source system is to obtain a rapid measure of the response of each scintillator in the detector. Short stainless steel tubes are attached at either end of a detector module as described in Section 5.4.3.7. A tube acts as a guide track for a 3 mC ^{137}Cs source attached to the end of a piano wire. The source position is controlled by a drive mechanism under computer control. Modules are scanned with the ^{137}Cs wire source at the time of assembly and installation. When the detector comes on line to take data, the movable source can be used to verify other calibration methods or to troubleshoot. We do not plan to perform source scans on a regular basis, so only two source drivers are needed at each detector site.

There are two source tubes per module, one at either end. The ^{137}Cs source is inserted into the source tube via a plastic funnel tube that is connected (temporarily) to the source tube and runs back to the ^{137}Cs storage unit. Source tubes traverse all of the scintillators in a module within 60 cm of the scintillator ends. The source tube at the end-cap is positioned near the right edge of a module. It runs parallel to the strip direction in the end-cap, but as the tube reaches the scintillator strips it is bent with a 25 cm radius across the strips. After a bend of 60° the source tube traverses the remaining scintillator strips in the module in a straight line. This permits all strips to be illuminated in approximately the same location and keeps the bend radius large enough so that the source will not stick in the tube.

5.4.6.4 Calibration module

The calibration module is essentially a "test beam calorimeter" built with final production components. This detector will be exposed to hadrons, electrons and muons using the planned Main Injector test beam at Fermilab in order to determine the absolute light response and energy resolution for hadronic and EM showers. The initial module will use summed outputs from detector planes to provide the necessary calibration at low cost. Most of the components, except for the steel and scintillator planes, will be spares from the near and far detectors. If oscillation signatures are observed, further understanding of details of the response and resolution can be obtained by upgrading the calibration module with the full transverse instrumentation as in the near and far detectors. The module will be transportable in order to cross-check the response of muons in the module at the different detector sites, if deemed necessary. The module will be equipped with a source and light calibration devices as in the main detectors.

The features of the proposed initial calibration module are:

1. The module has 40 layers of steel, each layer being 2.54 cm in thickness. The total thickness of iron is 102 cm or 5.9 interaction lengths. The number of layers has been set based on the containment of showers from 30 GeV pions.

2. The dimensions of the calibration module are 2.4 m (longitudinal) by 1.0 m (transverse) and 1.0 m (height) with a rectangular cross section. The transverse dimensions have been set to permit containment of events, even with the detector axis rotated by up to 60° with respect to the beam axis (assuming 20 cm offset to one side for the incident beam).

3. The detector weighs about 8 tons.

4. There are 41 layers of scintillator strips with 24 strips per detector plane. All features of the scintillator strip assemblies mimic the construction of the near and far detector in order to ensure the same response to showers. The orientation of the scintillator strips is rotated by 90° in successive planes.

5. Clear fiber ribbon cables transmit light to MUX boxes and photodetectors as in the near and far detectors.

6. The photodetectors are identical to those used in the near and far detectors. The scintillator strips are read out at one end. The output of 8 neighboring strips in each detector plane are multiplexed onto a single pixel of the photodetector. Hence, a total of 123 pixels are required for the full detector, corresponding to 8 phototubes.

5.4.6.5   Cosmic ray muons

The MINOS near and far detectors experience a flux of high energy muons produced high in the atmosphere in primary cosmic ray interactions. They offer the possibility of direct calibration in the low energy range of the MINOS scintillators using minimum ionizing particles. There are two principal questions: First, are the rates of these muons adequate for calibration, especially at the deep location at Soudan? Second, are there significant differences in the energy deposited in the scintillators at the two locations due to the different muon energy spectra and angular distributions?

The rates and angular distributions of the underground muons at Soudan are well-known[19]. Using these, we have calculated the flux and the muon path length distribution through a single 8 m long MINOS scintillator, 1 cm × 4 cm in cross-section and oriented at 45° to the horizontal. The muon flux is is 1000±100 per month. The flux in the near detector will be 500 to 1000 times greater. The distribution of muon path lengths through the scintillator strips shows a well defined peak with median value 1.45 cm. Ten percent of the muons will have a path length greater than 3 cm.

The energy deposited in the scintillator strips is dependent on the muon energy spectra. This dependence can arise from the relativistic rise in dE/dx ionization loss as a function of primary energy, and also from differing bremsstrahlung, delta-ray, and pair production along the track of the muon. We have estimated the difference in average muon energy at the near and far detector halls. The median muon energy at Soudan 2 depth is 250 GeV and at Fermilab it is 40 GeV. We have estimated the average energy deposition rate in plastic scintillator due to ionization as a function of energy. Averaging over the muon energy distribution, we estimate that any difference between the two depths will be less than 1%. The probability of delta rays accompanying the muon is essentially energy independent and, indeed, is already accounted for in the the ionization prescription. Hence, the main concern for possible calibration differences are due to bremsstrahlung and pair production in the steel which sends extra particles into the scintillator strips.

The probabilities of bremsstrahlung, and pair production in the steel of the Soudan 2 detector have been calculated previously[19]. Energy losses via bremsstrahlung and pair production are strongly dependent on the muon energy. The former tends to produce large

bursts of energy relatively infrequently along the muon path. These electromagnetic showers have been studied in the Soudan 2 detector and will produce extremely large scintillator signals less than 3% of the time. They can be removed by a simple cut. However, the pair production process require more study.

We have made a Monte-Carlo calculation of photoelectron yields for muons at Soudan, based on the known angular and energy distribution of those muons and observed light output distributions for cosmic-ray muons in our prototype scintillator strips. Poisson statistics have been assumed for the observed photoelectron distribution. By calculating the mean on a truncated distribution, the Monte-Carlo calculation suggests that the light output of each scintillator strip can be calibrated to a precision of 2% in 1 month. In order to verify these estimates, we are undertaking a series of measurements at different depths underground, using scintillator strips located between 5 cm steel sheets.

Ultimately, if necessary, we can check the muon calibration at the different detector sites using the transportable calibration module. Finally, about 7% of the muons stop in the detectors. These will provide a source of muons of known energies (using range to determine energies) to provide another cross-check on the calibration.

5.4.6.6   Calibration plan

The goal of the calibration system is to permit the translation of the measured hadronic and EM shower response from a test beam to the near and far detectors and over the full time-period of data acquisition.

The calibration module will be used to obtain calibration data in a charged-particle test beam at Fermilab. Cosmic-ray muon data will be used to transport the calibration to the near and far detectors. The rate of cosmic ray muons is sufficiently low (especially at Soudan) that it is important to keep track of gain changes in the system over a shorter time scale. A 2% calibration for each far detector scintillator strip is possible with one month of muon data and an equivalent amount of data from the calibration module (at Soudan) will be required.

The near and far detector light injection systems provide the ability to track short-term gain changes and to measure the response curve to light of the full PMT/electronics system for each fiber independently. For each channel, a set of constants will be produced comprising a pedestal and one or more constants describing the shape of the light in/light out curve. The muon data provide a common fixed point in the light response curve for each fiber. The light-injection system also permits localization of any anomalies in light transmission through the fibers and connectors. The electronics is tested independently by direct injection of charge (see Chapter 6).

The above procedure provides a complete set of calibration information. However, we also have some cross-checks on this calibration. During installation the individual strips are tested with the ^{137}Cs source. This provides both an important debugging tool and a cross-check on the muon calibration of light output. At the near detector, through-going muons from neutrino events provide an independent data set for calibration. Finally, we could choose to operate the calibration module at the near detector site to obtain neutrino events. In this case, there will be a sufficient number of neutrino events in the calibration module to make a direct comparison of hadronic energy in those events to hadronic energy in the near detector target/calorimeter region.

5.4.7 Assembly and testing equipment (WBS 2.2.7)

Construction and testing of scintillator modules requires several specialized machines which are described in this Section.

5.4.7.1 Extrusion trimming machine

The extrusion trimming machine is used to cut the length of each scintillator strip to a tolerance of 1 mm. The trimming saw is a stock commercial cut-off saw equipped with a fine blade and an 12-m long custom cradle. This scintillator strip cradle has a graduated slide to enable a technician to quickly and precisely set the final length of the extrusion.

5.4.7.2 WLS fiber gluing machine

This Section describes the machine which glues WLS fibers and reflective groove covers to the scintillator strips using a commercial glue dispensing system. The operation of the machine in production mode is described in Section 5.4.8.2. Figure 5.27 shows the conceptual design for the gluing machine. The machine performs three completely automated operations on scintillator strips in one pass. It lays a bead of optical glue in the extrusion groove, places a WLS fiber in the glue bead, and lays the reflective extrusion groove cover over the fiber.

The machine requires operator assistance to set up a WLS fiber in an extrusion prior to gluing, and to cut and set the fiber after gluing. The machine transports strips lengthwise underneath three work heads. Scintillator strips, which have already been cut to length, are fed to the gluing machine from preloaded magazines. Magazines are used to provide a continuous supply of strips to the glue machine with minimal operator intervention.

Glued strips coming off the glue machine are placed in a curing rack which contains horizontally indexable shelves, each holding the 20 or 28 strips needed for a single module. After gluing the strips for one module, the operator adjusts the height of the curing rack to bring an empty shelf into alignment with the exit of the gluing machine.

The WLS fiber gluing machine contains five functional modules: a glue dispenser, a WLS fiber unwind stand, a reflective extrusion groove cover unwind stand, an extrusion feed mechanism, and a central programmable logic controller (PLC). In addition, the machine includes three auxiliary modules to perform quality control and inspection functions. The first auxiliary module checks for cracks in the WLS fiber cladding, the second measures the width of the scintillator strip at several points along its length, and the third tests the light output of the scintillator by shining a UV light into the groove and measuring the blue light emitted.

A commercially available glue dispensing system mixes the two parts of the glue in a specially designed disposable dispensing nozzle (replaced after each shift). The glue dispensing system meters the resin and hardener glue components (supplied from five gallon buckets) and is insensitive to variations in viscosity.

The WLS fiber and reflective groove cover unwind stands are equipped with commercially available tension controllers. The PLC matches the length of the glue bead dispensed to the length of the strip being processed. The central PLC controls both the glue dispenser and the unwind stand tension controllers.

Fiber Roll

Tape Roll

Tension Sensors

Glue Dispensing Head

Conveyor Belt
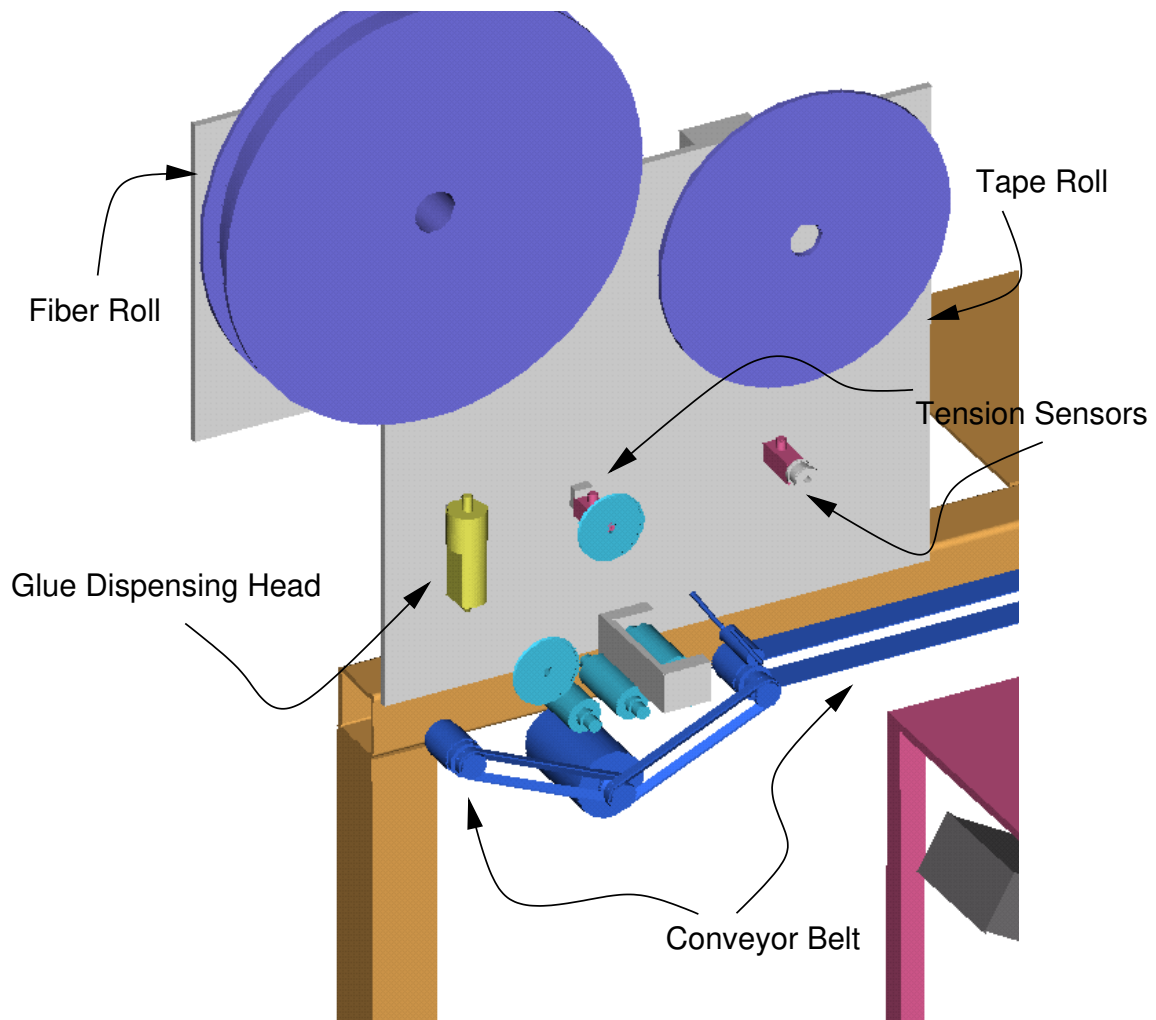
Figure 5.27: Conceptual design for WLS fiber gluing machine.

The curing rack holds the 96 strips required for one shift of assembly. The filled rack is moved to the assembly area when the glue has cured and the extrusions are ready for assembly into modules.

The WLS fiber gluing machine has a special accommodation for strips interrupted by the magnet coil bypass hole. The machine is equipped to glue one continuous WLS fiber across two extrusion sections, each approximately 4 m in length, for these modules. A dummy section of extrusion, matching the free fiber length required to clear the bypass hole, is temporarily placed between the two extrusion sections. The PLC shuts off the glue supply as the dummy section passes beneath the glue dispenser. The dummy section is removed after the glue cures, leaving the correct length of WLS fiber for routing around the bypass hole.

5.4.7.3 Scintillator/fiber gluing templates

The WLS fibers extend for some distance (enough to reach the optical connector) past each end of each scintillator extrusion, so the fiber extensions must be protected during gluing and handling (prior to installation in the module). Each scintillator strip is placed in an aluminum channel which is just large enough to hold the strip. In addition, extra pieces of actual scintillator strip are placed at each end of the strip being worked on. The end pieces are custom-length "tools" which hold the extra fiber (without glue) while the glue in the center strip cures. The entire assembly is run through the glue machine and the end pieces of scintillator are used to determine when to start and stop the glue flow. The fibers are clamped at the outside ends to hold them in place while the glue is curing. The very end of the fiber will be cut off after installation in the module and does not need to be protected.

5.4.7.4 Light case rolling machine

The module factory is equipped with a rolling machine to form the aluminum light case U channels. The machine allows the aluminum sheet for the light cases to be purchased in convenient roll form.

5.4.7.5 Module assembly tables

The module factory is equipped with two equivalent module assembly tables. The tables provide fixturing for technicians to manually assemble modules accurately and efficiently. The module assembly is done in two main stages. In the first stage, a bottom light case is placed on a support tray, scintillator strips placed in it on top of a glue layer, fibers are routed through the end manifolds and potted into connectors, and the top light case put into place on top of a second layer of glue. This assembly is sealed between two sheets of Mylar and evacuated with a mechanical vacuum pump in order to compress it uniformly while the glue sets. Following this, the modules are left overnight to allow the glue to cure completely. The following day, the aluminum case is crimped to produce a light-tight seal, the top manifold cover is installed, the manifold edges are glued, and the connectors are cut and polished.

5.4.7.6 Assembly table glue mixing machine

Substantial quantities of epoxy must be mixed to glue the scintillator strips to the top and bottom U channels of the light case. More epoxy is needed to glue the source calibration tubes to the light case. One automatic glue dispensing machine mixes the glue for both assembly tables. The machine has a mixing nozzle similar to that used on the WLS fiber gluing machine, but it is used only to supply precisely mixed batch lots of glue in disposable containers.

5.4.7.7 Optical connector polishing machine

A portable fly cutting machine is used to face the optical connectors utilized in the end manifolds of each module. Our application requires only minor modifications to the holding fixture of an existing Michigan State University machine to conform to MINOS connectors. The machine consists of a precision electrical motor with a fly cutter attached to its spindle. This assembly is affixed to a dove-tailed linear slide driven by a pneumatic piston. The fly cutter passes at right angles to a tool holder which grips the optical connector.

5.4.7.8 Curing racks

The module factory requires two styles of curing racks. The first holds groups of individual strips after they exit from the WLS fiber gluing machine, as described in Section 5.4.7.2. The second type of curing rack holds up to six trays that support assembled modules while the structural glue is curing.

Two sets of racks are required per shift. One set is filled with newly-glued components fabricated during the shift. The second set has strips or modules which were glued the previous day and are ready for the next steps in assembly.

5.4.7.9 Module mapper

The light yield due to variation in scintillator light output, attenuation length of WLS fibers and features of assembly could vary from batch to batch. Therefore it is important to quantify the response of each scintillator-fiber element within a module following the assembly. This map will be used for future understanding of the module performance and allow rejection of any modules which have poor response features. Furthermore, we will provide the capability to subject modules to a "quick-scan" at the detector sites prior to installation onto steel octagons in order to ensure that no damage has occurred during shipping and handling.

The module mapper is an automated device which consists of a large flat table with a collimated ^{137}Cs source that can be moved quickly to any location over the surface of the module. The response over a predetermined x-y grid will be measured for each module immediately following assembly. The source is located 5 mm above the module's skin. The distance between source and module skin will be controlled by a feedback mechanism.

Drawings of the module mapper are shown in Figures 5.28 and 5.29. The source is driven in two orthogonal directions: the long direction spans the full length of scintillator strips and the short direction spans the module width. The drive mechanism positions the source

TOP VIEW

SIDE VIEW

8m

MN3209
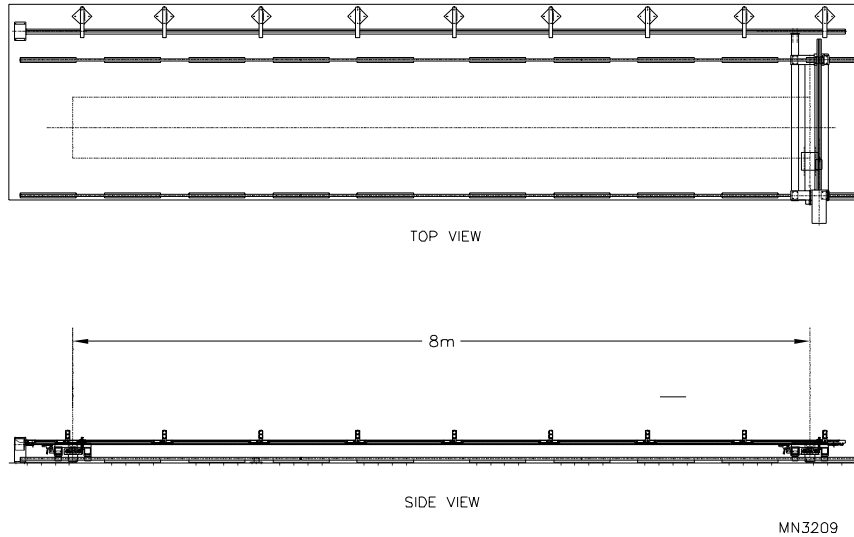
Figure 5.28: The module mapper. The top and side views of an 8 m long scintillator module are shown.

DRIVE MOTOR

Z LEAD SCREW SUPPORT

← X MOTION →

Z LEAD SCREW

SUPPORT RAIL
TYP.

PANEL

SOURCE
CONTAINER

TABLE

END VIEW

MN3208
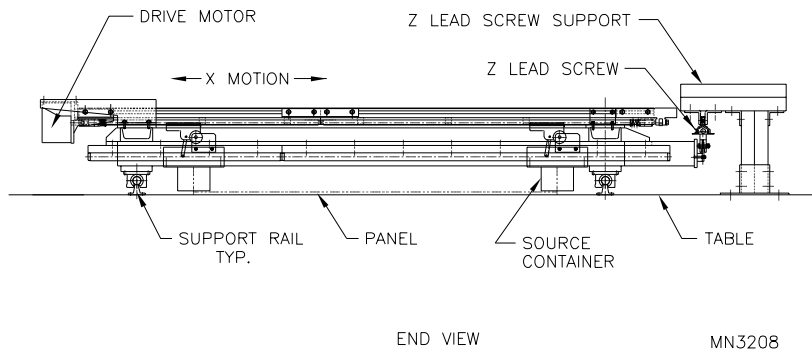
Figure 5.29: End view of mapper shows details of scanning device and the source container at two extreme positions.

with an accuracy of ± 1 mm in the short direction and ± 3 mm in the long direction. Drive speed is 30 cm/s in the long direction and 7.5 cm/s in the short direction.

Calibrated photodetectors are read out by the same processor that controls the source position. The response of each scintillator strip will be measured every 50 cm (or less, if necessary) along its length at the assembly factory. The capability will be provided to perform a quick-scan at the near and far detector sites using the module mapper. This will permit checks of module integrity following shipping as deemed necessary based on experience.

The response maps of each module will be entered in a database. As a cross-calibration, a radioactive source (see Section 5.4.6.3) will be inserted into the calibration tube at each module end and the response recorded in the database. This will permit an easy check that the module performance after installation in the detector is the same as when it was mapped.

5.4.8 Module factories (WBS 2.2.8)

The scintillator modules could be produced at a single production site running two shifts per day. However, we expect that the optimal production scenario will include two factory locations for module production. This permits faster production (and provides some schedule contingency) and efficient use of collaboration resources while keeping costs low. The layout and materials flow plan of the module factory are shown in Figure 5.30. The boxes correspond to the machines described in Section 5.4.7. The arrows indicate the flow of module components between machines. Each factory will have a seven person crew and will produce an average of four modules per shift. Module assembly tests have verified that this is a realistic rate for production. The following Sections describe factory operations in the order indicated in Figure 5.30.

5.4.8.1 Prepare scintillator strips

Scintillator strips are purchased in several lengths and are fine cut on the factory floor. Trimming is especially important for 45° angled modules, where the length of every extrusion in the module is different. During the trimming, the extrusion is visually inspected for any signs of external damage. The trimmed strips are loaded into magazines used to feed the WLS fiber gluing machine. Handling, inspection, trimming, and loading time is estimated at 2 minutes per extrusion.

5.4.8.2 Glue WLS fiber and reflective cover to extrusion

The WLS fiber gluing machine is operated by one technician. The gluing machine is fed by magazines of 20 to 28 strips to reduce the labor of loading each extrusion individually. Furthermore, the magazines help to preserve the order of strips cut to different lengths. Gluing templates with clamps are used to keep the fibers in place during glue curing and while feeding the strip through the machine. These also keep the scintillator piece from moving during the necessary handling. The machine glues the WLS fiber and attaches the reflective groove cover for the length of the extrusion. Once the fiber is glued and clamped, it is rough cut to an appropriate length beyond the end of the strip. The glue machine is also designed to test the quality of the fiber and scintillator strip as each pass through test points, prior to gluing. The average gluing time for each extrusion is estimated at two minutes per extrusion.

5.4.8.3 Prepare light case U channels

The light case U channels are formed from a roll of sheet aluminum using the light case rolling machine described in Section 5.4.7.4. The same machine is used for both the bottom and top U channels. The width of each light case can be adjusted to accommodate different widths of scintillator strips used in each module. The total time required for all operations associated with the rolling machine is estimated at 20 minutes per module. Rolling operations are performed by the same technician that operates the extrusion trimming station.
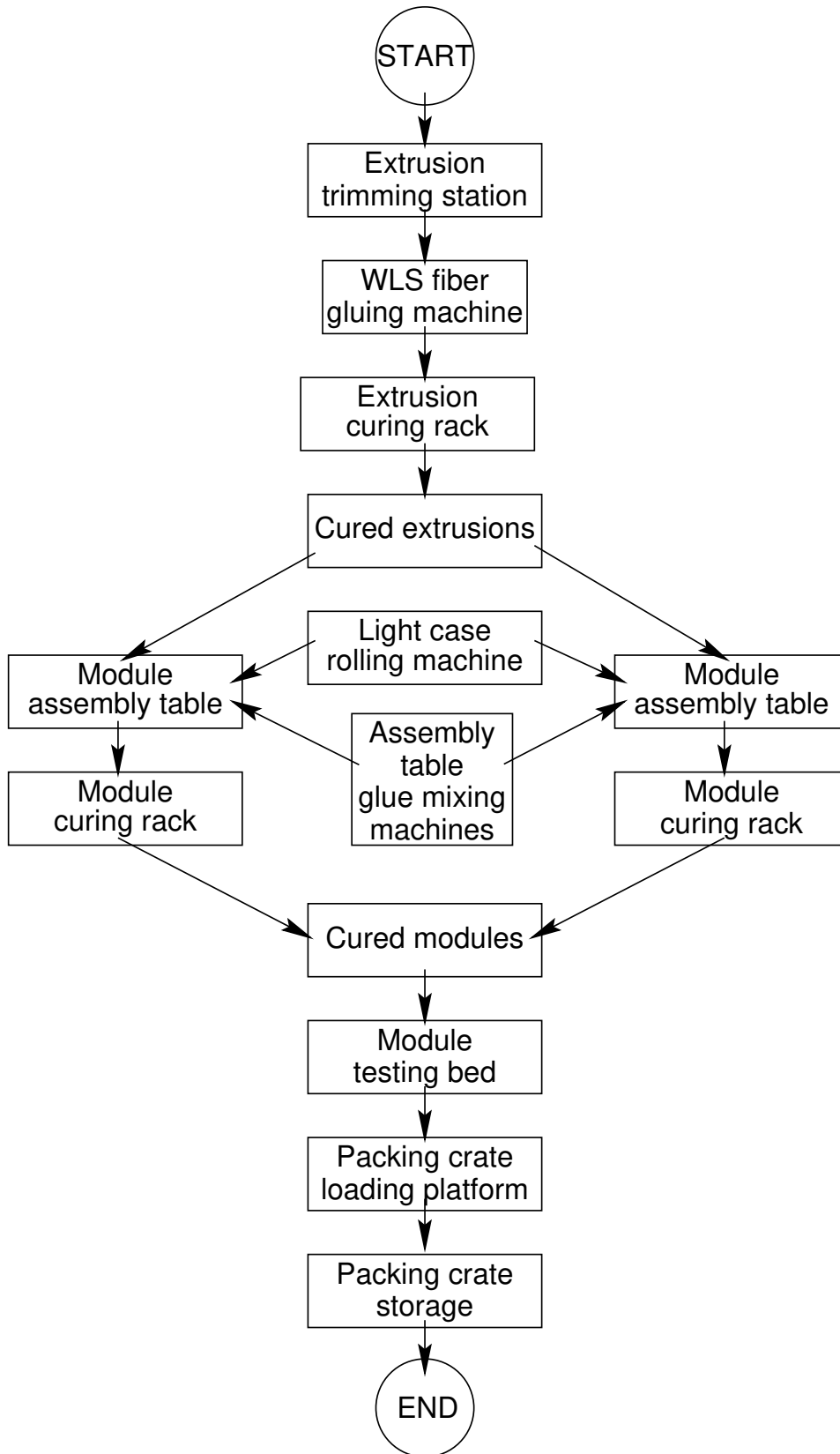
Figure 5.30: Floor plan of equipment layout and materials flow in module factory.
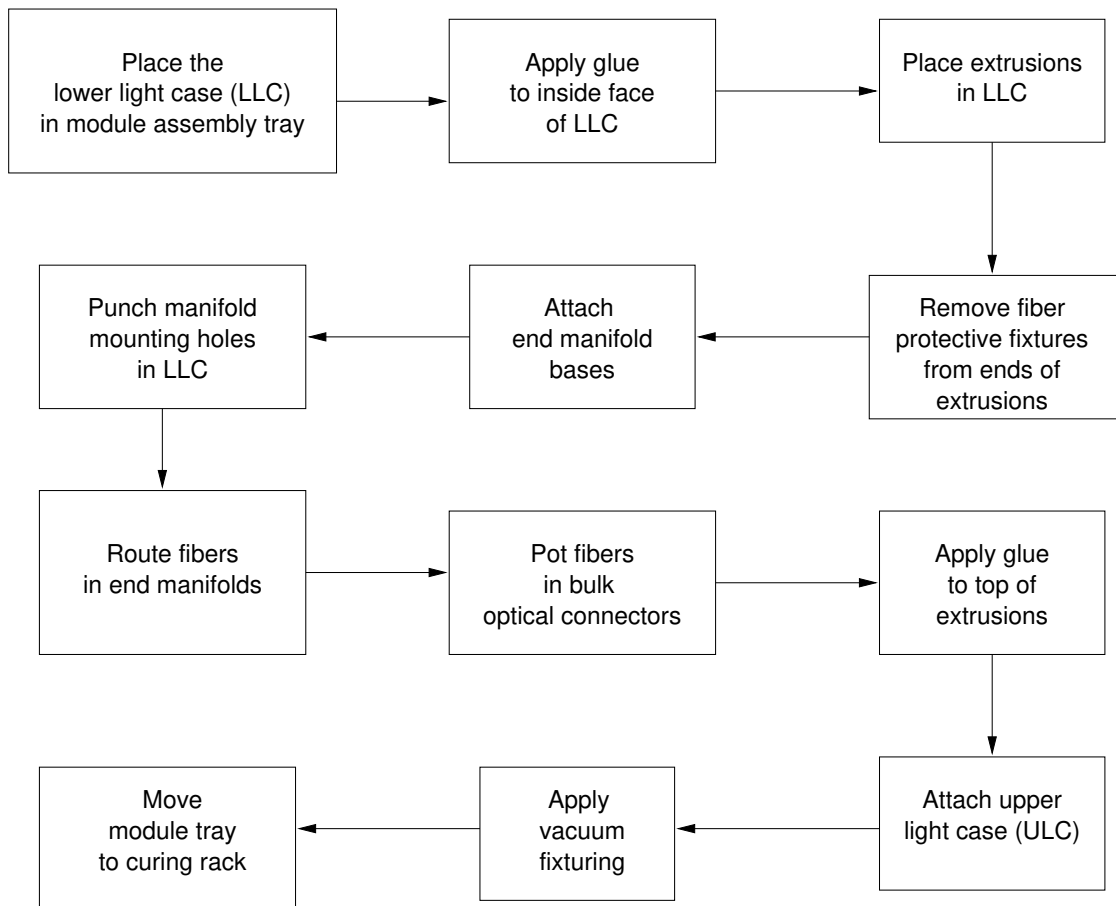
Figure 5.31: Flow chart of module assembly operations performed at the first stage of module assembly.

5.4.8.4 Assemble strips in light case and route fibers

The first step to assemble a complete module is to glue the strips into the aluminum light case and route the WLS fibers in the manifolds to the bulk optical connectors. The module is compressed using a vacuum table while the glue sets, and is then left overnight to allow the glue to cure completely. A flow chart of operations required for this stage is provided in Fig. 5.31. Most operations are self-explanatory. Two technicians are required for the operations in this step. Fibers are routed into the manifold and connector as each strip is layed into the bottom light case. This helps to keep fibers in order and protects them from damage. This step requires about one hour per module.
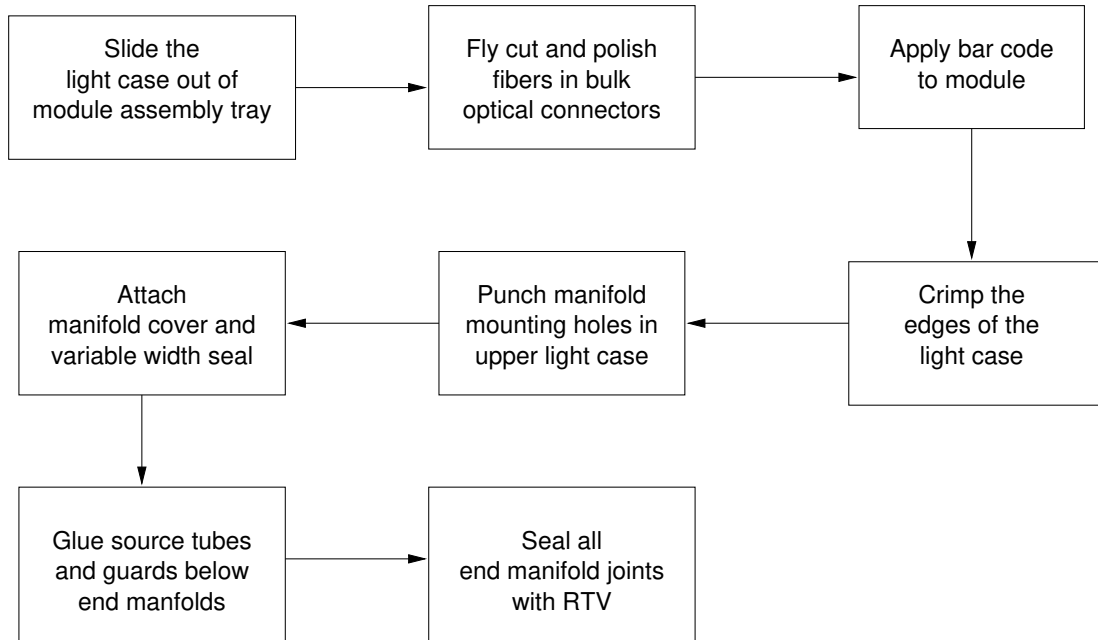
Figure 5.32: Flow chart of operations needed to complete module assembly.

5.4.8.5 Finish module assembly

Once the glue in modules has been allowed to cure overnight, the steps needed to finish the module assembly are done. A flow chart of operations required at this stage is provided in Fig. 5.32. Most operations are self-explanatory.

The portable optical connector polishing machine described in Section 5.4.7.7 is used to face all optical connector plugs in one module. The operations in this step are estimated to require a total of one hour per module

5.4.8.6 Source map module and light-leak check

Completed modules are moved to the source-mapping table for checks for light leaks and mapping with the radioactive source. Light leaks are detected by anomalously high count rates using slightly higher than normal ambient light levels. Any leaks are located using a bright local light and covered. When the module is light tight, the automated mapping machine is started and runs on its own. Each strip of the module is mapped at 50 cm intervals along the length. The computer controls the source location and collects data which are stored for future reference. Finally, the wire source is inserted at each end to establish the light yield response of the module for this source at the time of production.

5.4.8.7 Packing and shipping of modules

Shipping crates will be of a very rigid construction, fabricated from a combination of angle iron, 13 mm diameter steel rods, and plywood sheets. The deflection of the crates when picked up from the ends is approximately 6 mm. Modules are supported in the crate hori-

zontally. It is estimated that the modules can easily handle deflections of up to 25 cm over their length. The total weight of the largest crates and modules is approximately 6,000 lbs. There are two types of crates, one for each module width, with different lengths for near and far detector modules.

The crates will be insulated with 5 cm thick styrofoam which provides cushioning to the modules and insulates them from temperature extremes. It is expected that modules will be fabricated and shipped in temperature controlled conditions. However, during the transfer of crates from temperature controlled trucks to the underground entrance shaft, some crates are likely to be briefly subjected to temperatures as cold as -20° C. The insulated crates will prevent any possibility of damage during this transfer.

A total of 20 crates are needed during peak production and installation times to permit buffering of production and storage of modules at the near and far detector sites awaiting installation. The maximum weight that can be transported on a standard semi-trailer is 40,000 lbs, thus limiting each shipment to six full-size crates. Trucks delivering modules will pick up empty crates for delivery back to the module production factory.

5.4.8.8 MUX box assembly

The MUX boxes for MINOS will be assembled at two sites. These sites will require only a small amount of specialized equipment: a fly cutting machine, a computer controlled LED array and three PMTs for testing the boxes. Other equipment is assumed to exist at established laboratories. The MUX box front plate, chassis, chassis cover, back plate, and PMT cover box will be stamped and formed at a sheet metal shop. The cookie, cookie holder, and PMT holder will be fabricated by computer numerically controlled machines. The PMT jackets will be extruded.

The procedure for assembling the internal components of the MUX boxes includes the following steps:

1. The clear optical fibers are cut and trimmed to size, and then inserted and glued into the connectors.

2. With the aid of the computer controlled LED array, the fibers from the first group of 128 fibers are routed to the first cookie in the box and then glued into place.

3. The lacing pattern is tested using the computer controlled LED array.

4. The connectors and cookie are fly cut and polished.

5. The preceding three steps are repeated for the other two cookies in each box.

Prior to installation, PMTs are fit to PMT-holders and the assemblies are aligned with the cookie holders. The PMTs will be installed at the detector sites to reduce any chance of damage. Once PMTs are installed, the whole readout chain from the optical inputs at the front plate to the signal outputs at the electronics is tested, channel by channel using the programmable LED array.

5.4.9 Management (WBS 2.2.9)

Two of the scintillator system managers are engineers and require salary support for the fraction of time which they spend on management activities. This effort is estimated to be one month per year.

Several managers require travel support for regular interactions with the Fermilab management, other MINOS managers and interaction with the collaboration and vendors. Specific travel allocations have been made for the scintillator Level 2 manager and for the module, assembly equipment and factory managers. In addition, several "generic" trips per year have been allocated for other members of the scintillator management staff.

5.5 Future optimization and engineering

5.5.1 Purpose and goals

The scintillator system described in this Chapter is a complete design which meets the physics requirements specified for MINOS, using demonstrated technology and known costs. However, the engineering of the system, including essential large-scale prototyping, must be completed prior to proceeding with production. The baseline design is now at a stage where fine tuning of components is under way. This fine tuning is aimed at obtaining the best possible light output and at reducing production costs. Some examples of fine-tuning design changes we have already adopted are:

- Scintillator fluor concentration: Our studies have shown that a 0.03% concentration of POPOP gives 10 to 15% more light output than the old baseline of 0.015% POPOP (which had initially been determined from cast samples). The cost impact of this change is minimal and is an excellent value for the gain in light output. Large scale assemblies with strips made with 0.03% POPOP will be built within the next two months.

- "In-line" fluor infusion: We have recently developed a technique for mixing fluors into polystyrene as the scintillator strips are extruded rather than in a separate step. It is estimated that the one-step, or "in-line" process saves about $1M in the production cost of scintillator. We note that this single cost savings is more than all the R&D funds we have spent on the development of the scintillator system to date.

- Fiber diameter: Based on a series of measurements of light collection in our scintillator with different fiber diameters, we have decided that 1.2 mm fiber is optimal for MINOS. This maximizes light output and use of the effective area of the phototube pixels in the Hamamatsu M16 PMT. It is possible that some small additional tuning of the fiber diameter will be optimal for light transmission at connectors.

We note that, during the last year, our "fine tuning" of the baseline design has resulted in about a factor of two increase in light output. We anticipate that there are additional improvements on the order of a few tens of percent to the light output which will be realized in the next few months of additional fine tuning. Examples of such work now under way are

further studies of scintillator production techniques, optimizing the design of the bulk optical connectors, fine tuning of the thickness of the scintillator, optimizing the manifold design and production techniques, and fine tuning of module design and construction techniques. An activity of increasing importance as we head towards production is involvement of industrial suppliers in the production of our components. We are working with potential industrial suppliers to ensure that we will have a cost-effective and reliable supply of components for module assembly.

The schedule for scintillator optimization and engineering is set by the requirement of having modules ready for prompt installation as soon as occupancy in the near and far detector halls permits. We have used the January 2001 date for occupancy of the far detector hall for purposes of planning the schedule for scintillator engineering and startup of production. Our schedule includes the following milestone dates:

- **Nov. 1998:** Lehman Review of baseline design.

- **Oct. 1998 - June 1999:** Fine tuning of detector components. Small modifications to the baseline design such as exact fiber diameter (1.0 to 1.2 mm with or without steps at connectors), thickness of scintillator (1.0 to 1.2 cm), design of connectors and manifolds, etc. will be studied and considered for potential cost savings or improvement in light output.

- **June 1999:** Review light output and modifications to design. Decide all design issues. Start final engineering of design.

- **Nov. 1999:** Final review and approval of engineering design.

- **Dec. 1999:** Place first commercial orders for assembly prototype (at Fermilab).

- **Jan. 2000:** Start factory setup. Produce modules for assembly tests.

- **June 2000:** Place orders for components for first supermodule.

- **Oct. 2000:** Ramp-up production of modules for first supermodule.

- **Dec. 2000:** Two planes of modules at Soudan, ready for installation.

- **Mar. 2001:** Scintillator module production at full rate.

The following activities will be pursued during the engineering and optimization phase:

1. Extruded scintillator production: We will continue to work with both industrial plastics extruders and scintillator manufacturers to improve light output and/or decrease the cost for extruded scintillator. Due to the industrial nature of this process, any iteration in the production technique takes a minimum of 3 months. The optimization includes possible small changes in the geometry of scintillator strips to improve light output and/or collection.

2. Wavelength-shifting fibers: We have found some batch variation in WLS fibers delivered over the last two years, and are working with manufacturers to define testing standards for long fibers in order to improve their quality control.

3. Scintillator module construction: Additional work on engineering and prototyping will be undertaken to ensure understanding of construction issues and to arrive at an optimal design for cost. Full size prototypes are being constructed and tested for light output and mechanical properties. Full-scale planes of scintillator will be assembled on prototype steel octagons and mounted as in the final detector to ensure that all integration issues have been understood.

4. Clear fiber ribbon cables: We must establish production of clear fiber cables which meet the needs for MINOS. We will arrange orders from Mitsubishi and Kuraray and Chinese vendors. An attractive possibility is to have the complete clear-fiber assemblies produced by our IHEP Beijing collaborators.

5. Connectors: We are investigating a custom-built optical connector for MINOS which is based on designs built for other experiments.

6. Photodetectors: The baseline photodetector is the Hamamatsu M16. This device meets all of the technical requirements of the proposed physics measurements, for the cost stated in our baseline documentation[1]. Our future work with this tube will further develop our understanding of tube-to-tube variations in response, in parallel with testing of improved versions of the tube which Hamamatsu is continuously developing. We have performed considerable R&D work to compare the possibility of using an HPD (hybrid photodiode) rather than the M16 PMT. The use of an HPD offers some potential advantages compared to the PMT due to various technical differences, including better intrinsic stability and uniformity of HPD photon response compared to PMTs. We have not identified any sufficiently large advantage of the HPD for MINOS which would justify changing our baseline design. Some work continues on study of the HPD as a possible design contingency to the baseline.

7. Calibration: A complete calibration system has been described for MINOS, based on experience and specific designs used in previous calorimeters. However, there are several aspects of deployment in MINOS where further reductions in cost are possible with additional optimization work.

8. Aging tests: Most detectors built with solid scintillator display a mild drop in light output as a function of time due to yellowing and other aging effects. The light output of the MINOS baseline design is high enough that the sensitivity of physics measurements will not be degraded by such effects. Although the MINOS scintillator design incorporates a number of features which have not been used in earlier experiments, all of the components of our scintillator modules have been used in previous detectors with no significant problems due to aging. However, we must ensure that new features of the MINOS application do not introduce an unacceptable rate of decrease in light output versus time. We have already begun a program of aging tests to demonstrate the long-term stability of all of our components and assemblies.

9. Full-plane prototypes: In order to understand system integration issues we will assemble a series of full-size prototype planes of scintillator, mounted on steel octagons,

and will study these with calibration systems and cosmic rays as part of the 4-plane prototype studies in the New Muon Lab at Fermilab (see Sections 4.4.5 and 7.5.1).

10. Test beams studies: In order to ensure that the full system works as expected, test beam measurements of hadron calorimetric response will be made (see Section 5.5.3).

5.5.2 Aging tests

Long term effects of various stresses on the scintillator strip assemblies are being studied. The aging tests are planned to continue for the next several years to quantify the effects of aging. We have placed fibers, scintillator strips, glue samples and full scintillator/fiber/glue assemblies in several aging conditions including:

- High temperature ($50°C$).

- Cycled temperature ($-30°C$ to $+50°C$ every 4 hours).

- High temperature + high humidity ($50°C$ and 90% relative humidity).

- Mechanical stress (assembled strips bend around a 2.0 m radius).

The main effects have been observed in high temperature and for fibers high humidity as well. Aging in the glue has a negligible effect (due to the thin layers which will be used in MINOS). Aging in both the scintillator and fibers contributes to a slow drop in light output at high temperature. In 8 months of aging at $50°C$ we have observed a drop in light output of about 30 to 35% in complete assemblies. The expected acceleration factor is around 10 (or more) so that this corresponds to about 80 months of aging at normal temperature. We have concluded that we can expect less than a factor of two drop in light output over a period of ten years.

5.5.3 Test beam studies

Should signatures of neutrino oscillations be observed in MINOS, it will be of interest to reduce all systematic errors as much as possible in order to get the best precision in oscillation parameters. In this case, it will be of interest to undertake an expanded effort on test beam measurements beyond that described in Section 5.4.6.4. We anticipate that with such an effort, the systematic uncertainty in the absolute energy scale in the near and far detectors could be reduced to less than 2%. In addition, more detailed information on the topology of showering events in the detector could be obtained. The plan is that the calibration module will be built from modules with connectors identical to those used in the near and far detectors. By simply purchasing additional photodetectors and electronics, it will be possible to instrument the calibration module with the full transverse granularity as in the near and far detectors. This would also help to check for any systematic effects which might arise due to differences in summing of signals between the initial calibration module and the near and far detectors.

In addition to the extra instrumentation, the calibration module could also be magnetized in order to provide a direct measurement of the change in response in this condition. Previous

measurements have shown that the response of hadronic showers can change when the iron is magnetized[20, 21]. To first order, the change can be corrected without a direct measurement.

Finally, it will be possible to move the calibration module to the near and far detector sites. In both locations, data from cosmic ray muons could be collected and compared to ensure a complete understanding of the energy deposition at the two sites. In addition, neutrino events could be measured at the near site and compared to those observed in the near detector target/calorimeter region.

Chapter 5 References

[1] Detailed costs and schedules corresponding to the design described in this Chapter are given by the Fermilab NuMI Project Staff in "NuMI Project Cost and Schedule Plan," October 1998, Fermilab report NuMI-362.

[2] M. Adams et al., Nucl. Instr. Meth. **A366**, 263-277 (1995).

[3] M. Adams et al., Nucl. Instr. Meth. **A378**, 131-142 (1996).

[4] Kuraray Co., Methacrylic Resin Division, 8F, Maruzen Building, 3-10, 2-Chome, Hihonbashi, Chuo-ku, Tokyo, 103-0027, Japan. Kuraray America Inc., 200 Park Avenue, New York, NY 10166.

[5] Quick Plastics, 3530 Wayland Dr., Jackson, MI 49202.

[6] Polycast and Royalite are divisions of Uniroyal. Royalite Thermoplastics 2001 W. Washington St., P.O. Box 1836, South Bend, IN 46634. Polycast Technology Corporation, 70 Carlisle Place, Stamford, CT 06902.

[7] Dow Chemical Company, 2040 Dow Center, Midland, MI 48674.

[8] Chroma Corporation, 3900 Dayton St., McHenry, IL 60050.

[9] Bicron Corp., 12345 Kinsman Road, Newbury, Ohio 44065.

[10] G. Apollinari, P. de Barbaro and M. Mishina, "CDF End Plug Calorimeter Upgrade Project", Fermilab-Conf-94/030-E, CDF note 2432.

[11] M. Chung and S. Margulies, "Aging studies on stressed and unstressed scintillating, wave-shifting and clear fibers," Proceedings of SPIE 2551, 2-9 (1995).

[12] Epon is a trade name for Epoxy resin manufactured by Shell.

[13] Manho Chung, University of Illinois, Chicago, DO Collaboration, private communication.

[14] Hamamatsu Photonics K.K., 325-6, Sunayama-cho, Hamamatsu City, 430, Japan, U.S. Main Office: 360 Foothill Road, P.O. BOX 6910, Bridgewater, NJ 08807-06910.

[15] The HERA-B experiment at DESY is designed to study B meson decays produced by 800 GeV protons striking an internal thin wire target. Two types of photomultipliers are employed by HERA-B ring imaging Cerenkov counter: Hamamatsu R5900U-00-M16 and M4. There are 1500 M16 tubes and 750 M4 tubes used.

[16] CDF collaboration, The CDF II Detector, Technical Design Report, November 1996.

[17] J. Bahr et al., Nucl. Instr. Meth. A330, 103 (1993).
G. Apollinari et al., Nucl. Instr. Meth. A324, 475 (1993).
Yu. Bonushkin et al., Nucl. Instr. Meth. A381, 349 (1996).
M. Lindgren et al., Nucl. Instr. Meth. A387, 53 (1997).

[18] DDK electronics, 3001 Oakmead Village Dr., Santa Clara, CA 95051.

[19] S. Kasahara, Ph.D. thesis, U. Minn (1997).
K. Ruddick, "Underground particle fluxes in the Soudan mine," NuMI-L-210.
R.K. Menon and R. Murthy, Prog. Elem. Part. and C.R. Phys., 9, 162, (1967).

[20] S. Kunori, "B-Field effects on scintillator and calorimetry," VII International Conference on Calorimetry in High Energy Physics, Nov. 1997, Tucson, AZ.

[21] V.V. Abramov, Nucl. Instr. Meth. A374, 34 (1996).

Chapter 6

Electronics, data acquisition and database

6.1 Overview

This Chapter describes the systems which digitize the electrical signals from the photodetectors and select events of interest for mass storage and physics analysis. The database is also described in this chapter. It maintains permanent records of the construction, installation and history of the experiment. It is used by all other subsystems and is essential to the offline data analysis.

In addition to digitizing the signals from the photodetectors, the electronics systems supply the high voltages to the photodetectors and provide monitor and control functions. Information from the monitoring systems is regularly recorded in the database to provide a history of the experiment; faults and errors detected by the monitoring systems are logged to the database as and when they occur. The configuration of the database and the types of information recorded are discussed further in Section 6.4.5. Many of the monitoring functions are provided by processors embedded in the main electronics systems and are described with those systems.

The principal function of the electronics is to digitize and record the signals from the photodetectors; the following steps are involved:

- The time and the charge of each pulse from the photodetectors exceeding a (programmable) threshold of 0.3 photoelectrons is measured and digitized as a hit by the front end units.

- The hit information is time-ordered and passed from the front end units to one of several hub crates.

- The hubs combine the data streams from the front end units and pass them to an interface crate.

- The single interface crate receives all the hub data streams and passes them to the central system and trigger farm.

- The central system and the trigger farm together time-order the entire data stream and divide it into partially overlapping time blocks.

- The processors in the trigger farm examine the data in units of single time blocks and apply a software trigger algorithm to separate the interesting events from noise.

- Finally hits from real events are passed to the `data acquisition system` which provides data storage, run control and user interfaces.
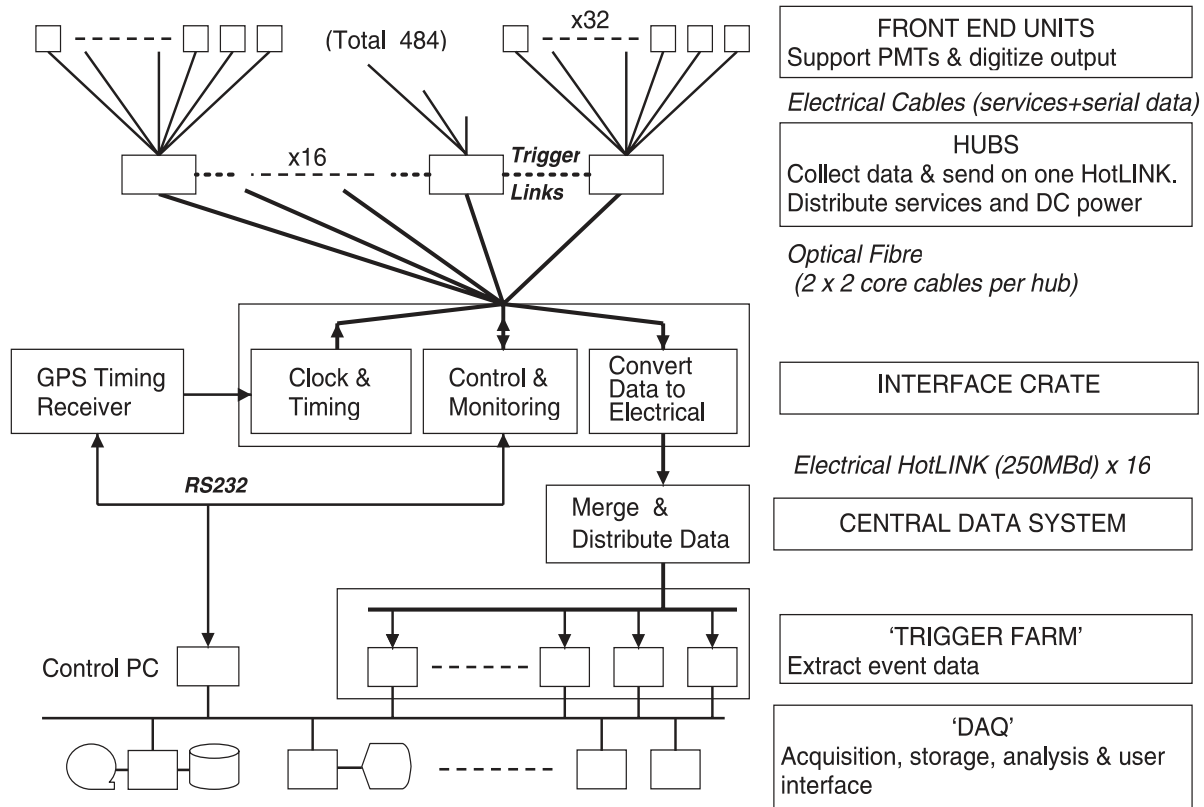
Figure 6.1: Schematic diagram of the principal components and organization of the far detector electronics system.

Figure 6.1 shows the principal components of the far detector electronics system. The near detector system has the same organization but is smaller. The architecture and rate-handling capabilities of the far detector system have been designed to allow the eventual addition of a third supermodule with minimum reorganization.

6.1.1 Physics requirements

The primary physics measurements in the MINOS experiment rely upon the:

1. measurement of the length of events to differentiate between NC and CC neutrino interactions;

2. reconstruction of long muon tracks for momentum measurement by range or magnetic deflection;

3. differentiation between electromagnetic and hadronic showers by their characteristic longitudinal and transverse energy deposition profiles;

4. calorimetric measurement of hadronic and electromagnetic energy; and,

5. recognition of certain simple event topologies characteristic of τ decays.

The provision of timing measurements with sufficient accuracy to determine the direction of a track will allow an extension of the physics capabilities of the far detector to studies of upward-going muons from neutrino interactions in the surrounding rock and atmospheric neutrino interactions in the detector.
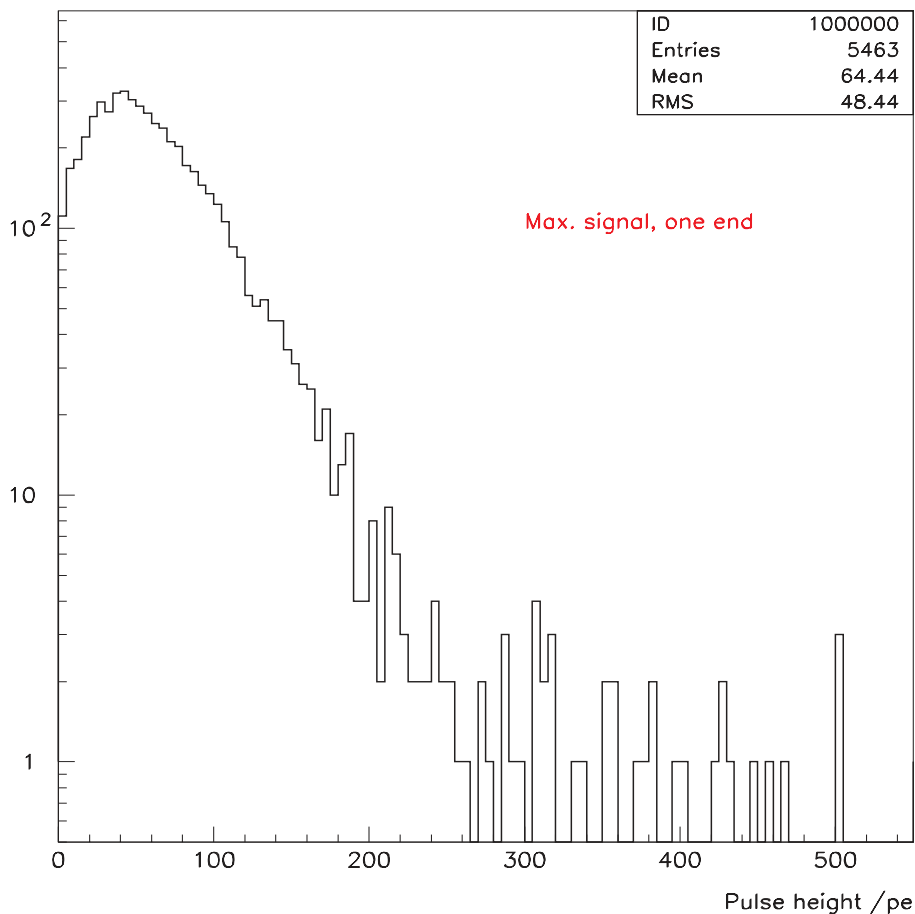
Figure 6.2: Distributions of the maximum pulse heights (in terms of photoelectrons) for interactions of electron neutrinos with the energy spectrum of the highest energy NuMI beam.

The calorimetric energy measurements and the separation of hadronic and electromagnetic showers rely upon the proportionality of light-yield to deposited energy. Figure 6.2 shows distributions of the maximum pulse heights, in terms of photoelectrons, that would

be recorded for electron neutrinos with the same energy spectrum as the muon neutrinos in the highest energy neutrino beam. The maximum signal to be recorded to achieve electromagnetic calorimetry over the entire energy range is equivalent to a 200 – 250 photoelectron signal from the photodetectors. The maximum signal to be recorded by the electronics has been set at the equivalent of 500 photoelectrons for a photodetector channel with normal gain.

Because it is important to maintain high efficiency, the effective thresholds must be set at the equivalent of 0.3 photoelectrons (pe) or less for all channels. The front-end noise must therefore be kept to a small fraction of the single photoelectron signal for a low gain channel. The electronics must have sufficient dynamic range and low noise to handle the maximum signals on normal channels and to resolve the smallest signals of interest from low gain photodetector elements [1].

The event rate of ~150 interactions per 1 ms spill in the entire near detector is relatively high although the interactions are distributed uniformly along the detector. The highest instantaneous single-channel rate will be ~10 kHz and shaping and dead times must therefore be sufficiently short that the pileup of hits and deadtime losses on a single channel are negligible.

The times of hits must be recorded with sufficient accuracy ($< 1 \ \mu s$) to enable events which overlap in one or both views to be resolved using timing information. The ability to flag hits potentially corrupted by pileup from a previous hit on the same channel is desirable, as is the ability to examine the history of the detector for a few microseconds before the time of an event.

Cosmic ray muons will be the main method of cross-calibrating the energy scales of the near and far detectors. It is therefore important that both detectors are able to record cosmic ray muon tracks. The flux of cosmic ray muons at the near detector (~300 Hz)[2] is expected to be ample for this purpose; the relatively low muon flux at the far detector (~1 Hz) means that the detector must be sensitive for a high fraction of real time.

Radioactive sources will be used as a secondary method of calibration and for setting up detector elements, operating conditions and photodetector gains. The electronics must be able to measure and record the DC current from the photodetectors produced by the sources. Current measurement is also a useful diagnostic tool for the detection of faulty channels.

The absolute rate of beam neutrino interactions at the far detector is extremely low (about 1 mHz) and to control possible backgrounds from cosmic ray interactions it is important to associate an event with the 1 ms spill of the Main Injector. This can be achieved by recording the absolute times of events to $\ll 1$ ms and correlating the event time with the times of machine spills recorded at Fermilab.

Since the thresholds must be low to ensure high efficiency, the singles rates in the two detectors will be determined by radioactivity in the cavern rock and in the detector steel, and the dark-counts from the photodetectors which are predominantly at the level of a single photoelectron. The total counting rate above a threshold of 0.3 photoelectrons due to radioactivity is estimated to be 510 kHz for the far detector and 145 kHz for the near detector[3, 4, 5]. The photodetector dark-count rate has been measured to be ~1 Hz per mm^2 of photocathode although it is rather sensitive to temperature. Singles rates are shown in Table 6.1, assuming both the nominal dark-count rates and a worst case of ten times nominal. All the single-channel rates are very low; the higher rates are associated with

Dark count rate per mm² of photocathode	1 Hz	10 Hz
Far detector maximum rate/channel	88 Hz	230 Hz
Far detector typical rate/channel	28 Hz	170 Hz
Far detector rate/plane	900 Hz	4400 Hz
Far detector total rate	0.9 MHz	4.3 MHz
Near detector maximum rate/channel	140 Hz	290 Hz
Near detector typical rate/channel	21 Hz	160 Hz
Near detector rate/plane	3.2 kHz	24 kHz
Near detector total rate	320 kHz	2.4 MHz

Table 6.1: Expected singles rates in the MINOS detectors due to radioactivity and photocathode dark counts for a threshold which detects 1 photoelectron. 8-fold optical multiplexing is assumed for the per-channel rates.

channels connected to strips at the outside of the detector. Because of the large number of channels the overall total rates are high. Since there is still some uncertainty about the dark-count rates, the electronics has been designed to handle a maximum rate of 20 Mhit/s for the far detector (distributed over three supermodules) and 10 Mhit/s for the near detector, a safety factor of four over the worst-case rates. The design of the back-end of the system can easily be scaled down, with a consequent saving in cost if the rates prove to be less.

An important consideration in the design of the electronics for the far detector is that the power dissipation is limited by the cooling power planned for the Soudan cavern. The design described here is conservative and the power consumption has been kept low (< 25 kW), with the consequent constraint on the speed of the electronics.

Because the experiment will rely upon a detailed comparison of the characteristics of events recorded in the near and far detectors the same electronics will be used for both detectors.

6.1.2   Architecture

The electronics uses a simple continuously-sensitive readout architecture. The times and amplitudes of all signals from the photodetectors above a pre-set threshold are digitized, 'stamped' with real-time and sent to processors in a 'trigger farm' where a software trigger is implemented. The trigger algorithms which have been studied select events by correlating hits first in time and then space. The use of processors, rather than a hardware trigger, allows great flexibility and event selections could, for example, be made based on the pulse height of hits. The event selected by the processors are then passed on to the data acquisition system for any further analysis or selection and subsequent mass storage.

Such a triggerless readout scheme has the advantage that a large degree of flexibility is retained for the eventual event selection algorithm and does not require the complexities of programmable trigger logic or the distribution of fast trigger signals over a physically large distance. Data links with the necessary bandwidth and the processors necessary to implement such a triggerless system are currently available commercially. They are relatively

Component	Near detector	Far detector	Total	
Front end units	212	484	696	One per 48 photodetector pixels
Hub crates	7	16	23	
Interface crate	1	1	2	
Central system crates	3	4	7	
Trigger farm crate	1	1	2	
Trigger processors	≤ 5	≤ 10	≤ 15	Minimum of one at each detector site; 10 is maximum required for a 20 MHz singles rate distributed over three supermodules
GPS timing systems	2	1	3	One to record real time of MI beam extraction at Fermilab

Table 6.2: Component numbers for the MINOS electronics systems for the two detectors.

inexpensive and since this is a rapidly developing area of technology it is likely that future commercial developments will reduce costs in the next few years.

The principal components of the electronics system are shown in Figure 6.1. They are:

1. front end units;

2. hub crates;

3. interface crate;

4. trigger farm hardware;

5. trigger farm and event selection software and,

6. GPS timing system.

The numbers of each component are given in Table 6.2; their functions are now described in detail.

6.1.3 Front end units

A front end unit is a self-contained, screened assembly which houses the electronics to digitize the signals from three 16-channel PMTs, as well as control and monitoring electronics, and power supplies. Thirty two front end units are connected to a hub crate, each by a single cable which provides power, timing and control, and carries the digitized output data in serial form.

The electronics for each channel provides amplification and pulse shaping, with a discriminator controlling a track-and-hold to store the peak of the pulse. As each pulse is detected its time is recorded, and it is entered in a queue to have its peak value digitized. The outputs of 16 channels are multiplexed on to a single ADC which digitizes the stored peaks, taking them in order of their arrival.

One 16-channel sub-assembly serves one 16-channel PMT. Three such sub-units are included in each front end unit. Each outputs data on any pulses at its inputs as a time-ordered stream. The shared part of the front end unit electronics merges these three streams into one, also time ordered, and outputs it over a serial link. The data transmitted for each hit consists of the channel address, the time stamp, the pulse amplitude and status flags which indicate the origin of the hit (data, pedestal, calibration) and possible corruption by pileup.

Other parts of the front end electronics provide essential support functions:

- Calibration: charge injection and phototube current measurement.

- Control and monitoring: make settings and report operating conditions.

- Clock and timing: provide synchronization with the central system.

- Power supply: convert and regulate supplies; supply HV to the photodetectors.

A major consideration in the design has been the need for immunity to electromagnetic interference (e.g., from the welding while detector planes are being assembled). This is especially true because of the wide dynamic range being called for, and the need to detect single photoelectrons. The signals from the photodetectors are low level signals. Inclusion of the photodetectors and all their associated low level electronics in a single well-screened box is of major importance. So too is connection through a single electrical cable, with a consequent absence of ground loops. Potential sources of noise and the strategy to reduce or eliminate them are further discussed in Section 6.1.9

A second important design feature is ease of maintenance. Packaging a set of detectors and their electronics as a single easily exchanged unit is advantageous. A possible bad channel needs only the one unit to be replaced with a new one which has been given a complete functional test in the lab. It is also relatively easy to make such a unit so it can be 'hot swapped' (safely exchanged without powering down any of the system or affecting its operation).

A constraint on the design of the front end units has been the ultimate limitation on power imposed by the problem of cooling the far detector cavern, the need to avoid unduly heating the photocathodes, the desirability of not introducing the further cost and complication of an elaborate cooling system for the electronics and the possibility of future detector upgrades such as a change in the degree of optical multiplexing. The total power dissipation of the far detector electronics has therefore been assumed to be limited to 25 kW for an eventual detector composed of three supermodules with four-fold optical multiplexing. Assuming 16 kW is available for the front end units (leaving 9 kW for the hubs, computers, and ancillary electronics), if the efficiency of the power supplies and distribution is 75% (after any local conversion and regulation) 4 kW is available for the front end units of each supermodule. Allowance for future expansion to three supermodules with optical multiplexing reduced to

four-fold therefore requires a maximum of 170 mW/channel; 200 mW/channel is regarded as the maximum tolerable power dissipation. The present design complies with these figures, including the allowance for possible future expansion. Power dissipation in each front end unit is ~10 W including losses in local regulation.

Each front end unit will serve three 16-channel Hamamatsu PMTs, giving a total of 48 channels per unit. This is a compromise between sharing the overheads (monitoring, power supplies, cables and connectors, and mechanics) over an adequate number of channels, without requiring an inconveniently large number of fibers to be concentrated into a single unit. It is also well matched to the far detector, with one unit serving one end of two planes.

The design of the amplitude digitization system is based on shaping the signal with a ~400 ns peaking time (which determines the extent of pileup errors), and a worst case dead time of 6 μs for the last channel to be read after all channels in a group of 16 have been hit simultaneously. These times have been chosen to give a similar effective speed to that possible in a simple triggered system. (Any such system, which does not pipeline the signals in analog form or after unconditional fast digitization, would be limited by the physical extent of the far detector.)

The dynamic range of the ADC system is nominally 14-bit, with full scale corresponding to 500 photoelectrons on high gain pixels. Assuming a 2.5:1 gain spread between pixels and no individual channel trimming, the 1 pe peak from a low gain pixel lies at 13 counts above the pedestal. This is comfortably good resolution. A true 14-bit system might be expected to have a noise level lower than the quantization noise from the ADC, i.e. ≤ 0.3 counts rms. This is clearly not needed for MINOS, especially as detection of pulses is by a hardware discriminator not the ADC. Around 1 count rms noise from the ADC is good enough. Hence, the design is only nominally 14-bit.

The A-D conversion accuracy required is modest: 5% over most of the range. Around 1% is, however, desirable for calibration purposes, which needs some provision for averaging out ADC non-linearities at the low end of the range.

It is crucial to achieve low noise at the discriminator since it is required to detect single photoelectron signals efficiently but not to trigger at an excessively high rate on electronic noise. The finite width (~100% FWHM) of the 1 pe pulse height distribution from the PMTs means that the discriminator threshold must be set at the equivalent of 0.3 – 0.5 pe for efficient detection of single photoelectrons. The rate that the discriminator fires on electronics noise must be much less than the dark count rate of ~1 Hz. The rms noise at the discriminator must therefore be the equivalent of ~1 ADC count to give a low enough noise background rate for the lowest gain pixels.

The timing capability of the detector is ultimately limited by the scintillator and wavelength shifting fiber to around 10 ns rms when a single photoelectron is detected although this improves for larger pulses. A timing resolution of ~2 ns rms has been demonstrated for signals of > 10 photoelectrons. These factors guide the design of the signal channel up to the discriminator output. While the PMTs are very fast, making the electronics to match conflicts with the need for a wide dynamic range, low power consumption and moderate cost. The present design is conservative and it is expected that it can be improved. There will be variation between channels, due to component variations, of up to 15 ns from the mean. This will be stable and easily corrected using the calibration system. There will also

be some dependence on pulse height; total 'timing walk' should be under 10 ns, and could be corrected offline when maximum accuracy is needed. Time is measured on each channel in units of 5 ns which seems the best that can be assured if Field Programmable Gate Arrays (FPGAs) are used; further work, and faster devices, may better this.

The data transfer rate from a front end unit will be ~50 khits/s, which is much lower than the peak rate at which it can digitize. This rate is also higher than the average rate per unit of 28 khits/s derived from the very conservative system design criterion of 20 Mbits/s for the whole far detector. The peak rate from the near detector will be high during spills with around 250 hits expected from a unit in one spill. Sufficient buffering is provided to smooth out these bursts of data.

6.1.4 Hubs and interface crate

The hubs provide front end units with DC power, system-wide clock and timing, and connection to the control and monitoring system. The data are passed via the interface crate to the trigger farm. For convenience and economy the data are multiplexed into a single serial stream.

Hubs are placed relatively close to the front end units. Each hub serves up to 32 front end units and is connected by a small number of fiber optic links to a single interface crate, providing a single point of connection to the whole system.

The interface crate connects to a GPS timing receiver, which is the source of clock and timing, and also to the computer which manages the control and monitoring. The interface crate outputs the data from all the front end units into the central trigger farm and data handling system. A particular consideration in selecting this organization is to limit the effect of faults, and to permit their easy localization and repair. It also complies with the requirement to avoid ground loops and their risk of introducing interference.

Data rates. The data rate is assumed to be distributed evenly across the hubs. Each hit will be represented by 6 bytes of data, the time stamp and the channel number both being extended later in the central system to give 8 bytes of data per hit. The link from front end unit to hub must handle 165 kByte/s (or, since it is serial, 1.3 Mbit/s). Serial operation at about 2.5 MHz allows a comfortable margin while at the same time limiting the rate possible from a malfunctioning front end unit so that the system cannot be overloaded. Each hub must be able to send 5 MByte/s of data to the interface crate. The links chosen are capable of 25 MByte/s, giving an ample margin.

The near detector system is designed for the same rate from each front end unit as the far detector. The figure is actually slightly higher, as there is more of a contribution from real events, but the difference is not significant. The same system is thus adequate, with a smaller number of front end units, and the number of hubs reduced proportionately from the far detector.

Control and monitoring. The system provides control and monitoring connections to the front end units. The performance requirements for this are minimal; only low speed is

required. Simplicity of development, ease of fault-finding, and ability to operate without interacting with data taking, are more important criteria.

For this reason control and monitoring is based on 'RS232' type serial links, communicating with microcontrollers in various units throughout the system. Those in the hubs provide for local control and monitoring, and by means of address commands, communications with those in the front ends. The system is entirely independent of the timing and data systems. The monitoring in the front end units also provides a readout of the PMT integrated current which is used for radioactive source calibrations.

6.1.5 Central data system and trigger farm

The purpose of the central data system is to receive data from the front end units (via the interface crate) and to present it to processors in the trigger farm for the selection of events of interest by a software trigger algorithm. The data from the front end units consist of a series of short hit records, one for each digitized photodetector pulse. Each hit record consists of a channel address, a time stamp, the pulse amplitude and status flags. The time stamps are used to sort the stream of hit records from all detector channels into a single time-blocked and time-ordered data stream which is passed to the trigger farm processors.

The nominal hit rate from all sources is ~ 1 Mhit/s but, since there are still some uncertainties associated with the photodetector dark-count rate, the system is very conservatively designed to handle an absolute maximum rate of 20 Mhit/s which also allows for the addition of a third supermodule and a reduction in the degree of optical multiplexing.

The interface crate and the central data system will be adjacent. The serial links between these crates will use short twisted-pair electrical cables. Each link carries a stream of data from a single hub, serving 32 front end units, with each front end unit being uniquely identified in the outgoing data stream.

The architecture of the central data system has been designed to support an eventual three supermodule detector. It is shown in Figure 6.3. It consists of up to six VME crates (3 at the near detector) containing receiver cards and sorter cards. The receiver cards receive data from the interface crate on up to 24 serial links (7 at the near detector). Only four VME crates and 16 serial links are required for two supermodules. The hit data from each link is unpacked into 32 separate data blocks, corresponding to the front end units served by one support module. The receiver card then extends and completes the channel number and time stamp information received from the front end units into 8 bytes of hit information.

The sorter card comprises a VME single-board computer whose function is to assemble the data from the receiver cards into time-ordered trigger time blocks and pass the time-blocked data to the trigger farm.

The output of this VME system is connected to the trigger farm by two 132 Mbyte/s networks. The data rate on each network is not expected to exceed 80 Mbyte/s, leaving considerable reserve capacity over the already conservative design rate. The trigger farm and the central system communicate through the control network which is of the same type as the data network.

Two time block lengths will be used. In the receiver card input stage, the 'front end' time blocks are matched to the front end time-stamp counter wrap-around period of 1.3 ms (18 bits with 5 ns resolution). In the receiver card output stage the front end time blocks
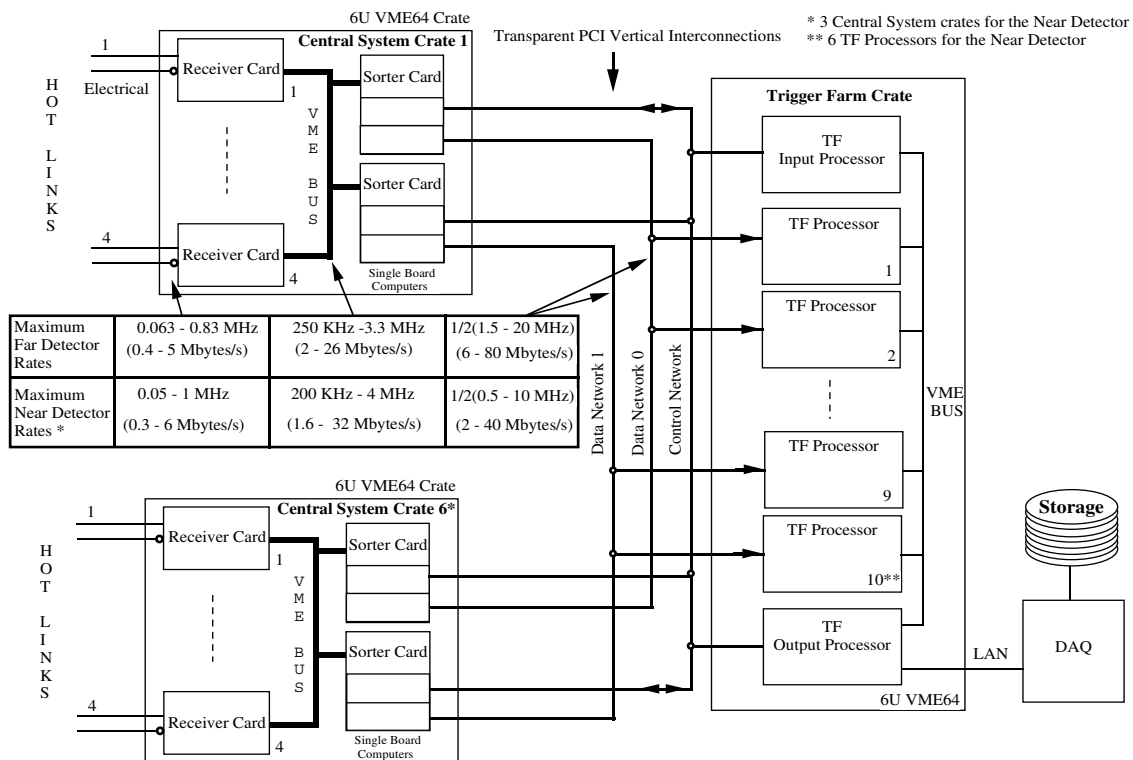
Figure 6.3: Central data system and trigger farm organization.

are assembled in sequence to form 'trigger' time blocks. The amount of memory allocated to the trigger time blocks is sufficient to contain the hits from 38 front end time blocks (50 ms) at the highest data rate. These trigger time blocks are then used by all subsequent stages in the system. The number of front end time blocks merged to form a trigger time block will be variable, controlled by software, to give flexibility in varying the average amount of data in the trigger time block in order to optimize system efficiency. Adjacent trigger time blocks will overlap by the period of one front end time block to ensure that there is no inefficiency for events straddling the boundary of blocks. Trigger time blocks are passed over the two data networks to the trigger farm, alternating odd and even numbered blocks.

Processing in the trigger farm is divided into two stages. The first stage is to merge-sort each set of trigger time blocks from the central system crates into a single block of time ordered hits. In the second stage a software trigger is applied to the time ordered data to select events of interest and pass them on to the DAQ system.

The trigger farm consists of a VME crate containing VME single-board computers with dual PCI Mezzanine Cards (PMC) slots for processing and sequencing. Additionally there are high performance PMC based network cards for data transfer. Two single board computers, the input processor and output processor, are dedicated to sequencing. The trigger processing is run on an array of single board computers (trigger farm processors) with a maximum capacity of up to 18 in the crate, although it is anticipated that no more than 10 such processors will be necessary.

Three networks are used between the central system and the trigger crate. The control network allows the farm input processor to identify the time blocks in the sorter cards and

sequence their transfer to allocated processors in the farm. The two remaining networks are used to transfer the data between the central system and the trigger farm. The data networks perform only one-directional block transfers which keeps the transfers efficient. The control network is random access which is less efficient but runs at the rate of the time blocks which is much lower.

The control network connects the input processor to each sorter card. The input processor uses the control network to determine when central system time blocks are available, where they are located in the sorter card's memory and to signal to the sorter cards when the time block data has been transferred to the farm. The data networks are used to transfer time blocks from the sorter cards to the farm trigger processors under the control of the input processor.

The farm trigger processors are divided into two equal groups, one for each of the two data networks. Each data network and trigger farm processor group handles either odd or even time blocks. The trigger farm receives time blocks for the same time period from the central system which are processed by the first free processor available within the appropriate odd or even trigger farm processor group. The input processor is responsible for coordinating the assignment and transfer of time blocks from the sorter cards to the farm processor groups. The output processor is responsible for coordinating the transfer of processed time blocks to the DAQ system. The output processor buffers and reassembles processed time blocks back into strict time order before sending them on to the DAQ system.

6.1.6   Trigger farm and event selection software

The functions of the software running in the trigger farm include:

- data transfer and scheduling software for the input processor;

- triggering software and trigger efficiency monitoring in the trigger processors;

- event collection, sorting and monitoring in the output processor;

- control and data transfer software for the interface to the DAQ system, and

- error detection and recovery.

The event selection (trigger) software is based on time-ordered blocks of data; a block of data (a trigger time block) is DMA transferred to a free processor in the trigger farm under the control of the input processor. These blocks are time synchronized and represent a complete time section of readout from the detector. The input processor ensures that no triggers are lost due to boundary effects by overlapping the time sections passed to the trigger processors; any identical triggers created by this overlap are identified and eliminated by the output processor. The length of the trigger time blocks into which the data are divided is programmable and will be at least 50 ms (depending on the actual singles rate); the blocks will overlap by 1.3 ms. The task of a trigger processor is to:

1. merge the blocks of data into a single time-ordered stream;

2. perform some basic monitoring of raw singles rates (more sophisticated monitoring using triggered events will be performed in the output processor and/or the data acquisition processor);

3. identify events within this time block of hits by applying a trigger algorithm;

4. pass triggered events to the trigger farm output processor for sorting and passing to the data acquisition system and

5. inform the control processor that it is free to accept another block of data.

The trigger algorithm must reduce the data rate into the data acquisition system by removing noise and background from the data stream in real time with minimal loss of events of physics interest. The dominant source of background in the data stream is expected to be the singles rate from radioactivity and photocathode noise, both of which should be relatively easily discriminated from physics events. Three types of information can be used to achieve this:

1. Time structure. Physics events will contain hits that are strongly correlated in time, i.e., the hits will occur within a narrow time gate defined by the propagation time of tracks through the detector and light propagation time in the scintillator.

2. Spatial structure. Physics events will contain spatially clustered and/or contiguously strung hits (showers/tracks) that span a number of detector planes.

3. Pulse height. Photocathode noise will have a lower pulse height (1 pe) than hits from a minimum ionizing particle. Imposing a threshold cut on hits allowed to contribute to the trigger could be a fast and powerful discriminant against this noise. However, in order to maintain independence of design parameters such as phototube gains and scintillator light yield at this stage, no use is made of pulse height in the trigger algorithm described here although a trigger based on summed pulse height could easily be implemented in the trigger processors and OR'ed with other triggers such as the one described below.

Since the trigger processors are required to operate in real time, a simple and fast trigger algorithm is required. The algorithm operates in two stages:

Level 0. A search is made through the readout in time order until a minimum of 3 hits are found to occur within any 50 ns window. This window is wide enough to accommodate expected fluctuations in the relative times of hits before the final timing calibration is applied. Simulation studies of neutrino events in the detector have shown that losses to neutrino events from this requirement are less than 0.5%; these losses consist entirely of neutral current events with very few hits. If this condition is satisfied the second, more stringent, level 1 criterion is tested.

Level 1. Require that at least M planes out of any group of N contiguous planes of the detector have at least one channel hit in the 250 ns following the earliest hit in the above 50 ns gate. A 250 ns window is chosen here as a conservative event size. If the M/N condition is not satisfied the trigger search continues where it left off in level 0. If the condition is satisfied an event trigger is generated and the event is passed to the farm output processor.

At this stage an event is defined as all hits contained within the 250 ns window plus any hits that occurred in a preceding (programmable) time window of T μs. Such a detector history allows the possibility that the event has been corrupted by pileup, or that hits have been lost due to single-channel deadtime, to be assessed. Although this means that the first T μs and last 250 ns of each trigger time block would not be scanned for a trigger, since it could not provide the full readout time span, this generates no trigger inefficiency since the 1.3 ms overlap ensures that triggers in these time regions are found in the preceding or following buffer by another processor. The performance of the trigger algorithm presented here has been timed with a trigger scan of these regions included.

Studies, using the simulation software described in Section 9.2, have shown that this 2-level trigger with $M = 4$ and $N = 5$ excludes a negligible fraction of charged current neutrino events and around 11% of neutral current events, these being events with very few detector hits. Changes to the (level 1) M out of N plane trigger are trivial to implement in this scheme and have no significant impact on the algorithm timings. For example if, following further trigger studies, the 4/5 plane trigger used here were required to be a 3/5, 4/6, ... plane trigger to accept a higher fraction of neutral current events, it could be accommodated easily. The first three columns of Table 6.3 show the level 0 and level 1 noise trigger rates for a 3/5 plane trigger and 4/5 plane trigger as a function of the detector singles rate (assumed to be distributed over three supermodules). There is no difference in processing requirements for the different trigger configurations.

Monitoring of the pre-trigger singles rates will be performed in the trigger processor farm on a channel basis. Channel rates exceeding an acceptable threshold will be transmitted to the output processor and thence on to the online system which will take the appropriate action. Simple monitoring of this kind has very little impact on the processing power required in the farm which is dominated by the data merging and trigger decision.

Prototype trigger processing code for the above algorithm was written in C to estimate the maximum number of processors the trigger farm will require to keep pace with potential noise rates. Noise data, including an assumed 5 kHz double-Compton rate from radioactive decays, were generated at a number of rates up to and including a worst case of 20 MHz. Timing tests were performed on a 300 MHz ALPHA RISC processor (Alpha Server 1000A 5/300, Alpha 21164 chip). The results are shown in Table 6.3. The timings include the histogramming of raw channel singles rates for channel monitoring.

The processing requirements are well within practical limits. Faster processors than a 300 MHz Alpha are available today and improvement in processor speed is likely over the next few years; the provision of sufficient processing power in the trigger farm is not expected to be a problem.

Triggered events are passed to the output processor when they are identified by the trigger processors. They can arrive out of chronological order by an amount defined by the

Singles Rate (MHz)	Trigger Rate (Level 0, kHz)	Trigger Rate (Level 1, Hz) 3/5 planes	Trigger Rate (Level 1, Hz) 4/5 planes	Max Processors
2	4	6	< 1	1
6	70	26	< 1	3
10	290	130	< 1	5
16	1100	750	< 3	8
20	2000	1500	< 5	10

Table 6.3: Trigger rates and processor requirements of the trigger farm. The processing power estimates were obtained using an Alpha Server 1000A 5/300, Alpha 21164 chip processor.

maximum length of time it takes a processor to trigger-analyze one trigger time block. In addition, because trigger time blocks overlap, some events will be found twice. The output processor is required to buffer the events it receives in a rolling buffer, time order them and remove or merge (as appropriate) event duplicates and overlaps before passing them on to the DAQ system.

The event rate to the output processor from beam and cosmic ray muon events will be relatively low. In the far detector the event rate will be dominated by around 1 Hz of cosmic ray muon events (2.4 kByte/s uncompressed). The near detector rate is more complex but will average at approximately 16 Hz of neutrino interactions, 8 Hz muons from ν interactions upstream of the target region and up to 270 Hz cosmic ray muons (virtually all out of spill), giving a total rate of just under 300 Hz equivalent to a data rate of about 240 kByte/s uncompressed. Cosmic ray muon events are essential for cross-calibration of the near and far detectors; the cosmic muon rate at the near detector is quite high and can be reduced by randomly vetoing out-of-spill triggers as part of the near detector trigger algorithm.

6.1.7 GPS timing system

For the analysis of the data it is necessary to know whether events occurred during the 1 ms period of a beam spill. Because of the remote location of the far detector the most practical way to determine this is to log the absolute times of events and spills, and correlate these offline. Each event will therefore be stamped with the real time obtained from the GPS clock.

The clock and timing of the entire system is derived from a GPS timing receiver connected to the interface crate. It is assumed to provide a 10 MHz clock, and 1 Hz pulse outputs, with an RS232 interface for status and time of day information. These two signals are multiplexed into a single signal suitable for distribution to the hubs over a single optical fiber. There they are converted to electrical signals, reformatted, and fanned out to the front end units. Conversion to a different clock frequency is made with Phase Locked Loop (PLL) clock multiplier chips. The design has to maintain minimum timing skew between front end units and therefore requires fast fiber optic transceivers, and ECL electrical transmission (with transformer coupling for common mode noise immunity). It will be easy to check the

equality of fiber lengths using optical time domain reflectometry (TDR) from the interface crate; this might be desirable after repair or replacement. The short hub-to-front-end cables can reasonably be assumed to be constructed to equal length. The electrical propagation delays cannot be so easily checked after installation; the best way to ensure they are nearly equal will be to keep them short.

Interface Crate and Central System

Hubs

Front End Units (groups of 8)
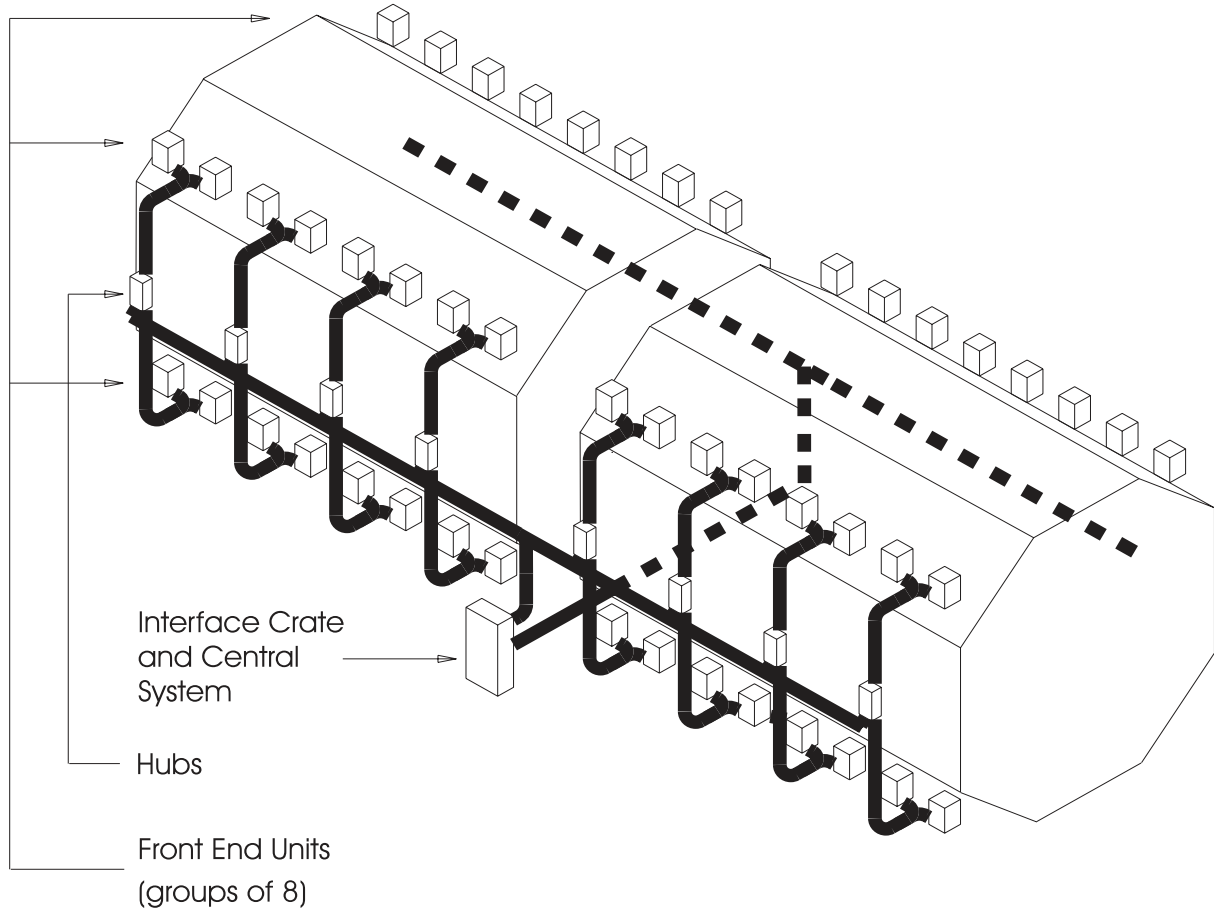
Figure 6.4: Layout of the electronics on the MINOS far detector.

6.1.8   Locations of the electronics components

The physical layout of the electronics for the far detector is shown in Figure 6.4. The front end units are arranged evenly along the length of the far detector, half on each side in two rows along the upper and lower corners. Each side is served by a single row of hubs at an intermediate height. The hubs are spaced about 3.5 m apart, with their front end units 4 to 5 m away. All hub-to-front-end cables are equal in length for equal clock propagation delay. Each hub serves up to 32 front end units, grouped as eight multiplexer box assemblies, two in each row. Some hubs will have slightly fewer units connected to maintain independence between supermodules.

The interface crate is placed in a central position along the detector. It is connected to each hub with fiber optic cables, again of equal length for equal delay. These cables will be

about 40 m long, depending on details of the installation. Excess length can be coiled up, or looped back in the trunking. Each hub has two cables, but they are slender (6 mm × 3 mm) and light: the total weight of each is under 1 kg.

The interface crate outputs one serial data link for each hub to the the central system. The central system crates and trigger farm crate will be housed in two enclosed racks adjacent to the interface crate.

The hubs will be installed on the lower walkway along each side of the far detector. The electrical cables from each hub to its front end units will run in bundles vertically, up and down, before fanning out. Each bundle of 16, assuming a 7 mm diameter, would be about 33 mm overall diameter. Support is required, in the form of trunking, or channel to which they can be tied.

The fiber optic cabling between the hubs and interface crate will run in trunking (or trays) along the length of the detector, and across the far (south) end. The interface crate and the central data system will be at that end on the same level. Fiber cabling is assumed to be with two core 'zip' type cable, as commonly used for patch cords. Individual cables are small and light, and can be factory terminated. They can then be unrolled into the trunking. A 30 mm bend radius is acceptable, so they can be looped back in 75 mm square trunking. Open cable trays might be used, but give less protection. The bulk of the fiber cabling is quite small: the cables along one side of the detector would form a bundle ~20 mm diameter. Excess length will be lost as coils or in the trunking, whichever is most convenient.

The layout of the electronics for the near detector will be similar but more dense since optical multiplexing is not used in the forward section of the detector and only four-fold multiplexing is used in the spectrometer section.

6.1.9 Minimizing potential noise sources

As discussed in Section 6.1.3, the front end electronics must digitize low-level signals. There are a number of potential electrical noise sources at both detector sites, including noise from welding operations, the magnet coils, the lights and high-current electrical apparatus such as pumps, the cranes and ventilation fans, all of which could introduce noise into the front-end of the system, either by radiation, induction or currents flowing in 'ground loops'. Care must be taken both in the design and the installation of the electronics and other detector components to ensure that the effects of these sources of noise are minimized.

The power distribution systems in the Soudan cavern and near detector hall are described elsewhere[6, 7]. The power for the ventilation system, the magnet coils, general use (e.g., welding) will be isolated from the power for the electronics by means of separate transformers. 'Quiet' AC power for the electronics will be supplied from shielded transformers. The power and ground lines from these transformers will run in separate conduits to circuit breakers and thence to receptacles mounted close to the electronics racks. The ground lines for this power will be isolated and run back to a common grounding point at the transformers. This 'quiet power' will be used only for electronics, computers and some test equipment, but not for high power devices such as pumps, large fans or welding apparatus.

Separate power distribution and grounding systems will be provided for the high-current electrical apparatus. The latter will consist of the grid of interconnected reinforcing bars embedded in the concrete floor slabs. Attachment points to the grid will be provided so

that short connections can be made between the apparatus and a low impedance path to the main power ground. The fluorescent lights will have electronic ballasts and filtering to minimize radiated noise, which is especially important as they start to reach the end of their lifetime.

The power supplies for the magnet coils are another potential source of noise. Power for the coils will be supplied from transformers used only for this purpose. Whilst it would be desirable to use linear power supplies for the magnets, the high current (40 kA) for the near detector coil, and efficiency and heat load considerations at the Soudan site, force the use of SCR controlled supplies at both locations. Sufficient filtering of the magnet supplies will be provided to eliminate the high frequency spikes from the SCRs, which are the main concern.

The DC power supplies for the front end units are located in the hub crates. Power-factor corrected, low-noise switching power supplies will be used in order not to introduce line-frequency harmonics on to the quiet power lines. If necessary, AC line conditioners can be used at the power receptacles.

The small size of the photodetectors and sensitive portion of the electronics makes them inefficient antennae at the frequencies of the noise radiated by electric motors and welders. As described in Section 6.1.3, all electrical connections to a front end unit are made by means of a single multi-conductor cable to the hub. This cable will have a ground jacket and run in a shielded cable tray. The front end units will be completely enclosed in aluminium boxes bolted directly to the MUX boxes which house the photomultiplier tubes. The aluminium boxes will be isolated from the steel detector structure to avoid ground loops. The PMTs and the front end electronics will therefore be in a Faraday cage whose only ground connection is back to the hubs and then to the quiet power ground.

During the installation and operation phases care will be taken to ensure that the quiet power grounds are not inadvertently connected to grounds used by other pieces of apparatus or to the detector steel plates and support structures. Tests of this isolation will be part of the installation procedure.

With proper attention paid to the control of the grounding, noise is not anticipated to be a problem. The CDF experiment has successfully used photomultiplier readout while welding was taking place nearby.

6.2   Requirements and performance criteria

The electronics and data acquisition systems for the MINOS detector will operate in a continuously-sensitive triggerless mode. The selection of events for physics analysis and calibration will be performed by software in one or more processors. The primary functions of the system are:

1. To record:

   (a) neutrino events during the Main Injector spill and

   (b) cosmic ray events in the time between Main Injector spills.

   The recorded data consist of the amplitudes and absolute times (derived from a clock synchronized to the GPS system) of all pulses from the photodetectors above a pro-

grammable threshold.

2. To record calibration pulses from:

   (a) the charge-injection system for calibration of the electronics system and

   (b) the laser light calibration system for calibration of the photodetection system.

3. To record, or automatically subtract, ADC pedestal values.

4. To record the DC currents from individual photodetector pixels for:

   (a) calibration of the combined scintillator and photodetector chain with radioactive sources and,

   (b) diagnosing faulty photodetectors.

5. To monitor components of the readout and other systems and log fault conditions.

6. To log environmental conditions.

The performance requirements for the electronics systems are shown in Table 6.4.

6.3 Interfaces to other MINOS systems

The electronics and data acquisition systems interact with the other detector systems in three ways:

- connection to the photodetectors;

- location and installation, and

- the exchange of information with other systems.

There are also requirements for power and data links, at both the near and far detector sites.

6.3.1 Connections to the photodetectors

The connection between photodetectors and the electronics is made at the front end units. The constraints are: the front end units must be close to the MUX boxes, which are positioned to keep the clear fibers to the scintillator modules as short as possible; the front end electronics must be well shielded because the signals from the photodetectors are very low level; the power dissipated by the electronics should not heat the photocathodes. It is also desirable that any maintenance required by the electronics should not interfere with the optical connections to the photodetectors and vice versa.

The photodetector-electronics interface is achieved in a composite MUX box-photodetector-front end electronics unit which serves three photodetectors. The front end electronics receives signals from the 16 pixels of a single photodetector (see Chapter 5) via a single mixed-contact D-type connector mounted on an interface unit to the photodetector-MUX box. The

Parameter	Near detector	Far detector	Comments
Spill length	1 ms	1 ms	Neutrino spill The far detector must have > 80% duty cycle for cosmic ray muons out of spill for calibration.
Repetition time	≥ 1.9 s	≥ 1.9 s	
Cosmic muon rate	$\sim$300 Hz	$\sim$1 Hz	Essential for calibration.
Max Instantaneous rate	≤ 10 kHz	< 200 Hz	Beam ν at near detector; radioactivity and PMT dark-current dominate at far detector.
Number of channels	9,408	23,232	
Threshold	≤ 0.3 pe	≤ 0.3 pe	
Front end rms noise	≤ 0.05 pe	≤ 0.05 pe	
Charge measurement range	0.005 – 80 pC	0.005 – 80 pC	Assumes PMT gain of 10^6.
Digitization accuracy	5%	5%	
Time resolution (1)	≤ 1 μs	—	Resolve overlaps in near detector; not critical for far detector.
Time resolution (2)	—	5 ns	For atmospheric ν and upward/downward muon separation in far detector.
Single channel deadtime	≤ 5 μs	10 μs	Pileup and losses in near detector; not critical for far detector.
Additional capabilities			
DC current measurement	50 nA	50 nA	Radioactive calibration source (3×10^5 cps from a source of $\sim$1 mCi).
Preamp charge injection	0.005 – 80 pC	0.005 – 80 pC	
Single-channel disable			Remove bad channels from readout.
GPS-based clock	< 1 μs	< 1 μs	Associate events with real-time of MI spill.

Table 6.4: Parameters for the MINOS electronics system.

interface unit is a simple assembly carrying a jumper cable from each photodetector base to the connectors at the rear. The cable allows a connection to be made without exerting force on the photodetector. Each interface unit has one back connector for each of the three photodetectors. The interface unit and the electronics housing are metal boxes to provide immunity from electrical noise pickup. The entire assembly is light-tight.

The high voltage power supplies for the photodetectors are mounted in the front end electronics boxes. These also contain a microprocessor for controlling and monitoring the front end systems and high voltage. Individually controllable high voltages are available to each of the three photodetectors. The high voltage also passes through the interface unit; since less than 1 kV is required the high voltage will use the same connector and jumper cable.

6.3.2 Location and installation

In this Section the location and installation requirements of the electronics systems are described; the installation of the detectors at Soudan and Fermilab is discussed in detail in Chapters 7 and 8.

Location. The physical location of the front end electronics is determined by the location of the photodetectors. Their location, in turn, is constrained by the maximum allowable length of the clear optical fibers. The MUX box-front end unit assemblies are located in a series of 64 short racks placed along the detector at the four 45° faces. Each rack has two shelves with each shelf supporting four MUX box-photodetector-front end electronics units and one rack services 24 photodetectors. At the two upper 45° faces of the detector, the racks are supported on a narrow walkway attached to the detector support structure beams. At the lower corners the racks are supported off the floor.

The rest of the electronics (the hubs and trigger farm) require very little floor space. The hub crates are placed on the intermediate height walkways along the detector, half on each side, and the central system and trigger crates are placed at the south end of the detector. Protected cable runs from the front end units to the hubs and from the hubs, along the detector to the central system are required. There must be room to store extra cable to ensure that all cables are equal in length.

Installation. The electronics is installed incrementally as the detector is assembled. The installation is largely independent of the work done on each steel-scintillator layer. The constraint is that the walkway which supports the front end racks cannot be installed until the steel planes below it are in place. Once the walkway is available, the racks and the MUX box-photodetector-front end electronics units can quickly be added. Each electronics front end box has a single cable which connects it to its hub crate. These are routed to minimize their length and to provide some physical protection.

Once a rack has been installed and connected it is tested, both with the laser calibration system and with the charge injection system to determine that everything is properly connected and operating.

For the commissioning of the electronics for the first supermodule of the far detector, whilst it is being installed, it will be necessary to locate the central system racks at the far end of the detector to avoid interference with mechanical installation work.

6.3.3 Exchanging information with other systems

The data from the trigger farm output processor will be passed to the DAQ system and then to an offline data storage system and, possibly, to offline processing computers. At the near detector site the data are sent directly to the Feynman Computing Center for storage, while at the far detector they are written to a permanent storage medium. A permanent copy of the data will be maintained at the Soudan site and copies distributed to Fermilab and other institutions.

There are also two semi-autonomous systems which can produce signals for the electronics to process. These are the laser calibration system and the radioactive source system, both of which are used for calibration and systems checks. The laser calibration system will produce light pulses in the wavelength shifting fibers which resemble real data pulses. The front end electronics will treat them identically to real data, but depending on the flash patterns, the trigger farm may need to have a different trigger condition to recognize them. The laser calibration data are taken as a separate run so the whole readout chain is notified and the appropriate configuration downloaded.

The radioactive source system produces slowly-varying DC currents from the photodetectors which the electronics measures via the monitoring system. When a certain section of the detector has a source passing through it, it will be necessary to inform the monitoring system to sample the photodetector current for the corresponding set of channels. Any real data taken during this time may be corrupted and therefore the position of the source must be recorded concurrently with the event data.

The monitor and control system has connections to systems other than the electronics readout system. It monitors, among other things, temperature, humidity, magnet currents, and power supplies for all systems. Standard interface modules provide monitor inputs and output signals from the control systems.

6.3.4 Data links

The electronics for the both detectors will require fiber-optic links for timing signals from the GPS receivers to be brought from the surface to the underground detector halls.

A high speed data link between the near detector hall and the Feynman Computing Center (for the transmission of data to be stored), and a link to the Main Injector (to obtain spill timing information) will be required.

6.3.5 Power requirements

The electronics will be connected to the AC power mains. The connection must be to a separate 'quiet' power feed with a single solid ground connection. The electronics has been allocated 75 kW of power at the Soudan site.

6.3.6 Division of responsibilities among subsystems

Item	Subsystem
MUX boxes	Scintillator
Photodetector	Scintillator
Crates	Electronics
Racks	Electronics
Platforms	Near and far installation
Quiet power	Near and far installation
Clean (filtered) magnet power	Magnet steel & coils
Fiber-optics links for GPS timing signals at near detector	Near installation
Fiber-optics links for GPS timing signals in Soudan shaft	Far installation
Data links to Feynman Computing Center	Near installation

Table 6.5: Division of responsibilities among subsystems.

The division of responsibilities among the various subsystems for the provision of items described in this Section is shown in Table 6.5.

6.4 Description of WBS elements

6.4.1 Front end units (WBS 2.3.1)

A front end unit is an assembly which houses the electronics to digitize the times and amplitudes of the pulses from three photodetectors. It contains Field Programmable Gate Array (FPGA) logic to control this process and send serial data downstream to the data acquisition system. As well as supporting these functions it contains the high voltage supplies for the photodetectors and a microcontroller to provide monitor and control functions. A functional diagram of a unit is shown in Figure 6.5.

6.4.1.1 Channel electronics

Introduction. Each input from the photodetector has a separate channel of electronics, whose main function is to capture the peak value and time of each pulse. The signal path of a single front end channel is shown in Fig 6.6. After preamplification and shaping a fast branch of the signal path feeds a discriminator that detects the occurrence of the pulse and causes it to be sampled at its peak; this also permits the time of the signal to be recorded. In addition there are circuits for calibration. One is provided for charge injection, the other for measurement of the phototube DC output. The design described is simple and conventional. It is largely conditioned by the dual requirements for low power consumption and wide dynamic range. The first forces operation from 5 V supplies. It also means the design must be kept simple. It is expected that modest elaboration will prove necessary after initial prototyping, and allowance has been made for this.
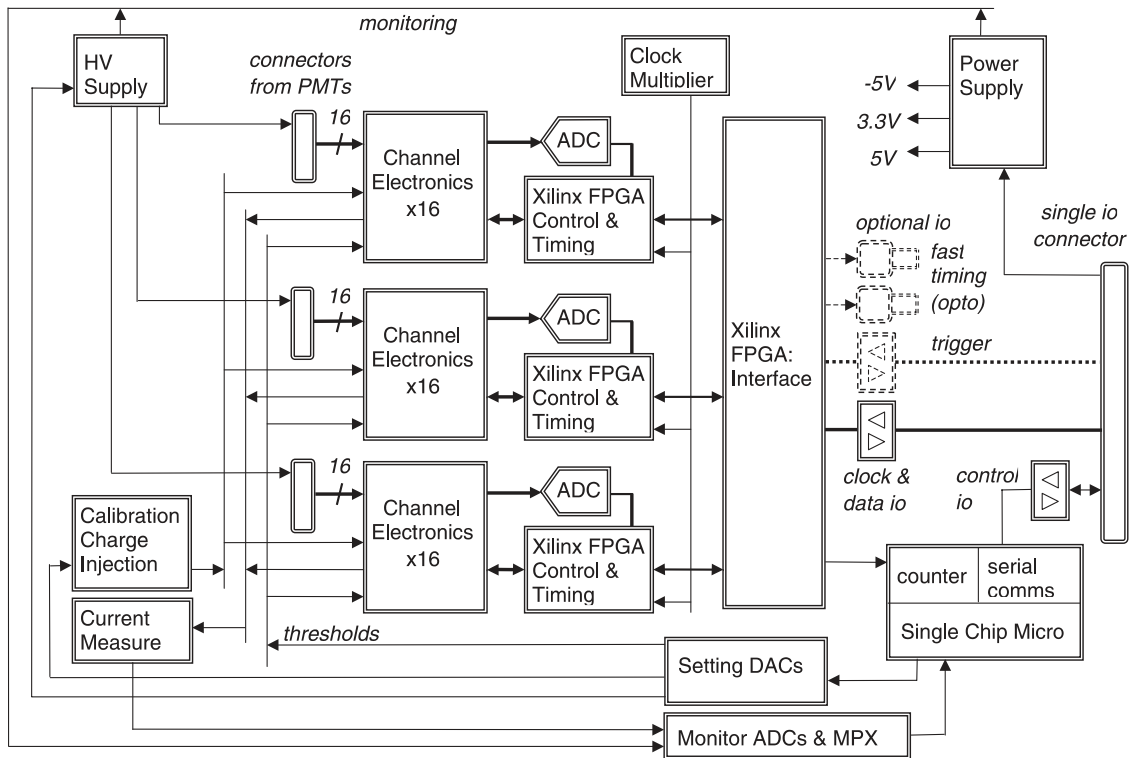
Figure 6.5: Block diagram of one front end unit serving 48 photodetector channels.

Gain and shaping.

Input shaping. A passive input network converts the pulse of charge from the PMT to a somewhat slower voltage pulse. The maximum output pulse amplitude will be a few hundred millivolts: low enough to not cause excessive crosstalk through capacitive coupling to other anodes in the PMT, but large enough to give a good signal to noise ratio. Protection against overvoltages is included.

Preamplifier. An op-amp is used as a preamp, taking a voltage input. It provides modest gain (about 8) to buffer the signal and lift it well above noise, while keeping within the output amplitude possible with 5 V supplies. A little extra high frequency roll-off suppresses noise from its input. It needs ∼100 MHz gain-bandwidth, and low noise: the AD8005 chip has been used.

The output is a pulse with a peaking time of ∼100 ns, amplitude from 2.5 mV for 1 photoelectron from a low gain PMT channel, to 3 V for 500 photoelectrons and a high gain channel. The input may be changed to a charge sensitive amplifier, once a satisfactory design can be completed. This would give a slightly better performance at similar cost and complexity.

Slow shaper and buffer. The relatively fast signal from the preamp is reshaped to give a peaking time of ∼400 ns, and buffered to drive the sampling circuits. This uses another
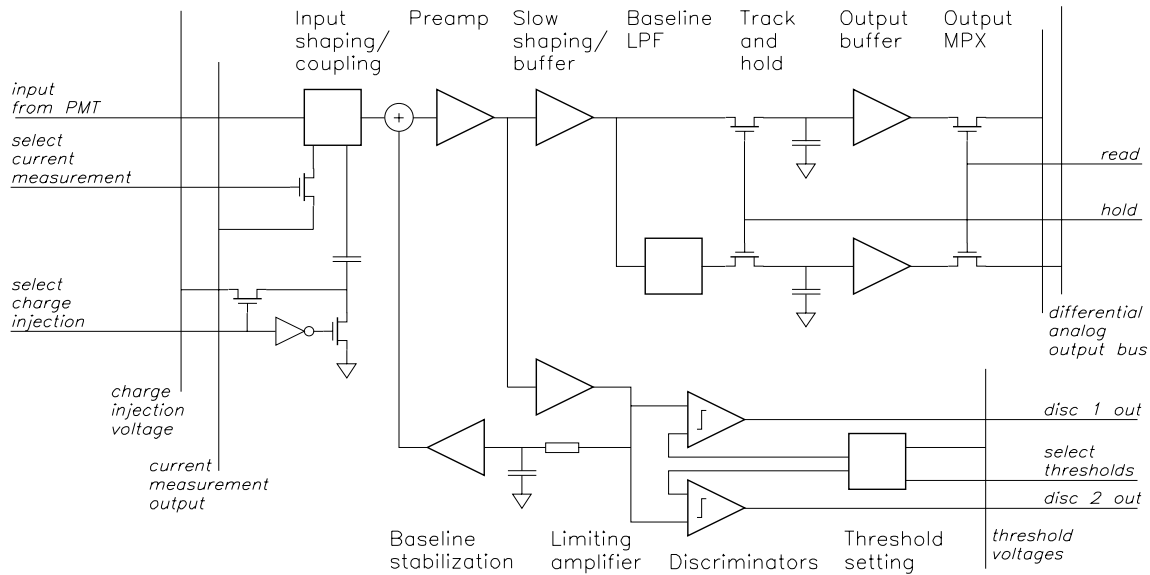
Figure 6.6: Signal path of a single front end channel.

op-amp, and has to have a low output impedance.

Peak sampling.

Baseline tracking. The signal path is DC coupled and there can be a significant offset voltage and, possibly, low frequency (e.g., 60 Hz) interference. The mean baseline of the signal is tracked by splitting the signal and passing one branch of it through a low-pass filter. Both the unfiltered and the filtered signal outputs are sampled and passed differentially to the ADC thereby rejecting DC and low frequency signals.

Track and hold. The low pass filtered and unfiltered signals are fed through two sections of a switch IC to hold capacitors. The voltages on these track the inputs until the switches are turned off. The instantaneous voltages are then held for subsequent readout until the switches are turned back on. The performance of such a circuit is dominated by the switch. The limiting factor is injection of charge when the switch is turned off; the differential arrangement used makes this balance as far as possible. It also makes it necessary to use as large hold capacitors as will give acceptable speed, and to provide low driving impedance. Performance is better the slower the system; the 400 ns shaping is fast enough to make this a critical part in attaining the required dynamic range. The DG611 D/CMOS quad switch is used.

Output buffers and switches. The hold capacitors are read out through unity gain FET op-amp buffers, which are relatively non-critical parts; their low bias current is needed to avoid the stored voltage on the hold capacitors drifting too rapidly. Finally, two more

sections of the quad switch are used between the buffers and an analog output bus (still differential). This allows the output from one channel to be selected for digitization.

Discriminator system.

Limiting amplifier. The output from the preamp also feeds the discriminators. Since fast comparators need their threshold to be set at 20 mV or more, the minimum pulse height at this point has to be ~50 mV. Additional gain of about 20 is therefore required, and large pulses will saturate. The amplifier is thus designed to limit, and recover from this condition with minimal delay. This has been designed around a fast op-amp and needs extra components for limiting. The amplifier is fed with a sum of the preamp output and the inverted slow shaper output, thus forming a bipolar shaped signal which allows the comparator to act as a type of constant fraction discriminator.

Baseline stabilization loop. The threshold, at its lowest setting, corresponds to only 0.1 mV referred to the preamp input. This is too low to ignore offset in the amplifiers. The problem is circumvented by adding a low frequency feedback loop from the output of the limiting amplifier to the preamp input. This is a standard form of baseline stabilization. It uses a cheap FET input op-amp configured as an integrator to give the long time constant desired. It also adds limiting on the input to the amplifier; this is not strictly needed, but is a refinement that greatly reduces baseline shifts produced by large pulses at high rates.

Comparators and threshold setting. Two comparators are provided; one is an auxiliary to allow a higher threshold and could be used for an input to a trigger system. The MAX907, a very low power dual comparator, is used. A faster part could be substituted at the cost of increased power consumption. Individual channel threshold setting is provided to take account of variations in PMT channel gain. This may be done by selecting between four possible voltages derived from upper and lower values set by DACs for a group of channels. This is a coarse setting, but seems sufficient.

Calibration.

Charge injection. The input to each channel includes provision for charge injection. It has a capacitor, which can be switched between ground (normal operation) and a charge injection line. This line receives a variable voltage step by the common driver circuit. It is possible to inject charge into one or more selected channels.

Current measurement. The input network is arranged to exhibit a moderately high impedance to DC. The currents from the PMT during source calibration generate easily measurable voltages which can be switched with CMOS switches to a common output line for measurement. The network isolates the signal pulses from this DC path. Coupling to the preamp is AC, so the amplifier bias current can not affect the measurement.

6.4.1.2 Measurement circuits

Digitization.

ADC multiplexing. It is not practical at present to use one ADC per channel to obtain 14-bit resolution. Even though each ADC could be quite slow, they are too expensive and need too much power. Much better results are obtainable sharing one faster converter among several channels. This multiplexing is done by using the output switches on each front end channel to put the held voltage on a common pair of lines for measurement; these lines feed through a buffer amplifier to the ADC. Sixteen channels are multiplexed to one ADC. Suitable 14-bit ADCs have recently become available: the Analog Devices AD924x family. The 3 MS/s AD9243 is used here.

Mode of operation. Operation starts with the channel control logic noting that a hit has been detected on a channel, holding its peak voltage, and recording its time. The control logic of the channel mezzanine continuously scans the status of all its channels, comparing times and selecting the earliest with a hit. As soon as the ADC is free, the output switches of this channel are turned on and its stored voltage is converted. The channel control logic is told the hit has been processed, the track-and-hold reverts to track, and the channel is readied for the next hit. The data from the conversion are paired with the recorded times and channel numbers, and output to the control logic on the main board. There the streams of data from the three channel mezzanines are merged, keeping the data in time order. The data are then passed back to the hub with sufficient buffering to smooth the flow.

Sweeping. The ADC, like all fast, high resolution parts, has significant nonlinearities. Measurements made over a narrow range cannot be relied upon to much better than one count. This is an issue for calibration using muons which measure only over the low part of the ADC range. To overcome this an offset voltage is added into the ADC input. This is derived from a DAC set through the control system, and is able to move the zero over approximately 10% of the range of the ADC. This allows adjustment so low level signals do not use any point in the range of the ADC that proves to be particularly bad; commonly, the differential linearity of ADCs is much worse than average at a just a few points in the range. It would also permit the more sophisticated approach of gradually sweeping the zero position to average out nonlinearities.

Timing.

Channel timing. Timing with 5 ns resolution is provided for each channel. It is implemented in the FPGA which contains all the logic for a group of 16 channels. It uses a 100 MHz clock to drive a 4-bit Gray code counter, with transitions on both clock edges. The outputs from this are distributed to latches, one for each channel. Because the clock and fast counter outputs are not widely distributed on the chip, power dissipation remains low. Note that present FPGAs are capable of being driven by and counting 200 MHz clocks; the present design is slightly conservative.

The Gray code counter provides fast timing, but with only an 80 ns wrap-around period. A separate counter and set of latches, driven by a slower clock which is also used to synchronize the inputs to be timed, provides low resolution timing with a wrap period long enough to avoid ambiguities. Logic combines the two parts of the time into a single binary coded output (18 bits long).

Plane timing output. A high resolution timing output will be provided for groups of channels, rather than each separately. This will use a separate very fast amplifier and discriminator serving a group of 8 channels, inductively coupled to all the channel inputs in the group, to sense the leading edge of the first photoelectron of an event. The discriminator outputs of the groups of eight channels belonging to a plane will be OR'ed and taken to fast optical fiber outputs to allow connection to external TDCs, without risk of interference to the operation of the system. The outputs will be reconfigurable to work in a test mode, allowing operation of the unit to be monitored without interference and without involving other parts of the electronics system.

Clock. The high frequency clock is generated by a clock synthesizer IC, with an internal VCO and dividers forming a frequency multiplying PLL. This gives a flexible choice of clock speed (up to at least 160 MHz, at present), and maintains synchronism to the system clock without having to distribute an inconveniently high frequency. It will be located on the main board.

Control logic.

Functions. The basic function of the logic on the channel mezzanines is to time and sequence the hits, convert their amplitudes, buffer the hit data, and output it in time order to the main board. The FPGA there merges the three streams keeping the hits in time order, and transmits the output stream back to a hub.

An important secondary function of the logic is to detect, as far as is practical, hits that can be detected separately but which cannot be completely or accurately handled by the system. For example, the occurrence of a second hit during the dead period of a channel after a first has been registered can be detected, and indicated by flag.

The logic also has to monitor its own operation. Most important, it has to detect if operation goes outside normal parameters. It should detect if, for example, buffers become fuller than is anticipated, thereby giving warning of problems, as well as detecting when overflow actually occurs. Similarly, it should check that when times with a short cyclic period have to be extended to longer ones, that no errors are occurring (this is a statistical check only). It also has to make the basic check that its internal time counters remain synchronized with the system time; as long as this is true no action is needed, but a reset has to be made and reported if a deviation is found and confirmed.

Special modes. Various other special modes are required. Some are already included in the design; others are likely to be wanted. Most important are those for measuring the ADC pedestals. This may be done during normal operation by causing a low rate of

conversions to occur at random in the absence of a detected pulse. The data from these are flagged, but otherwise pass through the normal path. If this method is not wanted it can be disabled. It is also possible to command sampling to occur with no pulse detected; data can be returned over the usual path suitably flagged, or via the control system. The various options will be selectable.

The charge injection system is also controllable. It uses the normal operating mode to acquire the data, though this may be modified to gate it to select just the wanted signal. It can however also allow variations to permit more extensive testing of the system. For example, varying the delay from trigger to sampling, and timing sampling from the charge injection rather than the detected pulse.

Diagnostic modes are also needed. For example, to generate dummy data. This allows independent checkout of the later stages of the system, and simplifies diagnosis of data handling errors. It is also easy to generate controlled data rates, continuous and burst, to check the system. Charge injection can also be used for this: and it can be extended so operating across multiple units it can mimic events and test processing algorithms.

A major advantage of putting the logic in FPGAs is that it will usually be possible to add such features after the basic hardware is developed.

Implementation. All the logic for 16 channels are implemented in one Xilinx FPGA. This includes the timing, and buffering the data output. The configuration ROM for the FPGA is on the main board, so the same configuration is applied to all three mezzanines.

Calibration.

Charge injection. Each channel has a charge injection capacitor and switching; a group of these is driven by a single low impedance source of a voltage step, the amplitude of which is accurately variable over a wide range.

The driver uses a bipolar differential pair to rapidly switch the tail current between two loads of $\sim$50 Ω. The tail current is set by a precision feedback loop from a DAC driven by the control system. The current consumption is reduced by turning this current off when charge injection is not in use.

To get good accuracy ($\sim$1%) over a wide range in amplitude requires careful neutralization of stray coupling capacitances and may require two drivers for high and low parts of the range. A fast risetime and very accurate timing should be possible, allowing reliable calibration of channel timing.

Source current measurement. The front ends can measure the DC current from the PMTs. This is mainly used during the radioactive source calibration mode, but it also allows effective monitoring of the tube leakage currents which will be useful for diagnostic purposes. Each channel can multiplex a voltage representing its DC input onto a single line for measurement. This will be done using a precision op-amp, a low pass filter, and a low-speed high-resolution ADC connected to the control and monitoring microprocessor. This could be the ADC used for other monitoring functions but a separate ADC is used for

simplicity: the cost can be very low. High resolution is not strictly needed, but allows for considerable variation in the strength of radioactive sources that might be used.

Laser calibration system. The laser calibration system is used to inject light pulses into the the wavelength shifting fibers and to test the readout chain from the WLS fibers, through the PMTs, to the front-end electronics. The laser system can inject light pulses of varying amplitude, and so allows us to measure the linearity of the entire scintillator system and its readout chain on a regular basis. In addition, the short duration of the laser pulses allows us to calibrate the relative timing and time walk of each detector channel.

6.4.1.3 Ancillary functions

Monitor and control.

Concepts. A wide variety of monitoring and control functions is required. In normal operation settings have to be made, such as thresholds. It is also desirable to monitor conditions such as supply voltages, and status signals that are not conveniently handled through the main data path. There are also special operating modes to be supported, such as PMT current measurement and pedestal measurement.

These requirements are sufficiently complex that handling them independently by a microcontroller is the easiest and most flexible way. The required data rates are low, so communication over the serial interface included on the chip is adequate. A major advantage of this approach is that development of the monitoring and control is essentially independent of the signal handling.

Microcontroller. The microcontroller should be a mid-range single chip microprocessor. Speed is not important. It would have a few kBytes of program memory, and a few hundred bytes of RAM. Most of its I/O will be through local serial interfaces to ADC, DACs, and the various FPGAs, so a large number of pins will not be required: a 28 pin device is probably adequate. Choice is largely a matter of convenience: for example, the inclusion of a high-resolution ADC in the PIC14C000 which would avoid the need for an external part, or flash program memory allowing in-circuit reprogramming during development.

Required functions. Many control and monitoring functions will be required. A partial list of required functions includes:

1. setting operating mode (triggerless, or various triggered);

2. disabling unwanted or bad channels;

3. initiating pedestal measurements;

4. setting discriminator thresholds and selecting which to apply to each channel;

5. setting ADC offsets (statically, or with a slow sweep);

6. setting tube voltage(s);

7. reinitializing unit hardware;

8. selecting charge injection mode; setting pulse amplitude and channels to inject; and initiating operation;

9. selecting channel to measure tube current, and making measurement;

10. checking incoming and local supply voltages;

11. checking tube voltages;

12. checking tube currents;

13. checking unit temperature;

14. measuring count rate from a selected channel or channels, and

15. reporting status flags in the logic indicating incipient problems or actual errors.

Clock and timing. A local synchronized clock and timing mark must be derived from the system timing. It is adequate that the relation between these is stable, but it desirable that they have a minimal offset. It is also necessary that they are free from glitches. The clock and timing mark signals are transmitted differentially from the hub over two pairs in the cable connecting the hub to the front end unit.

Power supplies.

   Low voltage. The multiple low voltage supplies needed within a front end unit are assumed to be derived from a nominal 48 V input through a DC/DC converter and additional regulators. The unit will draw this power from the hub to which it is attached.

   High voltage. The design of the front end units includes local generation of the high voltage for the PMTs which offers considerable advantages. It is safe, it allows units to be 'hot swapped', it does not introduce ground loops, it limits high voltage faults to the single unit, and saves cabling. A low power DC/DC converter, with an added filter, and an output stabilization feedback loop regulating the input voltage is used to generate the HV. The load is essentially static, the tube currents being negligible compared with the divider chain current. Individual adjustment of each tube voltage will be provided.

Interface. The only connection between the front end unit and the rest of the electronics is by a single cable to a hub. The use of a single cable avoids ground loops and injects minimum interference into both the front end unit, and the signals carried over the cable. Even so, for reliability the signals are differential and should have good immunity to common mode interference. A screened twisted-pair cable up to 6 m long, with 25-way D-subconnectors, is used to connect a front end unit to a hub. The functions of the conductors are:

1. Data output. The data are output serially using one pair of conductors. The average rates are so low that there is no technical difficulty, and buffering handles the peaks.

2. Power to the front end unit is supplied from the hub using a single pair of conductors in conjunction with a separate 0 V connection.

3. Clock and timing signals require two pairs of conductors; one for the 10 MHz clock, the other for the timing mark.

4. Control and monitoring use two pairs, as separate serial links. Rates are low and a separate link for each direction to the control microprocessor is simple and cheap.

The remaining pairs of conductors in the cable could be used to carry trigger signals if necessary.

6.4.1.4 Mechanical construction
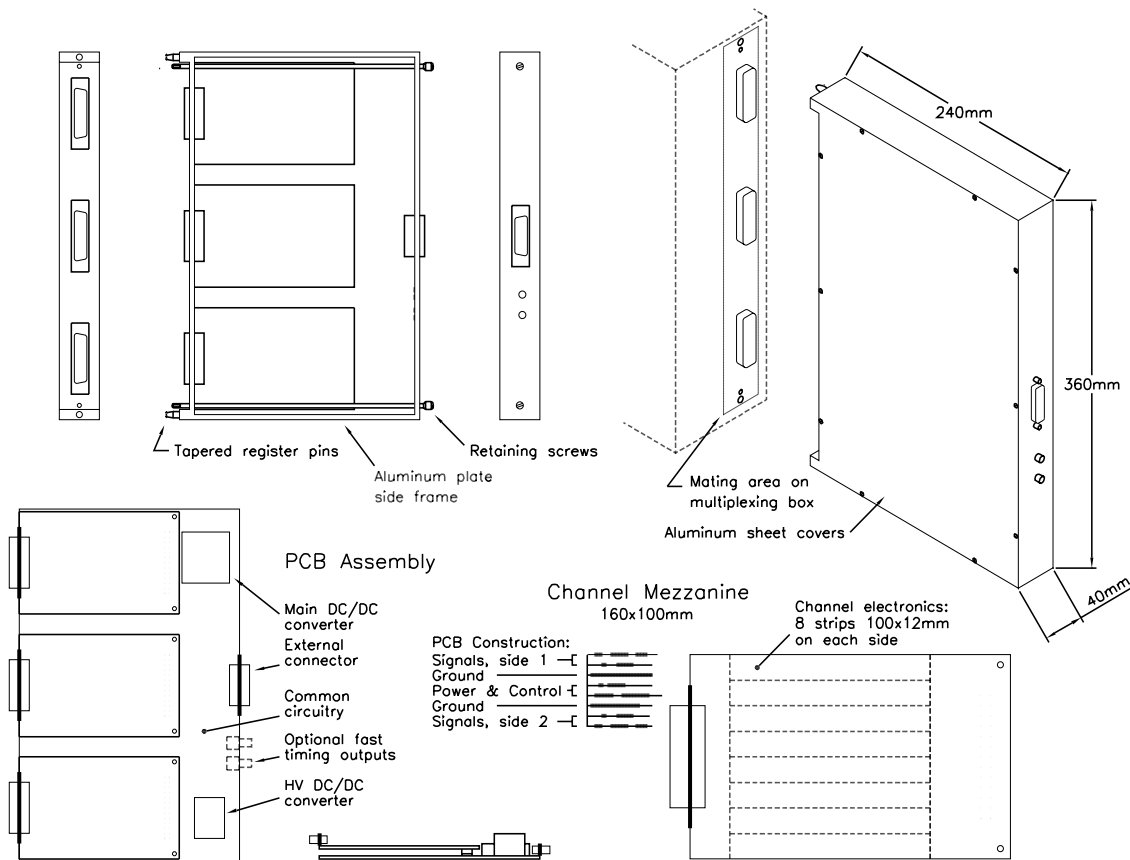
Figure 6.7: Mechanical construction of the front end unit electronics.

The mechanical construction of a front end unit is shown in Figure 6.7. Details are still not finalized, and it is hoped to reduce size and cost, although this would not affect the general organization described.

Electronics. The electronics for each group of 16 channels is built as a separate channel mezzanine board. Three such boards plug on to a main board with the common parts of the system. Each mezzanine has an external connector to one PMT assembly; all other external connections are to the main board.

Channel mezzanine. The channel mezzanine is an 8-layer, 100×160 mm printed circuit board. Construction is entirely surface mount (except connectors), using both sides. Eight channels are laid out on each side, occupying strips approximately 12×90 mm, with the remaining length of the board used for the connectors, the ADC, logic, and other parts common to all channels. The signals are carried on the outer two layers on each side. Layers 3 and 6 are ground planes, and layers 4 and 5 are for power and control signals. Component density is low enough that through vias should suffice. Efficient automatic assembly should be possible.

At the front of the board is a mixed-contact D connector which provides the 16 external signal connections from the PMT, as well as supplying high voltage via a high voltage insert. It is fastened directly to the case, and supports the front of the mezzanine.

Main board. The main board is a 4-layer, 340×200 mm printed circuit board. The mezzanines occupy the larger part. Its own circuitry is in a strip along the back, with the IO connector in the middle of the rear long edge. Power supply components are well clear of the sensitive input circuits, and are electrically screened.

Mechanics. The electronics is housed in a shallow case without ventilation. The case is a little bigger than the main board, and about 50 mm deep. It consists of a frame made of four lengths of 6 mm thick aluminum, to each side of which a cover plate is screwed. Connector apertures and fixings are machined in the front and rear of the frame.

The unit assembles vertically to the rear of the associated MUX box. Two tapered register pins on the front of the unit mate with holes in the MUX box to guide the connectors into alignment. The unit is held in place by two long clamping screws passing through the entire depth of the box and operated from the rear. The front of the unit fits securely against mating areas on the MUX box–PMT combination, the whole forming a rigid assembly.

Environmental. The closed front end case will be heated by the power dissipated inside; the outside surface temperature is predicted to rise by about 8 K above ambient. The thermal coupling to the PMTs is poor enough that the electronics should raise the temperature of the photocathodes by no more than 2 K. The air temperature within the case will rise by about 15 K, which causes no problems for the electronics.

The case, while closed, will not be sealed. The unit could thus be affected by high humidity, which is a possible problem at the near detector. The internal temperature rise helps, and a conformal coating will be applied to the high voltage circuitry. There should be no problem if the ambient relative humidity remains below 90%, given that the temperature is relatively stable.

6.4.2 Hubs and interface crate (WBS 2.3.2)

6.4.2.1 Hubs
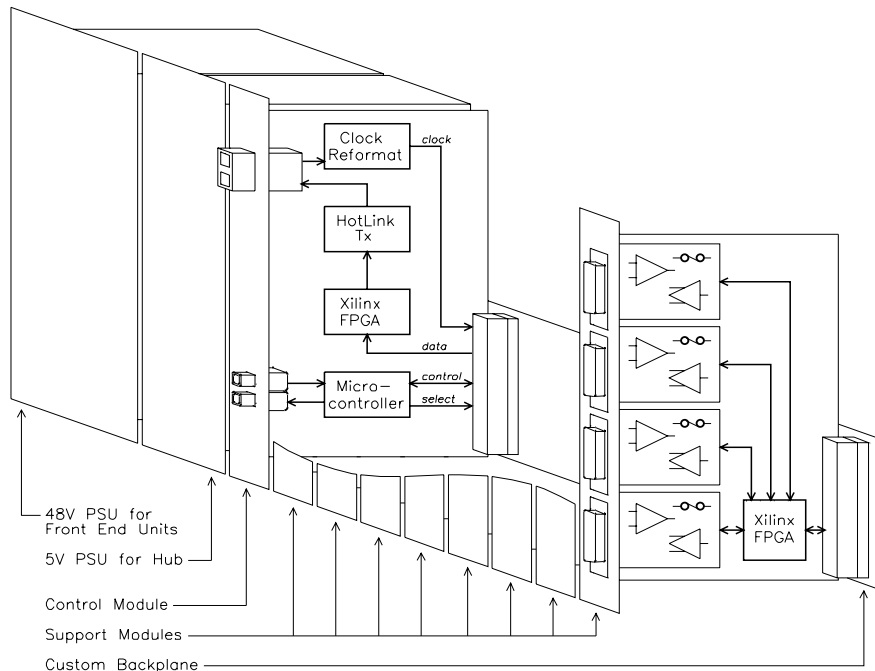
Figure 6.8: Diagram of a hub unit showing the major components.

A hub is a single crate which distributes services and DC power to up to 32 front end units, and accepts data from them for transmission to the central system. It contains a number of support modules and a control module and will be connected to the interface crate of the central system with two 2-core optical fibers. The data are sent out over one fiber, in the form of a 250 MBd serial link. A second provides a low-skew clock and timing signal. The other pair provide monitoring and control. No elaborate processing is provided. The data are merely concentrated onto the one output link for convenience, but not otherwise manipulated. Monitoring and control is likewise simple, though here local decoding of address commands allows individual front end units to be selected.

Figure 6.8 shows a diagram of a hub crate. It is a single 6U crate, though the height might be increased to 9U with power supplies in a 3U subdivision, if support for 64 rather than 32 front end units is required. All modules are VME compatible, using rows a and c only of the P2 connector position for signals, though this is not required in the system as designed.

Support module. The support module has four panel connectors for cables to front end units. It distributes 48 V power to these through protective Polyswitch fuses, and the clock through ECL drivers and coupling transformers. Differential drivers and receivers are

provided for the signal lines. These connect to a small Xilinx FPGA. This reduces the four serial data streams to one multiplexed stream which is clocked at 10 MHz and passed to the control module. It also combines the four serial control and monitoring connections into one, using address lines from the control module; this includes broadcasting, and activity monitoring. Finally, it provides the logic required when the triggered operating mode is selected.

Control module. The control module has a fast fiber optic transceiver taking duplex SC connectors. The input is a multiplexed clock and timing signal which the module reformats for distribution through the support modules to the front end units. It may convert the clock frequency. The output carries the data from all the front end units in one serial stream. It is driven by a Cypress HotLINK transmitter chip at 250 MBd. This in turn is driven by a Xilinx FPGA which takes the serial data from all the support modules. The data from each front end unit remains in time order but the 32 streams are combined without regard for their relative timing. A second fiber optical transceiver, using separate low speed devices, also accepts a duplex SC connector to provide monitoring and control. It connects to a microcontroller, as well as to the support modules. The microcontroller implements local control functions, in particular decoding and applying address commands, passing addressing information to the support modules. It also provides monitoring for the hub itself. This is independent of the main data path, except that some control and monitoring functions will be implemented.

Hub crate and ancillaries. A standard 6U subrack is fitted with a 48 V, 360 W plug-in power supply for the front end units, a second power supply for local power, and a simple custom backplane. The backplane distributes power, and connects the support modules to the control module.

6.4.2.2 Interface crate

A single crate provides an interface to all the hubs on a detector. It distributes clock and control, and receives data and monitoring information. The function of the crate is primarily the conversion and redistribution of signals.

The interface crate connects directly to each hub; fiber optic cables are used for electrical isolation. All are of equal length to avoid introducing skew in the clock distribution. One cable (two core, 'zip' type) with duplex SC connectors handles clock and data; a second handles the control and monitoring.

The interface crate passes the data, as electrical high speed serial links, to the central data handling system. It provides control and monitoring connections as electrical low speed links (RS232) to the computer managing these functions. It accepts the clock and pulse outputs from the GPS timing receiver and uses these to generate system timing. The timing receiver also has an RS232 link to the control computer, providing status and time of day information.

Clock and data interface module. A 6U board provides 8 fiber optic transceivers for the clock and data cables from 8 hubs. These are high speed (266 MBd or better) for low clock

skew and jitter. For purposes of costing, the 1.25 GBd HFBR5305 is assumed. The board takes the clock and pulse outputs from the timing receiver, and produces a multiplexed signal for distribution. These inputs will go to only one board, with provision for slaving others to it so as to minimize skew. Clock frequency multiplication will be included if necessary. The received data is transformer coupled onto the output, to give best common-mode noise immunity, and protect against accidental damage. The electrical connections are on the rear connector (arranging this so the board is compatible with a VME system, in case this should ever be desirable).

Control and monitoring interface module. This is of similar physical form (and again VME compatible), but with low speed optical transmitters and receivers in place of the transceivers. An RS232 electrical IO is on the rear connector. It is assumed that each link will be connected to a separate serial port in the control computer (so the board might be connected 1:1 to an octal serial PC card), but multiplexing so it can be connected to a single port will be included, and this will be extended to work across a set of boards. A microcontroller to provide local monitoring functions will be included, and this will have some spare inputs available for monitoring conditions off the board.

Crate assembly. For the far detector, three of each type of board are housed in a 6U VME format subrack, together with a plug-in supply for their power. No backplane is required; power is distributed by front-panel patching connectors. The assembly is similar for the near detector but only two of each board are required.

6.4.3   Central data system and trigger farm (WBS 2.3.3)

6.4.3.1   Hardware organization

The central data system for the far detector consists of four central receiver crates and one trigger farm crate; only 3 receiver crates are required for the near detector. The receiver crates receive and sort hit data from the interface crate and pass them to the trigger farm for software event selection, via dual high speed (132 Mbyte/sec) data links. A third, similar, link is used for communication between the trigger farm and receiver crates. Only two links (one for data and one for control) will be required if the total detector singles rate is less than 10 MHz.

Central receiver crates. The central receiver crates are small (seven slot) 6U VME crates which contain receiver and sorter cards. They are connected by high speed data networks to the trigger farm crate. Data from the receiver cards are available on the VME backplane and commercial off-the-shelf processors will be used for time sorting the hits and triggering.

Receiver cards. A receiver card is a custom-built unit containing the buffering and logic to prepare the data from the front end units for sorting into trigger time blocks by the sorter cards. The number of hits stored in these time blocks depends on the detector data rates and flexibility to change the size of the trigger time blocks is included.
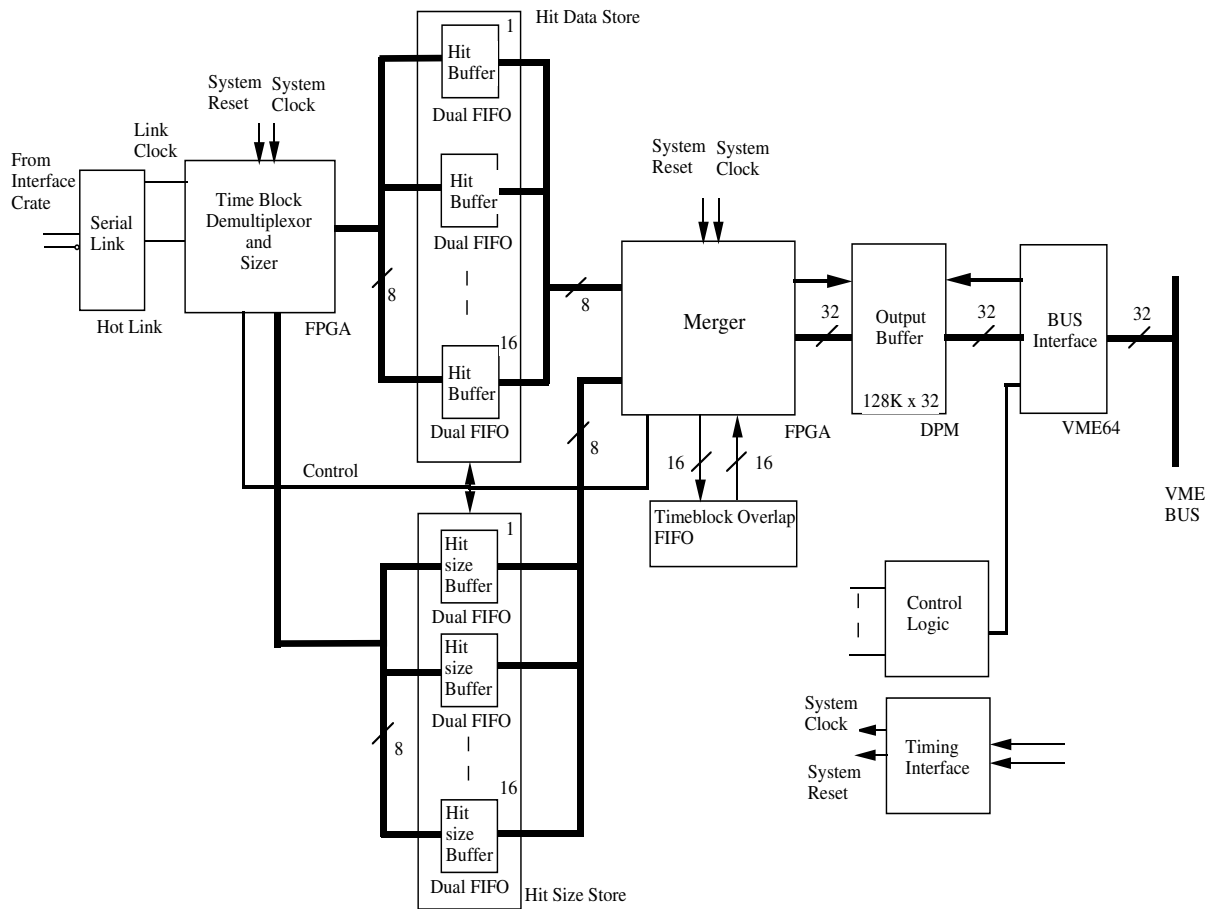
Figure 6.9: Block diagram of a receiver card.

A block diagram of a receiver card is shown in Figure 6.9. Each receiver card is a 6U VME card which receives a single cable from the interface crate. Each input cable is a short serial electrical link based on commercially available transparent point-to-point links (HotLINK). The data from the interface crate come from 32 front end units whose data have been packed together. The rate of this data stream will not exceed 5 Mbyte/s which is well below the limit of the HotLINK at 33 Mbyte/s.

The serial data are converted into bytes from the HotLINK receiver. Each front end unit data stream is processed by the time block demultiplexer/sizer which is a Field Programmable Gate Array (FPGA) connected to the HotLINK. The data are written into a hit buffer FIFO according to which front end unit it originated from. At the same time this FPGA will measure the length of the hit data and store this in a second bank of FIFOs, the hit-size buffers.

The two banks of hit and hit-size FIFOs are connected to a second merger FPGA which extends the hit data with the full time stamp and channel identity, as well as making time blocks of predetermined size for the trigger farm.

Trigger time blocks are made by first reading the hit sizes from the hit size FIFOs and then extracting the corresponding hit data from the hit FIFOs. At the same time 32 bit wide data words are constructed which are more suited for the VME64 bus at the back. The merger FPGA will also periodically preserve one of the front end time blocks to overlap with the next trigger time block.

A hit output from the merger FPGA will be in two 32 bit wide words which are stored into the output buffer dual-port memory. The same process of sizing the length of the time blocks is performed by the merger FPGA; their lengths are stored in the output buffer.

Sorter card. The receiver cards present the sorter cards with time blocks of data from 128 front end units. The time blocks contain hits from any of these units for a fixed period of time ready for time ordering. Time sorting is required to reduce the processing power requirements of the trigger farm processors. Each sorter card is a VME single board computer and the sorting is performed by software.

Each sorter card contains two main software algorithms: a data-sequencing algorithm and a merge-sort algorithm. The merge-sort algorithm merges the receiver card time blocks into a single trigger time block with the hits in time order. The data-sequencing algorithm manages the input/output transfers, calls the merge-sort algorithm and manages the onboard memory buffers.

Two sorter cards are used in each central system receiver crate, one for handling odd, the other for handling even trigger time block numbers. One of the sorter cards will be a master and the other a slave. The master data sequencing code is responsible for coordinating the allocation and availability of the time blocks to the trigger farm.

Each receiver card time block consists of 32 sub time-blocks, one from each front end unit, each of a different length. The data-sequencing extracts the lengths and base address pointers from each of the four receiver cards and transfers the data from the receiver cards to the sorter card input buffer.

The merge-sort algorithm then merges the 128 time blocks from the four receiver cards into a single output time block where all the hits will have been sorted in time order. The

merge-sort algorithm returns the length of the merged block, which is the sum of all the receiver card block lengths, to the trigger farm.

The software required to implement the sorting is quite simple. The processing time for these algorithms should be very similar to the ones used and benchmarked for the trigger farm.

Trigger farm. The operation of the trigger farm has been described in Section 6.1.5. The hardware comprises a VME crate containing up to 20 VME single-board computers each with dual PCI Mezzanine Cards and a high-performance PMC-based network card for data transfer. Two of the single-board computers, the input processor and output processors, are dedicated to sequencing. The remaining processors are used for the selection of events to pass to the data acquisition system. Only one trigger processor will be required if the nominal far detector singles rate of 0.9 MHit/s is achieved; no more than 10 would be required to handle the maximum design rate of 20 Mhit/s.

Trigger farm - receiver crate networks. A maximum of three 132 MByte/s PCI–PCI transparent bridge networks will be used to connect the central receiver crates to the trigger farm. Two of these are used for high speed data transfer; the third is used for controlling the data transfers. The CES PCI vertical interconnect bus has been assumed in the cost estimate.

6.4.3.2 Software algorithms and organization

The software algorithms that will be used in the trigger farm have been described in Section 6.1.6. The algorithms are simple and efficient and should not require extensive software development effort.

6.4.3.3 Interface to the data acquisition system

The interface from the trigger farm to the data acquisition system will be from the output processor Ethernet port using standard TCP/IP protocols.

6.4.4 Data acquisition system (WBS 2.3.4)

The main function of the data acquisition system (DAQ) is to receive events from the detector electronics and record them on a mass storage device. Because the event rates are low, the requirements of the MINOS data acquisition system are not demanding. The central system and the trigger farm build events and present them to the DAQ.

The Fermilab DART system[8], which is flexible, supported and tested, will be used. The anticipated data rates, which are described in Section 6.4.3.2 and Chapter 9, are low and well within its capabilities. DART will run on a PC and an associated cluster of PCs linked by Ethernet will provide real-time data analysis and diagnostic capabilities.

DART provides a graphical user interface which allows the operator conveniently to control data taking runs. In addition it provides an online event buffer from which separate

programs on other PCs in the cluster can access and process events as desired to make (e.g.) online displays of events or monitor detector behaviour.

The DAQ receives events from the output processor in the trigger farm. The output processor single board computer runs the VxWorks real-time operating system and passes the data to the DAQ PC via the Ethernet LAN using conventional TCP/IP protocols.

The event data will be treated differently at the two detector sites. At Fermilab the data will be sent directly to the Feynman Computing Center and stored in the tape vault; at the Soudan site the data will be written locally to a mass storage medium and then copied and distributed to other institutions, including Fermilab, for processing.

Monitoring and control functions will be provided by PCs in the cluster and use custom software, as appropriate to the specific functions required.

6.4.5 Database systems (WBS 2.3.5)

The databases will maintain a record of the construction history of the detector components and the state of the detector during it operating life. Some of the information will recorded only once, or very infrequently; some will be recorded regularly to enable the performance of the detector to be tracked and calibrated. Information will be recorded either manually or will be derived automatically via software from the various monitoring subsystems (such as the embedded processors in the front end units and hubs) and the data acquisition system.

The information in the databases must be available in many places simultaneously; it will be used to ensure the smooth construction, installation and operation of the detector and will also be vital to the offline data analysis.

Examples of the the information that will be recorded in the database, together with the level of detail, the source of the information and the approximate frequency of recording, are given in Table 6.6. The list is by no means exhaustive and some experience will be necessary before the exact frequency at which some of the information is to be recorded can be determined.

As well as recording information about the hardware of the experiment the database will also be used to log book-keeping information such as run start and stop times, numbers of events and operator comments.

The information will be made available to the data processing computers by a single master database at Fermilab containing all the data and satellite synchronized copies at Soudan and the near detector. The satellites will primarily service the trigger farms and first-level offline processors, which will limit their usefulness to queries from remote locations. Physicists working elsewhere will either query the master database or make database copies for their own sites.

Some of the information in the database will be generated and entered remotely, for example at the scintillator factory or the extrusion plant. Since these locations may not have reliable network access, the data will be entered into a PC running mSQL in Linux or Microsoft Access and subsequently downloaded to the master database by dumping it to a flat file and reading it into the master.

The database will store the modification level and repair histories of the various electronics boards. It will be possible to consult the database for details of switch settings and board placement if items need to be replaced. The interface will be via a World Wide Web browser

Item	Information	Level	Source	Frequency
Construction				
Steel plates	mass	plate	installation	once
	thickness	plate	installation	once
	magnetic properties	plate	mill	once
Scintillator	QC tests (light yield)	batch	extrusion factory	once
WLS Fibers	QC tests (light yield)	batch	module factory	once
Scintillator modules	dimensions	module	module factory	once
	mass	module	module factory	once
Photodetectors	QE, uniformity & gain	pixel		once
	operating HV	unit		once
Electronics	modification level	board	factory	as req'd.
	switch settings	board	factory/test rig	as req'd
	calibration constants	channel	factory/test rig	once
Installation and survey				
Steel plates	positions	plate		once
	alignment			once
Scintillator modules	positions	module		once
	alignment			once
Scintillator modules	light yield	strip	source calibration	once
Photodetector	gain	pixel	light flasher	once
Electronics	calibration constants	channel	pulse injection	once
Operation				
Scintillator	calibration constants	strip	muons (software)	weekly
Photodetector	gain	pixel	light flasher	daily
	replacement history	unit		as req'd.
Electronics	calibration constants	channel	pulse injection	daily
	disabled channels	channel	software	as req'd.
	FPGA & ROM programs	unit	software	as req'd.
	Trigger farm software		software	as req'd.
	high & low voltages	each PSU	software	hourly
	repair history	board	manual	as req.
Magnet	current	each PSU	monitoring systems	hourly
	field	plate	monitoring systems	hourly
General	environmental conditions (e.g. temperature)		monitoring system	as req'd.

Table 6.6: Examples of the information that will be recorded in the database during the different phases of the experiment.

looking at a web page with a Java applet running a JDBC connection to the database, which will not only find the correct switch settings, but also invoke a picture of the board with the switches set correctly. The same applet will also request the serial numbers of the new and old boards, and put them in the database. Having the same program with the switch settings request the serial numbers will ensure that the new numbers will be entered immediately, correctly and promptly.

The size of the database is estimated to be about 4 GBytes after five years running. Over half the space will be occupied by calibration constants determined from throughgoing muons. The relationships between the individual data items is not sufficiently complicated to warrant an object-oriented database with its attendant expense and possible small company problems. The Oracle database system, which is a commercial, supported product, provides all the required functions. Fermilab has a great deal of experience with Oracle, which is used extensively on site. The Electronics and DAQ cost estimate assumes the use of Oracle as the MINOS database.

6.4.6   Auxiliary systems (WBS 2.3.6)

6.4.6.1   Monitoring

Monitoring functions (for high and low voltages, etc.) are built into the front end units, the hubs and the interface crates, and have been costed with these components. Monitoring of the central system crates uses the Canbus system and is included in the cost estimate. Other control and monitoring functions will be provided by simple custom or commercial standalone units linked to a control PC by Ethernet. One PC at each detector site is required to support the monitoring systems.

6.4.6.2   Absolute timing

The complete far- and near-detector electronics systems must be synchronized to absolute time. The absolute times of the Main Injector spills at Fermilab must also be recorded to allow events (especially in the far detector) to be associated with the MI neutrino beam. GPS timing receivers are the preferred source of absolute time and routinely give accuracies of 100 to 200 ns for moderate cost units.

GPS timing receivers will be used in all three locations: the far detector at Soudan, the near detector and the Main Injector. At Fermilab we assume the timing receiver output can be used by a spare channel of an existing timing module to make the spill time available from their computers over the Internet.

At both the near- and far detector sites the GPS receivers (which require minimal space) will be located on the surface to eliminate the need for low-loss coaxial feeders to be installed in the shafts. Timing signals from the receivers will be sent to the interface crates over fiber-optic cables installed in the shafts.

Distribution of the system clock derived from the GPS system is by way of the interface crate and the hubs; the costs of clock distribution have been included in the costs of these subsystems.

Communications between Soudan and Fermilab are assumed to be by Internet. Timing

is only a minor use of the communications links, and the fiber optics cables are provided by the near and far detector installation tasks.

6.5 Future optimization and engineering

All components of the electronics system will require prototyping and optimization. The areas where this will be most necessary are the front ends and the central system; the goal will be to reduce costs and improve performance.

6.5.1 Front ends

The design described provides a conservative basis for the estimation of costs and schedules; it is not finished at the component level. The design is considered usable for full scale production, but we expect that further work will lead to higher performance and lower cost. Implementation of the channel electronics in an ASIC may prove worthwhile; this is not, however, part of the baseline design presently proposed.

The front end electronics described is specific to the baseline detector design: i.e., Hamamatsu 16 channel PMTs, and 23,000 channels at the far detector and 9,400 channels at the near detector. This system has, however, been designed to allow for some changes that are being considered.

The power dissipation has been kept low enough to allow for possible upgrading from eight-fold to four-fold multiplexing on the far detector, doubling the number of channels to 46,000 (or even 70,000 with the addition of a third supermodule).

The timing performance of the detector is limited by the scintillator and the wavelength shifting fibers to ~10 ns rms for a single photoelectron signal. In the current design of the electronics, time is measured on each channel with a resolution of 5 ns, which allows a relatively simple design using FPGAs; a high resolution timing output is provided for groups of channels. The inclusion of high resolution timing on a per-plane basis internal to the front end units by the use of an existing TDC chip is anticipated.

If there is a substantial increase in the light yield from the scintillator it may be worthwhile to improve the single-channel timing resolution. A modest improvement may be possible with the design as described: a factor of two seems as if it may be possible, but this would need to be demonstrated.

Two 16-channel units, each with one M16 phototube, are currently under construction. Although they are considerably simpler than a full front end unit they are designed to be used to demonstrate that the required noise performance and noise immunity (e.g., to welding noise) can be achieved with the proposed scheme, to study timing performance and to study the effects of fringe magnetic fields on the DC – DC converters. The experience gained with them will allow the final front-end design to be optimised; in particular these units have exchangeable mezzanine cards to allow details of the critical analogue first stages to be studied.

6.5.2 Hubs and interface crate

The hub-interface crate system uses well-established technologies. Some prototyping and optimization will, nevertheless, be required. In particular, the scheme for clock distribution needs to be proven and optimised.

6.5.3 Central system

Development and prototyping will be needed to ensure that the desired performance requirements of the central system can be met, and to confirm the estimates of the size of the final system. The development program for the central data system and the trigger farm will make use of a prototype, scaled-down version of the hardware, the network connection and the software to develop and study the performance of the system.

Most of the hardware used will be commercial and, by developing a scaled-down version of the receiver hardware (as PMCs on the microprocessor boards), the real-time aspects of the system will be studied. With some added functions this test receiver card can also be used to act as a generator of simulated data for subsequent receiver card tests. The network performance will also be studied before the final system is assembled.

6.5.4 Trigger farm

Ongoing physics simulation studies will be performed to optimize the trigger algorithm as the detector design evolves. In addition, the special requirements for cosmic ray and calibration triggers will be investigated and the effect of overlapping events in the near detector on trigger algorithms will be studied.

Further analysis and design of software for the trigger farm will be undertaken leading to the production of prototype code, which will be tested and evaluated on a microprocessor system using simulated data as input. Simulation of the trigger farm will allow us to investigate communication, control and scheduling issues in a realistic environment and to ensure that processing, bandwidth and error recovery requirements are understood. This will require DART to be installed on a PC and interfaced to the simulated trigger farm output processor which, in turn, will allow us to acquire experience in the operation of DART in the MINOS context and in adapting it to our specific needs.

6.5.5 Triggered operation

The baseline electronics system is designed to be adaptable to operating in a simple triggered mode if this proves to be necessary.

Assuming a trigger output for each detector plane is available from the front end units, an 'M of N planes' hardware trigger can easily be implemented in the hubs, which are located in a single row along each side of the detector. A trivial addition to the support modules in the hubs would be needed to pass plane trigger outputs between adjacent boards. The simple logic required would be added to that already present on the Xilinx FPGA.

It would be necessary to pass plane trigger outputs between adjacent hubs to allow a M/N type trigger to be made fully efficient for planes at the boundaries between hubs. Only

$N-1$ signals, probably less than 8, would have to be passed. Direct electrical transmission as differential signals over the short cable required would be acceptable; the addition of a simple interface module to buffer the signals and bring them to a connector is all that is required. The hub is built so these trigger modules merely have to be plugged in if operation in a triggered mode becomes necessary. In this scheme a trigger from each side of the detector is formed separately. The two triggers would be combined before being distributed to the front end units. It is impractical to combine the outputs from both ends of each plane before building the trigger. Such a system would take a large amount of extra cabling, and considerably increase installation costs.

The FPGAs on the front end unit mezzanine boards and main boards can be programmed to operate in a triggered mode. The ready reprogrammability of these devices allows details to evolve as requirements become clearer. They would allow 'per plane' trigger outputs to be formed, which would be passed back through the connection to a hub. They would also accept the global trigger passed back in the same way. The sampling of peak values and recording of times of hits would be unchanged, but now, if no trigger were received within a preset time (say 750 ns) the recorded values would be discarded; voltages would be converted and data output only if there were a trigger signal within a preset time.

A second way a triggered system could operate would be to use slower shaping, and only sample the peak of the photodetector pulses on receipt of a trigger. All channels could then be read out, and it would not be necessary for pulses to have been detected totally reliably by the discriminators on each channel. This strategy would require a long enough shaping time to allow a global trigger signal to be formed, passed back to the front end units and still to sample the peak of the pulse with sufficient accuracy.

Variations would be possible within the triggered mode. Different logic to form the trigger outputs could be selected; times, such as how long pulses are stretched, could be varied. There could also be another input to the trigger system; a signal summed across all channels of one plane could be formed and provided with an additional discriminator to permit a 'total energy' trigger. It would not work well unless the spread in channel gains is corrected, and would not be practical at the near detector where one plane is spread across many front end units.

6.5.6   Test beam studies

MINOS test beam work will start in 1999 and will continue off and on for several years. Initially it will be directed to studying the scintillators being used for calorimetry. The final version of the electronics will not be needed, or available, for the initial tests; commercial digitizing and readout electronics will be sufficient to obtain an understanding of the behaviour of the scintillator and photodetector system. Later runs will be used to test modifications of the scintillator-photodetector system.

The most important part of the electronics system to test is the front end, where photodetector pulses are digitized. The back end (hubs to trigger farm) of the system can be sufficiently well simulated, and tested in the laboratory. Some channels of preproduction front-end electronics will be used with the test beam module for a combined system test in order to identify any problems before full-scale production is started.

The final running, which might take place as late as 2002, will be made to obtain a full

calibration of the complete MINOS detector and readout system. It will be important for these runs to use production electronics in order to understand the calibration and resolution achieved in the final detector system, including the electronics.

These schedules are compatible with the planned program of electronics development.

Chapter 6 References

[1] J.H. Cobb, "Dynamic range requirements of the MINOS electronics," April 1998, Fermilab report NuMI-L-368.

[2] J.H. Cobb, "Cosmic ray muon rates in the MINOS near detector," December 1996, Fermilab report NuMI-L-232.

[3] K. Ruddick, "Underground particle fluxes in the Soudan Mine," September 1996, Fermilab report NuMI-L-210.

[4] K. Ruddick, "Counting rates in the MINOS plastic scintillator detector due to rock and steel radioactivity," October 1997, Fermilab report NuMI-L-313.

[5] J.H. Cobb, "Singles rates in the MINOS detectors," July 1998, Fermilab report NuMI-L-372.

[6] The University of Minnesota, CNA Consulting Engineers, Ericksen-Ellison Associates, Inc., and Miller-Dunwiddie, Inc., "MINOS Far Detector Laboratory Technical Design Report (Including Basis of Estimate & WBS) for Cavern Construction, Cavern Outfitting & Detector Outfitting," October 1998, Fermilab report NuMI-L-263.

[7] The Fermilab NuMI Group, "NuMI Facility Technical Design Report," Chapter 5, October 1998, Fermilab report NuMI-346.

[8] Information about the DART system can be found at the URL http://www-dart.fnal.gov:8000.

Chapter 7

Far detector installation

7.1 Overview

This Chapter describes the installation of the MINOS far detector and its associated infrastructure in the new underground laboratory at Soudan. It includes the checkout and validation of completed sections of the detector and the transition to routine data acquisition operation. Much of the laboratory infrastructure needed for detector installation and operation has been designed as part of the MINOS cavern construction and outfitting tasks described in the MINOS Far Detector Laboratory Technical Design Report and Basis of Estimate documents[1, 2]. The transfer of control from the cavern construction and outfitting task to the far detector installation task will occur when beneficial occupancy of the new underground laboratory begins.

The detector installation procedures described in this Chapter were developed by MINOS Collaboration physicists and engineers during the preparation for the active detector technology choice, as described in the Report of the MINOS Installation Committee (MIC)[3]. Much of the material in this Chapter is described in more detail in the Basis of Estimate document for the far detector installation[4], which has evolved along with the MINOS detector design since it was started as part of the MIC process. The far detector installation task must be closely coordinated with the fabrication of detector components: the magnet steel and coils (Chapter 4), the scintillator detector (Chapter 5) and the electronics systems (Chapter 6). In general, the transfer of control from these tasks to the far detector installation task occurs when fabricated components arrive at the Soudan mine headframe.

An overview of the design of the far detector has already been given in Chapter 3 and the details of its construction have been discussed in the three Chapters preceeding this one. The main parameters of the detector, laboratory infrastructure and installation are summarized in Table 7.1.

7.1.1 Far detector facilities

The facilities required to install and operate the MINOS far detector consist of the underground laboratories (the MINOS and Soudan 2 caverns), the surface building and receiving areas, and the equipment needed to move, assemble and install detector components. In somewhat more detail, the following facilities are included:

System	Parameters
MINOS cavern	82.3 m × 13.8 m × 11.6 m (height)
Supermodules	2 supermodules, each 2.7 metric kt, 14.4 m long × 8 m wide
Planes/supermodule	243 steel planes and 242 scintillator planes (5.94 cm pitch)
Detector units/plane	192 scintillator strips packaged in 8 modules
Readout	2-ended, with 8 × multiplexing
Channel count	484 planes × 192 strips × 2 ÷ 8 = 23,232 channels
Photodetectors	1452 16-channel PMTs in 484 MUX boxes
Installation rate	1 plane/1.85 shifts or 24 planes/month (maximum)
Installation time	12 months for first supermodule, 22.5 months for two
Magnetic field	1.5 T at 2 m radius in steel octagon planes
Magnet coils	15 kA-turns, water-cooled copper wire, 58 kW total
Total cavern cooling	257 kW maximum (at the end of the installation period)

Table 7.1: Summary of some of the major parameters of the far detector and its requirements on the infrastructure systems of the MINOS cavern in the Soudan mine.

- MINOS cavern infrastructure: utilities (electrical and lighting systems, magnet coil cooling system, compressed air, fire protection), environmental control equipment, large steel structures such as the detector support, overhead bridge crane, observation deck.

- Soudan 2 cavern facilities: counting house (upgraded for MINOS), elevated platform for scintillator testing and storage.

- Surface facilities: a new building, provided by the State of Minnesota, for receiving, materials staging, offices.

- Soudan mine hoisting facilities: shaft station and cages (upgraded for MINOS), and equipment for loading and unloading large components from the shaft cages.

- Equipment needed to assemble and install the far detector: fixtures, tooling and procedures for handling, assembling and testing the large planes of steel and scintillator.

- Associated work space, storage and office areas, and facilities for the workers who will assemble and install the far detector.

7.1.2   Soudan infrastructure

Most of the infrastructure needed to install and operate the MINOS far detector is provided as part of the cavern construction and outfitting task[1]. These systems (described in Section 7.3.2) include the underground cavern itself, the 25-ton overhead bridge crane and detector support structure, devices for handling the large steel plates of the MINOS magnet, electrical power and other utilities, most safety systems (summarized in Chapter 12) and the surface receiving building. Far detector safety systems, which are described in Reference [5],

are very similar to those for the near detector[6]. Although some office facilities will be provided in the new MINOS cavern, most computers, terminals, office areas and lunchroom will be located in the existing Soudan 2 counting house. The existing lunchroom and sanitary facilities in the Soudan 2 cavern will be substantially expanded.

The electrical power required to operate the completed MINOS detector along with the other experiments located in the MINOS and Soudan 2 caverns will average about 250 kW, which is well within the capacity of the Soudan mine electrical system. About 25% of the total heat energy produced underground is from the MINOS magnet coils. The heat generated by this electrical power will be removed from the underground laboratories by a heat exchange system which will transfer the heat to an air-cooled water chiller located on the surface (see Section 7.4.1.6 below).

Most of the underground infrastructure requirements of the MINOS far detector are similar to those of a typical fixed target experiment at Fermilab. MINOS has modest requirements for electrical power, compressed air, air circulation and conditioning, counting house and computer facilities. MINOS requires only standard fire protection systems: smoke detectors, automatic electrical power cutoffs, and sprinkler systems. The surface infrastructure required for MINOS installation is very similar to common commercial facilities; it consists of standard office areas and an enclosed receiving area near the mine headframe.

Although nearly all infrastructure will be provided by other tasks, the far detector installation task includes responsibility for maintaining and operating these facilities. A small MINOS "startup" crew is already working with the architect engineering firm (CNA Consulting Engineers) on infrastructure design. The startup crew will also work with the excavation and outfitting contractors to ensure that all infrastructure systems are operating satisfactorily when beneficial occupancy occurs.

7.1.3   Detector assembly

The MINOS far detector installation task includes the procedures used to move steel and scintillator detector components into the underground laboratory, to assemble the 8-m wide octagonal planes of steel and scintillator at two workstations, and to install these planes on the rails of the hanging-file detector support structure. Detector assembly techniques will be optimized at Fermilab during the trial assembly of prototype planes (see Section 7.5.1). The far detector installation "startup" crew will participate in this activity, beginning about one year prior to beneficial occupancy of the MINOS cavern at Soudan.

The 82.3-m long by 13.8-m wide by 11.6-m high MINOS cavern is designed to accommodate two identical 2.7 kt "supermodules," two assembly workstations, and a 10-m long area reserved for a possible future detector at the upstream (south) end of the cavern. In addition, the cavern is long enough for a third 2.7 kt supermodule, but the upstream workstation would have to be removed to provide room to install it. (The third supermodule and upstream detector are not part of the baseline experiment design.) Figure 7.1 shows a plan view of the new MINOS cavern and the existing Soudan 2 laboratory. The workstations are located at the downstream (north) end of the MINOS cavern, where the cavern width is increased to 15.9 m. Figures 7.2 and 7.3 show elevation views of the MINOS cavern at the location of the detector supermodules and the workstations, respectively. Detector assembly begins with the upstream supermodule, which will be ready to operate when the NuMI
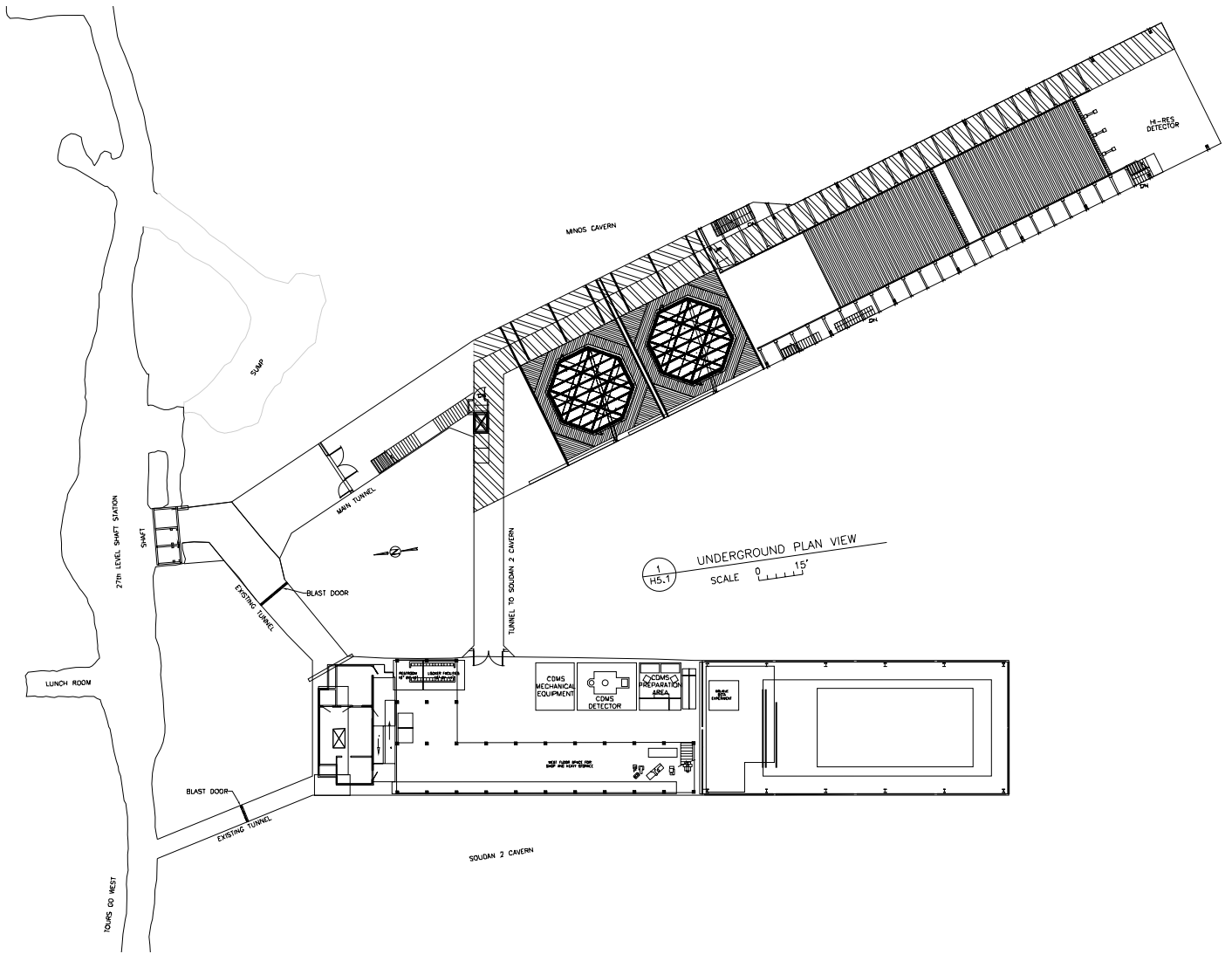
Figure 7.1: Plan view of the new MINOS cavern (top) and the existing Soudan 2 laboratory (bottom). The neutrino beam enters the MINOS cavern from the South (upper right) end, parallel to the cavern axis in this view. The two supermodules, separated by a 1.5 m gap, are shown as edge views of their steel planes, perpendicular to the cavern axis. The two octagonal workstations are shown at the North (left) end of the MINOS cavern. The 10-m long space at the upstream end of the MINOS cavern is reserved for a possible future detector.
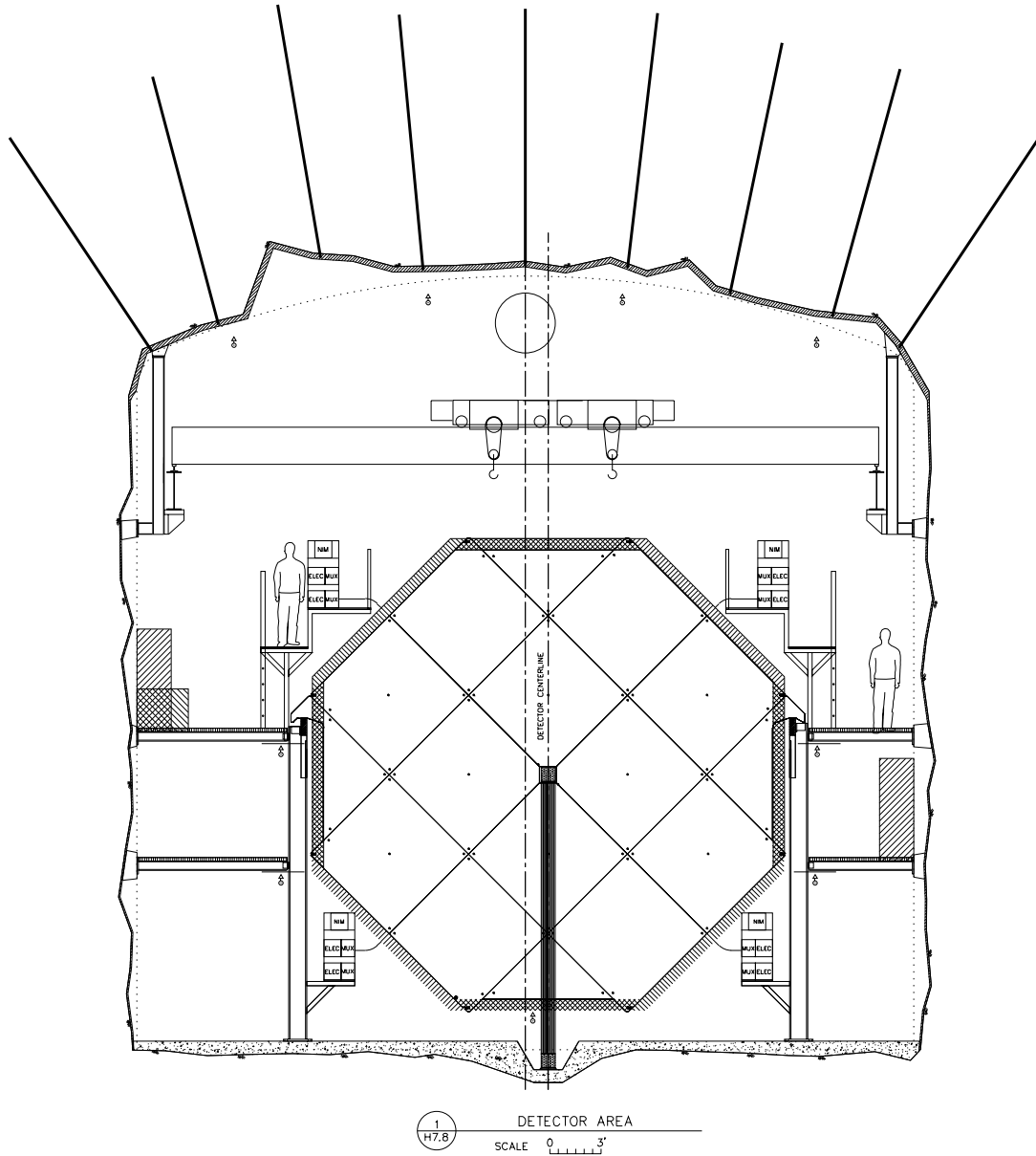
Figure 7.2: Elevation view of the MINOS cavern at the location of the first or second supermodule. The detector support rails, side walkways, electronics support platforms, magnet coil and overhead bridge crane are also shown.
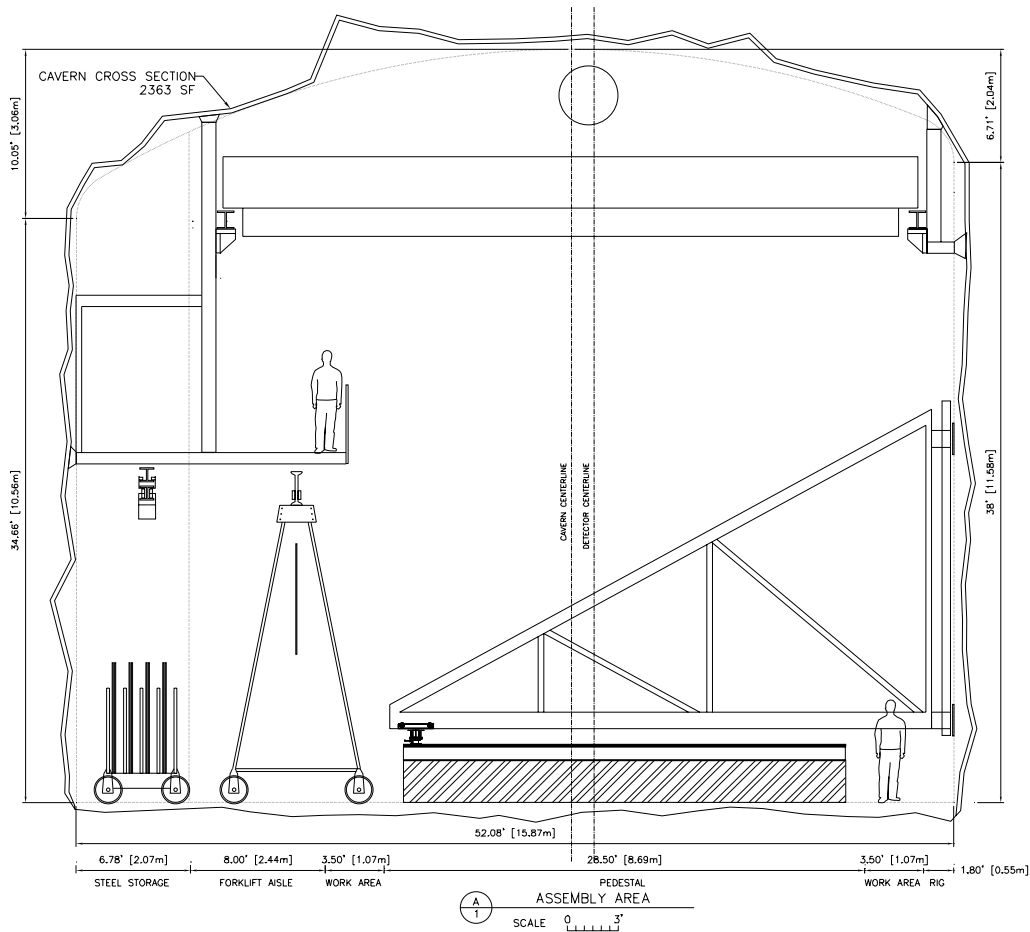
Figure 7.3: Elevation view of the MINOS cavern at the location of a detector assembly workstation. The cavern is 2 m wider at this location than at the supermodules to provide space for steel handling fixtures and for traffic to pass while plane assembly is in progress. The Figure shows (from left to right): the observation deck, the monorail, a steel storage cart, a gantry crane, a compression rig, and an assembly pedestal.

neutrino beam turns on in 2002. This first supermodule will be operated while the second supermodule is being assembled. Each supermodule coil is fabricated and installed after all the supermodule planes are mounted.

Assembly procedures are described in detail in Section 7.4 and in the far detector installation Basis of Estimate[4]. The far installation cost estimate is based on detailed installation plans and schedules developed by the MINOS Installation Committee (MIC). The technical effort for the labor-intensive installation process is the most costly component of the far-installation WBS task[7]; the effort requirements are described in detail in Section 7.4.3.

7.1.4 Testing of scintillator modules

Detector and infrastructure components which are delivered to the Soudan site will have already passed strict quality control inspections and performance tests before being shipped from commercial vendors (e.g., steel plates) or MINOS fabrication facilities (e.g., scintillator modules). Nevertheless it will be important to repeat some of these tests after arrival at Soudan to check for shipping damage. It is important to perform these checks before plane components are moved to the assembly workstations in order to maintain the required assembly rate of one plane per 3.7 shifts per workstation.

Performance tests of scintillator modules, preassembled panels of plastic scintillator strips which are 82 cm and 115 cm wide by up to 8 m long, are particularly important because internal damage may have been caused by mechanical shock or temperature stresses experienced during shipping and handling. Malfunctioning modules will delay the installation schedule if they have to be replaced after they are mounted on the steel planes. More serious delays will result if faults are detected on planes which have already been mounted vertically on the detector itself. It will be very difficult to remove a plane from the detector support structure after subsequent planes have been installed. Scintillator modules will be tested with the built-in WLS fiber light injection system and radioactive source tubes using a portable photodetector system which can be plugged directly into each module's fiber optics connectors. These tests, which are summarized in Section 7.4.5 and described in detail in Section 5.4.6, will be performed immediately after modules arrive at Soudan, after installation on the steel planes, and again after each plane is mounted vertically. The last set of tests will use the final detector-plane photodetectors and electronics, and will make use of cosmic ray muon tracks in addition to the light injection and radioactive source tubes.

7.1.5 Detector operational requirements

The MINOS detector must be able to acquire data from the first supermodule while the second supermodule is being assembled. Potential conflicts between construction and operation include the effects of electrical noise from steel plane welding, the overhead crane, and other large machines, as well as the effect of construction dirt and debris. None of these is expected to be a significant problem. The use of fiber optics for signal transmission will reduce sensitivity to noise pickup in ground loops. The design of the cavern infrastructure includes electrical power sources and grounds for the crane, welding machines, and other heavy equipment which are separate from the detector and electronics power supplies and

grounds. A low-impedance ground grid will be imbedded in the concrete cavern floor for construction equipment which could generate electrical noise.

The noise, dust and dirt from some types of heavy construction could adversely affect operation of completed sections of the detector. The welding of the steel plane assemblies can be physically isolated from the completed detector sections.

Electronics will be installed on completed sections of the detector as soon as possible so that the performance of the scintillator, photodetectors and electronics can be evaluated and monitored continuously. Performance will be monitored using charge injection, light injection and cosmic ray muons, and will allow any system-level problems to be identified at the earliest possible time. The magnet coil of each supermodule will be installed and energized as soon as the supermodule is complete. The experiment-control and monitoring systems, described in Chapter 6, will be installed and brought into operation at the earliest possible time. Many data acquisition and electronics functions will be remotely controllable, so that some diagnostic and calibration studies can be performed from remote locations over computer networks. The occupancy of the underground laboratory is therefore not expected to increase as the operating detector mass increases. Routine operation of the completed detector will require only a small on-site crew of technical experts.

Electrical power consumption and the resulting heat generation will gradually increase as more of the detector comes into operation. As this occurs, cavern air heaters will be turned off and, eventually, cavern air cooling (see Section 7.4.1.6 below) will be turned on to maintain a constant air temperature of about 70° F. Experience with the Soudan 2 cavern shows that the dry-rock conditions prevailing at Soudan allow the relative humidity of the cavern air to fall as the air temperature is raised. (The ambient mine air temperature is 52° F with 100% humidity.)

7.2   Technical requirements

The goal of the far detector installation task is to assemble and install the MINOS far detector and data acquisition system, to verify that its performance meets physics requirements, and to provide the infrastructure needed to install, maintain and operate the detector and associated systems to record neutrino interactions and cosmic ray muons. The following sub-tasks are included in the far detector installation WBS element:

- **Infrastructure installation and maintenance tasks:**

  1. **Environmental conditions.** Maintain the laboratory air temperature around 70° F and relative humidity around 50%. Control electrical noise and airborne dirt and dust as required by the electronics.

  2. **Laboratory utilities.** Establish stable and reliable operation of the electrical power, air handling and heat removal systems, and supplies of laboratory water and compressed air. Provide operational support for safety systems and protocols for maintaining them, including fire alarms and fire suppression, and control of physical, electrical, magnetic, radioactive and chemical hazards.

3. **Worker facilities.** Maintain lunchroom and sanitary facilities, offices and office machines. Establish safety training protocols for the laboratory technical staff and for visiting scientists and engineers. Establish and maintain an appropriate inventory of laboratory supplies and chemicals for general use: screws, bolts, plumbing supplies and other mechanical hardware, electronics components, solvents and cleaning supplies.

4. **Communications.** Establish and maintain communication equipment including telephones, computers, terminals and computer network connections. Establish systems for coordination of detector operation with the neutrino beam and the near detector, including absolute time (GPS clock) and clock synchronization.

5. **Materials handling machinery.** Establish procedures for operating and maintaining materials handling equipment provided by the cavern outfitting task: steel plate handling between the mine shaft and the compression rig, steel plane welding and inspection equipment, overhead bridge cranes, fork lifts, machine shop tools and hand tools.

6. **Detector access.** Establish protocols and maintain hardware for safe use of detector access facilities including the top surfaces of the detector, the detector support structure, walkways, cable trays and electronics racks.

- **Installation tasks:**

7. **Materials receiving.** Design and operate facilities for receiving detector components (steel, scintillator modules, electronics, photodetectors and fiber optics connections). Design and set up work and storage areas required to perform this task efficiently. This task includes unloading delivery trucks, transporting material underground, providing intermediate storage facilities on the surface and underground, performing inspection, inventory and performance tests.

8. **Detector plane assembly.** Set up, operate and schedule the detector plane assembly workstations and associated equipment. Design and set up work and storage areas required to perform this task efficiently. Coordinate tasks involving the supply of components to the workstations, scheduling of workers and shared equipment including use of the overhead bridge cranes. Maintain a database of all detector elements which allows the history and past performance of all components to be determined after installation in the detector.

9. **Detector plane mounting.** Establish and schedule procedures for mounting the steel and scintillator planes on the body of the detector. This includes the installation of fiber optics connections to the scintillator modules.

10. **Electronics installation.** Establish and schedule procedures for installing multiplexing boxes (including photodetectors), front end electronics, and other electronics hardware and power supplies, including the hubs, central data system, trigger farm and data acquisition equipment.

11. **Detector performance tests.** Set up, operate and maintain test equipment and protocols for scintillator modules, fiber optics connections, photodetectors,

and electronics systems. Design and set up work and storage areas required to perform this task efficiently. Perform tests at specific stages of the detector assembly process to ensure that detector performance meets established criteria. Coordinate test procedures with those at the fabrication facilities, the test beam calibration setup, and the MINOS near detector laboratory to obtain reliable comparisons of performance criteria such as efficiencies, energy calibrations and resolutions, and neutrino event characterizations. Maintain an inventory of spare detector components and establish procedures for diagnosing and replacing faulty components during and after installation.

12. **Magnet coil.** Set up, operate and schedule the magnet coil fabrication and installation. Design and set up work and storage areas required to perform this task efficiently. Establish safe and stable operation of the coils, power supplies, and cooling systems.

13. **Alignment and survey.** Design procedures for measuring and recording the locations of all components within the assembled detector. Provide measurement tools and maintain the database required to manage this information. Provide procedures and alignment templates for locating scintillator modules, mounting hardware and other components on the steel detector planes.

14. **Transition to physics operation.** Establish operating procedures and performance criteria for installed sections of the detector and begin routine data acquisition of cosmic ray and neutrino events. Begin operation of the data recording and distribution system, and of the software systems for identifying and characterizing events of interest.

7.3 Interfaces to other MINOS systems

7.3.1 Soudan detector halls

The Technical Design Report for the Soudan site preparation[1] describes the excavation of the underground cavern for the MINOS far detector at Soudan (including the rockbolting and concreting of the floor, walls, and ceiling), the outfitting of this cavern with utilities (electrical systems, electronics grounding grid in the concrete floor, air handling and conditioning, lighting, fire protection systems), the 25-ton overhead bridge crane, the support structure for the 5.4 kt detector and other detector installation equipment. The outfitting also includes all materials handling equipment (e.g., the monorail system for moving steel plates), the preparation of work and storage areas in both the MINOS and Soudan 2 caverns, and surface facilities (e.g., office areas, storage areas and receiving facilities for large detector components). The site preparation TDR includes compliance with State and Federal regulations, for example, the preparation of an Environmental Assessment Worksheet[8]. It also covers the upgrade of the hoist system and the fabrication of the new West shaft cage, which is needed for moving large detector components underground. Two existing shaft cages will be modified for rock removal during the MINOS cavern excavation.

7.3.2 Soudan steel structures

The MINOS far detector cavern construction and outfitting task[1] includes the design and fabrication of the following steel structures in the new MINOS cavern:

- **Utility deck.** This 240 m^2 steel-grating platform is suspended 7 m above the cavern floor at the downstream end of the MINOS cavern. It provides a large visitor observation area, a mechanical-electrical utility room, office areas and storage space.

- **Bridge cranes.** Two bridge cranes share the same set of rails and serve the entire underground cavern area including the most of the observation deck. The 25-ton bridge crane has two 15-ton hoists and is used mainly for mounting assembled steel and scintillator planes on the body of the detector. The 2-ton bridge crane, which is installed upstream of the 25-ton crane, has two 2-ton hoists and is used mainly to provide personnel access to the upper surfaces of the detector.

- **Shaft cage.** A new, custom-built MINOS shaft cage will be used in the West Soudan mine shaft during the outfitting and installation phases of the experiment. This 3-deck cage can be configured to transport personnel (e.g., tourists and MINOS technicians), 2 m by 8 m steel plane components, scintillator module shipping crates, and other materials between the surface and the underground laboratory shaft station. The cage can carry a 6-ton load and is equipped with a 7-ton electric hoist to aid in loading and unloading heavy objects. The underground shaft station will be modified to permit loading and unloading of plane components. Both steel and scintillator plane components will be specially packaged to fit into the new cage and for handling by special rigging equipment.

- **Monorail steel transport.** The ceiling-mounted monorail system is used to move steel plates and other equipment from the shaft station to the workstation storage areas.

- **Detector support structure.** This steel-beam structure supports the rails on which the 8-m wide octagonal detector planes rest and also provides elevated access and work areas on steel-grating decks adjacent to the detector planes. The structure supports the platforms and walkways which give access to the four 45° sides of the octagonal detector, where the photodetectors and associated electronics are mounted. The structure includes the "bookend" supports to which the first steel plane of each supermodule is attached. Electronics support platforms will be permanently installed only after the planes which they serve are in place.

- **Assembly pedestals.** Each of the two assembly workstations is built around a central assembly pedestal. The pedestals are steel and concrete structures which support the strongbacks on which the octagonal steel and scintillator detector planes are assembled.

- **Strongbacks.** A strongback is used at each assembly workstation as a rigid support upon which the eight steel plates of an octagon plane are assembled, compressed and plug welded. After the scintillator modules are mounted on the steel plane, the strongback and detector plane assembly is raised into the vertical orientation by the 25-ton

bridge crane and set on the detector support rails where it is supported by the steel plane "ears."

- **Compression rigs.** The compression rigs are used to apply 10-tons of compression to the octagonal steel plane assemblies while plug welds between the two layers of a plane are being made. Each rig consists of a rigid truss frame which mounts to the cavern wall and swings out over the assembly pedestal and strongback. Four compression jacks and a plug welder are mounted on the under side of each rig on a roller system.

- **Rolling gantry cranes.** Two 2-ton rail-mounted gantry cranes are used to transport steel plates and scintillator modules from storage racks to the two workstation assembly pedestals.

- **Steel plate storage carts.** These 45-ton capacity, 8-m long carts are used to store the steel plates delivered by the monorail, and to move them under the coverage of the workstation gantry cranes.

- **Scintillator carts.** These 2-ton capacity, 8.5-m long carts are used to move scintillator module crates from the shaft station to the Soudan 2 cavern testing and storage area, and from there to the MINOS assembly workstations.

- **Scintillator storage and test area.** A 150 m^2 elevated platform will be constructed in the Soudan 2 cavern for use as a scintillator storage and test area. This area is large enough to store 60 planes of scintillator modules, so that scintillator shipments can be suspended to avoid extreme weather conditions if necessary. The platform also provides space for testing scintillator modules as soon as they arrive underground.

Because each 11-ton detector plane is supported only by its two 1-inch thick ears, the hanging file support rails on which the ears rest are located as close as possible to the edges of the octagons. However, the ears have been lengthened to provide additional space between the sides of the steel planes and detector support structure columns. This allows the periphery of the detector planes to extend beyond the steel planes to accommodate the detector "hair" – the endpieces of the scintillator strip modules containing fiber optics and connectors, the WLS fiber light-injection hardware, and the radioactive source tube access points. The hair must not extend beyond the following maximum distances from the edges of the steel planes: 20 cm on the sides, 40 cm on the top, and 25 cm on the bottom. The bottom hair allowance corresponds to a distance from the bottom edge of the steel plane to the floor of 75 cm, which gives access for work on the bottom ends of detector elements. Any hair which is installed while the plane is horizontal (e.g., cable trays and clear-fiber-optics harnesses) must be protected from damage as the plane assembly is raised into the vertical orientation and rigged into place on the detector. For this purpose, an extra 10 cm of "keep clear" space has been provided on each side, between the vertical sides of the hair boundary and the vertical detector support columns.

In addition to these restrictions, the scintillator detector planes must be designed to fit under the steel plane ears and around the central magnet coil hole, both of which are rigidly connected from plane to plane, to set the spacing between the steel planes. The ends of the

detector modules must also be tailored to fit under the axial bolts which connect each steel plane to its neighbors at the eight corners of the octagons.

7.3.3   Magnet coil

Each MINOS far detector supermodule is toroidally magnetized by a water-cooled copper-wire coil[9]. The coil for a supermodule is assembled and installed after all supermodule planes have been mounted. Each coil consists of a central section, in a water-cooled bore tube through the axial coil hole of a supermodule, and an air-cooled return section located in a floor trench directly beneath the central coil section. Each coil has 150 to 180 turns of 1.48 cm diameter insulated, stranded copper wire which is pulled through the bore tube along with additional cooling-water tubes. Each turn includes air-cooled vertical segments which connect the central and return sections. The turns are connected by crimping near the bottom end of one of the vertical segments. The 15,000 Amp-turn coil is designed to provide an average toroidal magnetic field of 1.5 T with minimum electrical power (and heat generation) and minimum temperature rise at the center of a supermodule (which could affect detector performance). Each coil dissipates 20 kW of electrical power and each coil power supply requires 29 kW of input power. The coil cooling-water transfers the heat generated by the coils to the cavern cooling system (described below in Section 7.4.1.6). The magnet steel and coils task (Chapter 4) provides the coil materials, assembly fixtures, power supplies, cooling system and field monitoring devices. The far detector installation task is responsible for installing and operating these systems. In particular, the coil cooling water system must be integrated into the MINOS cavern utilities infrastructure.

7.3.4   Scintillator planes

As described in Chapter 5, the MINOS active detector elements consist of 1-cm thick, 4.1-cm wide strips of plastic scintillator which are packaged into "modules" of 20 or 28 strips each. Each of the eight modules needed to construct a plane of MINOS scintillator detector is designed to fit around the steel plane support structures (ears, axial rods, and coil collars) while still allowing access to its fiber optics connectors. Scintillator modules are packaged at the fabrication facilities in special shipping crates which are designed to be easily rigged onto the Soudan hoist cage.

Storage space is provided in the Soudan 2 laboratory for up to five truckloads of modules (each truckload contains scintillator modules for about 12 detector planes), allowing shipments to be suspended during the coldest part of each winter if necessary. Empty shipping boxes are returned to the fabrication facility as soon as modules have been installed. Scintillator modules which fail performance tests will be returned to the fabrication facility for repair or rebuilding.

The far detector installation task also includes the installation of fiber optics connections between scintillator modules and multiplexing boxes, the multiplexing boxes themselves, the photodetectors and front end electronics. This is described in the following Section.

The scintillator modules and associated test equipment and protocols are supplied by the scintillator fabrication task (Chapter 5). This task also provides the barcode reader

hardware and the database software system used to manage the inventories of scintillator, steel, electronics and other components at the Soudan site.

7.3.5 Electronics and data acquisition

Electronics and data acquisition hardware will be installed on each plane after it is mounted vertically on the completed detector. Front-end electronics will be located in crates at regular intervals along the four 45° faces of the octagon. Crates along the two upper faces will be supported on special cantilevered platforms attached to the side support structures, and can be accessed from the upper side walkways. Crates along the two lower faces will be located on similar platforms attached to the lower part of the detector support structure. These platforms will be built as part of the cavern construction and outfitting task. The arrangement is shown schematically in Figure 7.4. Each set of platforms is installed only after all nearby detector planes have been mounted in place. In addition, the installation task includes the complete installation, checkout and validation of all electronics components, including the photodetectors, multiplexing boxes, and fiber optics harnesses which connect them to the scintillator modules. All these components will be inspected and inventoried after arrival at Soudan, and a supply of spares will be maintained to replace faulty units.

As soon as a set of planes has been successfully read out through the electronics and data acquisition system, it becomes part of the operating detector, and will record calibration data from cosmic ray events while the remainder of the supermodule is being assembled. Operation of completed detector planes while others are being assembled and installed requires special precautions to suppress electrical noise generated by welders and other heavy equipment. Special quiet power circuits, with rf shielded transformers and a separate ground system, is provided for the electronics, and a low impedance ground grid is imbedded in the concrete floor to provide good grounding for welders and other construction equipment.

The electronics task supplies all electronics and data acquisition hardware, power supplies, crates, cables, test equipment and operating protocols. The installation task must provide the required platforms, access walkways, cable trays, electrical power and grounding systems.

7.4 Description of WBS elements

This Section describes the far detector installation activities included in each WBS-2.4 Level 3 task. The associated EDIA activities are included in the individual tasks at Level 4, and in the FY 1999 optimization and engineering program (Section 7.5). Most far detector EDIA work is performed under other tasks, e.g., magnet steel and coils, scintillator fabrication, and electronics. However, EDIA effort for engineering liaison to other tasks, and for installation oversight, is included under the far detector installation task.

7.4.1 Infrastructure (WBS 2.4.1)

This Section describes the far detector installation tasks associated with Items #1-6 of the technical requirements listed in Section 7.2. Nearly all experimental infrastructure will be
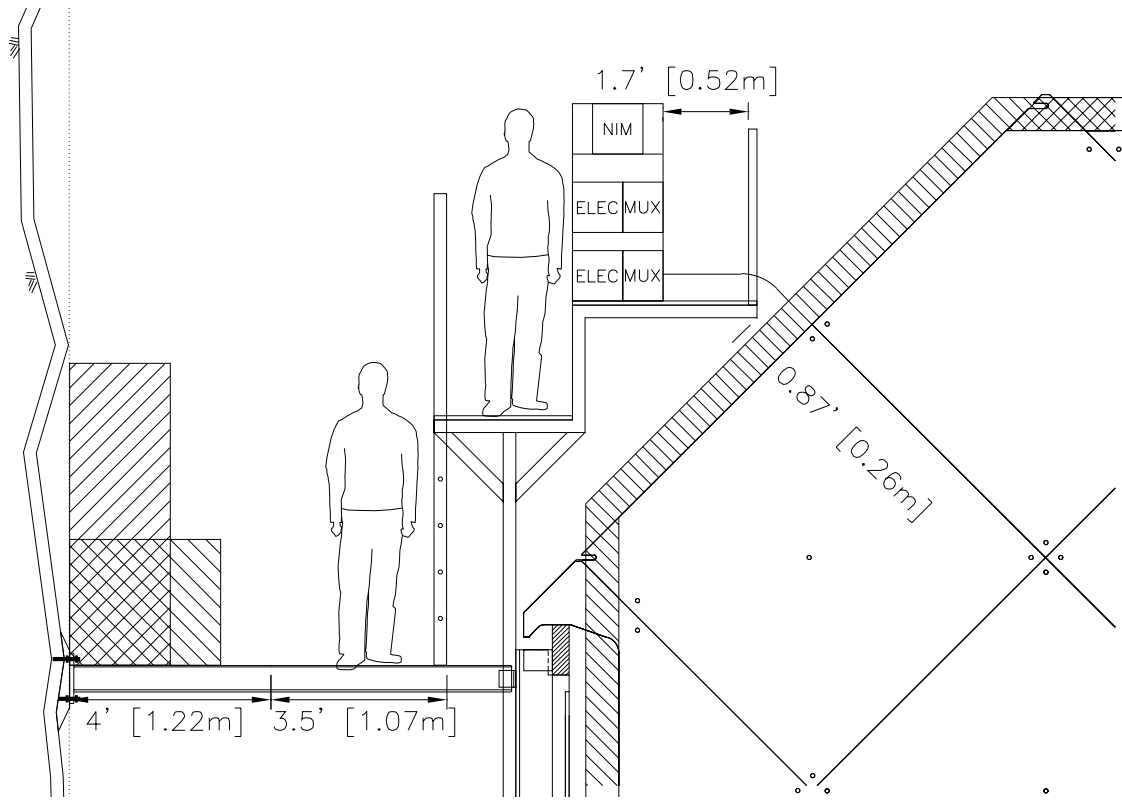
Figure 7.4: Sketch of one of the platforms used to support the multiplexing boxes and front-end electronics crates near one of the upper 45° faces of the MINOS detector. The walkway and personnel access platform is also shown. These platforms, and similar ones on the other three 45° faces, are installed only after all nearby detector planes have been mounted in place.

designed, fabricated and installed as part of the MINOS cavern construction and outfitting task. The surface building is being provided for MINOS use by the State of Minnesota. The far detector installation task includes performance tests of infrastructure equipment as well as its operation and maintenance.

7.4.1.1 Surface facilities

Receiving building. A 500 m^2 (15 m by 34 m) light industrial building will be constructed within one mile of the headframe for materials receiving and staging. The structure has a poured concrete floor, a 10-ton overhead crane and basic industrial building lighting and utilities. The structure has heat and air conditioning so that it can be used for storage of scintillator modules until they are moved underground. An additional 400 m^2 uncovered parking lot immediately adjacent to this building is used as a staging area.

During detector installation the receiving building facility is used for inspecting, sorting and packaging steel plates prior to loading onto the hoist cage. Each of the 486 8-m wide, 1-inch thick steel octagons of the MINOS far detector is assembled from eight 2-m wide, 0.5-inch thick plates which are up to 8-m long. These are delivered to Soudan from steel suppliers in large multi-truckload shipments. In the receiving building these shipments are unloaded, inspected and sorted into "bundles" each of which contains the four plates needed to construct one of the two layers of a steel octagon. These 5.5-ton bundles are loaded onto special "cage-loading" trucks designed to transport them to the headframe and transfer them to the MINOS shaft cage. The receiving building has enough space to store the steel plates and scintillator crates for one month's installation work (22 planes).

After the detector installation is complete, part of the surface receiving building will be converted for use as a computer center to support data acquisition activities. The remainder of the building will be used for office space and storage during the operation phase of MINOS.

Office space. The experiment will require some office space on the surface near the Soudan mine shaft headframe in order to coordinate detector installation activities. This is provided by a 100 m^2 enclosed area in the receiving building. The installation task provides office machines, telephone lines and necessary supplies for this facility.

7.4.1.2 Counting house and office areas

The existing Soudan 2 counting house facility will be converted for MINOS use as part of the cavern construction and outfitting task. This two-level facility contains areas for offices, computers, computer terminals and a lunchroom. The Soudan 2 lunchroom and sanitary facilities will be expanded to accommodate the large MINOS installation staff. Additional office space will be located on the Observation Deck (see Section 7.3.2). Some computer terminals will also be located along the East wall of the MINOS cavern, immediately adjacent to the detector supermodules and electronics, on the upper walkway. Detector electronics will be connected to computers in the counting house by a computer network fiber optics cable. The total area of underground office space will be about 40 m^2.

7.4.1.3 Mechanical work areas

The existing Soudan 2 staff shop, containing general purpose machine tools (lathe, milling machine, drill press, band saw), will be upgraded for MINOS installation work. The existing supplies of hand tools and mechanical parts will be maintained for MINOS use. New mechanical work areas will be set up at each of the two MINOS workstations, which will require supplies of general purpose hand tools and supplies in addition to the large steel plane assembly fixtures (plane assembly platforms, strongbacks, compression rigs) which are provided as part of the cavern outfitting task. Each workstation contains a work area of 120 m^2; other mechanical work areas will have a total area of about 140 m^2.

7.4.1.4 Electronics work areas

The existing Soudan 2 electronics work area, containing general purpose tools and instruments, will be upgraded for MINOS installation and repair work. Existing supplies of electronics components will also be maintained and expanded for MINOS use. New electronics work areas will be set up along the walkways adjacent to the supermodules for use during the cabling and checkout of newly installed detector planes. The total area of underground electronics work areas will be about 70 m^2.

7.4.1.5 Communications

The existing communications infrastructure which is already operating for the Soudan 2 experiment will be upgraded for MINOS. The current system relies on a number of twisted-pair telephone lines installed in the 713-m deep mine utilities shaft for telephone and computer network (Multinet-TCP/IP) connections to local telephone lines on the surface. These lines are also used to transmit data, including GPS clock data, from cosmic-ray surface detectors to the Soudan 2 underground data acquisition system. In addition, the underground experiment records the absolute time of every triggering event from an underground WWVB clock receiver which is connected to a surface antenna through a coaxial cable in the mine shaft.

For MINOS, a high-bandwidth fiber-optics communications line will be installed in the mine utilities shaft to supplement the existing surface-to-underground connections. This will support a high-capacity data link between the underground experiment and a local surface computer facility, and will also improve internet service. In addition, the WWVB clock system used for Soudan 2 will be upgraded to a GPS-based system, using a receiver on the surface to provide precise absolute time information to the underground data acquisition system over the fiber optics data link. The MINOS GPS timing system is an essential part of the communications link between the Fermilab Main Injector and the MINOS far detector, as described in Chapter 6. Installation of the improved communication lines in the Soudan mine utilities shaft is the responsibility of the far detector installation task. It will occur at the same time as the installation of the water-cooled chiller lines in the shaft, as described in the next Section.

7.4.1.6 Environmental control and monitoring

The basic infrastructure needed to maintain comfortable temperature and humidity levels in the MINOS laboratory is provided as part of the cavern construction and outfitting task. Operation and maintenance of these systems is transferred to the installation task at the time of beneficial occupancy of the MINOS cavern. During detector assembly it is also necessary to control the dust and dirt generated by construction activities, particularly welding. Electrical noise from welding and electrically powered machines is isolated from the detector electronics by using separate "quiet power" circuits and ground systems for the latter. A low impedance steel mesh built into the concrete of the cavern floor provides grounding for electrically noisy equipment. As data acquisition begins, environmental conditions are recorded from a number of sensors and transducers which are provided as part of the monitor and control system (supplied by the electronics task, described in Chapter 6).

As the installation process proceeds and the mass of operating detector grows, the electrical power consumption and heat generated in the cavern will gradually increase. Electrical heaters in the air ventilation system will be adjusted, and eventually turned off, to compensate for heat generated by detector systems. Eventually the air-cooling and magnet-coil cooling-water systems will be activated. Maximum power usage will occur when both detector supermodules and magnet coils are in full operation. This anticipated average power usage is summarized in Table 7.2. The heat generated by the magnet coils will be transferred directly to the cavern cooling system by an extension of the chilled water system.

Equipment	Average power
Soudan 2 Lab and detector	70 kW
CDMS experiment (Soudan 2 Lab)	50 kW
MINOS Lab lights and utilities	25 kW
MINOS electronics	25 kW
MINOS magnet coils	58 kW
MINOS cavern cooling	20 kW
Total Lab power	**248 kW**

Table 7.2: Time-averaged electrical power requirements of equipment in the MINOS and Soudan 2 laboratories during routine data acquisition operation. The total power load is the basis for the calculation of the 257 kW cavern cooling requirement, which includes an additional 9 kW for heat produced by personnel.

Most of the heat generated by the experiment will be removed from the underground laboratories by a heat exchange system which will transfer the heat to an air-cooled water chiller located on the surface. Piping will be installed in the mine utilities shaft between the MINOS cavern and the surface, and then extended horizontally to the chiller, which is located some distance from the shaft. Three intermediate heat exchangers with circulation pumps will be installed at intervals along the mine shaft to separate the system into pressure zones. A small fraction of the required cooling will be provided by the natural flow of cool air up the Soudan mine shaft. The cavern cooling system is described in detail in the Cavern

Construction and Outfitting Technical Design Report[1].

It is difficult to determine accurately the cooling capacity of the Soudan mine's natural air flow, which is currently adequate to cool the Soudan 2 laboratory. We expect that this natural air flow can supply substantial heat removal capacity, reducing the cost of the MINOS cavern cooling system described in the previous paragraph. We therefore plan to install the water-cooled heat-transfer system only after the MINOS cavern installation work is well under way and is generating sufficient heat for the cooling capacity of the natural air flow to be determined. The water-cooled system has been designed, and its cost estimated, under the assumption that it must remove all the heat produced by MINOS and CDMS (Table 7.2). The cavern cooling system has been designed to remove approximately twice the heat load which is currently anticipated.

The far detector installation task includes responsibility for maintaining and operating the cavern electrical utilities and the cooling and environmental control systems. Members of the far installation "startup" crew will work closely with the contractors during the cavern outfitting period to gain a working knowledge of all infrastructure systems and to ensure that they satisfy MINOS requirements.

7.4.1.7 Safety

Safety considerations have been included as integral design requirements for all far detector installation tasks. Issues which are specific to the Soudan underground environment, installation and operation are described in Reference [5]. Safety issues related to far detector systems are very similar to those for the near detector, which are discussed in the NuMI Project Preliminary Safety Assessment Document[6]. Safety protocols related to the underground environment are subject to review by the State Park DNR management, and are nearly the same as those which are currently in effect for the Soudan 2 experiment. Safety issues related to the rigging of massive detector components down the mine shaft and into the underground laboratories are discussed in the MINOS far detector cavern TDR[1] and in Reference [5]. Chapter 12 gives a summary of safety issues and responsibilities for the experiment.

7.4.2 Materials handling and testing (WBS 2.4.2)

This Section describes the far detector installation tasks associated with Item #7 of the technical requirements listed in Section 7.2. All major materials-handling equipment are designed, fabricated and installed as part of the cavern construction and outfitting task, as described in Section 7.3.2. The far detector installation task includes the assembly and performance testing of this equipment, as well as its operation and maintenance.

The present Section gives a detailed description of materials handling tasks during the installation period; the installation crew effort levels required to accomplish this work are summarized below in Section 7.4.3.

7.4.2.1 Moving components to workstations

The steel plane assembly process begins by moving the 8-m long steel plane sections and the crates of active detector modules underground using special fixtures and the west shaft cage. The procedure is optimized to maximize the number of cage loads which are moved per shift. The crew which moves materials underground is also responsible for keeping workstations supplied with all necessary components. Steel plane sections are delivered directly to the MINOS cavern by the monorail system, and the scintillator modules are tested in the Soudan 2 cavern before being delivered to workstations. Steel plane sections are stored in the plate storage carts in the workstation area, and moved onto the strongbacks by the 2-ton gantry cranes as needed to assemble the steel detector planes.

The following paragraphs describe the details of the steel handling procedures which have been used to estimate to cost of moving steel and scintillator detector components from the arriving delivery trucks to the underground workstations.

Surface day shift, 3 FTEs. When a shipment of steel plates arrives at Soudan, the delivery truck backs into the loading bay of the surface receiving building under the 10-ton overhead crane. The plates are unloaded using magnetic lifters and sorted into four piles: one pile for the two top-layer edge pieces, one pile for the top-layer middle pieces and the same for the bottom layer. Two work areas are provided for sorting the plates into "bundles" for shipping underground. The storage area has a capacity for 160 to 240 plates of steel (enough for 20 to 30 completed planes). As the steel is unloaded, each piece is inspected, weighed (using a built-in scale on the crane) and tagged with a barcode. These data are entered into a database to keep track of the location of specific plates after they are installed in the detector (e.g., for calculating the mass of each plane and for magnetic field modeling). The barcode reader and database system is the same one used for scintillator and electronics components.

Each bundle contains the four plates needed to construct one of the two layers of a single steel detector plane, arranged to minimize handling time underground. They are oriented so that their cambered edges match up, in order to reduce the widths of the gaps between plates in an assembled plane. Once the four plates are lined up, special bundle bolts with lifting hooks are inserted into the three central holes. For top-layer bundles, the lifting bolts use the plug-weld holes; the bottom-layer bundles have special lifting-bolt holes. All plate holes are provided by the steel fabricator.

After the steel plates are arranged in pre-sorted bundles for shipment underground, the bundles are placed on a special "cage-loading" truck which moves them to the mine shaft headframe. The truck is outfitted with special frames which guide the bundles as they are loaded into the shaft cage. Three plate bundles are loaded onto the truck, side by side with the plates oriented vertically and the long axis parallel to the truck bed, as shown in Figure 7.5. The truck is also equipped with an over-the-cab boom that holds the back end of each bundle as it is pulled into the cage.

Fourteen bundles of steel must be moved underground each week to keep up with the underground assembly schedule. At 50 minutes per cage load, only six bundles can be moved in one 8 hour shift (reconfiguring the cage takes a total of about 3 hours per shift). Thus two cage-loading trucks are provided so they can be loaded and ready at the beginning of

the evening shift. The day-shift crew members also handle all other shipments arriving at Soudan, e.g., scintillator modules, electronics, office supplies.
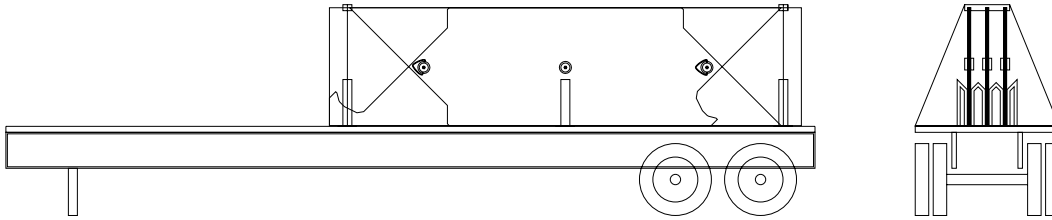
Figure 7.5: Sketch of one of the cage-loading trucks used to move bundles of steel plates from the receiving area to the mine shaft headframe. Each of the three bundles contains the four plates needed for one of the two layers of a steel detector plane.

Surface evening shift, 3 FTEs. Nearly all MINOS materials are moved underground during the evening shift (4 pm to midnight) in order to avoid interference with State Park and tourist activities. At the start of each evening shift the underground moving crew prepares the three-deck west shaft cage for MINOS use by removing the personnel decks and the front and back doors and panels of the cage (as described in the following Section). The cage-loading truck is backed up to the headframe so that the ends of the three steel bundles are close to the empty shell of the west shaft cage. The 7-ton hoist on the top of the cage is connected to electrical power. (A safety interlock ensures that the cage cannot move with the power cable plugged in.) The cage loading procedure, described in the next paragraph, is shown schematically in Figure 7.6.

The cage hoist attaches to the front lifting hook of a steel bundle and the cage-loading truck boom attaches to the back lifting point. The bundle is stabilized by the bundle frame on the truck as it is raised into the vertical orientation. As the cage hoist operator raises the bundle up into the cage, the truck boom operator slowly pays out cable, until the entire bundle is suspended in mid-air. The cage hoist continues to pull the bundle into the cage until it is suspended vertically, inside the cage, by the cage hoist. It is raised until the steel hooks mounted from the roof of the cage can be attached to the top lifting hook of the bundle. The load is now supported from this fixed point instead of from the two cables. Special clamps that can be quickly engaged are now used to secure the bottom of the plate. Once the load is secured, the truck moves out of the way and the power cord to the cage hoist is removed. The load is now ready to move underground. This loading procedure takes about 20 minutes. The cage now moves the steel bundle underground, where it is unloaded as described in the next Section. The surface crew prepares the next bundle for loading onto the cage while the underground crew unloads the previous bundle.
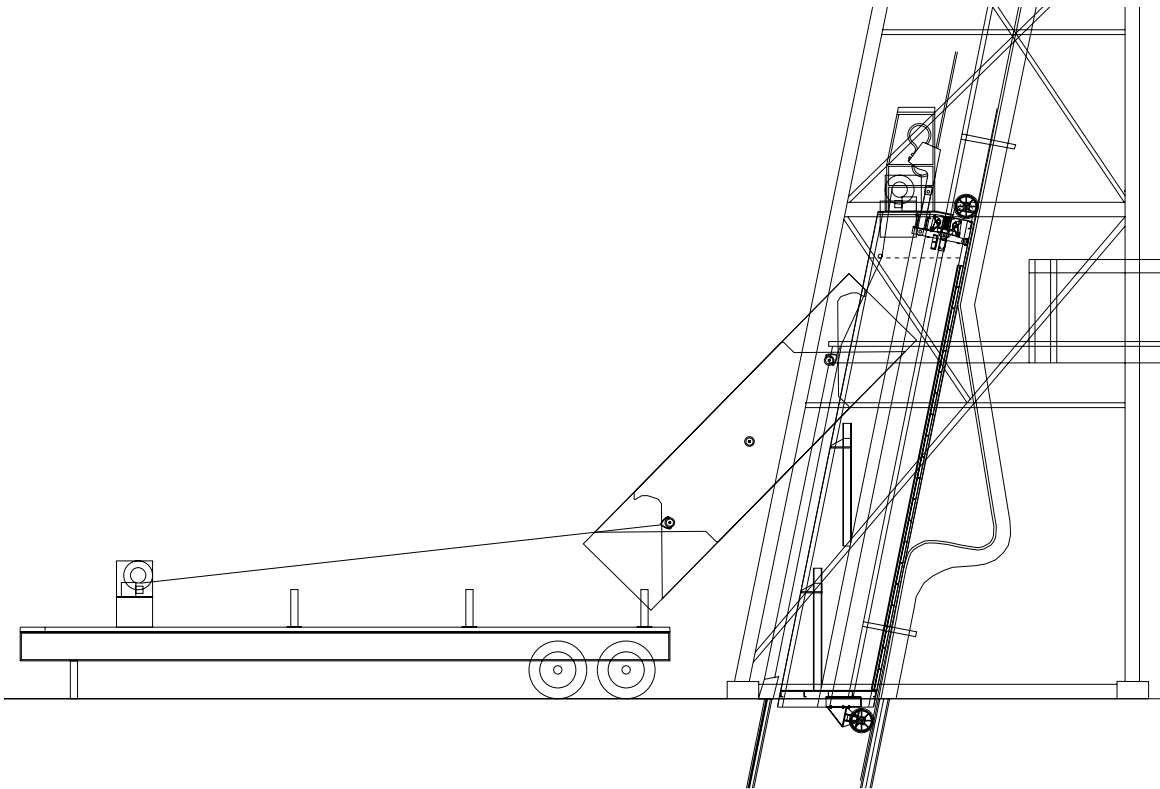
Figure 7.6: Sketch of the procedure used to load one of the presorted bundles of steel plates from the cage-loading truck (left) onto the Soudan mine shaft cage (right).

Underground evening shift, 3 FTEs. At the start of each evening shift (4 pm) the underground crew prepares the west-side shaft cage for moving steel plates (or scintillator module crates) underground. The procedure is similar to that used for the existing Soudan 2 cage. All the doors, internal floors and back panels are removed. The back panels and doors are light enough that they can be unbolted and removed by hand. The floor sections are removed as single pieces using a forklift. Depending on whether steel or scintillator is to be shipped that evening, the appropriate clamping fixtures (to hold the loads in place) are bolted in. Total time to take the cage apart is about 1.5 hours; the same time is required to clean and reassemble the cage at the end of each shift, if it is needed for tours the next morning. During the winter months the west cage can remain apart, saving 3 hours of work each evening shift.

The empty cage is sent to the surface where the surface crew loads the first steel bundle (or scintillator crate), as described in the previous Section. When the load arrives underground the cage is placed on the mine shaft "chairs" and the mine hoist cable is allowed to go slack. The chairs hold the cage in a stable position during the unloading process. The cage hoist is now powered up to assist with the unloading of the bundle. The cage hoist raises the bundle until it is free of the cage hooks. A cable is then used to attach the lower bundle hook to the "far" monorail hoist. The bundle is slowly pulled up until it is horizontal. Then the upper bundle hook is attached to the "near" monorail hoist. Once the monorail is supporting the load, the cage hoist is disconnected from electrical power and the empty cage is prepared to

return to the surface. Figure 7.7 shows the unloading process schematically.
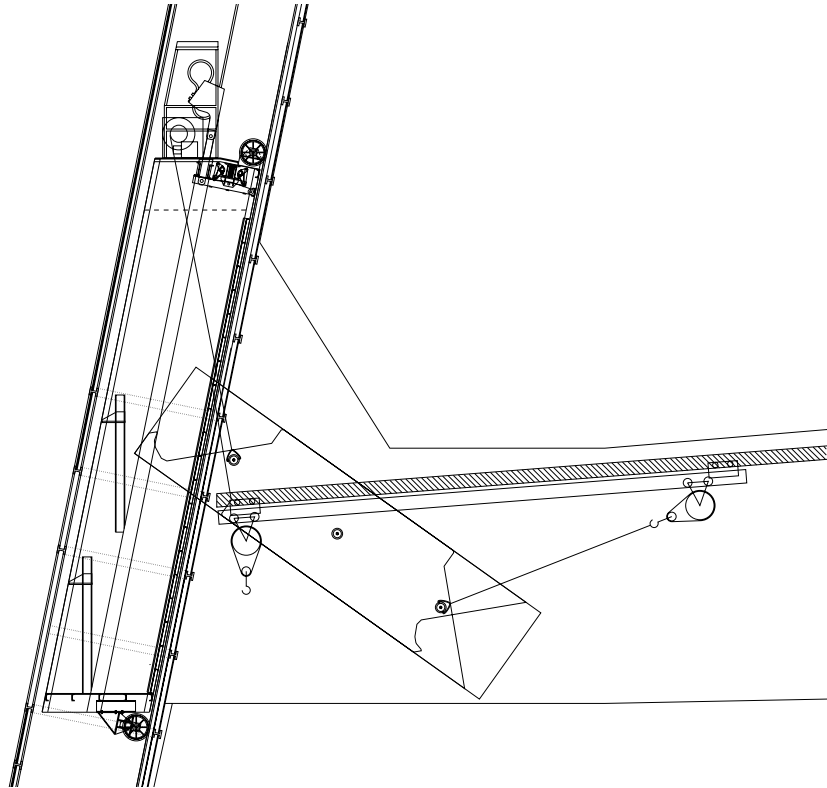
Figure 7.7: Sketch of the procedure used to unload one of the steel bundles at the Soudan mine underground shaft station. The shaft and cage are on the left and the entrance to the MINOS cavern is on the right. The monorail is the shaded bar along the entrance tunnel ceiling. The monorail's "near" hoist is on the left and the "far" hoist is on the right.

While the bundle is being moved into the MINOS cavern by the monorail, at a speed of 15 ft/min, the cage clamps and cage hoist power cable are stowed for the trip to the surface. Safety indicators in the engine house prevent the hoistman from moving the cage until the power cable is removed and all shaft doors are closed. When the steel bundle arrives in the MINOS hall it is placed in one of the two 45-ton plate storage carts. The bundle lifting bolts are removed and shipped to the surface for later use. The monorail trip and unloading procedure takes about 0.5 hour.

The total time to move one load underground is about 50 minutes, including the 5 minutes for the cage trip. Since there are effectively only 5 hours of hoist time per day, we can move only 6 bundles (or 3 planes) underground each evening. Thus, to keep the workstations stocked, steel is moved underground on three evenings/week or two evenings/week on alternate weeks.

Scintillator module handling. The handling procedure for scintillator shipping crates is very similar to that used for steel plate bundles. The same crew members who handle steel bundles also move the scintillator crates underground. During the winter months, if crates cannot be moved underground immediately after arrival at Soudan, they can be stored in a

heated section of the surface receiving building to protect them from thermal stresses. The crates are not as heavy as the steel bundles but they are larger and more fragile. The same cage-loading truck is used for the steel plate bundles and the scintillator crates. The loading and unloading procedures are very similar to those described above for the steel bundles. When a scintillator crate arrives at the underground shaft station, it is lowered onto hand carts and rolled into the Soudan 2 cavern.

Once in the Soudan 2 cavern the scintillator crates are raised onto the elevated storage and testing area, shown in Figure 7.8. This platform is serviced by a local monorail trolley and hoist system, and is large enough to store 30 scintillator crates or about 60 planes of scintillator. This gives a three-month buffer so shipping from factories can be suspended during the coldest (and perhaps the warmest) months of the year.

Before the cage returns to the surface for the next scintillator crate, an empty scintillator crate is loaded into it for eventual return to the scintillator fabrication facility. The required storage area for 10 to 15 empty crates is provided in the surface receiving building.

The total loading time, including hauling the empty crate to the surface, is about 1.5 hours. This means that only three crates per evening can be moved underground, so it takes two evenings to move one delivery truckload of six scintillator crates underground. This provides enough scintillator modules for 12 detector planes, so scintillator crates need to be moved underground only every other week, on average, to keep up with the installation schedule.

Additional materials handling. During some evening shifts only pallet loads of miscellaneous materials and small equipment items are moved underground. For these shifts, only the cage doors and back panels need to be removed, and the smaller East cage can be used in addition to the 3-deck West cage. The use of both cages saves on expensive hoist trips because one cage automatically moves from the surface to the underground shaft station when the other moves in the opposite direction.

7.4.2.2 Storage requirements

Substantial storage space is required at Soudan for the largest detector components, the steel plates and the scintillator modules. As described in Section 7.4.1.1, steel plates are manufactured and delivered in large lots. The surface receiving building provides storage space for one month's supply of steel plates and the underground assembly workstation storage carts can hold a one week supply. These are inspected, packaged and stored until they are needed underground.

Scintillator modules are produced as needed by MINOS fabrication facilities, but are delivered in truckloads containing modules for approximately twelve detector planes. Since scintillator modules could be subjected to thermal gradient stresses (caused by differential contraction of components) during the extreme cold of midwinter in northern Minnesota, it may be desirable to avoid shipping during very cold weather. Module shipments are made in heated trucks and shipping crates are insulated. Shipments during the summer months utilize air-conditioned trucks, but could also be suspended if necessary during extreme temperature conditions. Nevertheless, underground storage is provided for up to five truckloads of scintillator modules (60 planes, or about two months supply). Large storage racks with
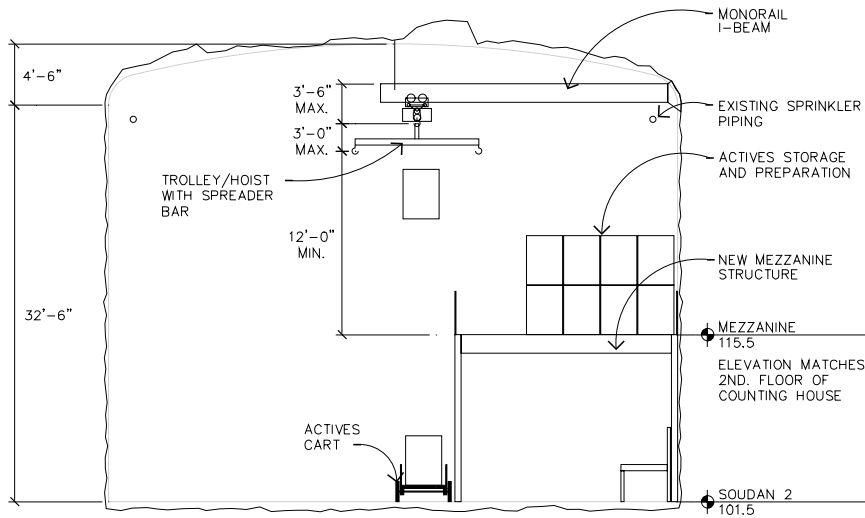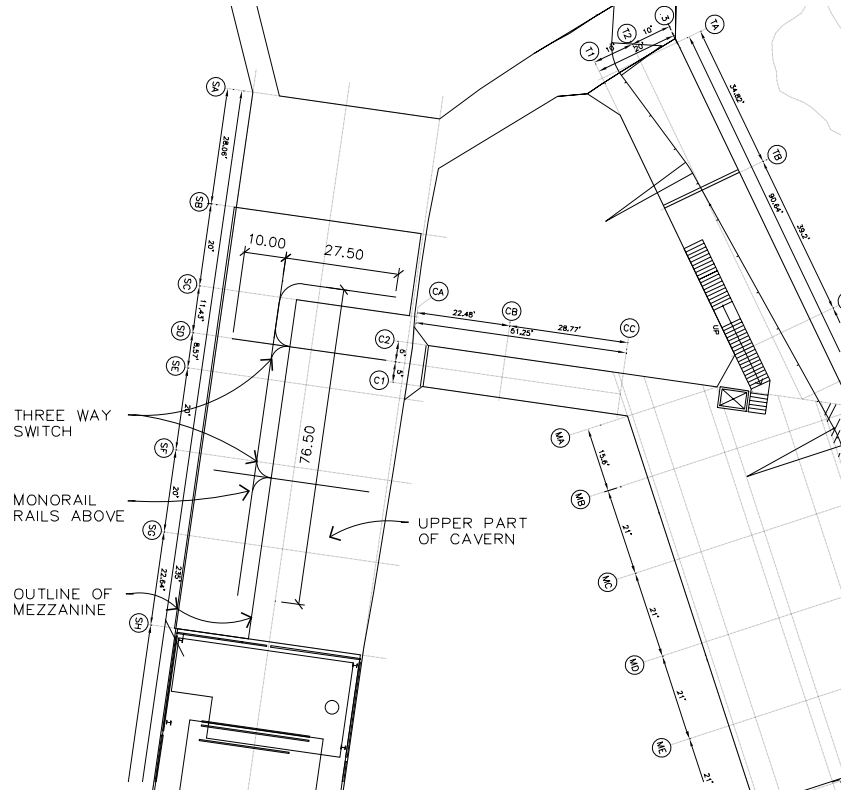
Figure 7.8: Sketches of the scintillator module storage and testing area in the Soudan 2 cavern. The top drawing is a plan view showing the outline of the new mezzanine platform and the track of the overhead monorail trolley/hoist system. The shaft station and entrance to the MINOS cavern are shown in the upper right corner. The bottom drawing is an elevation view of the mezzanine platform.

the required capacity are provided in the Soudan 2 cavern. Since it takes two evening shifts to move the scintillator crates from one truckload underground, heated and air conditioned storage space for scintillator shipping crates is provided in the surface receiving building.

Conflicts between use of the Soudan mine shaft cages by MINOS and for State Park tourists during the summer months require that all movement of MINOS equipment down the shaft occur during the evening (one shift per day) from mid-April through September. This imposes some scheduling constraints and requirements for short-term storage facilities. The Soudan 2 cavern is used for storage of smaller detector components such as photodetector and fiber optics assemblies, electronics modules and other supplies. A total storage area of 45 m² is provided for these materials.

7.4.2.3   Setup of installation fixtures

As described in Section 7.3.2, the detector plane installation fixtures are provided by the far detector cavern outfitting task[1]; conceptual designs for most of this equipment have been completed. The strongbacks, pedestals and compression rigs are assembled underground as part of the installation task. Other installation fixtures are assembled during the cavern outfitting period, before beneficial occupancy begins. Practical experience with prototypes of all of these assembly fixtures will be obtained as part of the steel plane prototype studies at Fermilab, as described in Sections 4.4.5 and 7.5.

7.4.2.4   Detector support structure

The support structure for the 5.4 kt MINOS far detector is provided by the far detector cavern outfitting task; it is described in Section 7.3.2 and in Reference [1]. Completed planes of steel and scintillator modules are mounted vertically on this structure using the 25-ton bridge crane. As shown in Figures 7.1 and 7.2, the detector support structure provides work space and access to the sides of the detector by steel-grillwork walkways which extend along its entire length. The structure also supports a set of special cross-bracing beams, called a "bookend," at the upstream end of each supermodule. A bookend acts like a permanent strongback, which rigidly constrains the first steel plane of each supermodule to be in a vertical plane, as described in Section 4.4.1.2. This first steel plane does not have a scintillator plane mounted on it. Each bookend structure also supports a crossover walkway which allows workers to cross between the elevated walkways on the two sides of the detector without returning to ground level. The bookend components are supplied by the magnet steel and coils task.

Special electronics platforms, which will be installed after detector planes are in place, allow photomultipliers, multiplexing boxes and front-end electronics crates to be arrayed along the centers of the four 45° faces of the octagonal detector. The electronics platforms are shown in Figure 7.4.

7.4.3   Detector assembly (WBS 2.4.3)

This Section describes the far detector installation tasks associated with Items #8 through 12 of the technical requirements listed in Section 7.2. Nearly all detector assembly equipment

is designed and fabricated as part of the cavern outfitting, magnet steel and coils, and scintillator fabrication tasks. The far detector installation task includes the underground assembly and performance testing of some of this equipment, as well as its operation and maintenance.

The installation of the 486 planes of scintillator modules and steel, along with associated electronics, calibration and data acquisition equipment, is by far the largest part of the far detector installation task. Most of the cost of installation is for technical effort: 39 FTEs are be required during the peak installation period, as summarized in Table 7.3. This total includes the surface and underground moving crews described above in Section 7.4.2, but it does not include the "startup" crew described in Sections 7.1.2 and 7.1.3. The startup crew began its work in FY 1998, about three years before beneficial occupancy of the MINOS cavern; its strength increases from two to six people over the three year period. Startup crew members work closely with the architect engineering firm and with the cavern outfitting contractors. It also participates in the trial assembly of steel and detector planes at Fermilab to ensure that detector installation work gets off to a fast start as soon as beneficial occupancy of the Soudan cavern begins.

Worker/activity	Day shift	Eve. shift	Total FTEs
Supervisor	1	0	1
Coordinator	1	1	2
Crew boss	3	3	6
Welder	1	1	2
Steel/scint. assembler	6	6	12
Module tester & surveyor	2	1	3
Mat'l/supply mover	3	6	9
Plane installer	2	2	4
Total FTEs	**19**	**20**	**39**

Table 7.3: Summary of the technical effort required to install the MINOS far detector during the maximum installation-rate period. In addition to this effort, four physicists per shift are provided by the MINOS Collaboration to assist the technical staff. Effort units are FTEs (full time equivalents).

The three month period immediately following beneficial occupancy of the MINOS cavern is devoted to setup of installation fixtures and equipment. Installation of the first supermodule begins at the end of this time (when full beneficial occupancy occurs) with a technical effort level of 10 FTEs. This increases to the full 39 FTEs during the following three month startup period. Including this ramp-up process, the total technical effort needed for far detector installation is about 70 FTE-years over a 2 year period. In addition to this effort (shown in Table 7.3), the MINOS Collaboration will provide four physicists per shift (including postdocs and graduate students) to assist with the detector installation and performance testing.

The following schedule assumptions have been incorporated into a detailed installation model[4], which is used to determine the 2 year installation period for the 5.4 kt far detector:

- 250 day per year operation, two 8-hour shifts per day, 6.5 working hours per shift.

- Realistic allowances for vacations, holidays, illness and inefficiencies due to assembly flow and shift changes.

- Two workstations operate in parallel.

- Three month setup-commissioning period between beneficial occupancy of the MINOS cavern and the start of the plane installation start-up period.

- Three month start-up period for assembly crew training and manpower ramp-up.

- One week to install each magnet coil.

- Two detector planes completed and installed every 3.7 shifts after the start-up period, with two workstations.

- 12 months to complete the first supermodule (including startup).

- 10.5 months to complete the second supermodule.

The duties of the workers listed in Table 7.3 are described in detail in the far detector installation basis of estimate document[4]. These duties are summarized here:

- **Supervisor.** Perform high-level supervision of installation work and provide interfaces among installation workers, MINOS scientists and engineers, and the DNR.

- **Coordinator.** Provide the interface between installation workers and the University of Minnesota (assumed to be the employer of the installation workers). Order supplies, coordinate shipments of detector components, manage office machines and telephones.

- **Crew boss.** Manage daily activities of steel and scintillator installation workers and provide smooth transitions between shifts. One crew boss is assigned to each workstation and one to the materials moving crew. Provide the interface between the supervisor and the installation workers. Act as foreman and as a general replacement worker and troubleshooter.

- **Welder.** Certified welder: perform a small number of specialized welding operations, assist with routine welding and provide spot checks of routine operations.

- **Steel/scintillator assembler.** Assemble steel and scintillator components into detector planes at two workstations.

- **Module tester and surveyor.** Open scintillator module shipping crates in Soudan 2 cavern and perform radioactive-source and light-injection tests. Perform minor repairs. Place modules for each detector plane in a single crate to facilitate rapid mounting onto its steel plane, and move crates to workstations as needed. Operate detector plane survey cameras, survey detector plane locations. Assist with installation of detector planes as time permits.

- **Material/supply mover.** Surface crew: unload arriving trucks, inspect and repackage steel plates, load arriving materials onto shaft cages. Underground crew: perform cage configuration changes between personnel and material usage, unload material from cages and transport to MINOS and Soudan 2 cavern work areas using fork lifts, monorails and carts.

- **Plane installer.** Operate overhead bridge crane to move completed detector planes from workstations to the detector. Connect fiber optics harnesses and install photodetectors, multiplexing boxes, electronics crates and cabling. Assist physicists with detector plane turnon and calibration.

Table 7.4 gives a breakdown of the time allocated for the different steps of the plane assembly and mounting procedure. Each of the two workstations can assemble and mount a complete detector plane in three shifts. By coordinating their schedules, the two workstations together can install a plane every 1.85 shifts on average.

7.4.3.1   Steel plane assembly

The far detector installation tasks described in this Section are associated with Item #8 of the technical requirements listed in Section 7.2. Each 8-m wide, 1-inch thick steel detector plane is assembled from eight 2-m wide, 0.5-inch thick plates up to 8-m long. These are arranged in two overlapping horizontal layers with the plates in the top layer oriented perpendicular to the plates in the bottom layer. At each workstation the plates are stored in 45-ton carts, which are rolled out from under the overhead monorail using electric trolleys. The gantry crane is used to pick up each plate with plate clamps and place it in position on the strongback. The plates are then wedged together using hydraulic jacks mounted around the strongback. This minimizes the widths of the cracks between plates.

Plates in the top layer have 76 predrilled 1.0-inch diameter holes which are used to plug weld the two layers together under compression, as described in Section 4.4.2 and Section 7.3.2. Once all 8 plates are in place, the compression rig is positioned over a weld point. Typically four plug welds are made in one area. Four 5000-lb jacks compress the area around the welds before plug welding begins. The welding pattern starts in the middle and spirals to the outside of the plane. A total of 35 moves of the compression rig are needed to complete a plane. Each compression rig move, setup and set of plug welds (up to four welds per setup) takes 10 to 15 minutes. A total of 8 hours per plane is allotted for this welding procedure.

The plug welding makes use of a custom-built automated weld head incorporating an automatic wire feed, a submersed arc and a fume extraction system which eliminates nearly all air contamination. This device can be operated legally by the assembly technicians and does not require the services of the certified welder except to spot-check weld quality. The plug-weld areas are cleaned and painted while mounting fixtures for detector modules and fiber optics cables are being attached to the completed steel plane, as described in the next Section.

A magnetic flux integration coil[10] is installed on each plane just before the scintillator modules are mounted. This consists of a multi-turn pickup coil which passes through the central magnet coil hole at a single azimuth and terminates in a readout connector on the

Procedure	Time
Steel plane assembly (14 hours total)	
Align 4 bottom-layer plates	1.0 hour
Align 4 top-layer plates	1.0 hour
Move compression rig/welder into position	0.3 hour
Compress/weld at 35 locations, up to 4 welds each	8.0 hour
Remove compression rig/welder	0.2 hour
Tack weld switch plates on top steel face	1.5 hour
Install mounting tabs, bars, pickup coils	1.5 hour
Clean up surface for scintillator modules	0.5 hour
Scintillator plane assembly (6 hours total)	
Install 4 center modules	1.0 hour
Install remaining 4 modules	1.0 hour
Drill module mounting tabs, screw to modules	1.0 hour
Install fiber optics cables	1.0 hour
Performance tests and survey	2.0 hour
Detector plane mounting (4 hours total)	
Inspect plane, attach lifting fixture	0.5 hour
Raise plane to vertical orientation	0.5 hour
Move plane to working face of detector	0.5 hour
Position plane on detector face	0.5 hour
Connect axial rods, coil collars	1.5 hours
Return strongback to workstation	0.5 hours
Total assembly and mounting time	24 hours

Table 7.4: Breakdown of assembly and mounting times for one far detector steel-scintillator plane. Two workstations operate in parallel, so two planes can be mounted on the detector every 24 working hours, or two planes every 3.7 shifts at 6.5 working hours per shift.

edge of the steel plane. Sensitive current integration electronics is used to measure the change in flux through the pickup coil as the magnet coil is energized, and provides a measure of the effective magnetic permeability of each steel plane. These flux measurements are made on individual planes during the initial checkout of each supermodule's magnet; the pickup coils are not monitored during routine operation.

The steel plane assembly operation is performed on two planes in parallel at the two assembly workstations. Each assembly workstation operates independently, and has its own tools, fixtures, and 2-ton gantry crane. Each workstation is continuously staffed by three technicians; a single certified welder serves both workstations.

7.4.3.2 Detector plane assembly

The far detector installation tasks described in this Section are associated with Item #8 of the technical requirements listed in Section 7.2. Scintillator planes are assembled from eight scintillator modules, each one 82 cm or 115 cm wide, which are positioned on the steel plane to form an 8-m wide octagon. The detector plane assembly procedure involves the attachment of an array of scintillator modules to the face of a steel plane after the latter has been assembled, as described in the previous Section. Figure 7.9 is a flowchart of the detector plane assembly procedure. The mounting scheme secures the modules to the steel in a manner which is flexible enough to prevent damage from flexing of the steel plane as it is raised from the assembly pedestal and mounted on the detector. Any distortions of the 2.54-cm thick steel plane which stay within an idealized 4.04-cm thick planar volume will not damage the scintillator, as described in Section 4.2.2.

The scintillator modules, shown in Figure 5.11, are secured to the steel plane by three different mechanisms:

- **Switch plates.** The assembly technicians tack weld an array of switch plates to the plane's face, positioned at intervals of 2 m along the edges of the scintillator module locations. A special template is used to mark the locations of the switch plates before welding. Each switch plate assembly includes a steel packing strap which is pre-formed before installation to the shape required to hold a scintillator module in place. The switch plate design is shown schematically in Figure 7.10. The strap locations on adjacent modules are offset by 1 cm to minimize the gaps between modules.

- **Edge brackets and mounting bars.** Each of the eight scintillator modules has a module mounting bar built into each end, as described in Chapter 5. Self-tapping screws are used to attach the module mounting bars to mounting-tab edge brackets on the top face of the steel plane. These steel strips are tack welded around six sides of the plane by a certified welder. Figure 7.11 shows a sketch of how the mounting-tab edge brackets are used to attach a lower module mounting bar to its steel plane.

- **Shelf bars.** A steel shelf bar is mounted along one edge of each steel plane, under the long side of the scintillator module which will be on the bottom after the plane is mounted vertically on the detector. The shelf bar supports the weight of the scintillator plane and prevents the strips in the bottom module from being deformed by the weight of modules above it. The shelf bar is the structure along the bottom right-hand edge

Mounting Module to Absorber Planes

Swipe bar codes of all modules to be mounted on the current plane → Lay out switch plate and edge bar positions using chalk line and tape rule → Measure, bend up and roughly position all packaging straps to be used on this plane

Tack weld the edge brackets to front face of the absorber plane

Thread packaging straps through switch plate holes and tack weld switch plates to plane face.

Position the four central modules onto the plane

Pull over the packing straps across the front face of the modules

Position the next modules on each side

Yes

Drill holes in the edge brackets to match the holes in the module mounting bars

Are there any more modules to be mounted

No

Attach the lower shelf

Screw module mounting bars to the edge brackets

Crimp the packing straps

Plane is now ready to be raised

Figure 7.9: Flow chart showing the sequence of steps in the detector plane assembly process.

of the plane shown in Figure 5.11. Each shelf bar is attached to its plane by six adjustable brackets, which allow the bar to conform to module edge which it supports. The brackets are attached to the steel plane edge by short pieces of angle iron which are welded by the certified welder.
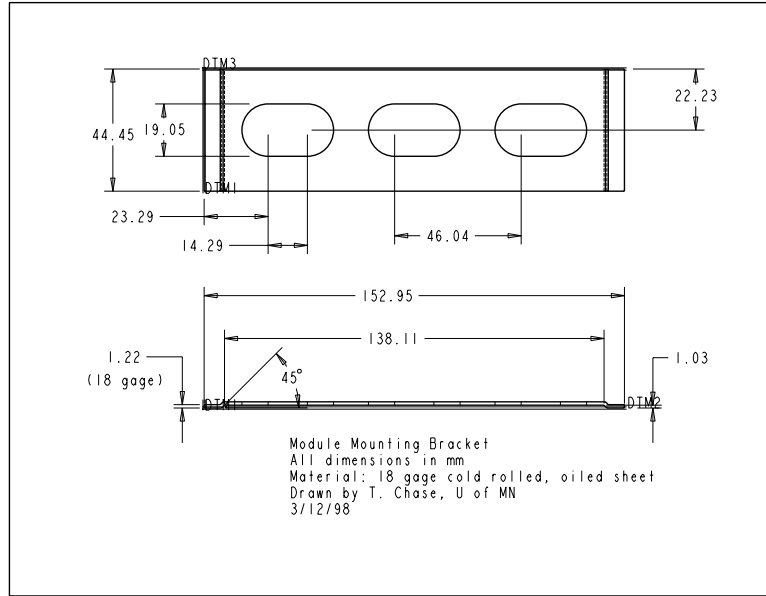
Figure 7.10: Sketch of the switch plate used to secure scintillator modules to steel detector planes with steel packing-straps.

After scintillator modules are mounted, they are given a final performance test using the WLS fiber light injection system and the portable photodetector system. Calibration tests and performance criteria are described in more detail in Chapter 5 and in Section 7.4.5 below.

Any detector modules which fail performance tests are replaced before the plane is mounted vertically on the detector. After a plane passes all tests, the clear fiber optics harnesses are installed in the cable tray around the periphery of the steel plane. The ends of these harnesses which will eventually plug into the multiplexing boxes are temporarily secured to the cable tray for protection during the plane mounting procedure. Finally, the locations of detector elements are recorded using a close-range photogrammetry camera system (see Section 7.4.4).

7.4.3.3   Detector plane mounting

This Section describes the far detector installation tasks associated with Item #9 of the technical requirements listed in Section 7.2. After the assembly and testing of each steel and scintillator detector plane is complete, the 25-ton overhead bridge crane raises the plane-strongback assembly into a vertical orientation and mounts it on the detector. While the plane is vertical, its weight is supported by the strongback support shelves along the bottom edge of the steel plane. The bottom layer of the steel plane rests on support shelves which

7-33
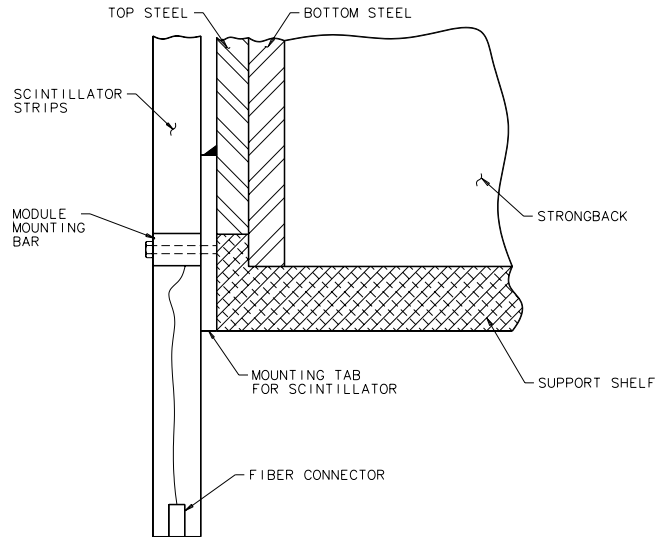
Figure 7.11: Sketch showing how the lower end of a scintillator module is attached to its steel plane using the module mounting bar and the mounting-tab edge bracket welded to the steel plane. The drawing also shows the strongback support shelf which supports the weight of the plane as it is raised into a vertical orientation prior to mounting. The other end of the scintillator module is attached in the same fashion, except that the strongback support shelf is replaced by a steel plane restraining clip on the upper end.

are configured to latch into the steel plane so that it cannot slip off the strongback during mounting. This is shown in Figure 7.11.

During the plane mounting procedure, the steel plane is prevented from tipping away from the strongback by special restraining clips which hold the top of the plane to the strongback. These top clips are released just before the plane "ears" are set on the rails, so that the strongback can be lowered away from the plane after the ears are resting on the support structure rails. In this way the weight of the strongback is never supported by the ears. Both the strongback support shelves and the restraining clips rely on having the width of the "top" steel octagon layer slightly smaller than the width of the "bottom" layer to allow them to grip the steel plane without touching the scintillator plane.

The crane uses a special lifting fixture connected to lifting points on the top end of the strongback. Clamps attached to the assembly pedestal hold the bottom end of the strongback in place while the top end is raised by the crane. A computerized crane control program controls the vertical and horizontal movement of the hook to simultaneously raise the plane-strongback assembly off the assembly pedestal. This program minimizes the force of the pedestal and safely raises the plane into the vertical orientation. The clamps on the pedestal automatically disengage when the plane is vertical, so that it can be moved down the length of the MINOS cavern to the detector planes which have been installed previously. During the lifting procedure all personnel at both workstations must stop work and move to safe locations for 10 to 15 minutes.

The clearance between the detector hair and detector support structure is only 10 cm. This tight tolerance will require the bridge to move rather slowly down the hall. Special

protection "bumpers" prevent the plane from hitting the sides of the supports. After the plane is mounted on the detector, the spacing between planes is set to the standard 5.94-cm pitch by rigid fixed supports between the ears and around the coil holes of adjacent planes. This standard pitch allows 2.54 cm for the steel plane, 1.9 cm for the detector plane, and 1.5 cm for steel plane nonflatness. Additional stabilization of the detector planes, which must be kept vertical for structural integrity, is provided by eight axial bolts which attach each plane to its neighbors at the corners of the octagons.

Once the plane is in position, an operator in the special installation "cage" carried by the 2-ton bridge crane (see Section 7.3.2) installs the axial bolts and coil collar piece which hold the plane in place against the previously installed plane. After the plane is securely bolted into place, the steel flatness and position are measured using survey techniques described in Section 7.4.4.

7.4.3.4   Electronics installation

This Section describes the far detector installation tasks associated with Item #10 of the technical requirements listed in Section 7.2.

Figure 6.4 shows schematically the layout of electronics around the far detector. Cosmic ray events which occur in completed detector sections will be recorded by this system as soon as possible in order to validate the operation of the complete system of scintillator modules, electronics and data acquisition. This means that the elements which are common to all supermodules must be installed and brought into operation by the time the first few planes are installed on the first supermodule. These common elements include the hub interface crate and the central system, the trigger farm and the data acquisition system. The hub for the first section of the first supermodule must also be operational at this time. This early availability of the main elements of the electronics system will also provide an operational monitor system. Early experience with the operation of these systems in the far detector laboratory environment will be very valuable in identifying potential problems with electrical noise, the stability of detector systems, and possible operational interference from ongoing assembly work.

After all of the planes which are to be served by a single multiplexing box are in place, the electronics mounting platforms shown in Figure 7.4 are installed and the final fiber optics connections made between the planes and the multiplexing boxes. Installed detector planes and associated front end electronics are turned on and tested with calibration systems (light injection and radioactive source tubes) and cosmic rays at the earliest possible time. The installation and turnon of electronics system components will be performed by teams of installation technicians, physicists and electronics engineers.

7.4.3.5   Detector plane cabling and certification

This Section describes the far detector installation tasks associated with Item #11 of the technical requirements listed in Section 7.2. The final certification of detector plane operation is performed by MINOS Collaboration physicists assisted by installation technicians. After each plane has been mounted on the body of the detector, the clear fiber optics harnesses already installed on the plane are used to check for proper operation while it is still possible to

remove the plane for repairs. A special portable multiplexing box, which can be temporarily attached to the fiber optics harnesses from the detector access walkways, is used for this purpose. The fiber optics harnesses are then connected to the permanent multiplexing boxes and read out through the experiment data acquisition system. Cosmic ray calibration data will be recorded continuously from all installed detector planes as soon as soon as they have passed all calibration performance tests.

7.4.3.6   Coil assembly, installation and certification

This Section describes the far detector installation tasks associated with Item #12 of the technical requirements listed in Section 7.2.

The design of the far detector magnet coils is described in Section 4.4.4. Each super-module's 150- to 180-turn coil[9] consists of a water-cooled central section and an air-cooled current return section, as shown in Figure 7.12. As soon as the last plane of each super-module is mounted, a one week coil installation period begins. First, the water-cooled bore tube is fabricated and inserted into the central coil hole of the supermodule. The bore tube is constructed from sections of 25 cm diameter, 3.2 mm thick rolled copper tube with eight longitudinal chilled water tubes (2-cm diameter copper refrigeration tubing) soldered to its inside surface. The bore tube is the same length as the supermodule, and provides chilled water cooling for the horizontal section of the central coil. It is fabricated in the area occupied by the plane assembly workstations.

After the bore tube is inserted into the supermodule coil hole, 150 to 180 flexible copper coil conductors and 7 additional copper cooling tubes are pulled through it. The conductors are commercial grade 1/0 stranded copper building wire (TGGT) with Teflon insulation, 1.48 cm in diameter. The coil conductors are pulled through the bore tube in small bundles, seven of which include 2-cm diameter copper cooling-water tubes. The procedure disperses the cooling tubes as uniformly as possible in order to maintain a homogenous temperature profile inside the coil. The bore tube is packed tightly to maintain good heat transfer between the conductor turns and the cooling tubes. After each coil turn has been installed in the bore tube, its remaining length is placed in fixtures provided for the horizontal and vertical return sections of the coil. The fixtures provide space between layers of the coil for air circulation. Coil installation requires 1.5-m long work spaces between supermodules.

Connections between the turns of the two coil sections and the power supply are made with a crimping tool and then insulated. The bore tube is designed to limit the temperature rise of the steel planes and scintillator near the coil hole to less than 2° C. The maximum operating temperature in all sections of the coil is expected to be less than 50° C, compared to the 200° C conductor temperature rating. The Teflon conductor insulation permits normal operation even if the return coil floor trench should be filled with water as the result of an accident. The 9° C chilled water for the cooling tubes removes heat from the central coil section directly to the cavern cooling system heat exchanger, as described in Section 7.4.1.6.

Magnet operation is monitored continuously by measuring the coil current. The relationship between the current and the toroidal magnetic field in each steel plane depends in a complicated way on the permeability of the steel and the geometry of the gaps between the plates which make up that plane. The average magnetic properties of each plane are measured using its flux integration coil soon after each supermodule's magnet coil is installed,
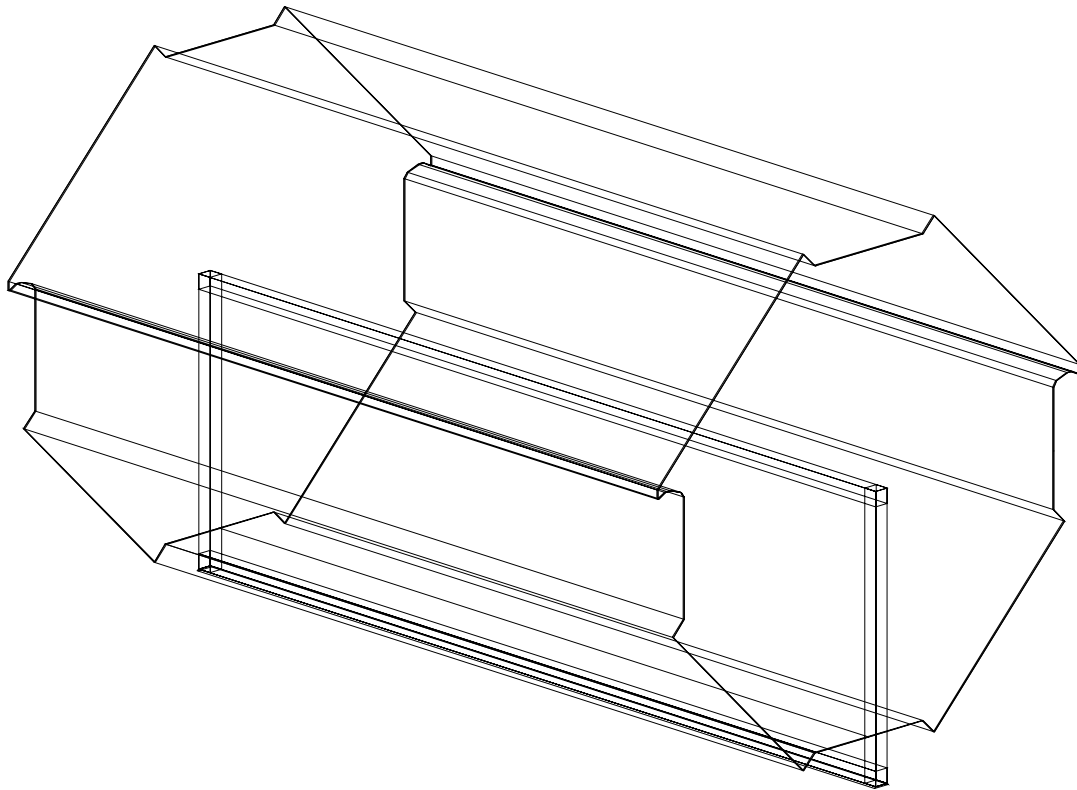
Figure 7.12: Sketch of the far detector coil geometry for one MINOS far detector supermodule. Each of the 150 to 180 turns of insulated copper wire is pulled through the water-cooled bore tube in the center of the detector. The return current section of each turn is supported by fixtures, which provide space for air circulation between layers of turns, along the vertical legs and in the horizontal floor trench. Splices between turns are made by crimping near one of the bottom corners of the coil.

as described in Section 7.4.3.1 above. Each plane is measured as part of the initial magnet certification procedure, but the pickup coils are not monitored during routine operation.

7.4.4 Alignment and survey (WBS 2.4.4)

This Section describes the far detector installation tasks associated with Item #13 of the technical requirements listed in Section 7.2.

The center of the several kilometer wide NuMI neutrino beam must be within about 75 m of the center of the MINOS far detector in order to be able to predict the energy spectrum in the far detector to 2%, or better than 1 GeV in each energy interval, based on the measured near detector spectrum. This is required for the CC-event-energy physics test, discussed in Section 3.7.1, which has the potential to measure neutrino oscillation parameters. Techniques for accomplishing this important survey task are described in the NuMI Facility Technical Design Report[11].

The orientation of the axis of the MINOS far detector relative to the axis of the NuMI neutrino beam will be determined by the accuracy of the underground survey measurements made during the MINOS cavern excavation at Soudan. The angle between the beam and detector axes is important only insofar as it affects the neutrino-event acceptance of the detector, primarily through the containment of muons. The MINOS detector magnet will focus most muons toward the detector axis, which removes most of the sensitivity to the angle between the beam and detector axes. This allows the far detector to be constructed on a flat, horizontal floor, and makes it insensitive to the 57 mr vertical pitch of the neutrino beam.

The absolute location and orientation of the MINOS cavern and detector support axis will be determined by standard underground survey techniques during the excavation phase of the experiment. Survey work will be performed under the joint supervision of CNA Consulting Engineers and the Fermilab Alignment Group. A final, precise survey of the detector orientation will be performed after the support structure is in place. Standard underground survey methods are expected to set the cavern axis orientation very accurately; for example, the Soudan 2 cavern axis was set parallel to the North-South direction to much better than 1° using these techniques.

The determination of the locations of all the scintillator strips in the MINOS far detector is the primary survey challenge for the far detector installation task. This information is needed for event reconstruction and as input to the detector-response Monte Carlo simulation program. This determination is expected to achieve an accuracy of ±2 mm, and involves the following steps:

1. The location of scintillator strips within each scintillator module will be determined at the scintillator fabrication facilities and entered into the survey database.

2. The locations of individual scintillator modules will be measured by a close-range photogrammetry camera system which photographs each detector plane just before it is raised into position on the body of the detector. This is described in more detail below.

3. Offline analysis of these photographs will provide module locations relative to the individual steel plane coordinate systems for the survey database (see description below).

4. Survey targets on the edges and downstream face of each steel plane will be measured after installation to determine its location along the detector axis.

5. The flatness of each steel plane will be measured from its downstream surface after installation. This is to ensure that the plane is hanging stably and has not been deformed during mounting (see Section 4.4.1.3), and that it is flat enough to permit installation of the next plane.

6. The absolute location and orientation of each scintillator strip will be determined from the database information provided by the steps above.

7. These survey coordinates will be used to reconstruct the trajectories of cosmic-ray muons (mostly vertical) and muons from neutrino interactions (mostly horizontal). Fits to these trajectories will yield small corrections to the strip locations, and will also detect most types of errors in the survey database.

An example of a photographic survey system which might be used for MINOS is provided by Eos Systems[12], whose close-range photogrammetry software can achieve 1:8000 accuracy. The system requires:

- A medium format camera (2-inch × 2-inch format).

- A PhotoCD Pro scanner (larger than the standard retail 35 mm PhotoCD scanner).

- Clearly identifiable fiducial marks.

- About 6 photographs per plane.

- Eos Systems PhotoModeler software[12].

Relatively inexpensive medium-format cameras suitable for this use are available from several suppliers. Eos systems estimates that it would be a full time job for one person to take the photos and determine the coordinates of 100 points per plane at the MINOS plane installation rate. Most of this effort is for processing the photographs, and can be supplied by inexpensive student labor at collaboration universities.

Additional survey tasks include the determination of the locations for scintillator module mounting hardware, fiber optics cable brackets, and magnetic flux integration coils on the steel planes before scintillator modules are mounted. These are low precision applications which can be accomplished by the plane assembly crews through the use of templates, and will not require significant effort from the survey crew after the initial setup period.

7.4.5 Final checkout and validation

The performance tests described in this Section are used repeatedly throughout the assembly and installation process to ensure that all components are working properly before final installation. The tests are finally performed after each plane is installed on the detector and connected to its final photodetectors and electronics. Successful completion of this step constitutes the transition to routine operation and the completion of Item #14 of the technical requirements listed in Section 7.2.

The main goal of the performance validation task is to ensure that the response of scintillator modules meets design specifications. Changes in the response of MINOS scintillator, WLS fibers, photodetectors or electronics could be caused by changes in temperature, humidity, pressure and by environmental conditions experienced during shipping. Near and far detector response differences could result in differences in energy calibration, leading to reduced sensitivity to oscillations or even to spurious oscillation signals.

Calibration techniques and instrumentation are described in detail in Sections 5.4.6 and 6.4.1.2. These same techniques will be used at the fabrication facilities, at the near and far detectors and at the test beam calibration setup:

1. **Radioactive source tubes.** Each scintillator module has two built-in guide tubes, one at each end of the module, which cross the ends of all scintillator strips. Radioactive calibration sources can be moved inside the tubes to determine the light output at both ends of each strip. This technique measures the scintillator light output in addition to WLS fiber attenuation. Cross calibrated sources (which have been compared to the same reference source) will be used at the near and far detectors. The system can also be used to set photodetector gains when a detector plane is first turned on after installation.

2. **Module mapper.** The module mapper is an automated device which can scan the entire surface of a scintillator module with a rapidly moving ^{137}Cs source to detect variations in scintillator response. Module mappers are used at the module factories to certify the response uniformity of modules just before they are packaged for shipping. A mapper will be set up in the Soudan 2 cavern testing area to check the response of arriving modules as they are removed from shipping crates. It will be used to perform detailed response studies on every module in the first few shipments, and to spot check modules after routine installation has begun.

3. **Light injection at WLS fibers.** The bundles of WLS fibers at each end of a scintillator module pass through light-flasher injection blocks near the fiber optics connectors. The light flasher intensity can be varied to measure system response over its entire dynamic range. Light flasher intensity also is measured by a standard photodetector system to allow comparison of the responses of modules illuminated by different flashers and in different locations. All photodetector pixels can be illuminated and measured by this technique.

4. **Light injection at photodetectors.** A second light flasher system is used to illuminate photodetector pixels directly. This system will be used primarily for troubleshoot-

ing, and will not have the absolute calibration capability of the WLS fiber light flasher system.

5. **Charge injection at front-end electronics.** A special charge-injection circuit at the input to every preamplifier channel allows the response of photodetector electronics to be calibrated independently from that of the photodetector. This pulser-driven system can be used to check automatically the response of the complete electronics readout chain over its entire dynamic range.

6. **Cosmic-ray and neutrino-produced muons.** After detector planes have passed all validation checks and are in full operation, high energy muons from cosmic rays and neutrino interactions will provide the best measurement of the relative dE/dx response of the MINOS near and far detectors. This technique can only be used when enough scintillator planes have been installed to permit the selection of events with isolated single muon tracks. Although the energy spectrum of cosmic ray muons will be slightly different at the near and far detectors, and the spectrum of neutrino-induced muons could be different because of oscillations, the measurement of muon energy by curvature and range allows absolute calibrations of scintillator charge response to be made with muons of known energy. The main drawbacks of this technique are the low rate of muons at the far detector and the fact that scintillation light from single muons calibrates only a single point at the low end of the dynamic range of the system.

The radioactive-source and WLS fiber light-injection techniques will be used to confirm the proper response of scintillator module strips immediately after modules arrive in the underground laboratory. These methods will be used again to certify proper operation of strips just before each detector plane is installed in the main body of the detector. For both of these tests a portable photodetector array will be employed. After each plane is installed in the detector, it will be connected through its fiber optics harnesses to its final photodetector and electronics readout systems as soon as possible, i.e., after enough of its neighboring planes are installed so that the multiplexing box platforms can be put in place. The radioactive source and light injection calibrations will be repeated, and the accumulation of data from muons will be started. Radioactive source calibration will be performed occasionally on individual modules after installation. There will not be a permanently installed source driver system for automatic calibration of the whole far detector.

A second important validation task is to determine the magnetic field in each steel detector plane to obtain the relative calibration of muon energy measurements at the near and far detectors. A magnetic flux integration coil will be installed on each plane as described in Section 7.4.3.1, and the current in the magnet coil itself will be measured precisely. A magnetic field simulation model will provide a cross check on the direct magnetic measurements for a subset of the steel planes; the simulation will use maps of the gaps between the 2-m wide plates and measurements of the magnetic properties of the plates. The magnet power supply will be able to produce currents higher than those required for normal operation for short periods of time, allowing the magnet to be taken through a full hysteresis cycle to remove the effects of any residual fields. The magnetic field validation techniques will be fully tested with full size steel planes as part of the detector plane prototype program at Fermilab (see Section 4.4.5 and Section 7.5.1 below).

Other validation tests consist of simple checks to confirm that the parameters in the Monte Carlo simulation of the far detector are correct. The mass and thickness of the individual steel plates making up each detector plane will be measured on the surface, immediately after the plates arrive at Soudan. The survey database will provide an accurate geometrical model of the detector. Test beam measurements on a model of the MINOS calorimeter will be used to calibrate the Monte Carlo response parameters, and the relative dE/dx response of test-beam and far-detector modules will be determined from the radioactive source calibration technique.

7.5 Future optimization and engineering

Most of the activities described in this Section will occur during FY 1999. They are part of the engineering and design phases (included under EDIA costs) of the far detector installation tasks described in Section 7.4.

7.5.1 Trial assembly of prototype planes

The assembly of full size prototype planes of steel and scintillator is an important part of the engineering optimization process for the magnet steel and coils task and the scintillator fabrication task, as described in Chapters 4 and 5. This process has already started with the construction of the first (2-cm thick) steel plane prototype in the New Muon Lab at Fermilab. A series of increasingly more realistic steel and scintillator prototype planes will be built to optimize the installation and mounting procedures.

The prototype plane program requires the construction of a second hanging-file support structure so that planes can be removed from the main support structure and temporarily stored while other planes are returned to the assembly pedestal to try alternative scintillator module mounting techniques. The culmination of this process will be the assembly at Fermilab of two 4-plane structures (4 steel planes and 3 scintillator planes) with magnetized steel and operating scintillator modules. The first 4-plane prototype setup will be used to test and certify the designs of all installation fixtures, machines and assembly procedures.

The second 4-plane prototype will be used to train the far detector installation technical staff supervisors and crew bosses in the construction, calibration and operation techniques, beginning about a year before installation starts at Soudan. This process will involve the far-installation "startup" crew (see Section 7.4.3) and some of the assembly technicians. This will assure that the installation procedures are well understood by the time the outfitting of the MINOS far detector cavern begins. Assembly fixtures will be built for the two far detector workstations around this same time.

Of course the main focus of the first 4-plane prototype studies will be to test the procedures for assembling the steel detector planes, for mounting scintillator modules on steel planes, and for installing the planes of steel and scintillator on the support structure.

A second important goal of these studies will be to test the handling system for steel plates, scintillator crates and peripheral equipment which has been designed for use at Soudan. Most of the equipment, methods and constraints envisioned for this system are commonly used in similar applications, and do not require extensive prototype studies. In

this category are both monorail systems, the gantry cranes, the bridge crane and the storage and transport carts. However, some of the equipment, methods and constraints have been designed specifically for MINOS, and do require prototype studies for engineering optimization. These procedures include the plate bundle sequence of surface unloading, hoisting underground, underground unloading, transfer by gantry crane from storage carts to the assembly pedestal, use of the compression rig, and plane-strongback pickup and transport. These installation issues will be evaluated during the initial 4-plane prototype tests. It is important to perform these tests before the new shaft cage is built because the mine shaft and headframe were designed for hoisting heavy loads from underground to the surface, but not for hoisting from the surface to underground. Neither may be significantly modified due to their historic nature.

The plan described below, using the plates acquired for the 4-plane prototype, would demonstrate that the currently proposed methods and equipment are suitable, provide time and motion information as a basis for better installation estimates, and provide a test bed for development of the bundling, strapping, packing and clamping hardware necessary. The entire plate bundling sequence will be simulated using the existing bridge cranes and related equipment present in the New Muon Lab at Fermilab, where the 4-plane prototype tests will be conducted. Specific stages are:

- Unload plates from a delivery truck, using a crane to simulate actual unloading procedures at Soudan.

- Rebundle the plates using the planned bundling holes, hardware and fixtures.

- Add banding and blocking to protect edges of plate bundles.

- Lift completed bundle on edge to test surface loading concept.

- Simulate loading in through the front of the cage, with the edge-stacked bundles lifted and rotated into position in a dimensionally-correct framework simulating the new cage. Accurately represent the load transfer from trailer to cage.

- Attach the plate bundle to the simulated cage, using bundling and clamping hardware.

- Detach the plate bundle from the simulated cage.

- Simulate unloading out through the back of the cage framework, with the bundle lowered and rotated into position for the monorail. Accurately represent the load transfer from cage to monorail.

- Place bundles in edge storage and unbundle.

- Simulate moving single plates from edge storage into place on the assembly pedestal.

7.5.2 Integration engineering

MINOS engineers have now completed detailed conceptual designs of all major detector systems in order to demonstrate technical feasibility and provide realistic bases for cost estimates and schedules. However, some of the interfaces between detector systems present engineering challenges which have only recently been addressed in detail, particularly for closely-related systems which have been designed by different groups. Further "integration" of MINOS detector systems will be the focus of much of the engineering optimization and prototype work during FY 1999. The final designs will be evaluated as part of the full-size detector plane prototype program at Fermilab. These studies will involve close collaboration among the installation, magnet steel and coils, scintillator fabrication and electronics tasks. Examples of integration areas include:

- Optimization of tradeoffs between labor-intensive procedures performed during scintillator fabrication and during installation. Installation tasks must often be performed serially because of limitations on space and manpower in the underground laboratory, so it is often efficient to expend extra effort for prefabrication at above-ground facilities in order to save time underground. Much engineering effort has already been devoted to optimization of such tasks, but more is needed.

- The mounting of detector modules on steel planes. Plans are now being made to test the designs for detector plane mounting described in this Report as part of the detector plane prototype program at Fermilab.

- The effect on scintillator modules of steel plane nonflatness, of steel plane deflections during installation and of stray magnetic fields.

- The mounting of photodetector and electronics hardware on the detector planes. Personnel access to this equipment, and the identification and replacement of faulty components, are issues of particular concern.

- The installation of the magnet coils in supermodules, the mechanical details of conductor splicing, and the installation and operation of the cooling system and power supply.

- Optimization of survey techniques and the required precision of survey measurements.

7.5.3 Electrical power and cooling issues

The engineering of the infrastructure systems needed for the MINOS underground laboratory at Soudan is already well advanced, as described in Section 7.4.1.6. The systems required are similar to those already in operation in the Soudan 2 laboratory, and will be built and installed as part of the MINOS cavern construction and outfitting task. Involvement of the installation "startup" crew (Sections 7.1.2 and 7.4.3) in the commissioning of the cavern infrastructure will ensure a smooth transition between the outfitting and far detector installation tasks. Two important differences between the MINOS and Soudan 2 infrastructure systems are the larger air cooling requirements of MINOS (260 kW *vs* 70 kW) and the larger

population of workers required to install MINOS (39 FTEs in two shifts *vs* 6 FTEs in one shift).

The air cooling needs are of particular concern because the Soudan 2 laboratory appears to be close to saturating the natural cooling capacity of the Soudan mine shaft air flow. For this reason a water chiller system, with twice the cooling capacity needed for the anticipated 260 kW heat load, is being specified as part of the MINOS cavern outfitting bid package. However, a much less expensive air-cooled system is also being developed as an alternative to the conservative design used for the cost estimate. The alternative cavern cooling system would use large fans to transfer heat from a water-cooled chiller outside the MINOS cavern to the natural flow of cool air up the Soudan mine shaft. Initial calculations show that this would heat the mine-shaft air to a temperature in excess of 100° F. In order to predict the impact of this temperature rise on the Soudan mine shaft air flow (and also on wooden shaft timbers, bats and tourists), experimental measurements of the effect of large electric heaters have been made in the Soudan mine shaft during the past year.

Finally, the power needs of all MINOS and CDMS systems are being continuously reviewed to ensure that cooling costs are properly taken into account as the design of these experiments proceeds.

Chapter 7 References

[1] University of Minnesota, CNA Consulting Engineers, Ericksen-Ellison Associates, Inc. and Miller-Dunwiddie, Inc., "MINOS Far Detector Laboratory Technical Design Report (Including Basis of Estimate & WBS) for Cavern Construction, Cavern Outfitting & Detector Outfitting," October 1998, Fermilab report NuMI-L-263.

[2] CNA Consulting Engineers, Ericksen-Ellison Associates, Inc. and Miller-Dunwiddie, Inc., "MINOS Far Detector Laboratory Design Development Report," September 1998.

[3] John Alner *et al.*, "Report of the MINOS Installation Committee," September 1997, Fermilab report NuMI-L-259.

[4] G. Alner, D. Ayres, W. Miller, "Basis of Estimate for the MINOS Far Detector Installation, WBS 2.4," March 1998, Fermilab report NuMI-L-312.

[5] University of Minnesota, CNA Consulting Engineers, Ericksen-Ellison Associates, Inc. and Miller-Dunwiddie, Inc., "MINOS Far Detector Laboratory Project Preliminary Hazard Assessment Report," October 1998, Fermilab report NuMI-L-419.

[6] The Fermilab NuMI Project Staff, "NuMI Project at Fermilab: Preliminary Safety Assessment Document," October 1998, Fermilab report NuMI-361.

[7] The Fermilab NuMI Project Staff, "NuMI Project Cost and Schedule Plan," October 1998, Fermilab report NuMI-362.

[8] The University of Minnesota and the Minnesota Department of Natural Resources, "Environmental Assessment Worksheet for MINOS Excavation at Soudan," August 1997, Fermilab report NuMI-L-297.

[9] N. Bednar *et al.*, "Basis of Estimate for the MINOS Far Detector Magnet Coils," September 1998, Fermilab report NuMI-L-404.

[10] P. Schoessow *et al.*, "MINOS Toroid Magnetic Measurements," February 1998, Fermilab report NuMI-L-347.

[11] The Fermilab NuMI Group, "NuMI Facility Technical Design Report," October 1998, Fermilab report NuMI-346.

[12] Eos Systems in Vancouver, B.C., Canada provides PhotoModeler software which would be suitable for recording the locations of MINOS detector elements. The software uses scanned or digital photos to do close-range photogrammetry with ± 1 mm precision.

Chapter 8

Near detector installation

8.1 Overview

This Chapter describes the installation of the MINOS near detector and the infrastructure required in the near hall, in the NuMI facility[1] and in other locations at Fermilab. It includes an overview of the detector, the near hall facilities, and other work and storage areas at Fermilab. Subsequent Sections discuss the technical requirements, the interfaces to other MINOS systems, and give detailed descriptions of the WBS Level 3 tasks, including materials handling and detector checkout and validation. Although the near detector installation procedures described in this Chapter are based on those developed for the MINOS far detector, described in Chapter 7, the installation effort requirements are quite different owing to the different labor environments at the Soudan and Fermilab sites. The near detector installation task must be closely coordinated with the fabrication of detector components: the magnet steel and coils (Chapter 4), the scintillator detector (Chapter 5) and the electronics systems (Chapter 6).

An overview of the design of the near detector has already been given in Chapter 3 and the details of its construction have been described in the Chapters 4, 5 and 6. The main parameters of the detector and laboratory infrastructure are summarized in Table 8.1.

8.1.1 The near detector facility

The MINOS near hall is located at the downstream end of the NuMI facility at Fermilab. Access to the underground hall is through a 98 m deep shaft approximately 70 m upstream of the hall entrance. The base of the shaft and the floor of the hall are at the same elevation, in contrast to the sloping tunnels in other areas of the NuMI facility. The upstream face of the near detector is located 290 m from the end of the decay pipe; 240 m of this distance is the muon shield (unexcavated rock), 10 m is for muon monitor pits within the shield, and 40 m is air drift space between the end of the shield and the near detector. The near hall is approximately 45 m long by 9 m wide and 10 m high. The ventilation, electrical, water control and safety systems are provided as part of the NuMI civil construction task[1]. Figure 8.1 shows plan and elevation views of the near hall facility.
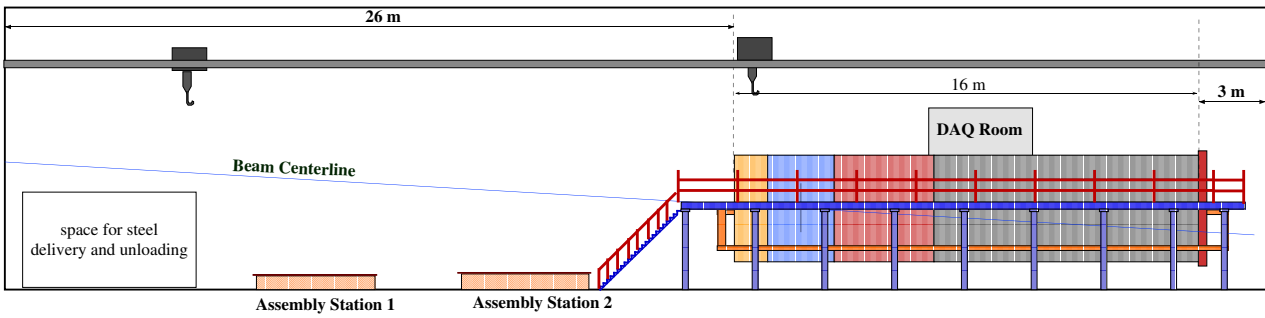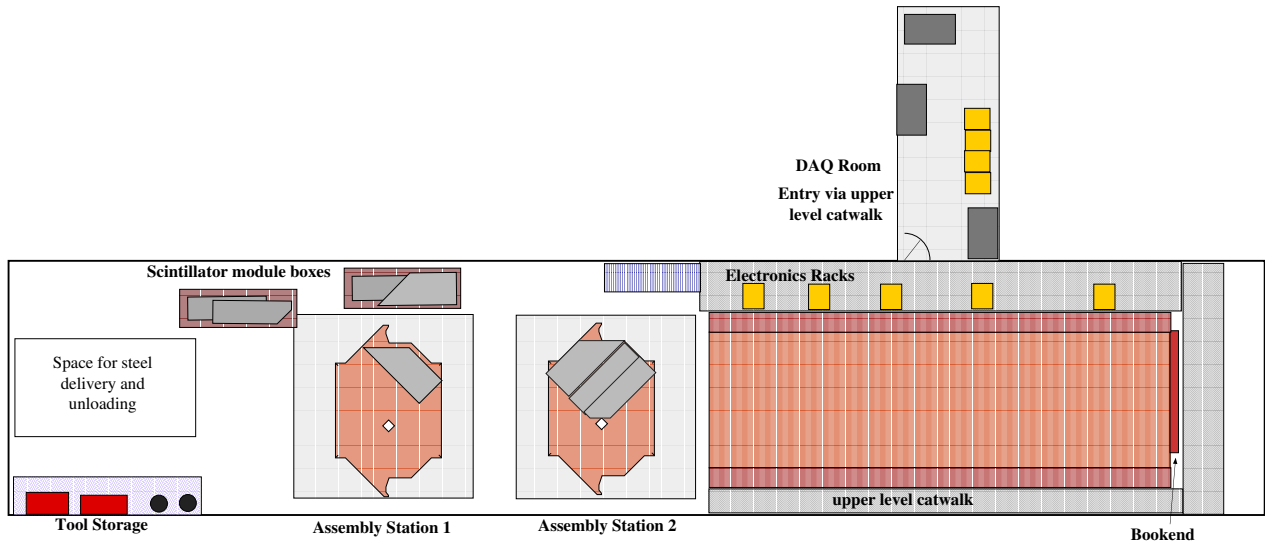
Figure 8.1: Sketches of the layout of MINOS near detector hall, showing the location of the assembly workstations and the size of the completed detector. The upper drawing is a plan view and the lower drawing is a side-elevation view of the facility.

System	Parameters
Near hall dimensions	45 m × 9 m × 10 m (height)
Detector dimensions	16.6 m long × 3.8 m high × 4.8 m wide
Detector mass	955 tons steel + 25 tons scintillator = 980 tons
Steel planes	280 "squashed octagons," 3.4 tons each (5.94 cm pitch)
Steel planes/section	Veto = 20, Target = 40, Shower = 60, Spectrometer = 161
Multiplexing	Forward section - none; muon spectrometer - 4 ×
Readout channels	8448 in forward section, 960 in muon spectrometer
Magnetic field	1.5 T at the neutrino beam location
Magnet coil	48-turn water-cooled aluminum, 40 kA turns, 80 kW
Installation time	8 months
Neutrino interactions	10 events/spill/0.5 m of steel
Muons from beam	20/spill entering detector, 130/spill exiting

Table 8.1: Summary of the major parameters of the MINOS near detector facility.

8.1.2 Design of the near detector

The main purpose of the near detector is to provide information about the characteristics of (unoscillated) neutrinos in the NuMI beam. That information is used to predict the numbers and characteristics of neutrino events which would be observed in the far detector in the absence of oscillations. Ideally both the beam and the detectors at the near and far locations should be identical, but in practice we must correct for small differences in beam and detector characteristics using detailed simulations. Predictions of the neutrino beam rate, composition and energy spectrum at the far detector are based on neutrino interactions recorded by the near detector within the central part of neutrino beam (r < 25 cm). This restriction minimizes near-far beam spectrum differences while maintaining an adequate interaction rate. The near detector will also record neutrino interactions at larger radii in order to verify the accuracy of the neutrino beam simulation which is used to predict beam characteristics at the MINOS far detector in the absence of oscillations. The detector size and density of instrumentation has been chosen to contain and measure neutrino interactions with the same energy and spatial resolutions as the far detector.

The near detector is an adaptation of the MINOS far detector design, and is rather similar to a far detector supermodule. Both are constructed of steel planes and use similar scintillator modules and electronics. The support structures and installation procedures are similar for the two detectors. Each will have a magnet coil inserted through its planes after the installation of planes is complete. The detectors differ primarily in size and shape, and in the fractions of the steel plane areas instrumented with scintillator.

The near detector is smaller, both in cross section and in length. The far detector consists of 2.7 kt "supermodules"; the near detector is one module weighing 0.98 kt. The near detector contains 280 1-inch thick steel planes on hanging rail support structure; the 3.4 cm gaps between planes (5.94 cm pitch) give a total length of 16.6 m.

The near detector is longitudinally divided into four logical sections, each with a different

number of planes. The first 20 planes are the Veto section, used to reject background events whose tracks could interfere with events of interest. The next 40 planes are the Target section; all interactions used to make comparisons between the near and far locations must occur within these planes. The next 60 planes are the Hadron Shower section, used to contain the showers from interactions occurring anywhere within the Target section. These three sections together comprise the Forward section of the detector and every plane is instrumented with scintillator. The last 160 planes are the Spectrometer section, where the momenta of muons from neutrino interactions are measured. One in every four Spectrometer planes is instrumented with scintillator. This design has been discussed in Section 3.5 and is illustrated there in Figure 3.5.

The near detector planes have an irregular "squashed" octagon shape, shown in Figures 8.2 and 4.5, roughly 3.8 m high and 4.8 m wide, with an area of 16 m^2 (excluding the support "ears"). This squashed octagon requires much less steel than a regular octagon with the same scintillator coverage. The different magnetic field shape in the irregular octagon does not affect the quality of the detector measurements compared to those in the far detector.
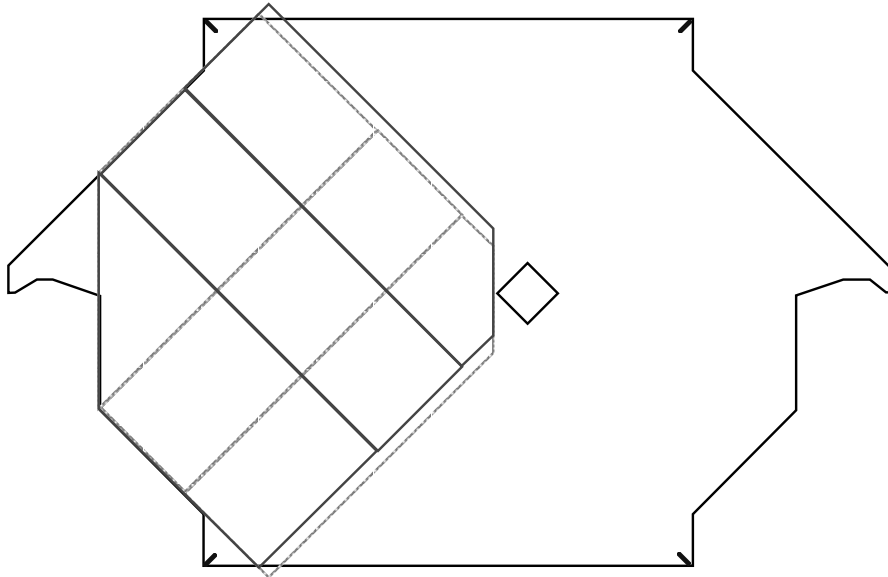
Figure 8.2: Sketch of the layout of scintillator detector modules on the partially instrumented planes of the three "forward" sections (veto, target, and hadron shower) of the near detector. Two 20-strip wide modules are located nearest the coil hole and a single 28-strip wide module is located along the 45° edge of the steel plane. The scintillator strips are read out from their outside ends only, and strip orientations alternate ±90° on successive plates. The two orientations are shown by solid and shaded module outlines.

Because the neutrino beam interactions occur within a small region, the upstream detector planes need to be instrumented only in this area. Only part of the area (∼6 m^2) of most Forward section planes is instrumented, as shown in Figure 8.2. The detector is positioned so that the beam is centered on the Forward section instrumented area, which avoids the magnet coil hole. Every fifth plane in the Forward section is covered with a

larger area of scintillator in order to have better tracking ability for muons which exit the partially covered Forward planes some distance upstream of the Spectrometer section. The instrumented Spectrometer section planes are similarly covered by 13.2 m^2 of scintillator. Figure 8.3 shows the layout of scintillator modules on a fully instrumented plane. In both sections, every other instrumented plane has its scintillator strips oriented perpendicular to its neighbors. Table 8.2 summarizes the near detector instrumentation.
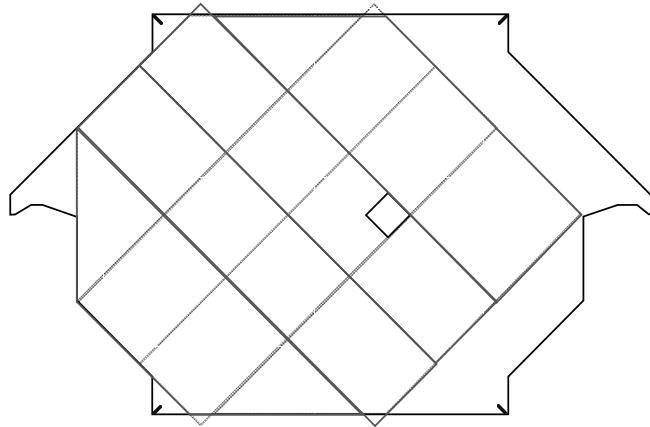
Figure 8.3: Sketch of the layout of scintillator detector modules on the fully instrumented planes (e.g., in the spectrometer section) of the near detector. Two 20-strip wide modules are located nearest the coil hole and 28-strip wide modules are located along the 45° edges of the steel plane. The scintillator strips are read out from their beam-side ends only, and strip orientations alternate ±90° on successive plates. The two orientations are shown by solid and shaded module outlines.

8.1.3   Near detector infrastructure

Installation of the near detector begins when the civil construction contractor has completed work and grants beneficial occupancy of the underground laboratory. At that time all environmental and water control systems, fire protection and life safety systems, and basic plumbing and electrical service are operational. These systems are specified in the NuMI Technical Design Report[1]. Operation and maintenance of these systems, including the FIRUS alarm system, is performed by the Fermilab Facilities Engineering Services Section (FESS).

The NuMI downstream access shaft contains a freight elevator and a hoist shaft serviced by a 20-ton crane. The surface building over this area is of sufficient size to contain a loading bay and storage space for staging one week's worth of steel and detector components at the shaft head. The 3.6 m wide access hallway in the tunnel between the drop shaft and the detector hall is of sufficient size to accommodate the movement of detector components and personnel.

System	Parameters
Forward section	
Number of planes	120 steel planes, 120 scintillator planes
Detector units	96 planes × 64 strips in 3 short modules/plane
	24 planes × 96 strips in 4 full-length modules
Readout	120 planes: 1-ended, not multiplexed
Channel count	6144 + 2304 = 8448
Photodetectors	528 16-channel PMTs
Spectrometer section	
Number of planes	161 steel planes, 40 scintillator planes
Detector units	40 planes × 96 strips in 4 full-length modules
Readout	40 planes: 1-ended, 4 × multiplexed
Channel count	40 × 96 ÷ 4 = 960
Photodetectors	60 16-channel PMTs

Table 8.2: Summary of the major parameters of the near detector. A 4 × multiplexing level means that fibers from 4 different scintillator strips are viewed by a single PMT pixel. The four strips in each partially instrumented plane (of short modules) which do not overlap the strips of adjacent planes (with orthogonal strip orientation) are not read out. This gives a convenient 64 active strips (4 PMTs) per plane.

The hall is outfitted with two bridge cranes on a single set of rails, covering the two assembly stations and the area occupied by the completed detector. One crane has a 15-ton capacity and the other a minimum 6-ton capacity. A room for the data acquisition hardware is carved into the west wall at a location near the center of the detector.

Other facilities required on the Fermilab site include an area for the initial delivery, inspection, and short-term storage of the steel delivered from the supplier. The scintillator modules delivered from the factories are also inspected and stored in this location until they are moved to the downstream surface building prior to installation.

8.1.4 Near detector installation

The near detector installation task includes the procedures used to move steel and scintillator detector components into the underground hall, to assemble the planes of steel and scintillator at two workstations, and to install these planes on the hanging file detector support structure. This procedure is described in detail in Section 8.4. The near detector construction cost estimate and schedule[2] are based on the detailed cost estimates and schedules developed for the MINOS far detector, described in Chapter 7. The cost of effort for the labor-intensive installation process is the largest component of the near detector installation task[3]. Safety considerations have been included as integral design requirements for all near detector installation tasks. Safety issues for all NuMI-MINOS facilities at Fermilab are described in the NuMI Project Preliminary Safety Assessment Document[4].

Figure 8.1 shows plan and side-elevation views of the near hall, with the locations of

the workstations, the completed detector, the DAQ room, and an area to unpack the boxes of scintillator modules. Before the assembly and installation of the steel planes begins, the detector support structure is constructed. Next the strongbacks are assembled; these are the steel frames used to carry the completed planes to the detector support rails. An area on the floor around each strongback defines an assembly workstation. Detector assembly starts with the most downstream section (Spectrometer) and proceeds upstream. The mounting of electronics crates and installation of readout cables proceeds in parallel with the installation of the planes. Once all the planes are installed, the strongbacks are removed and the magnet coil is installed.

8.1.5   Testing of scintillator modules

Detector components which are delivered to the near hall have already passed quality control inspections and performance tests before being shipped from commercial vendors (e.g., steel plates) or from the MINOS fabrication facilities (e.g., scintillator modules and electronics). Nevertheless, some damage may occur to the scintillator modules due to mechanical shock or temperature extremes experienced while being transported from the fabrication facility to the near hall. It is important to repeat some of the performance tests after arrival and before mounting the detectors on steel planes. Malfunctioning modules will delay the installation schedule if they have to be replaced after they are mounted on the steel planes. The performance tests are conducted after the scintillator modules are moved underground. Modules are tested before they are placed onto a steel plane, and again before the plane, with modules attached, is mounted onto the detector support structure.

8.1.6   Detector operational requirements

Electronics is installed on completed sections of the detector as soon as possible so that the performance of the scintillator, photodetectors and electronics can be evaluated and monitored continuously. There is a buffer zone of approximately 10 planes between the activated sections and the upstream end where installation of planes is still occurring. Electrical noise from the crane and heavy equipment is not expected to be a problem for the electronics. In part this is because the electrical systems for utilities and for electronics are isolated from each other; in addition the electronics components are packaged within shielded boxes, and long cable runs consist of optical fiber rather than copper signal cable. Dust and dirt from the ongoing installation process is isolated by simple protective covers for the electronics and multiplexing boxes.

8.2   Technical requirements

The goal of the near detector installation task is to assemble and install the MINOS near detector and data acquisition system, to verify that its performance meets physics requirements, and to provide the infrastructure needed to install, maintain and operate the detector and associated systems to record neutrino interactions and cosmic ray muons. The following sub-tasks are included in the near detector installation WBS element:

- **Infrastructure tasks:**

  1. **Design liaison.** Participate in the design specification and review processes for items in other WBS elements which affect the near detector infrastructure tasks. These include the footprint and layout of the hall, the power and environmental requirements, and the detector support structure. The liaison task involved with the layout of the hall also establishes the necessary training for personnel to access the underground areas and identifies hazards in accordance with FESH rules.

  2. **Detector support.** Install the detector support structure.

  3. **Electronics power installation.** Install outlets at all locations along the length of the detector where electronics will be located. The circuits for these outlets originate from the isolated power panels installed by the NuMI Civil Construction task.

  4. **DAQ room.** Install the racks, work benches, terminals and associated hardware for testing and operation of the detector DAQ. This includes the central data system, trigger farm, and networks. Install the outlets to supply all these systems; these circuits also originate from the isolated power panels.

  5. **Magnet power.** Install the power supply and connect cables for the detector magnet coil.

- **Materials handling and installation tasks:**

  6. **Design liaison.** Participate in the design specification and review processes for items in other WBS elements which affect the near detector materials handing and installation tasks. These include the access shaft lifting equipment, the underground transport carts, the near hall cranes, the magnet coil and cooling design, the scintillator mounting, and the electronics mounting and cabling.

  7. **Assembly workstations.** Install the strongbacks at the two assembly workstations. Establish an appropriate inventory of tools and supplies for general use during detector installation. Schedule and operate the detector plane assembly workstations and associated equipment. Coordinate tasks involving the supply of components to the workstations and scheduling of workers.

  8. **Transport systems.** Establish procedures for receiving detector components (steel, scintillator modules, electronics, photodetectors and fiber optics connections) at the staging area within the downstream surface building, and for moving them underground as needed. This includes handling materials around the access shaft and the use of the underground vehicles and carts to deliver materials to the hall.

  9. **Work and storage areas.** Set up the staging areas in the downstream access building for steel and scintillator. Set up a scintillator crate unpacking area in the near hall, and work bench space for the scintillator detector testing equipment.

  10. **Plane assembly.** Schedule and perform the tasks to attach scintillator modules to steel planes. Coordinate tasks involving the supply of components to the workstations and scheduling of workers.

11. **Plane mounting.** Schedule procedures for installation of steel and scintillator planes on the body of the detector. This includes the installation of fiber optics connections to the scintillator modules. Perform tests on the completed planes to ensure that detector performance meets established criteria.

12. **Electronics installation.** Schedule and coordinate the installation and checkout of photodetectors, front-end electronics, and other electronics hardware and power supplies.

13. **Magnet installation.** Install and check out the magnet coil.

14. **Alignment and survey tasks.** Install the survey monuments required to position the detector support structure, and install the equipment used to survey the detector planes as they are assembled and mounted. Design procedures for measuring and recording the locations of all components within the assembled detector. Operate the software required to manage this information.

15. **Transition to physics operation.** Establish operating procedures and performance criteria for installed sections of the detector and begin routine data acquisition of cosmic ray and neutrino events. Begin operation of the data recording and distribution system, and of the software systems for identifying and characterizing events of interest.

8.3   Interfaces to other MINOS systems

8.3.1   NuMI near detector hall

The NuMI Facility TDR[1] describes the excavation and outfitting of the near hall and gives the specifications for the access shaft, tunnel and near hall.

8.3.2   Near detector steel structures

The magnet steel and coils task (Chapter 4) includes the design and fabrication of the following structures and fixtures:

- **Detector support structure.** This steel-beam structure supports the rails on which the near detector planes rest and also supports elevated catwalks for access along both sides of the detector planes. The structure includes the "bookend" support to which the first steel detector plane is attached. Platforms used to hold electronics crates at the four 45° sides of the octagonal detector are also attached to the support structure. Electronics platforms are installed only after the planes which they serve are in place.

- **Steel plane design.** The steel plane design includes the details of the locations of axial bolts, the size of the support "ears" which rest on the hanging file rails of the support structure, and the placement of the central hole for the magnet coil.

- **Strongbacks.** A strongback is used as a rigid support upon which each steel plate is laid before the placement of scintillator modules. After the scintillator modules are

attached to a steel plane, the strongback and detector plane assembly is raised into the vertical orientation by the 15-ton bridge crane and set on the detector support rails where it is supported by the steel plane "ears."

- **Steel plate delivery cart.** This 6-ton capacity, 6 m long cart is used to move a single steel plate from the access shaft into the hall.

- **Scintillator module carts.** These 1-ton capacity, 6 m long carts are used to move crates of scintillator modules from the access shaft to the hall.

8.3.3 Magnet coil

The near detector is toroidally magnetized by a conventional water-cooled coil[5]. The coil is fabricated on site and moved into the near hall and installed in the detector after the detector plane installation is complete. Each coil has 48 turns and consists of approx. 18-m long central and return sections. The coil conductors are 1.5 inch by 1.1 inch aluminum (chosen to reduce the weight of the assembly), with a central cooling channel for low-conductivity water. The 40,000 Amp-turn coil has been designed to provide a toroidal magnetic field for muon momentum measurement similar to that in the far detector with minimum temperature rise at the center of the near detector (which could affect detector performance). The coil requires about 80 kVA of electrical power and operates at a temperature of 25° C. The coil cooling-water chiller uses heat exchangers to transfer the heat generated by the coils to the surface.

8.3.4 Scintillator planes

As described in Chapter 5, the MINOS active detector elements for the near detector consist of 4.1-cm wide strips of plastic scintillator which are packaged into modules of 20 or 28 strips each. The fully instrumented planes of the MINOS near detector hold four modules and the partly instrumented planes hold three modules, as shown in Figure 8.2 and Table 8.2. The modules come in several shapes which are designed for particular regions of the steel planes; each type has a unique geometry to fit around the support structures (ears, coil collars). The end pieces on the scintillator modules extend beyond the steel planes edges and contain the fiber optics connections, the WLS fiber light-injection hardware, and the radioactive source tube access points. These end pieces are constrained to fit within the following maximum distances from the edges of the steel planes so as to fit within the detector support structure: 20 cm on the sides, 40 cm on the top, and 25 cm on the bottom. The bottom allowance corresponds to a distance from the bottom edge of the steel plane to the floor of 90 cm, and allows sufficient access space for work on the bottom ends of detector elements.

Scintillator modules are packaged in shipping crates at the fabrication facilities for transportation to Fermilab. Each crate holds modules which are placed on a single steel plate; more than one such crate may be needed for each detector plane. The crates are inspected and stored at a receiving facility until the time nears for their installation. The underground crate unpacking area holds two to three crates. Empty crates are returned to the surface as soon as modules have been tested and installed. Scintillator modules which fail performance

tests are returned to the fabrication facilities for repair. Scintillator module test equipment and protocols are provided by the scintillator fabrication task.

The near detector installation task also includes the installation of fiber optics connections between scintillator modules and multiplexing boxes, the multiplexing boxes themselves, the photodetectors and front-end electronics. This is described in the following Section.

8.3.5 Electronics and data acquisition

Electronics and data acquisition hardware is installed on each plane after it is mounted vertically on the detector. Front-end electronics is located in crates along the two 45° faces on the left side of detector (the side away from the coil hole). The crates along the upper face are supported on special cantilevered platforms attached to the side support structures, and can be accessed from the walkways. The crates along the lower face are located on similar platforms supported from the floor. The arrangement is shown schematically in Figure 8.4.
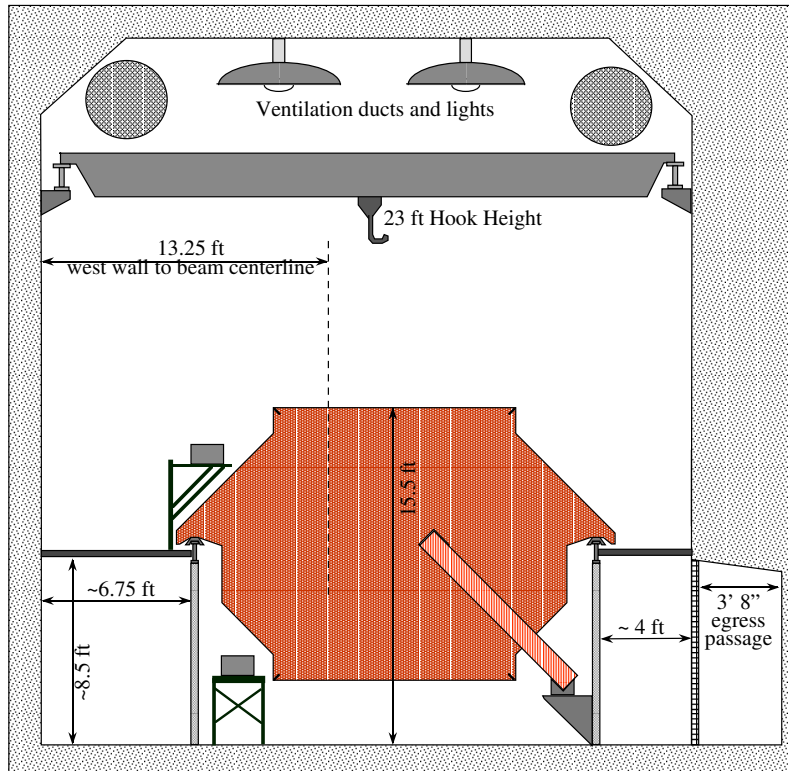
Figure 8.4: Elevation view sketch of the MINOS near detector hall at the location of the detector, showing the multiplexing boxes and front-end electronics crates. The crates are represented by the small shaded boxes near the upper and lower 45° octagon faces on the beam side of the detector (left side of the figure).

The installation task includes the complete installation and commissioning of all electronics components, including the photodetectors, multiplexing boxes, and fiber optics harnesses

which connect them to the scintillator modules. As soon as a set of planes has been successfully read out through the electronics and data acquisition system, it becomes part of the operating detector, and records calibration data from cosmic ray events while the remainder of the detector is being assembled.

8.4 Description of WBS elements

This Section describes the near detector installation activities included in each WBS-2.5 Level 3 task. Tasks under Level 4 EDIA consist mainly of items which are contained in other Level 2 WBS elements, but are entered under WBS 2.5 as a special class of liaison tasks. Input from the near installation project managers is a necessary part of the overall design and review process; the liaison tasks cover this effort. Installation oversight EDIA is included under various tasks at WBS Level 6.

8.4.1 Infrastructure (WBS 2.5.1)

This Section describes the near detector installation tasks associated with the facility and supporting components required by the detector.

8.4.1.1 Near hall footprint and layout

This is a liaison task to those items in WBS 1.2 (NuMI civil construction) which cover the physical layout of the near hall and the tunnel, the access shaft, and the downstream surface building. The liaison ensures that all the criteria and designs meet the needs of the near detector installation and operation. This includes defining the size and location of the DAQ room, and defining a "stay clear" zone for the beam which no walls or structures can intersect. WBS 1.2 covers the implementation of fire protection and life safety recommendations; the liaison task ensures that the detector installation does not interfere with any of these systems and coordinates the installation of rack fire protection and the inputs into the FIRUS alarm system from detector subsystems.

8.4.1.2 Power and cooling requirements

This is a liaison task to those items in WBS 1.2 which cover the underground environment (temperature, humidity, ventilation) and the types of AC power to be supplied to the near hall. Power circuit design includes requirements imposed by the detector electronics, such as quiet AC power and an isolated ground network.

8.4.1.3 Detector support design

This is a liaison task to WBS 2.1.3, the near detector support structure. The liaison ensures that the support structure meets the requirements for the elevation and transverse location of the detector with respect to the beam centerline. This task also ensures that sufficient space exists on and below the support structure catwalks for the detector electronics equipment.

8.4.1.4 Work and storage areas setup

The steel plates delivered from the fabricator are unloaded and checked at some appropriate location on-site. The downstream service building contains a steel staging area which holds 6 to 10 plates. The staging area is kept supplied during detector assembly. Plates are moved underground one at a time, as needed. There are no steel storage areas underground.

Crates of scintillator modules are also received at the staging area. The crates are likewise moved underground only as needed and empty crates are returned to the surface.

An assembly work area surrounds each strongback. Work benches and shelves to hold the tools and materials needed for the plane assembly procedures are set up in this location. Once modules are attached to planes, but before the planes are mounted on the detector, the scintillator is tested (see below). A work bench area is also set up for test equipment.

8.4.1.5 Detector support

This task covers the installation of the near detector support structure. The structure is prefabricated in pieces which can easily be transported down the access shaft and tunnel. A survey is first done to establish the locations of the support columns. After the columns are installed, the hanging file rails are placed and checked for flatness. The "bookend" is then installed at the downstream end. Finally, the upper catwalk, stairs, and guard rails are installed. After the detector planes are installed, brackets to hold the return coil are attached to the detector support columns in preparation for the coil installation.

8.4.1.6 DAQ room

A room for the DAQ equipment is carved into the rock on the west side of the hall, midway along the length of the detector, and is entered from the upper level catwalks. This task is concerned with setting up the supporting equipment required by the DAQ. HVAC, power, racks and tables are installed as required by the DAQ equipment. A controls end-rack placed here provides access to the ACNET, the Fermilab closed circuit TV system, and the hardware for distributing the accelerator clock signals. Connections to the site networks are also included, as are the lines needed to transmit GPS clock data to the DAQ system, as described in Section 7.4.1.5.

8.4.1.7 Magnet power supply

The power supply for the magnet coil is located at the upstream end of the near hall. The supply requires connections to the AC power and cooling water, similar to magnet power supplies used elsewhere on the Fermilab site. Power and water lines are supplied to this area as part of WBS 1.2 and as specified by the liaison task WBS 2.5.1.1.2. Bus lines from the supply to the coil are connected after the coil is installed.

8.4.1.8 Assembly crew training

The near detector installation uses two types of work crews, one to move materials into the hall and place completed planes onto the detector, and one to assemble planes. Before

starting the assembly process, the crews will spend approximately one week in training. This includes all safety training recommended by FESH.

8.4.2 Materials handling (WBS 2.5.2)

This Section describes the near detector installation tasks associated with supplying materials to the detector hall. Reference [3] describes the work flow for this task in detail, as well as its coordination with the effort requirements of the detector assembly task (WBS 2.5.3).

8.4.2.1 Shaft lifting equipment

This is a liaison task to those items in WBS 1.2 which concern the hoist in the downstream access shaft and the areas around the upper and lower ends of the shaft. The crane is rated for the weight of the items to be moved in, and the shaft dimensions are based on their size. The shaft must accommodate the near detector steel plates, the magnet coils, and smaller items. The areas at each end of the shaft must accommodate the rigging of these items into the shaft at the top and into the tunnel at the base.

8.4.2.2 Underground transport carts

This is a liaison task to the design of the underground transport carts. The carts are of two types, one to deliver single steel plates, and the other to deliver boxes of scintillator modules. Each has its own weight ratings and is sized to pass through the tunnel between the base of the access shaft and the hall. The steel carts are designed for efficient handling of the plates, which are held vertically on the carts.

8.4.2.3 Assembly fixtures

This is a liaison task to the design of the fixtures used to attach scintillator modules to the steel plates.

8.4.2.4 Install assembly fixtures

The installation fixtures consist of the strongbacks and a surrounding assembly area. The strongbacks are prefabricated on site in sections which are easily transported down the access shaft and tunnel, and assembled in the hall. A strongback is a simple welded and bolted steel frame structure the size and shape of a near detector steel plane. It is used as a work surface for mounting scintillator modules on a steel plane. The strongback supports the plane and keeps it flat while it is installed onto the detector support structure.

8.4.2.5 Transport systems

The transport systems consist of the carts and the vehicles to push or pull them. They are fabricated on the surface as part of WBS 2.1 and delivered soon after beneficial occupancy of the hall. Items such as steel plates or crates of scintillator are lowered down the access shaft and placed directly onto the appropriate carts. A single plate is placed directly on a

cart, oriented vertically, and bolted to the cart's supporting structures before the hoist is disengaged. The cart is then moved into the hall. Either of the hall cranes can be used to pick up the steel plate from the cart and place it directly onto a strongback. Crates of scintillator are lowered in an orientation which keeps the modules flat, and are placed directly onto a cart, and then delivered to the hall. The modules are removed directly from the crate and mounted onto a plane. Empty crates are returned to the base of the access shaft and the downstream surface building.

The transport system will be tested and used to train the work crews soon after beneficial occupancy of the hall.

8.4.2.6 Materials delivery

The downstream surface building holds a staging area for both steel plates and crates of scintillator modules. There are two assembly workstations in the hall. During part of the time while a plane is being assembled on one workstation, the other workstation's strongback is free for assembling the next plane. When a strongback is free, a single steel plate is lowered on the shaft hoist, delivered to the hall, and immediately unloaded from the cart and placed onto the free strongback. The crew doing this task then delivers the crates of scintillator modules to be assembled on the steel plate. At about the time all the materials for assembling a new plane are delivered, the assembly of the plane on the other workstation is finished. The crew which delivered materials then goes to work on the task of mounting the finished plane onto the detector.

For either steel or scintillator modules, one cycle of delivery is estimated to take a total of 2 hours: 15 minutes for hoist attachment and handling at the top of the shaft, 30 minutes for hoist drop time, 15 minutes for hoist detachment and handling at the base of the shaft, 45 minutes for transit time to the hall and parking the load, 15 minutes for forklift truck return time to the base of the shaft. The hoist is raised back to the top of the shaft while the load is being driven to the hall. Two 5-man delivery crews work one of two shifts each day, five days per week.

Forward section planes each require two delivery cycles, one for the steel plate and the other for the scintillator. Three out of every four Spectrometer planes are steel only, so fewer overall delivery cycles are required for the Spectrometer section than for the Forward section.

8.4.3 Detector assembly (WBS 2.5.3)

This Section describes the near detector installation tasks associated with assembling the detector planes and mounting them on the detector. Reference [3] describes the work flow for this task in detail, as well as its coordination with the effort requirements of the materials handling task (WBS 2.5.2).

8.4.3.1 Magnet coil

This is a liaison tasks to the design of the near detector magnet coil.

8.4.3.2   Scintillator mounting

This is a liaison task to the design of the scintillator module mounting system. The goal of the design is to make a mounting system which is robust but which is also simple to install and requires a minimum of parts. The liaison ensures that the procedures for mounting the modules are transferred to the crews who perform that task.

8.4.3.3   Near hall cranes

This is a liaison task to those items in WBS 1.2 which concern the bridge cranes in the near hall, ensuring that they meet the specifications of the plane assembly procedures.

8.4.3.4   Detector electronics mount and cable

This is a liaison task to the design of the mechanical aspects of the electronics design. The liaison ensures that the framework attached to the detector support structure can accommodate the electronics hardware. The design task also lays out the locations of racks and cable runs, and the liaison ensures that spaces in the near hall are reserved for these items.

8.4.3.5   Mechanical assembly procedures

This is a liaison task to assist in the safety review of the procedures used to install the detector.

8.4.3.6   Detector assembly

The plane assembly in the near detector is modeled on the procedure used for the far detector. As described in Section 4.1.2, the near detector planes are single plates of 1-inch thick steel cut by the manufacturer to the designed shape. The near detector workstations, defined by the area where a strongback is laid on the floor of the hall, are used as work spaces for mounting scintillator modules to steel planes. The strongback provides a flat surface and reference points for assembly, and then also serves as a lifting fixture when a plane is installed on the detector.

There is space in the near detector hall for two assembly workstations. A four-man crew is needed to assemble a plane. The assembly process begins when all the materials are in the hall: a steel plate is placed on the strongback and scintillator modules are delivered to the hall. The detector plane assembly procedure involves the attachment of an array of scintillator modules to the face of a steel plane. The far detector plane assembly has been discussed extensively in Section 7.4.3.2. The procedures used for the near detector are very similar. These techniques involve steel packing straps fastened to tack-welded switchplates, shelf bars, and edge bracket connections on one end.

The scintillator modules for the near detector are of the same widths as those used for the far detector planes (see Figure 8.2). However, the modules are shorter than those used for the far detector, and most of them do not extend across the entire width of the steel, even those termed "full length." Also, some of the shorter modules terminate near the central coil

hole. Supporting the ends of these and other near detector modules requires special fixturing and procedures.

Two types of near detector planes must be assembled, those with short modules and those with full length modules; the numbers of each are summarized in Table 8.2. For 96 of the Forward section planes, short modules cover approximately one third of the steel area. There are 96 planes of full length modules in the Spectrometer section, plus 24 more interspersed in the Forward section.

After the scintillator modules are mounted, they are given a final performance test using the WLS fiber light injection system and the portable photodetector system. Calibration tests and performance criteria are described in more detail in Chapter 5 and in Section 8.4.5 below. Any detector modules which fail performance tests are replaced before the plane is mounted. The locations of detector elements are recorded using a close-range photogrammetry camera system (see Section 7.4.4).

Once a plane is assembled and tested, it is mounted onto the detector. The plane mounting operation is very similar to the far detector mounting operation (see Section 7.4.3.3). The strongback serves as a lifting fixture, and maintains rigidity and alignment of the steel and scintillator plane assembly during the lifting and mounting operation. The plane-strongback assembly is lifted to a vertical orientation and moved to the detector by the 15-ton bridge crane. While the plane is vertical, its weight is supported by the strongback support shelves along the bottom edge of the steel plane. The support shelves are configured to latch into the steel plane so that it cannot slip off the strongback during mounting. The plane is transported, mounted and secured to the support structure as described in detail in Section 7.4.3.3. Assembly of the near detector proceeds from downstream to upstream because access to the near hall is from the upstream end.

The same crew which delivers materials to the hall also mounts completed planes onto the detector. The two tasks overlap the time required by the assembly crew to install modules on a plane.

8.4.3.7   Electronics installation

After each plane has been mounted on the body of the detector, the clear fiber optics harnesses are installed on the plane and used to check for proper operation. A special portable photodetector system, which can be temporarily attached to the fiber optics harnesses from the detector access walkways, is used for this purpose. After all of the planes served by a single multiplexing box are in place, the electronics mounting platforms are installed and the final fiber optics connections made between the planes and the multiplexing boxes. Installed detector planes and associated front end electronics are turned on and tested with calibration systems (light injection and radioactive source tubes) and cosmic rays at the earliest possible time. Cosmic ray calibration data are recorded continuously from all installed detector planes as soon as soon as they have passed all calibration performance tests.

8.4.3.8   Magnet coil installation

The near detector magnet coil is quite different from the far detector coil. As described above, the near detector coil is fabricated from 48 aluminum conductor elements in two

L-shaped sections[5], arranged in an 8 by 6 array. Each conductor contains a central cooling water channel, as described in Chapter 4.

The completed magnet coil sections are installed after the 280 planes of the near detector have been mounted. The near return coil is routed along the lower 45° face of the detector. Before the installation can proceed, brackets are mounted on the steel support structure to support the return coil.

The coil is mounted as described in Section 4.4.4.4. After the coil is delivered (in two long pieces, or "L's"), the first coil half is inserted into the central hole using special lifting fixtures. Rollers on the lifting fixture enable the coil half to slide smoothly into the bore hole of the near detector, where it rests on the central collar tube. The lower, return coil is inserted underneath the detector. When it is fully inserted, it is lifted, rotated 45°, and supported from the previously installed brackets. After the installation procedure is complete, the coil sections are self-supporting.

Installing the magnet coil requires splicing the sections of the coil to each other, and making connections to the power supply and to the cooling water system. The conductors are welded after insertion of a stainless steel plug at the join. Conductors must be bent to meet, and properly positioned. Each pair of joins forms a complete turn, which will be checked for electrical and water integrity. The splicing, insulating, leak checking and electrical checkout of the completed circuit are the dominant time components of the assembly procedure.

The average magnetic properties of each plane are measured by its flux integration coil, as described in Section 7.4.3.6, soon after the magnet coil is installed. Each plane is measured as part of the initial magnet certification procedure.

8.4.4 Alignment and survey (WBS 2.5.4)

The near detector is surveyed using many of the same techniques developed for the far detector. The positions of the plane assemblies along the detector axis, and the relative positions of scintillator modules within each plane assembly, are connected to the absolute locations of the near hall survey monuments.

The principal tool used to obtain relative positions of plates and scintillator within the detector is photogrammetry. The system is identical to that used for the far detector, as described in Section 7.4.4.

The higher rate of cosmic ray muons at the near detector location makes it possible to determine quickly any small corrections to surveyed strip locations, and to detect errors in the survey numbers. Once beam is available, neutrino interaction muons will also provide alignment information.

8.4.5 Final checkout and validation

The performance validation of the near detector is intentionally kept as similar to the far detector as possible. These tests are described in detail in Section 7.4.5 . The source, light injection, and charge injection tests described there are reproduced at the near detector. Magnetic field measurements are also the same for both detectors.

Quality control and basic measurement procedures (such as plane thickness) are implemented in the same way as at the far detector. The goal in all cases is to allow direct

comparisons which do not rely on complicated simulations.

8.5 Future optimization and engineering

Because of the similarity of the near and far detectors, many of the integration and large-scale prototyping activities described in Section 7.5 are directly relevant to the near detector installation task. An example is the construction of the 4-plane prototypes in the New Muon Lab to study the assembly and plane-hanging procedures; a 4-plane prototype of the near detector assembly will follow the far detector prototype studies. Since the crews performing assembly at the near and far detectors will be different, there is a need to ensure adequate documentation of the information gained by the testing, and to design adequate training programs and supervisory structures for the assembly activities.

There are, in addition, aspects of the near detector construction which are necessarily different from the far detector, and require special attention to ensure optimal design:

- The mounting procedure for short detector modules. This procedure needs to be well characterized, since mechanical stresses and alignment procedures will be different. The near detector 4-plane prototype study will validate the design and also be used to train near detector assembly crews.

- The layout of electronics and MUX boxes. This differs due to the different readout scheme for the partially instrumented planes. This has implications for space layout and service access.

- Hoisting, unloading, and underground transport of detector and coil materials. This should continue to be studied to optimize the procedures and minimize startup time after occupancy of the hall.

- Any differences in the near and far support structures. These are expected to be small (Section 4.1.2).

Chapter 8 References

[1] The Fermilab NuMI Group, "NuMI Facility Technical Design Report," October 1998, Fermilab report NuMI-346.

[2] The Fermilab NuMI Project Staff, "NuMI Project Cost and Schedule Plan," October 1998, Fermilab report NuMI-362.

[3] R. Plunkett, "Work flow of near detector installation," September 1998, Fermilab report NuMI-L-400.

[4] The Fermilab NuMI Project Staff, "NuMI Project at Fermilab: Preliminary Safety Assessment Document," October 1998, Fermilab report NuMI-361.

[5] J. Kilmer, R.W. Fast, R. Currier, and R. Stanek, "Specifications for Aluminum Conductor," September 1998, Fermilab report NuMI-L-411.

Chapter 9

Software and computing

9.1 Overview

The task of the MINOS offline software is relatively simple compared to that of the large collider experiments. The MINOS detector is monolithic, a simple repetition of scintillator and steel planes, whereas collider experiments contain a multiplicity of different and complicated detector elements. As discussed in Chapter 6, the data rates in the far detector are very low and even those in the near detector are small compared with a pp or $p\bar{p}$ collider. Thus writing the offline analysis code is not expected to be a major load and the processing and data storage requirements are modest. This chapter discusses our plans to provide the effort and resources that will be needed both to process our data and to provide the basis for the subsequent physics analysis.

The functional requirements of the offline processing software are four-fold:

1. Generating realistic Monte Carlo events.

2. Finding the hits associated with events, both real data and Monte Carlo.

3. Separating the hits associated with a muon and fitting its momentum and direction through the magnetic field.

4. Analyzing the hadron/electron shower at the vertex for flavor content, energy and direction.

A considerable fraction of the code that would be required for a final system already exists and has been used in the definition of the physics capabilities of MINOS and the design of the MINOS detectors. It is written in Fortran-77 and runs under UNIX. As described in Section 9.2, it uses the ADAMO system to define the data structures and GEANT3 together with the Soudan 2 neutrino generation routines for the Monte Carlo simulation. However work is required to improve and extend the current code. We are confident that this system will provide a well-engineered and user-friendly offline software system. An estimate of the effort needed is given in Section 9.2.

However the MINOS collaboration is becoming increasingly concerned about the future of Fortran, and in particular about future support for the tools (such as CERNLIB, ADAMO

and ZEBRA) which will be vital for the maintenance of a Fortran system over the lifetime of MINOS. In recognition of this concern, and of the potential advantages offered by recent progress in programming techniques, the collaboration is investigating the use of a new C++ Object Oriented offline program system[1]. Section 9.3 describes the advantages of such a system and the effort and costs involved in its production.

In Section 9.4 we discuss the event rates expected and estimate the computing power and data storage required to deal with MINOS data and Monte Carlo events. We find that the requirements are modest. At the far detector a farm of ten 300 MHz processors, 50 Gigabytes of disk storage and a small permanent storage facility compatible with the Fermilab central store is needed. About 700 Gigabytes of data per year will be produced. At the near detector a farm of 20 processors for data and 6 for Monte Carlo together with 1.3 Terabytes per year of data storage is required. We expect to use the Fermilab central facilities to provide the near detector requirements.

Our data processing model, data distribution scheme and plans for physics analysis are detailed in Section 9.5.

The overall status the MINOS offline software system is summarized in Section 9.6

9.2   The current Fortran analysis code

The current MINOS software[2] is based on Fortran-77 code supported by a variety of non-commercial libraries such as CERNLIB. Only minimal deviations from the standard were permitted; the allowed extensions are commonly supported features such as the use of long names and the `#include` facility for common block synchronization. The Fortran-77 approach allowed the MINOS software group to proceed without the learning curve that an Object Oriented (OO) model would have entailed – MINOS collaborators could contribute by taking advantage of their prior knowledge and familiarity with packaged software.

The major addition to the traditional HEP software tools used by experiments at Fermilab was the inclusion of ADAMO[3] as the interface to the data structures. The ADAMO package is a CERN/DESY-supplied set of routines for bridging the gap between a ZEBRA/BOS memory manager and a more OO-oriented model. This package has also been used by the Aleph, Hermes, Zeus and Selex experiments. ADAMO completely hides the complexity of the ZEBRA memory manager and substitutes a unified access to the structures which provides more security against data corruption. In addition it provides more portability. Event files contain an embedded representation of the data model at the time it was created; this allows the data structures to evolve as the understanding of our needs change, while retaining the ability to read previously generated files without significant user intervention. The files themselves are an ADAMO structure overlaying a ZEBRA machine-independent format; this allows the event files to be exchanged between platforms. Event generation and analysis has occurred on SGI, Sun, HP, IBM-AIX, and DEC OSF/1 machines with essentially no machine-dependent code written by the MINOS software group.

The conceptual model of ADAMO represents the data in tabular form. Columns represent attributes (e.g., volume identifiers, or components of a 4-vector), while each row represents an individual object. Relationship links allow connections between different objects of the same or different types. Intrinsic support routines furnish indexing (sorting and selection)

along different attributes or combinations of attributes. These sorted lists are automatically maintained by the ADAMO system and are handled without excessive overhead. They are then available to all routines accessing the data structure. Using the indexing capabilities avoids the need for much of the code users would write to perform looping and sorting and which is often error prone and time consuming. Data integrity checks are also a standard feature of ADAMO.

Long term prospects of this approach are uncertain to some degree. The ADAMO package, while stable and without known bugs, is receiving only minimal support – the authors have been pressed into service on other projects. The ZEBRA and GEANT3 packages are due to have CERN support dropped in the forseeable future. The source code for all these packages is available, but modifications to support the idiosyncrasy of new platforms may prove to be difficult. However we expect a substantial user community to be committed to these packages throughout the lifetime of MINOS.

9.2.1 Beam simulation

Some of the neutrino oscillation tests, such as the ratio of ratios of charged to neutral current events in the far and near detectors, are relatively insensitive to details of the beam and beam simulation. Others, however, such as the charged current total energy spectrum test, may be systematics limited by knowledge of the beam. Hence beam simulation and comparison to data will be an important and time consuming task. The most detailed feedback to the beam simulation will come from monitoring the charged current event rate in the near detector, as a function of event energy, event vertex radius, and event time (since the magnetic fields in the pulsed horn system vary over the spill). Comparisons will also be needed with the beam muon monitoring system. Understanding the hadron production model in the target is especially crucial to a good understanding of the beam, and will have to be much more developed than was needed for beam design.

Three particle physics Monte Carlo programs have been used to predict neutrino fluxes in beam studies so far. GNuMI, NUADA, and PBEAM ν beam simulation packages trade off speed versus range of effects that are included, as shown in Table 9.1. Being essentially independently developed, they also serve as cross-checks of the calculations.

NUADA, originally written by Wilber Venus at CERN and modified and extended by David C. Carey at Fermilab[4], generates a matrix of production angles and momenta for $\pi^\pm$ and $K^\pm$ at the target, and tracks this "mesh" through the focusing system. At each step along each track, it integrates a neutrino flux at the detector which combines the production probability for that angle and momentum, the decay probability for that track, and the acceptance of the detector. Thus it is actually a calculation rather than a Monte Carlo. Continuing care is required to ensure that the granularity of the mesh is fine enough.

PBEAM, written by Noel Stanton at Kansas State University and with weighting methods incorporated by Wesley Smart at Fermilab, generates $\pi^\pm$, $K^\pm$, and K^0 in a Monte Carlo fashion, and tracks them through the focusing system. Absorption of hadrons in the horns is taken into account, but secondaries are not generated. Each hadron is then decayed at one position. PBEAM contains the option of generating neutrino fluxes two ways, either selecting random decay angles (i.e. unweighted Monte Carlo), or calculating the weight for that decay to produce a neutrino in the detector acceptance, a method developed by Rick Milburn of

Tufts University.

GNuMI, written by James Hylen and Adam Para at Fermilab[2], generates neutrino fluxes in a manner similar to PBEAM. It differs from PBEAM in being GEANT based, and in the larger number of effects that it includes. GNuMI was developed specifically for NuMI beam design. It includes code to properly handle the effect of polarization in the $\pi \rightarrow \mu \rightarrow \nu$ decay chain, including the angle and energy correlations, which is not part of GEANT.

	NUADA	PBEAM	GNuMI
Typical run time	0.2 hr	2 hr	200 hr
$\pi^{\pm}, K^{\pm} \rightarrow \nu_{\mu}, \overline{\nu}_{\mu}$	yes	yes	yes
$K_L^0 \rightarrow \nu_{\mu}, \overline{\nu}_{\mu}, \nu_e, \overline{\nu}_e$	no	yes	yes
$\mu^{\pm} \rightarrow \nu_{\mu}, \overline{\nu}_{\mu}, \nu_e, \overline{\nu}_e$	no	yes (ignores polarization)	yes
3 body decay model	none	phase space	V-A
Hadron absorption by horns etc.	yes	yes	yes
Secondary interactions from horns etc.	no	no	yes
μ (for monitor chambers)	no	yes	yes
Baryons (monitor chambers, radiation)	no	no	yes
Unweighted decays	no	yes	yes
Weighted decay to detector	K, π	K, π	K, π, μ

Table 9.1: Comparison of programs used for neutrino beam simulation.

The speed of NUADA is useful when a large number of variations of parameters are to be considered, but care must be used when interpreting the results. The wide band beam horn shapes were optimized with NUADA. The alignment studies used PBEAM's more realistic Monte Carlo tracking, at some cost in speed. GNuMI's larger range of physics effects are necessary for background studies of wrong-flavor neutrinos, and for calculating effects of secondary production from the horns and decay pipe walls. Table 9.2 shows the list of decays which contribute significantly to neutrino production in NuMI, and how they are modeled in GNuMI.

The work necessary for beam simulation and comparison with data will probably involve:

- Replacing the current GEANT/FLUKA model of hadron interactions in the target with another model; perhaps with an updated version of FLUKA or MARS or with data from a dedicated measurement of the production spectra using the NuMI beam and target.

- Developing techniques to use simulated events in the near detector in a weighted fashion, or to use data driven event reconstruction efficiencies, since brute force simulation of events to model the time, position, and energy beam dependence in the near detector would be too expensive in CPU time.

- Making multiple runs of GNuMI or GNuMI-like beam simulation, with variations of production and alignment parameters.

Parent	$c\tau$	Daughter	Branching Ratio	Type
π^+	7.80 m	$\mu^+\nu_\mu$	100 %	Isotropic
π^-	7.80 m	$\mu^-\nu_{\overline{\mu}}$	100 %	Isotropic
K^+	3.71 m	$\mu^+\nu_\mu$	63.51 %	Isotropic
		$e^+\nu_e\pi^0$	4.82 %	Isotropic V-A
		$\mu^+\nu_\mu\pi^0$	3.18 %	Isotropic V-A
K^-	3.71 m	$\mu^-\nu_{\overline{\mu}}$	63.51 %	Isotropic
		$e^-\nu_{\overline{e}}\pi^0$	4.82 %	Isotropic V-A
		$\mu^-\nu_{\overline{\mu}}\pi^0$	3.18 %	Isotropic V-A
K_l^0	15.49 m	$\pi^- e^+\nu_e$	19.35 %	Isotropic V-A
		$\pi^+ e^-\nu_{\overline{e}}$	19.35 %	Isotropic V-A
		$\pi^-\mu^+\nu_\mu$	13.50 %	Isotropic V-A
		$\pi^+\mu^-\nu_{\overline{\mu}}$	13.50 %	Isotropic V-A
μ^+	658.65	$e^+\nu_e\nu_{\overline{\mu}}$	100%	Polarized V-A
μ^-	658.65	$e^-\nu_{\overline{e}}\nu_\mu$	100%	Polarized V-A

Table 9.2: Decays which produce neutrinos in GNuMI.

Based on experience with the current version of GNuMI, approximately one CPU-year will be required for the beam simulation, in addition to the time required for simulation of the events in the near detector.

9.2.2 Detector event simulation

The simulation of neutrino interactions in the detector is a significant portion of the MINOS computing effort. In order to accomplish this task, a GEANT-based Monte Carlo program gminos has been written. The gminos program combines a flexible description of the detector geometry, the flux from GNuMI, our best understanding of the neutrino interaction physics, and the simulation of the properties of the scintillator and photodetectors with the standard GEANT-supplied tracking and particle interaction routines.

Runs of gminos are controlled by FFREAD data cards which describe the run parameters; the geometry configuration; the event generator switches; and the tunable parameters in the active detector response. A gminos output file is an ADAMO structured file containing the data models and the actual data for once-per-run information (such as the geometry) followed by individual event records. Figure 9.1 shows a block diagram of gminos.

Most MINOS collaborators eschew the actual running of the gminos program which is generally left to a few experts. Conditions for runs are agreed upon by the collaboration as a whole. The experts set up the data card files to match the conditions and submit the jobs to various machines (including a farm of batch nodes) for event generation. At the time of this report the collaboration has generated hundreds of thousands of MINOS neutrino interactions under a variety of conditions. These files are available from a central location on the Fermilab AFS file system. Individuals with particular needs for runs with special
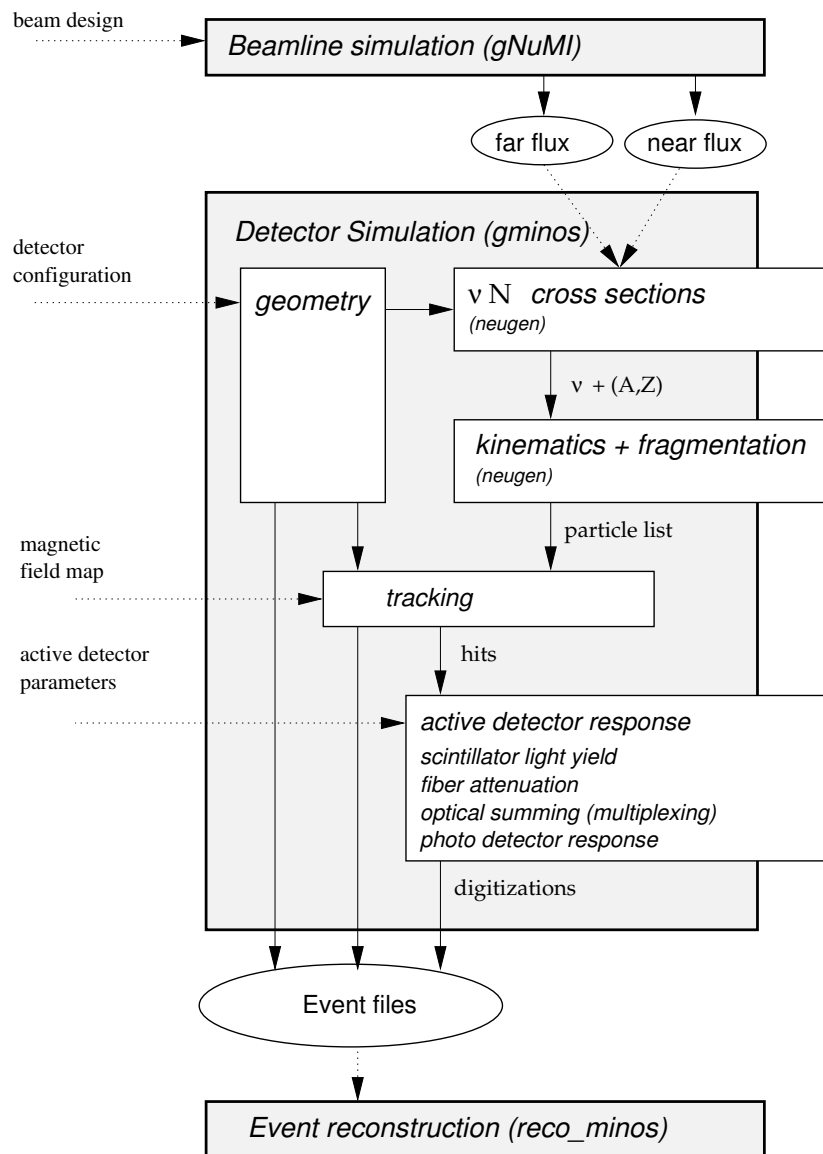
Figure 9.1: Block diagram of the `gminos` program. The major units of the detector simulation are shown. Their relationships with each other and outside elements are diagrammed schematically.

conditions are encouraged to run `gminos` on their own with support, as necessary, from the experts.

Modularity of the code functionality has been stressed so that sections of the code can be replaced without undue adverse effects. The following Sections describe the major components to the `gminos` program.

9.2.2.1 Interface to GNuMI flux

The output of the `GNuMI` simulation of the beamline is condensed into intermediate flux files by a separate stand-alone program. The flux files are a convenient format for use by `gminos`. By using a standard file format for the interchange, a user can change the flux used by `gminos` by simply changing a data card and supplying the new flux file. This provides a means for exploring the effects of different beamline configurations. Efficient near versus far detector event generation can be achieved by using different flux files derived from the same original `GNuMI` beamline simulation, resampled over the appropriate solid angle subtended by the detector.

In the case of the far detector, events can also be generated using a wide, artificial beam spectrum which can be weighted to simulate any of the three PH2 beam configurations (high, medium, low energy). This is possible because the beam at this location has a negligible divergence so there is no need to worry about the correlations of the neutrino direction with neutrino type and energy. The weighting factors are derived from histograms of the `GNuMI` flux. This approach reduces the need for a large Monte Carlo data sample for each beam configuration, which saves both disk space and CPU processing time.

9.2.2.2 NEUGEN: The MINOS event generator

All `gminos` simulations use the NEUGEN neutrino event generator to model the neutrino interaction, producing from an input neutrino and nucleus type a list of final state particles which are then returned to the detector simulation. In this Section we present a brief overview of the physics of the event generator and plans for further improvements.

At low energies, charged current neutrino interactions are predominantly quasi-elastic and single pion production, in which the neutrino scatters off an entire nucleon rather than the constituent partons. The cross section for quasi-elastic scattering is expressed in terms of the weak form factors of the nucleon. The vector components can be related to the well-measured electromagnetic form factors via the CVC hypothesis, and the axial vector form factor has been measured in numerous low energy bubble chamber (100 MeV - 10 GeV) experiments. For tau production, retaining terms proportional to the produced lepton mass leads to a significant contribution to the cross section from the pseudoscalar form factor. The contribution from this form factor is negligible for muon or electron neutrino scattering, and as such it is at present unmeasured in neutrino interactions. For the purposes of our simulations a theoretical expectation based on the PCAC hypothesis is used. Generation of single pion final states through resonance production is based on the neutrino production model of Rein and Seghal[5] and the Feynman, Kislinger and Ravndal model of baryon resonances[6]. This model treats the baryon resonances as the excited states of the 3-quark system bound by a relativistic harmonic oscillator potential. The matrix elements for neutrino induced res-

onance production are then calculated directly from the bound state wavefunctions. Single pion production is dominated by production of the $\Delta(1232)$.

At higher energies, the neutrino scatters off the partons within the nucleon. Neutrino deep inelastic scattering has been studied with high precision in the energy range 10 to 200 GeV by a number of experiments. DIS cross sections are again written in terms of form factors which can be now be expressed in terms of the constituent parton distributions. Tau production introduces an added complication in that form factors which are usually negligible (W_4 and W_5) must now be retained. Although unmeasured, their expectation in terms of parton distributions is known. Hadronization of DIS-generated final states is done using a scheme based on KNO scaling. The KNO model used has been tested and shown to be valid for neutrino induced hadronic final states.

NEUGEN also needs to take into account the fact that the nucleons participating in the interactions are not free but are bound within the nucleus. The two most important nuclear effects for low energy scattering are the Fermi motion of the struck nucleon and Pauli blocking of interactions with small momentum transfers. Both effects are modeled with a Fermi gas model of the nucleus. In this model all nucleon energy levels up to the Fermi momentum P_f are considered to be filled (thus generating the Fermi momentum spectrum), and momentum transfers which leave the final state nucleon with momentum smaller than the Fermi momentum are not allowed.

NEUGEN grew out of the neutrino event generator used by the Soudan 2 collaboration to model atmospheric neutrino interactions[7]. In this capacity the generator has been in use since 1987, and has been well tested - particularly at the lower neutrino energies of atmospheric neutrinos. Numerous comparisons to published data have been made, and experimental DSTs from the BEBC experiments, which took nearly 750,000 bubble chamber pictures in runs from 1977-1983, have been made available to the collaboration for more detailed comparisons which are currently underway. NEUGEN has also been made available to other neutrino experiments.

Ultimately one would like to address the question of the extent to which uncertainties in the physics models will affect the sensitivity of a given experiment. As a two-station experiment, MINOS is to first order insensitive to such uncertainties, as has been shown in previous studies. Nevertheless, it is for such studies that one would like to have a generator which incorporates the full range of physics models which have been proposed. One then uses existing data to determine the models and ranges of model parameters which are consistent with current measurements. This process of model inclusion and data comparison is an ongoing one which will continue over the next few years as NEUGEN continues to evolve and improve.

9.2.2.3 Interface with NEUGEN

NEUGEN outputs a list of particles in STDHEP form. The gminos-specific code pulls a neutrino from the flux file; samples the detector along the neutrino's path; decides on whether an interaction occurs; chooses a vertex position and nucleus type; calls the kinematics generator and enters the STDHEP list into GEANT's list of particles to track. This procedure correctly accounts for the distribution of material along the neutrino path and the relative proportions of nuclei, based on the geometry of the current run. The code is modular enough

that the cross section or kinematics routines can be improved or even completely replaced without major impact on the gminos code downstream from the interface.

9.2.2.4 Geometry

Although the finest-level details of the MINOS geometry are still being defined, handling future changes is not expected to require significant new code. The gminos code provides a simple user interface which allows substantial reconfiguration of the detector for a wide variety of parameters. These parameters are then converted into standard GEANT geometry descriptions of the detector. By making the geometry description sufficiently abstract one can describe both the near and far detectors without need for separate parallel code.

9.2.2.5 Tracking and hit storage

Particles are tracked through the GEANT geometry in the usual manner. Different maps for the magnetic field can be set along with the geometry specification. These field maps are generated by the MINOS magnet group (Chapter 4) and are specified relative to a single steel plane's local coordinates. The gminos code then performs the appropriate coordinate transformations.

Pertinent information is recorded for each particle traversing an active detector volume. These attributes include the volume identifiers, energy deposition, entering and exiting positions. These objects are designated as *hits* and contain the exact, unknowable information about the particle's traversal.

9.2.2.6 Digitization

The final step of the detector simulation process is collecting together the *hits* in a volume and converting them into *digitizations*. The digitizations (digits) are the combined effect of individual particles interacting within the active volume. These digits will closely mimic the types of signals that come out of the front-end electronics, described in Chapter 6. This process of modeling the active detector response encompasses the light production (including Birk's Law saturation effects[8]) in the scintillator, light collection and re-emission in the wavelength shifting fiber, attenuation in the fiber and photodetector response. The final result gives realistic results for the photoelectron statistics.

We have chosen to retain the *hits* in the data files. This imposes a large space penalty but allows us to reuse the same events while varying the specifics of the digitization process. By doing so we can investigate the effects of different scintillator light yields, fiber attentuation, and other possible changes in instrumentation details. The redigitization can be done in the analysis framework (described in Section 9.2.3) just prior to the event reconstruction.

9.2.3 Event reconstruction

A framework for event file processing has been developed: the reco_minos package standardizes the reading and processing of files currently generated by the gminos program and, when the time comes, real events written in a compatible format. This shell incorporates

ADAMO's ability to skip event input based on information in the header bank, allowing quick access to selected events in a file. Figure 9.2 shows a flow diagram of reco_minos.

At a minimum, the user need only supply routines for their own histogram booking and event processing, a list of event files and a set of data cards for controlling the analysis. Hooks are provided to allow users to supply routines to handle different phases of file processing.

The user's event processing routine can call upon collaboration supplied routines for basic reconstruction. These routines are still being developed and refined. While it is likely that much of the currently available code will not survive unmodified to the time data-taking begins, it is has been a good introduction to what the final requirements will need to be. This insight will lead to better algorithms in the future. Even these incomplete algorithms have provided feedback for use in detector hardware decisions.

9.2.3.1 Demultiplexing and attenuation correction

A framework for simulating the optical summing (multiplexing) of multiple fibers on single photodetector pixel has been developed. Simultaneously, a program to disentangle the multiplexing is being tested.

An algorithm has been written to account and correct for the light loss due to the attenuation in the wavelength shifting fiber, using nearby strips in the orthogonal view to determine the average position in a cell. This correction is necessary for achieving the good energy resolution which is intrinsic to the MINOS scintillator detector technology.

9.2.3.2 Vertex finding and event separation

A generic vertex finder has been written and gives adequate results. Alternative finders that improve on this for specific event topologies can be added to run in parallel.

Algorithms for separating out simultaneous events in the detector have not yet been considered.

9.2.3.3 Muon reconstruction

The problem of tracking and fitting muons in MINOS is more complicated than in conventional detectors as they lose a large amount of energy in traversing the steel plates, many coming to rest. Furthermore the toroidal field is different in direction at each point along the track and multiple coulomb scattering plays a large role in defining the track trajectory. A iterative least squares method of coping with these difficulties, patterned after the CDHS approach[9, 10], has been adapted for MINOS. Muon reconstruction is performed in two stages.

First, the hits associated with the muons are found by searching for track segments in each view. The longest segment is taken as the track basis and extrapolated out to the edge of the detector (or end of the track) and back to the hadron shower. Currently it does not attempt to extrapolate back to the vertex in the shower but ultimately this should be possible. Second, the muon hits are fitted to a curved trajectory. By tracking the muon through the detector material, the energy loss of the muon and its multiple Coulomb scattering can be calculated, producing a full non-diagonal weight matrix for the χ^2. The trajectory equations can be then solved by iterative least squares, yielding values for the parameters plus a full

initialize HBOOK and ADAMO

define system FFREAD cards

reco_init   *define user FFREAD cards*

read FFREAD data cards

reco_hist   *book user histograms + other user run independent initialization*

read from list of files to process

EOF? — no → open event file

yes

read ADAMO record → EOF? — yes

no

reco_notevt ← no — event?

process geometry records

yes

new run? — yes → previous run? — yes → **reco_end_run**

no   no   *(see below)*

reco_new_run

run dependent initialization

reco_event

user defined event processing - including:

  redigitization of hits
  photodetector response
  attenuation correction
  vertex finding
  muon tracking + momentum determination
  shower energy + angle determination
  event classification
  event display (graphics)

reco_end_run   *end-of-run processing*

reco_finish   *end-of-job processing*

Figure 9.2: Flow diagram for the reco_minos program. The routines that users write are shown as shaded boxes. Dummy routines are used if no routine is supplied.

error matrix. However, when the muon is close to stopping, its increasing departure from linearity means that care must be taken to avoid the final segment of the track in the fit. This procedure yields momentum errors of $\sim 13\%$ and angular resolutions of ~ 0.03 radians when muons are fitted over ≤ 400 planes.

For short, stopping muon tracks that are fully contained in the detector, a simple track length measurement will result in an even better estimate of the muon energy, although curvature is still necessary for determining the charge.

9.2.3.4 Shower energy and angle determination

Preliminary routines have been written for energy (photoelectron summing) and shower angle determination, but have not been extensively tested. In particular the energy sum is dependent on the attenuation correction; energy resolutions significantly suffer if it is not applied. The existing code does not yet attempt to remove the overlapping muon track, but this will be remedied in the future as both this code and the muon tracking code improve.

9.2.3.5 Event identification

We have used event classification heuristics (NC versus CC, ν_e versus ν_μ versus ν_τ, etc.) in various studies of MINOS sensitivity to neutrino oscillations[2, 11, 12]. We have not mounted a systematic attempt to generate the best-possible approach for all cases. Rather, estimates of the signal efficiency and background rejection set a lower limit on how well the experiment might perform. More sophisticated approaches will give some improvement but are not expected to change the conclusions of our current analyses.

The NC versus CC classification proceeds on two levels. The simpler approach is to not attempt event-by-event classification. Instead, we separate the events into two classes that to a large degree overlap the physical process, but are easily identified in real event topologies where an estimate of the cross contamination can be made. This is the approach of using "short" and "long" events as initial estimators of the NC and CC events. Once so classified then the unfolding of these into NC and CC events proceeds at the statistical level. The second approach to NC versus CC classification is to attempt pattern recognition of the muon track. This is part of the muon reconstruction code described above.

We have developed techniques for neutrino flavor determination in two broad categories. One approach has been to use cuts on the distributions of event characteristics and reconstructed quantities to distinguish the categories. The other methodology uses essentially the same quantities but presents them to an artificial neural network (ANN) for identification. The ANN is first trained to classify the events by presenting it with a test sample of known types. It is then tested with a separate sample of events; the result of the test is a value between 0 and 1 that serves as an estimator of how likely it is to be of the type represented by the output value. As the threshold on this output value is increased, the efficiency for correctly classifying the signal goes down, but the rejection of background goes up. The optimal value for the threshold may depend on the exact analysis in which the classification is being used. Generally the cuts and ANN approaches have yielded very comparable results in tests where both have been attempted. It is expected that the ANN method should generally lead to a slightly better separation.

Explicit identification of electrons is based on the fact that electron showers are shorter, narrower and denser than hadron showers. Thus, after selecting "short" events, cuts (or ANN inputs) based on the charge distribution in the remaining shower produce ν_μ charged current rejection factors of 700 for ν_e's. The charged current efficiency of 14% is sufficient to give limits for $\sin^2(2\theta)$ of 2×10^{-3}. This study was performed using the high energy beam configuration, but we have also developed similar algorithms for the low and medium energy neutrino beams.

Identification of explicit τ production can be made in various τ decay modes. In $\tau \to \mu\nu\nu$ and $\tau \to e\nu\nu$ the analysis is based on selecting quasi-elastic (low-y) τ production, where there is little hadronic activity at the production vertex. Then, for a given beam ν energy, the kinematics of the events with missing ν's gives lower lepton energies than for equivalent ν_μ events. Thus in the narrow band beam, kinematically unambiguous τ production can be observed, provided the tails of the beam energy distributions can be kept under control. The decay $\tau \to \pi + X$ can be isolated by selection of high energy π's which interact to produce hadronic "stars". The background from neutral current π production is suppressed because the energy distribution of these π's is much softer than that from τ decay. Limits on $\sin^2(2\theta)$ down to around 0.2 can be obtained[13].

All of these explicit tests for ν_e and ν_τ production involve detailed reconstruction of the hadron shower, including possibly the reconstruction of individual tracks and showers within the overall hadron shower. Techniques for this reconstruction are still rudimentary but are expected to be significantly improved before data is available.

9.2.3.6 Graphics

Computer graphics plays an important role in many aspects of an experiment. For the standard tasks of data analysis, fitting, and presentation graphics MINOS currently uses CERN software, including PAW and HIGZ.

Graphics are also used to display simulated data and reconstructed events both for algorithm development and to demonstrate event types and topologies. An X-based, interactive 3D graphics system based on VINES (Erik Gottschalk, Univ. of Illinois) is available on a few of the computer platforms used by the collaboration. A limited, static event display using HIGZ and HPLOT routines is available on all platforms. Rudimentary information about hit location and pulse height are displayed, but without any interactivity. Users can supply calls to familiar routines to add additional information.

We have begun work to produce a more flexible and portable display based on an OO paradigm. Two efforts are currently being pursued. In one project the MINOS event data and analysis code are being integrated into the ROOT software system currently under development at CERN by Rene Brun and collaborators. In the other, we are investigating the use of OO-based Internet tools to produce portable events displays. A prototype display employs Java and VRML to produce 3D virtual-reality event displays and associated analysis tools.

9.2.4 Code management

9.2.4.1 Code manager/librarian

The responsibility for managing packages in the MINOS collaboration central software repository and for maintaining their functionality will be vested primarily in the designated librarian or code manager. Deputy managers may have responsibilities concerning details of individual packages/libraries. In particular, the code manager will be responsible for:

- promulgating and enforcing coding practice standards

- regulating changes to the central repository

- informing collaborators of the use and availability of outside software packages required by collaboration code.

- disseminating documentation of collaboration code (via the World Wide Web).

- maintaining E-mail distribution lists for current software news and discussion.

9.2.4.2 MINOS software repository

The central repository makes the common code accessible to all members via the program CVS (Concurrent Versions System[14]). CVS allows access to a central repository by a remote computer. Thus it is only necessary to have a complete repository at one location, helping to minimize the possibility of divergence in collaboration-standard programs. The MINOS source code repository will eventually grow to include all collaboration-standard programs for simulations, event reconstruction, physics analysis, and event display. The GEANT-based detector simulation gminos, as well as analysis/event reconstruction routines in the context of the reco_minos program, are now available in the CVS repository. Checking a program module out of the repository provides the user with copies of all the source code files as well as the Makefiles necessary to construct libraries and executable programs.

9.2.4.3 Software development and distribution using CVS

CVS is a tool for version management and code distribution during the software development phase. Built on top of the older RCS (Revision Control System), CVS adds the flexibility of allowing multiple developers to work on the same source files concurrently. Each programmer/user checks out copies of the desired files from the central repository into a personal work area on his/her home computer. The local copies of the files can be modified or deleted as the user desires without effect on the standard repository version. The repository version is only changed upon the explicit request of the CVS user. Thus the system accommodates both users who wish to modify the source code for their own use or for redistribution to the collaboration, as well as those who merely want to build a standard executable program for their studies.

Once a file is stored in the CVS repository, a complete history of its evolution thereafter is recorded by CVS. Any version of a file can be reconstructed at any time based on one of the identifying characteristics: date, revision number or symbolic tag.

CVS has been designed to help resolve the inevitable conflicts that arise when more than one person edits a particular source file. CVS does not use file locking which would prevent concurrent development. Rather, CVS has conflict resolution algorithms which sense any incompatibility between the changes to the local copy and a new repository version. Changes that can not be resolved generate warnings and in-file delimited code lines. The user must then decide whether to alter their code to incorporate the newer revision, or to confer with the colleague who committed that revision.

The central repository can in principle be updated at will by a user with the changes they have made to their local source files. This introduces a conflict between program developers who want the most up-to-date version of the software and are prepared to tolerate bugs, and users who want only functional, reasonably well-tested code. To resolve this, we are developing a set of regulations concerning who may actually commit code and requirements on the functionality at the time it is committed. To date this has been generally very informal, but as the amount of code and number of users increase so will the level of software management with alpha, beta, and production code releases controlled by individual package managers.

9.2.5 Requirements to complete the Fortran offline system

Although a considerable amount of code has been written, there still remains a lot of work to complete a user-friendly, well-engineered system. The code will need revision and reworking to improve and extend its functionality. The present system also needs the addition of a database for storage of run and calibration constants along with all the miscellaneous data that are needed, as well as the raw detector data. The current graphics package is very rudimentary and will need complete reworking to be made into a flexible tool for diagnostic and debugging work.

It is difficult to estimate how much effort would be required to produce a system adequate for data taking in 2002, but it probably exceeds ten man-years. We believe that this effort can be found within the MINOS collaboration. The purchase of commercial software will probably not be required except for the (Oracle) database system.

9.3 The OO alternative

9.3.1 Motivation

It is difficult to overstate the importance of computing in experimental HEP. It is central, and essential, to all phases in the life cycle of an experiment, from detector design and construction through to its operation and analysis of the data it produces. Without the dramatic advances in computing technology over the past 30 years most of the HEP program would have been impossible. The clear lesson of this is that we have to keep up to date with mainstream developments if we are to continue to exploit these advances.

The disparity in the rate at which hardware performance improves compared to that of software has long been recognized. While hardware performance growth is essentially exponential, software growth is almost linear. A major part of this disparity comes from the way

hardware engineers manage complexity. By structuring systems into subsystems and hiding complexity behind simple interfaces, development is simplified. Individual subsystems can evolve independently and still remain compatible, while new systems can be produced by assembling the subsystems in different configurations. OO is the latest, and most successful, in a series software engineering paradigms that have attempted to achieve the same level of structuring in software. Modularization is achieved by hiding complexity through encapsulation. Larger systems are broken down into more fundamental ones by abstraction. These subsystems can then evolve over time through the mechanism of inheritance, while assemblies of evolved subsystems continue to cooperate.

OO is relevant to experimental HEP because of the common problem domain all experiments address. Common solutions to some of these problems have been very successful, for example ADAMO, which has been described above. Its success comes from its OO-like properties. Like any well defined class, it presents a simple rugged interface to the user and provides access mechanisms to the data it holds. However, it does not hide its data and is of limited help in building modular systems. Until now, most standard HEP software systems have provided support for the major off-line activities of Monte Carlo, Data Reduction, Event Reconstruction and Analysis, but have stopped short of providing these functions themselves. So each experiment has had to devote many man-years to developing code to do this, despite the fact that there are many shared problems and solutions. To pick just one example in MINOS, we have to be able to find and fit muons in our data and are producing code to to this, despite the fact that such codes were analyzing bubble chamber film 20 years ago. The code robustness that is inherent in the OO model is particularly important in HEP, where people, with a wide range of skills and understanding of the code, have to work with it. A properly designed system should allow much greater access to the code to those outside the core support group, because it is more modular, with fewer side effects to catch the unwary! Its stricter disciplines ensure cleaner code and facilitate code development, a process that continues throughout the course of an experiment.

As has been stated earlier, the offline software requirements of MINOS are very modest; it is not the case that OO is essential. Indeed, in the short term, an OO alternative will involve more effort. In the longer term this should be repaid in the reduced maintenance compared to systems such as ZEBRA and ADAMO where support is already becoming very fragmented. The simplicity of this experiment also makes it a very good one in which to migrate to OO, a migration that is already underway in all of the larger, next generation experiments. Beyond the fact that it will give us a natural interface to GEANT4, the OO replacement of GEANT3, it will ensure that we stay in the mainstream of HEP code development. Predicting the style of computing 5 or 10 years from now cannot be done with any great certainty beyond stating that it will be much more powerful and will be different! By investing the additional effort to master OO now we will maximize our ability to best exploit improvements in the technology.

A small group within MINOS is in the process of studying all the consequences of choosing OO as the basis of our off-line software. The remainder of this Section has to attempt to second guess what that group will learn.

9.3.2 Requirements for an OO alternative

Choosing the OO route would lead to a number of extra requirements that would not be necessary for the Fortran route. At least initially there will inevitably be extra costs and effort required. However neither is expected to be large on the scale of the full experiment.

9.3.2.1 Training

Members of our collaboration have little experience with OO and will have to develop their own set of experts. Fully understanding the subtleties of a language like C++, and how properly to analyze and design an OO system, demands a higher level of expertise than that required to understand Fortran-77 and to perform procedural analysis and design on a system based on a data structure manager. The conventional wisdom is that it takes of order 6 months to turn a good Fortran programmer into a good OO programmer. Although the same level of expertise is not required of the rest of the collaboration, anyone who wants to make a significant contribution to the software will have to become a competent C++ programmer which could take of the order of a month. New post-graduates joining will probably already be familiar with C++. We estimate that a total of about three man-years of training will be required within the collaboration.

9.3.2.2 CASE tools

The relationships between classes in OO are much richer than the relationships between routines of a procedurally based code. Classes may inherit, own or simply use other classes in a variety of ways. This richness makes the use of CASE (Computer Aided Software Engineering) tools much more compelling, to help people express, exchange and check consistency of the systems they are studying. If MINOS uses OO then we will probably need to buy some CASE tools although the number of licenses can be restricted to core group designing the heart of the system. Typical costs for popular tools would be around $10,000. However we do not currently know what tools we need, and might even decide to do without any.

9.3.2.3 Commercial packages

The standardization of interfaces between classes promotes the ability to integrate software from different sources. At least some parts of the HEP community are now concentrating their programming efforts on problems that are unique to the discipline and seeking commercial software solutions to more general problems. Indeed this is the philosophy behind LHC++: it puts great emphasis on the use of commodity software. They plan to use only one major software component entirely developed within HEP, namely GEANT4, an OO version of the GEANT simulation package.

This of course leads to another cost for any experiment that takes this approach. The whole collaboration will need to run the software; many more licenses are required than for CASE tools. Estimating the cost of this approach is fraught with difficulty: the result depends crucially on our computing model, something that the MINOS OO working group is studying. At one end of the spectrum of choice lies the LHC++ model, which will be expensive. At the other end is the tradition of sharing software written by and for the HEP

community. Here the only current candidate is ROOT, a system being developed at CERN for NA49 and also being studied by a number of other experiments. It appears that we could use both GEANT4 and ROOT as the basis of our computing model without the need for any commercial software. There are several advantages to this approach:

- Cost. This could be a zero cost option, at least in financial terms.

- An optimal match to the requirements of HEP. There is no need to support generic requirements that are not part of the HEP problem domain.

- Better control over its development. It responds directly to the changing needs of HEP.

- Long term security. It belongs to HEP with its own unique development time scales.

The last of this list, long term security, is currently the weakness with ROOT. Until further experiments invest in it, its long term future is uncertain.

9.3.2.4 An OO version of the offline system

The MINOS software group is now devoting significant effort to developing a new OO equivalent of the Fortran based system described above. Others working in OO have told us that the only way to learn is by trying and that it is very hard to get it right the first time. Here MINOS has an advantage, relative to other experiments embarked on this course, in that its requirements are comparatively simple. So we could plan to develop a first version on a one year time frame and then use the experience gained to build a second on a similar time frame. We estimate that this would require about 10 man-years of effort in addition to the effort involved in the updating and improving the algorithms already developed. As for the Fortran alternative, we expect that most of this effort will be available from the collaborating groups.

9.4 CPU and storage requirements

In this Section we attempt to estimate the amount of cpu power and data storage that will be required to process and store the data from the MINOS far and near detectors, as described in Chapters 5 and 6, and to perform high statistics Monte Carlo simulations of the experiment.

Such estimates are notoriously subject to under-estimate, particularly when the program systems are not complete and real data has not been experienced. We have tried to make realistic estimates, based on currently working code, including an allowance for reprocessing of data. However even with existing code, the variation in timing across different platforms is large. Also very little effort has currently gone into optimization of code and large factors may well be available. With these uncertainties the estimates given here are probably not accurate to better than a factor of two. Even thus inflated the requirements of MINOS are modest by today's standards. With the natural progression of computer power we expect to be able to keep pace with any unanticipated increase in the computer requirements or reduce our hardware requirements. However, if the worst should occur and both these estimates

are over-optimistic and extra computer power is not available, it should be noted that in the estimates below the vast majority of time is spent processing secondary data; cosmic ray muons or neutrino events outside the beam spot in the near detector. Fast filters for real physics data can be developed and the remainder of the data either sampled or processed with faster, less complete, algorithms.

The timings are in terms of a modern 300 MHz RISC processor which is equivalent to around 200 MIPS.

9.4.1 Far detector

We assume:

1. A trigger rate of 2 Hz, made up of 1 Hz of cosmic ray muons and 1 Hz of background noise (radioactivity or electronics). The 22,000 neutrino interactions per year are negligible in this calculation

2. An average of 300 hit scintillator strips per trigger. This is probably generous because noise events will be small. There are 192 scintillator strips in a plane. Most cosmic muons will hit fewer strips than this but high energy muons have a high probability of producing a showering bremsstrahlung electron in their passage through the detector.

3. Eight bytes per hit read out by the electronics

4. Five seconds processing time per event for a cosmic ray muon. Noise triggers will be fast, therefore the average processing time per trigger is 2.5 seconds.

5. Data expansion during processing by a factor of 5.

6. Continuous far detector operation with a 90% duty cycle. Running outside beam-on periods is probably necessary, first to obtain sufficient cosmic ray muons for calibration and second to be continuously sensitive for atmospheric neutrinos and other cosmic ray phenomena.

7. Storage of raw data and processed information for all cosmic ray muon events. This will probably not be necessary, after an initial running-in period. The muons are mostly required for calibration purposes and the data for this will be filtered off and stored as histograms for each scintillator strip. However, if raw muon data are not kept, the storage requirements are negligible so this represents a worse case.

8. At least in the first stages of data taking it will be necessary to reprocess data as the reconstruction algorithms are refined and developed. Since continuous operation is assumed, this will require that we double the computing power available to enable us to reprocess in parallel with data taking.

Table 9.3 gives some of the far detector requirements which result from this model.

It can be seen from the Table that a modest farm of 5 cpu's will be adequate to fully reconstruct all the cosmic ray muons, even assuming no increase in speed beyond today's models, and assuming that this process is necessary for calibration. Allowing for the data

Triggers/year	$2 \times 3 \times 10^7$	6×10^7 triggers
CPU processing time/year	$2.5 \times 6 \times 10^7$	1.5×10^8 sec
Readout bytes/year	$8 \times 300 \times 6 \times 10^7$	1.44×10^{11} bytes
Data stored/year	$5 \times 1.44 \times 10^{11}$	720 Gigabytes

Table 9.3: Summary of estimated far detector cpu and storage requirements, including generous contingency allowances.

reprocessing we will require a farm of 10 processors at the Soudan site. The data storage requirement is small by today's standards, even if we were to keep all the cosmic muon raw data.

9.4.2 Near detector

Rates in the near detector are much higher than in the far detector and the processing and storage requirements are more stringent. We assume:

1. Thirty ν events/spill in the target and veto regions of the near detector. Of these, the 0.5 events/spill produced in the central 25 cm radius of the target region are required for physics comparison with the far detector. The remainder will be used to monitor and model the beam and for other nonoscillation physics that may be performed with the near detector.

2. Event rates of 15 muons/spill entering the target region from upstream neutrino interactions and 270 Hz of cosmic ray muons crossing the full detector, in addition to the neutrino interactions. For calibration purposes the upstream muons, and an equal sample of the cosmic muons, will be fully reconstructed for each spill. Full reconstruction of the remaining cosmic muons is probably unacceptable for cpu time reasons but they may be used in a simple histogramming mode to obtain very high statistics calibration data. It may be that ultimately the full reconstruction can be dispensed with.

3. A negligible in-spill random trigger rate.

4. An average of 100 hits/trigger. Near detector events are smaller than the cosmic ray muon events in the far detector, the muon spectrometer sampling is coarser and the lower energy muons will not produce large bremsstrahlung showers.

5. Eight readout bytes/hit and 5 times the raw data stored per trigger.

6. One second processing time per trigger.

7. An effective year of 10^7 seconds.

8. One complete reprocessing of the data.

Triggers/year	$60/1.8 \times 10^7$	3.3×10^8 triggers
CPU processing time/year	$1.0 \times 3.3 \times 10^8$	3.3×10^8 sec
Readout bytes/year	$8 \times 100 \times 3.3 \times 10^8$	2.6×10^{11} bytes
Data stored/year	$5 \times 2.6 \times 10^{11}$	1.3 Terabytes

Table 9.4: Summary of estimated near detector cpu and storage requirements.

Table 9.4 gives the numbers for the near detector quantities.

Ten processors running continuously will keep pace with the incoming data integrated over a full year. Allowing for reprocessing we will need access to a farm of 20 processors. This is an upper limit on the cpu usage since less than 1% of the events being reconstructed are required for MINOS neutrino oscillation physics. If there should be cpu limitations, more stringent cuts on the events reconstructed could be applied. Similarly, although the data storage requirement is not large, it may be much reduced if only the calibration information for each scintillator strip is stored.

9.4.3 Monte Carlo simulation

We expect 22,000 neutrino events per year in the far detector and 2×10^6 per year in the restricted target volume of the near detector. The Monte Carlo calculation has to:

1. Determine and correct efficiencies and biases in the reconstruction and selection processes in the far detector. The Monte Carlo statistics must be overwhelming compared to the number of events in the far detector, by at least a factor of 10.

2. Translate the distributions measured in the near detector to those expected in the far detector, making allowances for differences in the beam and the detectors. The requirement on the accuracy of this transformation is only that the statistical error should be negligible compared to the statistical accuracy of the *far* detector data. Thus a Monte Carlo sample equal to the near detector data sample will be adequate.

We thus expect to require a Monte Carlo sample of approximately 2×10^6 events per year for the combined near and far detector analysis. In order to study the algorithms used in distinguishing neutrino types based on event topologies, we must generate events for the three possible modes of no oscillations and and for oscillations to each of the other flavors, tripling the the number of events necessary.

The current cpu time required for generating an event in gminos is ~ 20 seconds. Adding time to generate the beam neutrino and for reconstruction we estimate a total cpu time of 40 seconds per event. The average storage requirements for Monte Carlo events will be substantially larger than data events. Two contributions to this increase are the additional space necessary for storing generated truth information and the desire to store intermediate *hit* information as well as the final *digitizations*. The hit information allows us to study the effects of uncertainty in light yield, photodetector gain variations and other detector effects without performing the cpu intensive generation and tracking of events. Based on the

empirical estimates from the current data sets, Monte Carlo events average about 57 kbytes per event. Table 9.5 gives an estimate of the total cpu and storage requirements for the Monte Carlo.

Events generated/year	$3 \times 2 \times 10^6$	6×10^6
CPU processing time/year	$40 \times 6 \times 10^6$	2.4×10^8 sec
MC event size		57 kbytes
Data stored/year	$57 \times 6 \times 10^6$	330 Gigabytes

Table 9.5: Summary of estimated Monte Carlo cpu and storage requirements.

A modest processor farm of nine machines dedicated to MINOS Monte Carlo event simulation will provide these events. Generating events under different conditions or regeneration to correct early deficiencies could again double these estimates.

9.4.4 Summary of cpu and storage requirements

We have shown that the data processing and storage requirements for the MINOS far detector and Monte Carlo data are quite modest, even if we fully analyze and store every trigger. The near detector data rates are much larger but even there the reconstruction and storage of the full event sample in the target region of the detector is well within the capacity of the present day facilities at Fermilab. We expect that, with the usual growth in capacity of the computer industry, by 2002 the load that MINOS places on computing facilities and the expense of providing them will be minimal.

9.5 Data processing model

Given the event rates and computing requirements described in Section 9.4, we construct the following model of the data processing and analysis for MINOS:

1. Far detector

   - The far detector data will be immediately reconstructed offline at the Soudan mine site. That is, events will be transferred, probably in run-size batches, from the DAQ system to a small processing farm where full reconstruction will be performed.

   - Candidate beam neutrino events (and other small selected data samples, e.g., candidate atmospheric neutrino events) will be filtered and written to permanent storage. They will be transferred to Fermilab to the central store, probably by Internet connection but possibly on a hard storage medium.

   - Calibration data from cosmic ray muons will be processed at Soudan and condensed to calibration data sets at the processing farm. The calibration sets will be sent to Fermilab for permanent storage and distribution to the collaboration.

There will probably be no requirement for raw cosmic ray data to leave the Soudan mine site.

The processing hardware requirements at the mine will be:

- A farm of approximately 10 cpu's, of a type to be determined by cost and performance in the year 2001.

- Disk storage sufficient for a few days data, around 50 Gigabytes.

- A permanent storage medium compatible with the Fermilab central data store in 2001.

2. Near detector

- The near detector data will be processed in a farm of around 20 processors at Fermilab. It is expected that these will be part of the Fermilab central processor farm. Instantaneous data rates during runs can be rather high, thus it may only be possible to process sample runs during data taking, with the remainder of the data written to permanent storage for processing during beam-off periods.

- Calibration data will again be condensed to calibration data sets and raw muon data will not need to be stored.

- Local disk storage will be required only for buffering, and data will be written directly to the Fermilab data store.

3. Monte Carlo

- Monte Carlo generation can be done on the Fermilab farm, or possibly at collaboration computer centers. The load is not expected to be large.

- Monte Carlo data will be stored centrally in the Fermilab data store.

4. Data distribution

- All physics neutrino events will be stored with raw data and processed quantities in the Fermilab data store. These will be accessible to all the collaboration via AFS or equivalent. If required, local copies of the raw data can be kept at collaboration computer centers. This is particularly likely to be the case for overseas collaborators where link speeds to the U.S. tend to be slow.

- Ntuples will be produced for physics analysis via PAW (or OO equivalent). These will be generated and stored centrally but are likely to be copied to local areas. Users may, of course, generate their own ntuples from the raw data.

- Calibration databases will be linked and up-to-date calibration data automatically distributed to local sites.

9.6   Summary

The MINOS computing requirements are not large. Stripped to the bare minimum, MINOS computing could be carried out on a handful of PCs. In practice, rather more than the minimum of calibration data and events in the near detector are likely to be processed and kept, at least at the start of data taking. Even with this extra data, the computing load from the near detector will be well within the capacity of the Fermilab processing farm and data store, so we propose to use these facilities for MINOS.

We plan to install some computing capacity at the far detector laboratory, if only to provide insurance against failure or lack of capacity in the links to Fermilab. However the total hardware requirement will be small, less than $100k for processors and storage.

The bones of an offline analysis system already exist, written under Fortran-77. Sufficient physicist effort exists within the collaboration to complete this system before data taking. The conversion of the system to an Object Oriented C++ form will require more effort in the short term, but may save effort in the long term, as support diminishes for the Fortran tools we use. A group of physicists and physicist-programmers are studying the OO possibilities for MINOS and, if the collaboration decides to take that route, this group will provide the majority of the effort. However, the addition of one or two programmers from the Fermilab computing department would greatly ease this process.

The collaboration will require a computer manager to take overall command of the computing system at Fermilab, and a second-in-command at the second site (presumably the Soudan mine). Also the collaboration needs a systems programmer, or systems oriented physicist-programmer, to take detailed control of the writing of the offline system. If these people cannot be found within the collaboration we will request them from the Fermilab computing department.

Chapter 9 References

[1] "Object Oriented Analysis and Design with Applications" 2nd edition, Grady Booch, Benjamin Collins 1993.

[2] The MINOS Collaboration, "MINOS Experiment R&D Plan: FY 1996-1998," June 1996, Fermilab report NuMI-L-184.

[3] WWW page http://www1.cern.ch/Adamo/ADAMO_ENTRY.html.

[4] D.C. Carey and V.A. White, "NUADA, the Fermilab Neutrino Flux Program", Note PM0011, Fermilab, June 1975.

[5] D. Rein and L. Seghal, Ann. Physics (N.Y.) **133**, 79 (1981).

[6] R.P. Feynman, M. Kislinger and F. Ravndal, Phys. Rev. **D3**, 2706 (1971).

[7] H. Gallagher and M. Goodman, "Neutrino Cross Sections," November 1995, Fermilab report NuMI-112.

[8] J.B Birks, "Theory and Practice of Scintillation Counting", Macmillan, New York (1964) p40.

[9] Muon Momentum Measurement in Magnetized Iron, A.Para, NuMI-L-222.

[10] Review of Track Fitting Methods in Counter Experiments, CERN Yellow Report 81-06.

[11] The MINOS Collaboration, "Status Report on τ Identification in MINOS," January 1997, Fermilab report NuMI-L-228.

[12] The MINOS Collaboration, "MINOS Progress report to the Fermilab PAC," October 1997, Fermilab report NuMI-L-300.

[13] D.A. Petyt, "$\tau \rightarrow \pi + X$ analysis in MINOS," October 1997, Fermilab report NuMI-L-258.

[14] "Version management with CVS, Release 0.9 for CVS 1.3+", Per Cederqvist, Signum Support AB, Linkoping, Sweden (1993).

Chapter 10

Use of Soudan 2 in MINOS

10.1 Overview

It is the intention of the MINOS collaboration to use the fine-grained 1 kiloton Soudan 2 detector in conjunction with the new 5.4 kiloton MINOS far detector[1] to measure the properties of the neutrinos arriving at Soudan. The potential use of the Soudan 2 detector in a wide band beam from Fermilab has been described in considerable detail in previous documents which were submitted to Fermilab for proposal P-822[2]. At the present time, no upgrades or modifications of the existing detector are planned. The lower mass but finer granularity of the Soudan 2 honeycomb drift chamber complements the high mass magnetic 5.4 kt detector. In this Chapter there is a brief description of the Soudan 2 detector and an overview of the physics motivation for its continued operation.

10.2 The Soudan 2 detector

The design, construction, operation and performance of the Soudan 2 tracking calorimeter has been described in detail elsewhere[3, 4]. The central portion of the Soudan 2 detector is comprised of 224 rectangular modules each of dimension $2.7 \times 1 \times 1$ m^3. The detector is arranged in a $5 \times 8 \times 14$ m^3 array of modules. At roughly 4.5 tons per module, the total detector weight is 963 tons. Figure 10.1 shows a sketch of a Soudan 2 module.

Each Soudan 2 module contains a 241 layer stack of 1.6 millimeter thick corrugated steel plates. Between each layer of steel are sheets of Mylar ("bandolier") in which 14 mm diameter resistive plastic (Hytrel) tubes are inserted. The tubes are layed laterally, alternating between 31 or 32 per layer, and act as manifolds for a distribution of an argon and CO_2 gas mixture within the module. A plane of anode wires and cathode pads are mounted at each face of the array of Hytrel tubes. A section of a readout plane is shown in Figure 10.2.

As a charged particle penetrates a module, ionization occurs. The unbound electrons drift under the influence of high voltage copper electrode strips glued onto the bandolier. These electrodes vary in voltage (0 to 9000 volts) and are configured to force the electrons to drift up to 50 cm with a constant velocity (0.6 cm/μs) towards the readout plane of the module where the array of anode wires is held at a large positive potential (2300 volts). Figure 10.3 shows the drift tube and anode wire geometry and electric field configuration.
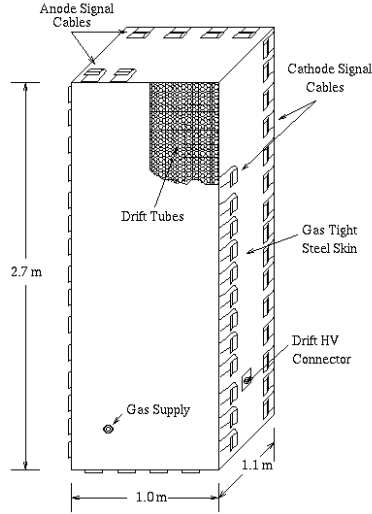
Figure 10.1: A single 4.5 ton Soudan 2 module.
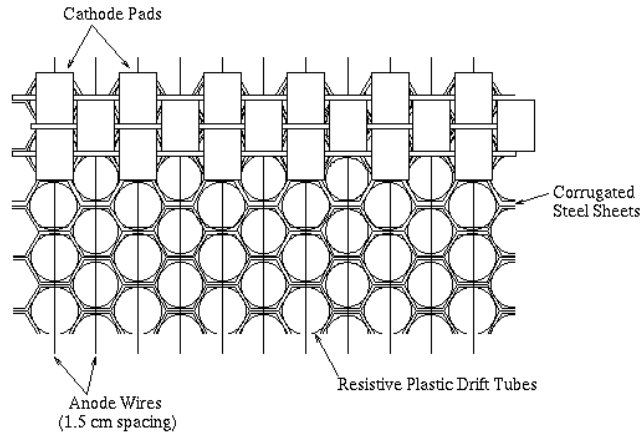
Figure 10.2: The readout-plane region of the detector, including the anode wires and three layers of the cathode pads.
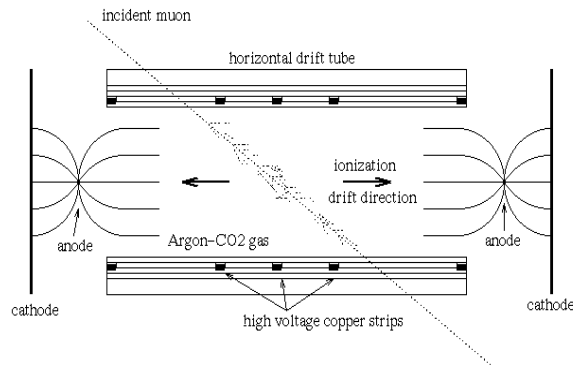
Figure 10.3: Cross section of a drift tube (not to scale).
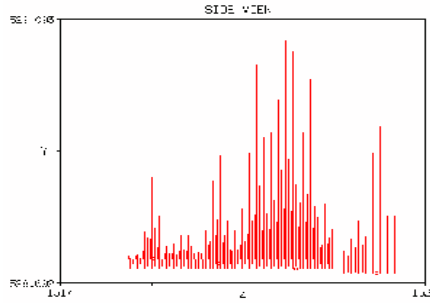
Figure 10.4: A Soudan 2 pulse on a cathode pad, showing several resolvable hits.

There are 63 anode wires and 240 cathode strips spanning both sides of each module. As the electron shower is collected onto the anode wire a mirror charge is induced on the adjacent horizontal cathode strip forming an electrical pulse. Each of these anode and cathode channels is connected to a signal preamplifier which is mounted directly on the module. The amplified signal feeds into a multiplexing ("summer") crate. There, the signals of up to eight channels are physically wired in parallel ("OR-ed"). The multiplexing scheme is done in such a way that hits can almost always be assigned to unique anode-cathode locations in the offline data analysis. The analog signal then is routed to the rack of Analog-to-Digital Converters (ADCs) which are monitored by a trigger logic circuit.

The orthogonal orientation of the anodes and cathodes forms two of the three orthogonal spatial dimensions that are recorded. The third dimension is calculated from the drift time and a determination of the initial time of the event, T0.

The currents on the anode wires and the cathode strips are sampled at 200 nsec intervals by flash ADCs. A raw pulse is defined as a contiguous sequence of measured voltages or micropulses which make up the pulse. Several cathode hits from such a pulse are shown in Figure 10.4. "Edges" occur when a particular ADC pulse is driven beyond a threshold voltage at a unique time. An event is triggered when a required cluster of eight anode edges or seven cathode edges is obtained.

The detector is surrounded ($\sim$ 99% coverage) by a 1700 m^2 active shield mounted on the cavern walls. The shield elements are double layer aluminum proportional tubes. A double layer hit is recorded for 95% of the charged particles which cross a shield element. The calorimeter and active shield are shown in Figure 10.5.

10.3   Soudan 2 as a complement to the 5.4 kt detector

Although it would be too expensive to build an additional 5.4 kilotons of the Soudan 2 detector, there are many reasons to want to keep the existing detector running through the MINOS long-baseline experiment. These reasons are:

1. Cost effective additional mass
   Soudan 2 will contribute 15% of the total mass of the MINOS far detectors for much less than 15% of the cost. The only costs involved are some additional (small) operating expenses.
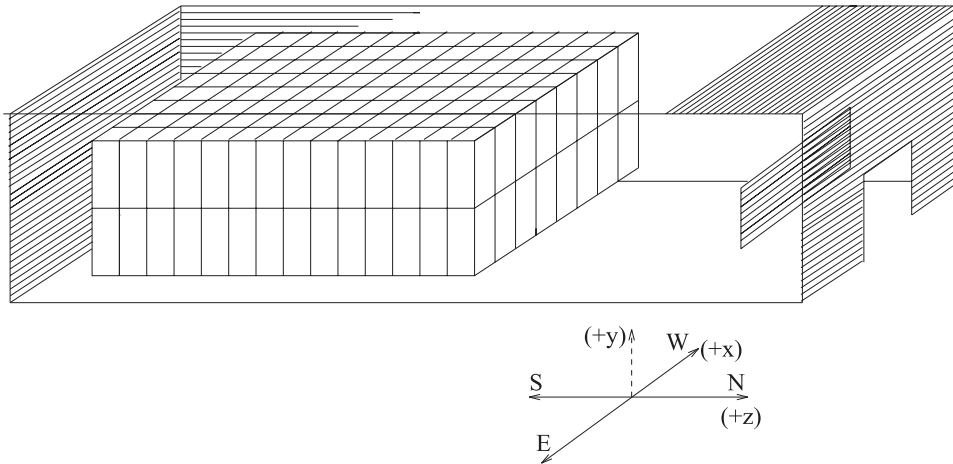
Figure 10.5: The relative orientation of the calorimeter (inner) and active shield (outer) for Soudan 2.

2. Readiness
   The detector is ready now so it will be ready at the time when the beam turns on in 2002. There are no known detector aging issues which would prevent this.

3. Granularity
   The steel thickness of 1.6 mm compares to the steel thickness of 25.4 mm in the 5.4 kt far detector. Due to the honeycomb nature of the detector, the amount of material between gas crossings is 8 times less than the 5.4 kt detector in the 0° direction, and 16 times less in the 60° direction. This finer granularity allows greater sampling of the ionization for a track or shower, which in turn can be a great aid in pattern recognition.

4. Area
   The rates of ν interactions are proportional to mass, but the rate of measuring ν induced muons in the rock upstream of the detector is proportional to area. This muon rate, which is independent of rock density to first order, will provide a high statistics independent measurement of the rate of charged current events. Although Soudan 2 has 18% of the mass of the new detector, it is comparable in instrumented area, so it would provide a significant and independent measurement of the rock muons.

5. Low energy trigger threshold
   The trigger threshold for the 5.4 kt detector will be a few GeV, and will not be known precisely until some of the detector is in place. It will fail to trigger on 10 to 30% of the neutral current events. Soudan 2 provides a detector with a very low energy trigger threshold. It is 50% efficient at 300 MeV kinetic energy and $> 98\%$ efficient above a few GeV. This will provide a check of the trigger threshold in the new detector, as well as a measurement of the lowest energy neutral current and ν_e events.

6. Systematic errors
   With Soudan 2, it will be possible to measure many of the properties of neutral and

charged current events in a completely independent detector. This will give an important systematic check on a number of the measurements in the new detector. Soudan 2 will be able to separate neutral current and charged current events based on both event length and tracking. For the lowest energy muons (< 2 GeV) it will measure the range distribution. And for both the NC and CC events, it will measure the hadron energy distribution with better resolution.

10.4   Unique capabilities of Soudan 2

The excellent granularity of the Soudan 2 detector allows for certain measurements that are not possible in the 5.4 kt detector. The issues of recoil proton identification, low energy electrons, μ^+/μ^- separation and modularity are addressed in this Section.

In its exposure to atmospheric neutrinos, the Soudan 2 detector has shown that it is able to measure recoil protons[5]. About half of neutrino induced recoil protons are clearly visible in the Soudan 2 detector. These protons can be cleanly identified and separated from pions based on their ionization and straightness[6]. A full Monte Carlo described in the MINOS proposal reported that it would be possible to separate quasi-elastic $\nu_\tau p \rightarrow \tau n, \tau \rightarrow \mu\nu\nu$ events from ν_μ quasi-elastic events using the angle between the outgoing muon and proton in the plane transverse to the beam. Intranuclear scattering of the proton was not included in that simulation and somewhat weakens the ability to separate signal from background. However, for large mixing angles, this still provides a powerful and expected signal for τ identification. In general, measurement of the recoil proton aids in the angle and transverse momentum measurements for all of the events in which the proton is seen.

Low energy electron identification is another comparative advantage of the Soudan 2 calorimeter. The fine granularity of Soudan 2 couples with the fact that the radiation length of an electron from the vertex is very different from the interaction length of a pion. A ν_τ quasi-elastic event, followed by $\tau \rightarrow e\nu\nu$ decay, would produce a unique topology, in which an electromagnetic shower and a proton are identified, and transverse momentum is not balanced. The rates of high energy electron events in Soudan 2 would also be a valuable consistency check for the electron identification in the 5.4 kt detector.

Another advantage of the fine granularity is the ability to see μ^+ decay hits. In iron, μ^-'s are absorbed, while most μ^+'s decay at rest to make a positron. This allows for some μ^+/μ^- separation and will be a complementary measurement to the method of separation using the magnetic field in the new detector.

The modularity of the Soudan 2 detector allowed for a calibration using the ISIS test beam at the Rutherford Laboratory[7]. It also provides a great deal of flexibility for repairing module faults and for further calibration of any module in which an unusual event takes place. The modularity of Soudan 2 makes it possible and straightforward to assemble a near detector version of the Soudan 2 calorimeter should a clear motivation arise.

Chapter 10 References

[1] The MINOS Collaboration,"P-875: A Long-baseline Neutrino Oscillation Experiment at Fermilab," February 1995, Fermilab report NuMI-L-63.

[2] The P-822 Proposal is described in the following documents submitted by the P-822 Collaboration:
"Proposal for a long baseline neutrino oscillation experiment using the Soudan 2 neutrino detector," March 1991;
"Progress report and revised P-822 proposal for a long baseline neutrino oscillation experiment from Fermilab to Soudan," October 1993;
"Update to P-822: proposal for a long-baseline neutrino oscillation experiment from Fermilab to Soudan," March 1994;
"P-822 response to the PAC's questions of 11th April 1994," May 1994. There is also a further discussion of the measurement of quasi-elastic events on pages 168-172 of the MINOS proposal[1].

[3] W.W.M. Allison *et al.*, Nucl. Instr. Meth. **A376**, 36 (1996).

[4] W.W.M. Allison *et al.*, Nucl. Instr. Meth. **A381**, 385 (1996).

[5] W.W.M Allison *et al.*, Physics Letters, **B427**, 217 (1998).

[6] "Protonicity" by Peter Litchfield, March 1998, Internal note PDK-696.

[7] Proceedings of the First International Conference on Calorimetry in High Energy Physics, Ed. D.F. Anderson *et al.*, 1990, World Scientific (426). Also C. Garcia-Garcia, "El Experimento de Soudan 2 para el Estudio de la Establilidad de la Materia: Interacciones de Neutrinos," Ph.D. thesis, Universidad de Valencia, 1990.

Chapter 11

The hybrid emulsion detector

11.1 Overview

11.1.1 Sensitivity of a low background appearance experiment

The sensitivity of a neutrino oscillation search using the techniques discussed in Chapters 2 and 3 is limited by statistical fluctuations of the background ν_μ interactions. Hence it improves with the $\sqrt{mass}$ (or $\sqrt{running\ time}$) of the detector. A background-free appearance experiment which detects the oscillated neutrinos directly has a sensitivity proportional to the detector mass (or running time). For oscillation probabilities on the order of 0.01 its sensitivity approaches that of a thirty times more massive experiment using the NC/CC test.

In addition, a ν_τ appearance experiment with explicit detection of τ leptons is insensitive to the details of the parent neutrino beam (provided that the beam has no ν_τ component). Hence it is probably the only way to detect $\nu_\mu \to \nu_\tau$ oscillations if the mixing angle is smaller than $\sim 10^{-2}$.

In this Chapter we describe a hybrid emulsion detector which would complement the physics capabilities of the 5.4 kt MINOS calorimeter. Considerable R&D remains to be done to work out technical details, but we are confident that the experiment is feasible and could be an early addition to the baseline MINOS detector.

11.1.2 Progress in emulsion and automatic analysis techniques

Nuclear emulsions have a long history of use in high energy physics. Their unsurpassed spatial granularity and resolution make them particularly suitable for the detection of very short lived particles. In recent years nuclear emulsions have been used in a number of neutrino experiments as a tool for detecting τ leptons, including CHORUS[1] at CERN and E-872[2] at Fermilab. In addition, nuclear emulsions remain an important technique for studies of the highest energy cosmic ray interactions, for example in the JACEE Collaboration[3].

The nuclear emulsions used today are very similar to those used fifty years ago[4]. The analysis techniques, however, have changed dramatically: electronic detectors are used to localize events and advances in microcomputers have been exploited to increase scanning speed. The Nagoya University group has constructed several stations consisting of computer controlled microscopes read out with CCD cameras and equipped with automatic hardware

track recognition and reconstruction processors[5]. These stations are being used to analyze hundreds of thousands of events from the CHORUS experiment.

These capabilities for large scale automatic analysis of emulsion data are changing the way that emulsion sheets are used in experiments. The ECC approach[6], in which thin emulsion sheets interspersed with passive material serve as a target, is becoming widely used in cosmic ray studies. The nuclear emulsion sheets are used as very fine granularity, high spatial resolution tracking detectors with the particles of interest traversing the sheets perpendicular to the surface. Such a configuration has been employed recently in an experiment designed to directly observe ν_τ's, E-872 at Fermilab[2].

11.1.3 The principle of the emulsion experiment

If $\nu_\mu \rightarrow \nu_\tau$ oscillations take place, τ leptons will be produced via the charged current interaction. These leptons will decay with a typical path length of a few hundred microns. In three pronged decays (14.4%) there will be three charged particles leaving the decay point. One pronged decays (85.5%) are characterized by a substantial "kink" on the original trajectory, with a typical kink angle of the order of a hundred milliradians.

The experiment will consist of three components:

- Target planes. These will be thin plates of a dense material where the neutrino interactions take place. The number of registered interactions is proportional to the total mass of the target planes, whereas the number of τ leptons leaving the target, and hence detectable, is inversely proportional to the thickness of a target plane. Thus a high density target material is optimal. Lead is a natural candidate.

- Tracking planes (τ detecting planes). The tracking planes follow the target planes. They must provide enough tracking information to identify three body decays and/or to identify the decay kink. The short lifetime of the τ lepton requires these measurements to be made in the space of $\sim$1 mm. There are several possible geometries of the emulsion sheets which can accomplish this task. The most conservative uses two 2-sided emulsion sheets at the entry and exit of the tracking volume (see Figure 11.1). The first emulsion sheet will measure the direction of the incoming τ, the second will measure the direction of the outgoing daughter from the τ decay. The emulsion sheets are composed of a 100 μm thick plastic base and 100 μm thick emulsion layers on both sides of the base. A 400 μm thick plastic layer separates the emulsion sheets and provides the decay volume.

- Triggering/event localization planes. These planes, spaced with a frequency of about a quarter of an interaction length throughout the entire detector, will be electronic detectors, used to identify where neutrino interactions took place and reduce emulsion scanning effort.

11.1.4 A modular, extensible design

We plan to construct the detector from a large number of small "modules," each of which is an independent subassembly of target and emulsion planes. A module is built as a mechanically
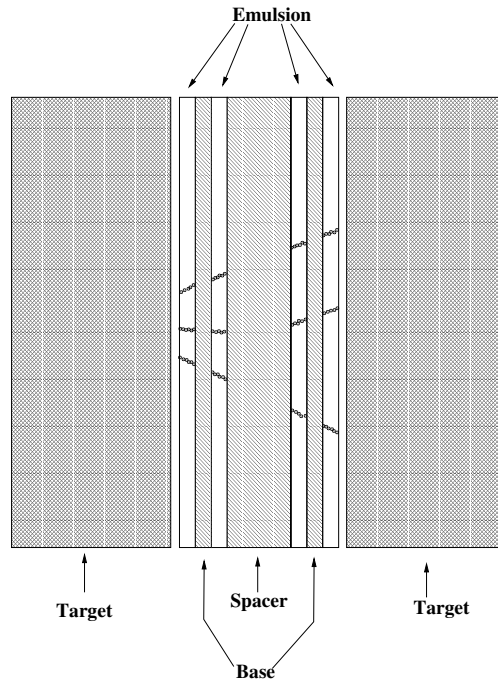
Figure 11.1: Target and tracking plane geometry of the hybrid emulsion detector. Two double-sided emulsion sheets measure the angles of particles at the entrance and exit planes of the tracking volume.

separate box which contains ~50 planes of emulsion and target material. Each module is approximately 10 cm thick and 15 × 15 cm² in transverse dimensions. Large planes of modules (~1000 for a 5 × 5 m² detector) are interspersed with triggering planes. Module planes are constructed so that individual modules can be extracted and replaced by fresh ones as interesting events are identified by the triggering planes. This might be done on a weekly basis, thus permitting near-on-line analysis of the emulsion data. The triggering planes also localize charged particles with an accuracy of the order of 1 mm, which greatly reduces the scanning effort.

The modular design allows an adiabatic extension of the size and potential of the experiment. New modules can be added to the detector, thus extending the sensitivity to neutrino oscillations, without disruption of the data taking. It offers significant flexibility and enables a physics- or fiscally-driven optimization of the experimental strategy.

If $\nu_\mu \rightarrow \nu_\tau$ oscillations occur with a large mixing angle, and Δm^2 is in the upper part of the range suggested by Super-Kamiokande's atmospheric neutrino results, then a modest size detector of ~100 tons is sufficient to observe an unambiguous signal.

If the oscillations are suppressed due to the low value of $\sin^2(2\theta)$ (< 0.01) or Δm^2 (< 0.001 eV²), then future extension of the emulsion detector to a total mass of 1000 tons, exposed for several years, is probably the only practical technique to detect these oscillations.

11.2 Physics potential

11.2.1 Event rates

We assume the high-energy neutrino beam configuration with a ν_μ CC interaction rate of 3000 ev/kt/year and an average neutrino energy $\langle E_{\nu_\mu} \rangle = 17.6$ GeV. The rate of ν_τ interactions is reduced by kinematic effects depending on Δm^2. We assume here $\sigma^{CC}_{\nu_\tau} / \sigma^{CC}_{\nu_\mu} \approx 1/3$.

11.2.2 Tau neutrino detection efficiency

The detection of a τ lepton requires the identification of a decay kink in the space between target plates, or of a track which does not come from a common neutrino production vertex. If the event has more than one track at the production vertex, an extra track with a finite impact parameter relative to the reconstructed vertex is required. Otherwise two non-intersecting tracks signal a τ decay. The combined detection efficiency ε, estimated with a detailed GEANT simulation, is of the order of 50%.

11.2.3 Background rejection

The chief background for τ detection will probably come from D meson production and subsequent decay in ν_μ CC interactions. In addition to the suppression of the charm cross section, due to the low energy of the beam, the main rejection factor will come from detection of the accompanying muon in the large MINOS spectrometer following the emulsion detector. It is important to notice that this background rejection technique does not imply that the $\tau \to \mu$ decay mode cannot be used to detect τ's. In the case of τ decay the decay kink occurs on the muon track, in contrast to the charm decay topology.

Associated production of charm particles, both in CC and NC interactions is further suppressed by kinematical factors to a level well below the single charm production.

The decay or interaction of π and K mesons produced in NC ν_μ interactions are yet another potential source of background but they are expected to be negligible in the very short distances in which τ's decay.

The detailed evaluation of background requires the detector geometry and composition to be defined in a full GEANT simulation and the analysis procedures to be established, hence it is not yet possible. Based on the initial estimates and on the experience of other emulsion experiments, we do not expect the total background rate to exceed a small fraction of one event per kt-year.

An important feature of this experiment is the ability to measure actual background levels in a small emulsion detector installed in the MINOS near hall, where we expect the flux of ν_τ's to be very low. Because of the high ν_μ rate in the near hall, this detector can be small, and will allow any unexpected background to be identified very early in the experiment.

11.2.4 Electron identification capability

The strength of nuclear emulsion is its high granularity and spatial resolution, making it the only detecting technique capable of unambiguous event by event τ identification. It

should also be noted that nuclear emulsions provide a very good tool for the identification of primary electrons.

Electron candidates can be recognized by the presence of converted photons from the electromagnetic cascade along the initial charged particle trajectory. Emulsions provide a very good rejection power against photons from π^0 decays. Most photons will convert at an observable distance from the primary vertex. The majority of photons which convert in the immediate vicinity of the interaction vertex, and electrons from Dalitz decays of π^0's, can be rejected by the presence of two charged tracks, taking advantage of the spatial granularity of nuclear emulsions.

With these very good background rejection capabilities, the potential for discovery of $\nu_\mu \rightarrow \nu_e$ oscillations will be limited only by the statistical fluctuations of the intrinsic ν_e component of the beam and the systematic error on the extrapolation of this component from the near to far detector locations.

11.2.5   Oscillation discovery potential

We assume a 1 kt-year exposure for illustration.

The number of observed ν_τ interactions will be

$$N_\tau = P \times N_{\nu_\mu} \times \frac{\sigma_{\nu_\tau}}{\sigma_{\nu_\mu}} \times \varepsilon,$$

where P is the average oscillation probability. For large Δm^2, $P = \frac{1}{2}\sin^2(2\theta)$.

If no ν_τ events are observed, the experiment will set a 90% CL limit at

$$\sin^2(2\theta) < \frac{2 \times 2.3}{4000 \times 0.33 \times 0.5} = 7 \times 10^{-3}.$$

The limit improves with the running time like t, assuming no background.

The lowest Δm^2 detectable in the experiment is related to P via

$$\Delta m^2 = \frac{\sqrt{P} \times \langle E_\nu \rangle}{1.27 \times L},$$

and for the above conditions is $\Delta m^2 \geq 1.6 \times 10^{-3} eV^2$. This limit improves with running time like $\sqrt{t}$.

11.3   Module construction

11.3.1   Target planes

The target planes serve as a source of τ's. They should be as massive as possible to maximize the interaction rate, and as thin as possible to maximize the number of τ's escaping. Practical considerations favor lead as a target material.

The determination of the optimum thickness of the target plates requires an optimization of the overall number of detected τ's vs size and cost of the detector. Our present design is based on 1 mm thick lead sheets cut to 15 cm $\times$ 15 cm size.

Prolonged contact with most metals, including lead, leads to severe fogging or even decomposition of nuclear emulsions. The emulsions will be insulated by a protective layer of acrylic paint on the lead surface, following the technique developed by JACEE[7].

11.3.2 Emulsion tracker

Typical nuclear emulsion yields some 40 developed grains per 100 μm of a minimum ionizing track, thus offering a considerable potential for particle identification via dE/dx. In this experiment we will use emulsions only for position and direction measurements, therefore our requirements on the grain density will be dictated by pattern recognition considerations. It is expected that emulsions produced and exposed in the mine will provide a very clean environment[8], therefore of the order of 20 grains per 100 μm should be sufficient for high efficiency track detection.

Studies of diluted emulsions[9] show that the desired grain density can be achieved with a significantly lower concentration of silver halide in the gel, thus offering the potential for a substantial reduction in the cost of the nuclear emulsions. We envisage using the emulsions diluted by a factor of four with respect to the standard composition. Such a dilution has an additional advantage: the shrinkage of the emulsion during the fixing process is reduced from a factor 2.4 to 1.34. This, in turn, leads to a substantial reduction of distortions in the emulsion, making the angular measurement less prone to systematic errors.

The 100 μm layers of emulsion will be poured (in turn) on both sides of a 100 μm thick polystyrene base. After the drying process the emulsions sheets will be imprinted with fiducial marks and cut to 15 cm $\times$ 15 cm.

11.3.3 Packaging

Modules will be packed into thin stainless steel cans 15 cm $\times$ 15 cm $\times$10 cm, resembling those used in the canned food industry.

Packaging of the target plates and emulsion sheets into modules will be carried out in a darkroom. Lead plates, emulsion sheets and the spacer plastic sheets will be loaded into the steel can. The can will subsequently be evacuated and hermetically sealed. It is expected that the pressure loading of the plates will ensure that the relative positions of the emulsion sheets will not change with time.

11.4   Trigger and event localization detectors

The trigger plane detectors will be used to record neutrino interactions and identify the tracking modules traversed. These modules will be subsequently removed from the detector for the analysis of the nuclear emulsions. Position and directional information from the trigger planes will be used to direct the track search in the emulsion sheets and to reduce the analysis load. For this purpose a position measurement accuracy of a few mm is adequate.

11.4.1 Iarocci tubes

Iarocci tubes have been extensively used in high energy physics experiments[10]. They are an attractive solution when a robust and inexpensive tracking detector is needed, and can be used either in drift mode or with cathode strip readout. Recently Iarocci tubes have been proposed as the forward muon tracking detectors for the D0 upgrade project[11]. We have considered Iarocci tubes as a possible active detector for MINOS and have acquired a substantial amount of experience with these detectors.

Several experiments have demonstrated that Iarocci tubes can be reliably operated in large scale systems, with detection efficiency in the active areas close to 100%. Geometrical effects, mostly due to the walls of the chambers, reduce the efficiency to a typical level of 95%, dependent somewhat on the angular spectrum of incoming particles.

11.4.2 System layout

The Iarocci tubes will be organized into tracking planes, 5 m × 5 m in size. Each plane will be built out of 8-cell modules, 8.34 cm wide and 5 m long. Two-dimensional position information will be derived from the wires and from signals induced on the cathode strips running across the modules. Both sides of the tracking plane will be covered with thin aluminum sheets, serving as a Faraday cage. A complete plane will have 480 wires and 500 strips. It will have an overall thickness of 1.5 cm.

D0 is planning to use Iarocci tubes in drift mode with a fast gas mixture (90% CF_4 + 10% CH_4) to keep the maximum electron drift time below 60 ns and give a position resolution of ~1 mm. For our application the requirements on speed, rates and radiation damage are relaxed significantly; our most important requirements are those of safety and reliability. We expect to replace the D0 gas mixture with some more standard and less expensive mixture. We plan to use the tubes in counter mode and expect a resolution of about 3 mm from anode wire information. Position determination using cathode strips will be significantly better, depending on strip width. In the test beam studies of MINOS prototypes a resolution about 1 mm was obtained with 1 cm strips. Typically Iarocci tubes with 1 cm cathode strips have resolutions of ~0.5 mm[12].

11.4.3 Design of an 8 cell module

These modules will be built in a manner similar to the D0 muon chambers, with the equal length of modules offering a significant simplification.

An individual module will have 8 cells with 9.4 mm × 9.4 mm internal cross section and with a 50 μm W-Au anode wire in the center, as shown in Figure 11.2. The tubes will be made from commercially produced aluminum extrusions with a wall thickness of 0.6 mm. They will be inserted into 5 m long PVC plastic sleeves.

The tubes will be closed by endcaps which will provide accurate positioning of the anode wires together with electrical and gas connections. The mechanical tolerance of the wire position within the tubes, ensured by automated assembly procedures, is 160 μm, well below the intrinsic coordinate resolution of the detector. The bottom endcaps will have gas connectors, HV connectors and individual signal connectors for 8 wires. The top endcap will
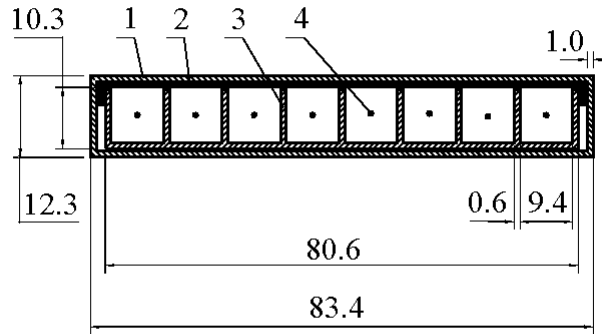
1 − envelope
2 − cover
3 − profile
4 − wires

Figure 11.2: End view of an 8-cell module of Iarocci tubes. The dimensions shown are in mm. The "cover" is not needed for our application.

have gas connectors only. The modules will be glued on the surface of the external cathode strip boards. The U.S. CMS muon system project has constructed a facility for strip board production at Fermilab. It produces boards with a dimensional tolerance on strip locations of about 50 μm, which is more than adequate for our purposes.

As a part of D0 muon upgrade project, the front-end electronics (8-channel amplifiers and discriminator chips) have been developed by the Dubna group and the Integral company in Minsk, Belorussia. These amplifiers are adequate for our purposes.

11.5 Detector construction

11.5.1 Honeycomb construction

We plan to construct 5 m × 5 m × 10 cm target and emulsion planes in a honeycomb box geometry, as shown in Figure 11.3. Each box will be constructed from 1 mm thick front and back steel plates interconnected every 15.5 cm with horizontal steel strips, forming a set of 10 cm wide, 15.5 cm tall and 5 m long channels. A series of 2.5 m long trays loaded with the emulsion modules will be inserted into these channels from both sides of the detector.

At regular time intervals during the experiment, some of the trays will be slid out of the detector, the modules indicated by the tracking planes will be removed and replaced by new modules, and the whole assembly will be placed back into the detector.

An individual module will weigh some 13 kg, thus allowing easy manipulation. The entire tray of modules will weigh 250 kg. The removal and replacement of the modules will therefore require the construction of a movable support structure with appropriate lifting capabilities.

A single plane with modules will have a mass of about 15 tons. It is expected that its
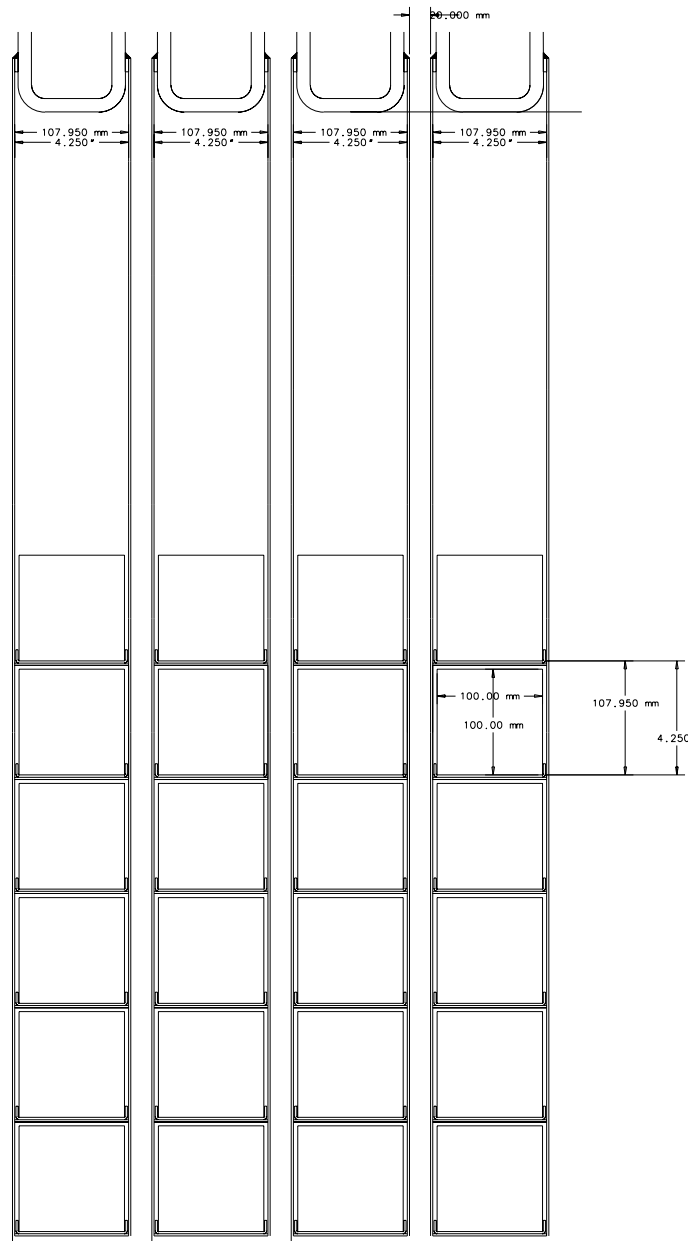
MINOS EMULSION RACK
DETAIL

Figure 11.3: Side view of the honeycomb box structure containing the target and emulsion modules. The modules are shown as 100-mm wide × 100-mm tall boxes. (Note that 100-mm wide × 155-mm tall modules are described in the text.) The four planes shown are suspended from the structural beams at the top. The triggering planes, which would be located between the planes of emulsion modules, are not shown.

load will be transferred by the front and back steel plates to a structural member on top of the plane, which in turn will be hanging off the support rails on both sides of the detector, as shown in Figure 11.4.
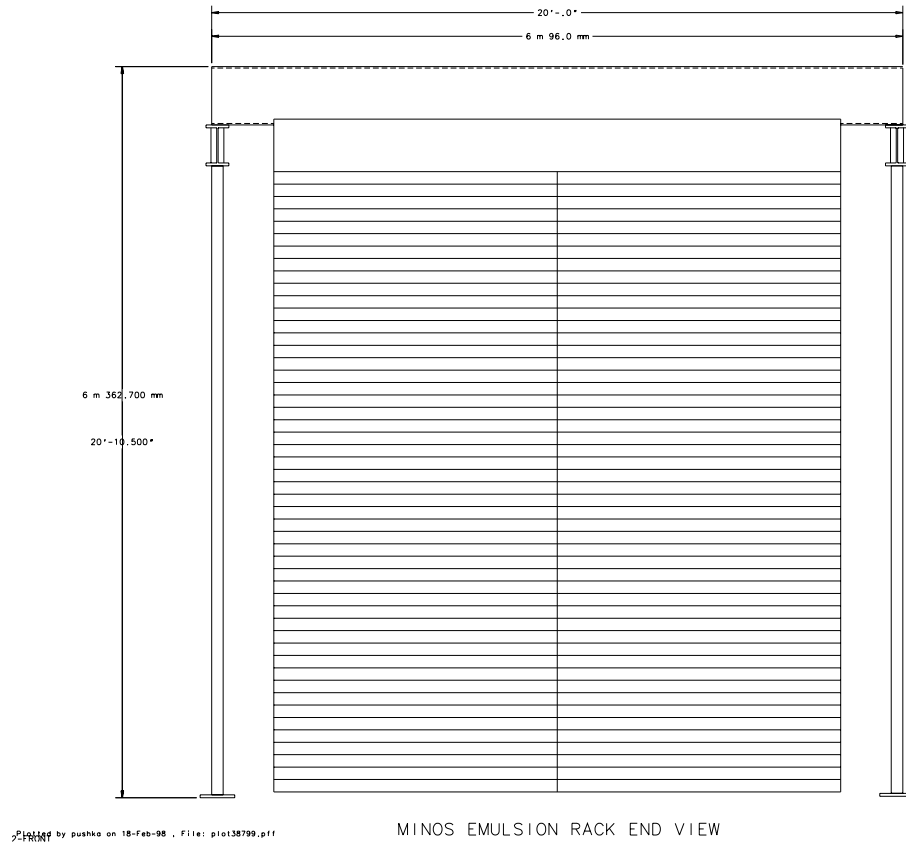
Figure 11.4: End view of an emulsion detector plane, as seen by the neutrino beam. The 5 m × 5 m detector planes are suspended from the structural beams at the top, which are supported by rails on the two sides of the detector.

11.5.2   Detector support structure

The detector will consist of an alternating series of target/emulsion planes and triggering/event localization planes. Both kinds of planes will hang from the structural member on top of each plane. These structural members will be supported by two rails on both sides of the detector (hanging file design) as shown in Figure 11.4 .

The target/emulsion planes will be separated by 2 cm from the triggering planes. This leads to an average density of the detector of 125 tons/meter.

11.5.3 Space requirements

Muon identification requires that the detector be placed in front of the 5.4 kt MINOS detector. The MINOS baseline design includes a 10-m long section of the underground cavern, upstream of the 5.4 kt detector, for future upgrades such as the emulsion experiment. As discussed above we expect the emulsion detector to start with a limited mass, of the order of 100 tons, and grow with time subject to physics and fiscal considerations. We envisage that the total mass of this detector can reach up to 1 kt. The emulsion detector would be constructed in the upstream direction, starting from the modules immediately in front of the MINOS toroids.

11.5.4 Module assembly factory

We consider it desirable that the entire construction of the emulsion detector, including manufacturing of the emulsion sheets, should be conducted in the Soudan mine to reduce cosmic ray background in the emulsions.

Module production in the mine will necessitate construction of several underground facilities for pouring and drying the emulsions and for construction of the target/emulsion modules. These facilities must be equipped with darkroom lighting conditions and with adequate environmental control, humidity being the most critical factor.

We expect that these facilities will be constructed in the area in front of the MINOS toroids or in the Soudan 2 cavern. Neither the space requirements nor safety considerations are expected to make construction of these facilities difficult.

11.5.5 Near detector

The sensitivity of the hybrid emulsion experiment relies on its ability to detect τ's with no background. The lack of background will be demonstrated by measurement in an environment where it is known that the flux of ν_τ is very small, i.e., at the near detector. We propose to measure background levels with a small detector in the form of a $4 \times 4 \times 6$ array of modules (60 cm $\times$ 60 cm $\times$ 60 cm deep). This would cover the central portion of the beam which, in the absence of oscillations, has a neutrino energy spectrum very similar to that at Soudan.

11.6 Research and development program

There is little doubt that the hybrid emulsion experiment described above can be constructed, and that it would be capable of highly efficient detection of τ's while maintaining background-free conditions at our desired sensitivities. Its construction is well within our present technical capabilities. The data analysis load, other than emulsion processing, is expected to be minimal.

The main obstacle is financial. The cost of construction of a 1 kt detector with present technology would be of the order of $100M, well outside practical bounds, although a 100 ton detector could be feasible. We plan to conduct a vigorous program of R&D to optimize the detector design and its construction techniques to reduce the cost by an order of magnitude.

This program is focused on the likely cost drivers: the nuclear emulsion and the module construction.

11.6.1 Nuclear emulsion optimization

Nuclear emulsions are a very mature technology. Modern emulsions offer high sensitivity, yielding some 40 grains of developed silver per 100 μm of minimum ionizing track, while maintaining very low random grain backgrounds at the level of 3 grains per 10 μm $\times$ 10 μm $\times$ 10 μm volume[13].

In the proposed experiment a thin sheet of nuclear emulsions will be used as a high resolution tracking detector. The grain density requirements will be dictated by the detection efficiency and pattern recognition considerations. The former will be satisfied by having 20 or more grains per 100μ, the latter depend very much on the environment in the emulsion.

The current generation of neutrino experiments is carried out in a high background environment, far exceeding cosmic ray backgrounds. This will not be the case in the Soudan mine. We expect the environment there to be very quiet for emulsions[8]. Although we need to evaluate the environment at Soudan, we expect that emulsion with a grain density of the order of 20 will be sufficient for our purpose. In this case, considerable savings can be achieved by diluting the standard emulsion with gelatin. Studies have shown that a four-fold dilution of emulsion leads to less than a factor of two reduction of the grain density on the charged particle trajectory, see Table 11.1[9]. This somewhat surprising result is probably due to the increase of the sulphur density around the silver halide grain in the diluted emulsion.

Designation	$\frac{\text{Halide vol.}}{\text{Total vol.}}$	Shrinkage factor	Density g/cm^3	n_{min} (100 μm)$^{-1}$
"Normal" (G.5)	0.49	2.30	3.9	36
2 $\times$ normal	0.35	1.67	3.2	33
4 $\times$ normal	0.23	1.34	2.5	21
8 $\times$ normal	0.13	1.17	2.0	10

Table 11.1: Properties of nuclear emulsion as a function of dilution with gelatin.

We plan to repeat these studies with the currently produced emulsions. In particular we plan to construct emulsion stacks using diluted emulsions and to evaluate the track finding efficiency as a function of the dilution factor.

11.6.2 Evaluation of the Soudan environment

Pattern recognition efficiency and potential error rates are strongly related to the background environment. In our case the background will be a combination of randomly developed grains, cosmic ray muons, muon-induced electrons and Compton electrons due to the ambient radioactivity. The cosmic ray-related component will be strongly dependent on the emulsion

production and processing conditions. One day on the surface is equivalent to several years underground.

We plan to conduct a systematic study of the backgrounds for emulsions produced on the surface and in the Soudan mine. The results of these studies will provide a quantitative input to the emulsion optimization discussed above and will determine whether the production of emulsions and of the target/emulsion modules should be conducted underground.

Taking advantage of the low background environment, the Soudan mine is currently used to store emulsions for the E-872 experiment and in the past has been used for emulsion storage for other experiments

11.6.3 Optimization of the emulsion sheets geometry

The function of the emulsion tracker is to determine the angles of the tracks entering and leaving the space between the target plates. We have adopted a conservative design using two pairs of double sided emulsions to measure the track angles at both sides of the gap. This technique is relatively insensitive to systematic problems related to distortions of the nuclear emulsions during the processing, as the grains in the vicinity of the base plate remain stationary and thus provide reliable direction information. At the same time they can be used to self-calibrate the distortions of the emulsion sheets, provided there are enough tracks in the region of interest.

Distortions in the emulsions are, in large part, due to the fact that almost half of the emulsion volume is removed during the fixing stage and the collapse of the resulting voids leads to displacement of gelatin molecules. This effect will be greatly reduced in the diluted emulsions, as the total reduction of the volume is much smaller. It is therefore possible that the angle measurement in a single 100 μm thick layer will be accurate enough for our purposes. Should this be the case, a simpler geometry with 800 μm plastic base and double-sided 100 μm emulsion would be much more economical and easier to manufacture and to analyze.

We plan to construct several stacks of emulsion sheets and evaluate their measurement capabilities in these two geometries. Stacks will be exposed to an 8 GeV Fermilab booster beam which will provide a flux of particles with well known directions.

11.6.4 Construction techniques

The geometrical layout of the proposed experiment is very similar to that used in present experiments, E-872 and JACEE, hence the intrinsic feasibility of the construction is not in question. The biggest challenge comes from the scale. We are planning to construct a detector up to three orders of magnitude bigger in total target mass than anything currently existing (the anticipated amount of emulsion required is only a factor of 30 greater, however). Although the present pouring and construction techniques are in principle applicable, we believe that a significant increase in the quality of the large scale detector and a reduction of manufacturing cost can be achieved by employing automated production techniques. This need for automation arises from an expected shift in the relative costs of different components. With the expected reduction of cost of the nuclear emulsion, due to dilution of the silver

halides, the construction cost will become a much bigger fraction of the overall costs than in the past.

We plan to experiment with more automated processes to produce emulsion sheets, perhaps with some of the processes used in the photographic film industry.

We also plan to experiment with various methods of automated packaging: stacking, vacuum wrapping, canning etc.

11.6.5 Measurement of backgrounds

We expect that the background to the τ sample will be small and will come predominantly from charm particles produced in the ν_μ interactions. Detailed simulations indicate that the background due to scattering and/or interaction of pions produced in NC ν interactions in the plastic layer separating the emulsions will not produce any significant background. We plan to measure this background component by exposing prototypes of our target/emulsion modules to a low energy hadron beam before neutrino running begins. The total number of pions produced by neutrino interactions in a one year exposure at Soudan is of the order of few thousand. Therefore it will be very simple to determine the background level to below 0.01 event in a short experiment. At the same time, such an exposure will be of great value as a test of the detector construction, performance and analysis techniques. Our calculations of background levels can be convincingly verified by the exposure of an emulsion near detector, as described above.

Chapter 11 References

[1] M. de Jong *et al.*, (CHORUS) "A new search for $\nu_\mu \rightarrow \nu_\tau$ oscillations," CERN-PPE/93-131.

[2] B. Lundberg *et al.*, 1994, Fermilab Proposal P-872.

[3] T.H. Burnett *et al.*, "JACEE Emulsion Chambers for Studying the Energy Spectra of High Energy Cosmic Ray Protons and Helium," Nucl. Instr. Meth. **A251**, 583, (1986).

[4] C.F Powell, P.H. Fowler and D.H. Perkins, "The study of elementary particles by the photographic method," Pergamon Press (1959), W.H. Barkas, "Nuclear research emulsions," Academic Press (1963).

[5] T. Nakano, Ph.D. Thesis, University of Nagoya (1998).

[6] O. Minakawa *et al.*, "Emulsion Chamber Project," Institute for Nuclear Study, Univ. Tokyo Report, INSJ-7, Tokyo (1958).

[7] R.J. Wilkes, private communication.

[8] J.J. Lord, private communication. He has poured, exposed and processed nuclear emulsions in Homestake mine.

[9] Dodd and Waller in J.W. Mitchell (Editor), "Fundamental mechanisms of photographic sensitivity," proceedings of a symposium held at the University of Bristol, March 1950, London, Bitterworth's Scientific Publications, 1951, p.266. Also quoted in M. Shapiro, "Nuclear Emulsions," and in S. Flugge (Editor), "Encyclopedia of Physics," Vol XLV, Springer-Verlag, Berlin (1958).

[10] W. Busza *et al.*, "Experience with Iarocci tubes produced on a large scale," Nucl. Instr. Meth. **A265**, 210 (1988); G. Alexeev *et al.*, "Studies of stability and systematics of operation of DELPHI plastic tubes," Nucl. Instr. Meth. **A292**, 551 (1990).

[11] G. Alexeev *et al.*, "Technical Design Report for the D0 forward muon tracking detectors based on mini-drift tubes," D0 Note 3366 (1997).

[12] N. Khovansky *et al.*, "Spatial resolution of profile-based detectors with external pick-up strips," Nucl. Instr. Meth. **A351**, 317 (1994).

[13] K. Niwa, Nagoya University, private communication. This figure applies to typical Fuji emulsions.

Chapter 12

Safety considerations

12.1   Fermilab ES&H requirements

The Fermilab ES&H Manual (FESHM) delineates laboratory policy regarding personnel and line management ES&H responsibilities, as well as providing technical standards for control of hazards which are peculiar to Fermilab. Pursuant to Chapter 2010 of the FESHM, the Fermilab Directorate has determined that the NuMI Project changes laboratory operation sufficiently to require the drafting of a Safety Assessment Document (SAD) and adherence to the requirements of that Chapter. An analysis of hazards associated with both near and far MINOS detectors is included in this document. A Preliminary Safety Assessment Document[1], describing safety considerations for the NuMI Project on the Fermilab site, and a Preliminary Hazard Assessment Report[2], describing safety considerations for the experiment at the Soudan site, have been prepared and are under review.

In addition, the MINOS Collaboration must comply with Particle Physics Division "Procedures for Experiments" [RD-2] for identifying and characterizing hazards in proposed experiments, and reviewing the engineered and administrative controls developed to mitigate these hazards. Experimenter and Spokesperson responsibilities during the life cycle of the experiment are also specified.

The hazard thresholds specified in RD-2 have been applied to detector systems to identify those systems which require independent review and approval prior to commissioning. Reviews are conducted by the MINOS ES&H Review Committee, which reports to the head of the Particle Physics Division. The Division head grants an Operational Readiness Clearance for initial operation of each system when all findings from the review committee have been resolved.

The cost and schedule implications of all ES&H systems and protocols required by the experiment are included in the MINOS Cost and Schedule Plan[3].

12.2   Minnesota ES&H requirements

For the past decade, adherence to industry consensus standards such as OSHA and NFPA has been adequate to maintain safe operation of the existing Soudan 2 detector in the Soudan mine. The University of Minnesota holds ES&H responsibility for the Soudan 2 cavern with

oversight from the State of Minnesota Department of Natural Resources.

These responsibilities are now expanded to include the MINOS cavern during and after detector construction. Operational Readiness Clearances for far detector systems are approved by a University of Minnesota representative as well as the Fermilab Particle Physics Division head. Since the detector is located on State property, structural components are stamped by a professional engineer licensed in the State of Minnesota.

12.3 Description of hazards

As for most other neutrino experiments, the MINOS detectors present a small set of well defined personnel hazards and negligible environmental hazard. From a hazard standpoint, the detector caverns are similar to a light industrial environment with the addition of several unusual hazards. Common workplace hazards such as working at elevated heights are addressed by adherence to OSHA, NEC and NFPA. The more unusual hazards and their associated controls are summarized in the following Sections.

12.3.1 Mechanical hazards

The most significant mechanical hazard is a potential buckling failure of a steel absorber plate during assembly. Without axial constraint, a single steel absorber plate could deform sufficiently to shear off the support ears. The assembly procedures described in Chapter 4 ensure that axial loads are properly transferred from the strongback to the previously installed detector planes. All mechanical hazard controls are reviewed by the MINOS ES&H Review Committee prior to commissioning.

12.3.2 Electrical hazards

There are numerous high and low voltage supplies which power the photomultiplier tubes and readout electronics. These are commercial supplies which are appropriately fused to the rating of the power distribution systems.

Electrical conductors for magnetizing the steel absorber are electrically insulated and water cooled. Thermal and voltage interlocks trip off the power supplies in the event of conductor failure or ground fault.

All electrical systems comply with the NEC and the FESHM and are reviewed by the MINOS ES&H Review Committee prior to commissioning.

12.3.3 Radiation hazards

Radioactive sources are used in two performance-testing devices which are needed at the two module assembly facilities and also at the near and far detector sites. One of these devices is the module mapper, an automated machine with scans the surface of each scintillator module with a 3 mC ^{137}Cs source to measure the energy response uniformity. The second device is wire-source driver used for calibrating module response by driving a 3 mC ^{137}Cs source, on the end of a wire, inside the source tubes attached to both ends of each module.

The use of these sources on the Fermilab site is controlled by adherence to the Fermilab Radiological Control Manual. Source hazard control at other sites is the responsibility of the institution which owns the site.

12.3.4 Fire hazards

The large inventory of polystyrene scintillator poses a fire hazard. This is largely mitigated by the highly segmented construction of the detector, since it is difficult to conceive of a credible accident scenario in which multiple detector modules are ignited. In particular, the aluminum sheets which enclose individual scintillator modules make ignition of the scintillator strips very unlikely.

The MINOS cavern is provided with smoke detection and sprinkler systems which are appropriately designed for the inventory of scintillator.

12.3.5 Laser hazards

Several pulsed UV lasers are used for calibration and monitoring. The optical paths are shielded to prevent accidental exposure. Access to the laser enclosures requires adherence to laser lock-out tag-out procedures mandated by the FESHM. These controls are reviewed by the MINOS ES&H Review Committee prior to commissioning.

12.4 Public access

The Soudan mine is a Minnesota State Park as well an underground laboratory. During the summer months, public tours of the 27th level, where the MINOS far detector is located, are conducted daily. Public access to the MINOS cavern is restricted to a viewing area on the mezzanine.

12.5 Summary

Physical hazards associated with the MINOS detectors are similar to those encountered in an industrial setting. Administrative controls are defined to ensure the detectors are constructed and operated safely. The only conceivable environmental hazard would be airborne hydrocarbons in the unlikely event of a fire.

Chapter 12 References

[1] The Fermilab NuMI Project Staff, "NuMI Project at Fermilab: Preliminary Safety Assessment Document," October 1998, Fermilab report NuMI-361.

[2] The University of Minnesota, CNA Consulting Engineers, Ericksen-Ellison Associates, Inc., and Miller-Dunwiddie, Inc., "MINOS Far Detector Laboratory Project, Preliminary Hazard Assessment Report," October 1998, Fermilab Report NuMI-L-419.

[3] The Fermilab NuMI Project Staff, "NuMI Project Cost and Schedule Plan," October 1998, Fermilab report NuMI-362.

Chapter 13

Cost and schedule summaries

13.1 Detector scope

The MINOS detector includes the following six subsystems: Magnet Steel and Coils; Scintillator Detector Fabrication; Electronics, DAQ and Database; Far Detector Installation; Near Detector Installation; and Project Management[1]. Costs associated with use of the Soudan 2 detector for long-baseline neutrino oscillation studies (Chapter 10), and with the potential emulsion detector upgrade (Chapter 11), are outside the scope of the baseline MINOS detector.

The cost estimate presented in Section 13.2 is a very brief summary of the detailed information given in the NuMI Project Cost and Schedule Plan (CSP)[2]; it is based on the baseline detector design described in the earlier Chapters of this Technical Design Report. Although the cost estimate covers a 5.4 kt far detector composed of two 2.7 kt supermodules, the cost and schedule plan for the Soudan site preparation includes an underground hall designed to accommodate an 8.1 kt, three-supermodule far detector[3]. This is to allow for the possibility of upgrading the experiment by increasing the mass of the far detector sometime in the future, in response to physics developments.

Although the funds allocated for contingency are not meant to allow scope changes[1], we anticipate that the uncertainty in MINOS cost estimates will be reduced substantially as the result of value engineering, firm vendor quotes and detector plane prototype time-and-motion studies. This would lead to lower contingencies and the possibility of moving funds from the present contingency pool to the project's scope reserve. Such funds might then be used for a future upgrade of the experiment, for example, a third far-detector supermodule, a hybrid emulsion detector and/or a narrow-band beam.

13.2 Cost estimate summary

Bottoms up cost estimates for the three competing active detector technologies were developed during 1996 and 1997, under the auspices of the MINOS Installation Committee[4]. Prior to the technology decision of September 24, 1997, the MINOS Collaboration focused substantial effort on the identification of significant cost differences among these technologies, which was one factor used in the technology choice. As a result of this exercise, the

Collaboration determined that the plastic scintillator detector described in this TDR was cost competitive with the other technologies.

Also during 1996 and 1997, bottoms up cost estimates were developed by the MINOS Installation Committee for the Magnet Steel and Coils and Far Detector Installation tasks. Recent effort has focused on developing bottoms up estimates for the remaining subsystems.

Detector costs at WBS Level 3 are summarized in Figure 13.1. The column labeled 'M&S' shows the direct costs associated with purchased Materials and Services. The 'SWF' column (Salary, Wage, Fringe) shows the direct costs for all skilled labor used in fabrication, assembly, testing and installation. Appropriate EDIA (Engineering, Design, Inspection and Acceptance) costs are included at Level 4 for engineering and design effort as well as management and administrative effort. The 'M&S + SWF + G&A' column includes the 'G&A' (General & Administrative) institutional overhead charges applied to the various direct-cost categories in each WBS element. The 'Contingency' and 'Cont %' columns show the weighted average contingencies in dollars and as percentages of the total costs (direct plus G&A). Contingency allowances are calculated using a detailed item-by-item analysis. The 'Escalation' column shows the cost increment resulting from inflation between the base year (FY 1998) and the year in which funds are obligated, assuming the construction schedule described in Section 13.3. The 'Total Cost' column shows the total cost in as-spent, then-year dollars.

Detector funding is primarily through the Fermilab NuMI Project, using funds provided by the U.S. DOE and Fermilab. We anticipate a U.K. contribution to the construction of detector electronics and calibration systems of approximately £1.3M for M&S, plus an additional contribution to cover the U.K. equivalent of all associated SWF, EDIA, G&A and escalation costs. Because the details of this funding arrangement are not yet finalized, the electronics and calibration system cost estimates included in the CSP are calculated under the assumption that this work is performed in the U.S. The value of the expected U.K. contribution, including the 34% contingency allowance, is subtracted from the total cost estimates in the second-to-last line of the table in Figure 13.1. The final MINOS cost estimate includes an average contingency of 37%.

The estimated total U.S. cost of the MINOS baseline detectors, with a 5.4 kt (two supermodule) far detector, is $44.6M in as-spent dollars, including contingency, compared to the $45M Fermilab guideline budget for the MINOS Detectors subproject. Any difference between the actual cost and the guideline budget would be added to the scope reserve for the project.

Further cost details are available in the NuMI Project Cost and Schedule Plan[2]. We anticipate a dramatic improvement in our understanding of costs and schedules when the 4-plane prototype studies, described in Chapters 4 and 7, are completed. The MINOS detector is rather different from conventional high energy physics experiments because such a large fraction of the detector cost is associated with the setup and operation of assembly lines. Time and motion study results and construction procedures based on final steel and detector designs will allow substantial refinement of the current cost and schedule estimates.

13.3 Schedule summary

The overall project schedule is shown in Figure 13.2. The summary task durations represent the time from the beginning of the first task to the completion of the last task. Much more detailed schedules are available in the CSP[2].

13.4 Manpower resources

Currently there are 21 institutions and more than 100 physicists actively participating in the MINOS Collaboration. The substantial physicist effort which is being provided by the collaborating institutions in support of the construction project is not included in the CSP. However, all U.S. nonphysicist technical effort is funded through the construction project and is included in the CSP. Because institutional indirect cost rates may differ, all CSP cost estimates display the overhead (G&A) costs explicitly.

Chapter 13 References

[1] The Fermilab NuMI Project Staff, "NuMI Project Management Plan," October 1998, Fermilab report NuMI-359.

[2] The Fermilab NuMI Project Staff, "NuMI Project Cost and Schedule Plan," October 1998, Fermilab report NuMI-362. Complete Microsoft Project and Excel files for the costs and schedules summarized in this document are available from the NuMI/MINOS project management office at Fermilab.

[3] The University of Minnesota, CNA Consulting Engineers, Ericksen-Ellison Associates, Inc., and Miller-Dunwiddie, Inc., "MINOS Far Detector Laboratory Technical Design Report (Including Basis of Estimate & WBS) for Cavern Construction, Cavern Outfitting & Detector Outfitting," October 1998, Fermilab report NuMI-L-263.

[4] J. Alner *et al.*, "Report of the MINOS Installation Committee," September 1997, Fermilab report NuMI-L-259.

WBS	Name	M&S (FY98k$)	SWF (FY98k$)	M&S + SWF (FY98k$)	M&S + SWF + G&A (FY98k$)	Contingency (FY98k$)	Cont %	Escalation (FY98k$)	Total Cost (Then Yr k$)
2.1	**Magnets: Steel & Coils**	$ 5,846	$ 621	$ 6,466	$ 7,442	$ 2,580	35%	$ 788	$10,810
2.1.1	Steel Plane Fabrication	$ 4,759	$ 75	$ 4,834	$ 5,370	$ 1,686	31%	$ 628	$ 7,684
2.1.2	Steel handling fixtures	$ 151	$ 102	$ 253	$ 325	$ 125	38%	$ 24	$ 474
2.1.3	Near Detector Support Structures	$ 88	$ 8	$ 96	$ 116	$ 41	35%	$ 11	$ 168
2.1.4	Magnet Coil	$ 746	$ 192	$ 938	$ 1,161	$ 471	41%	$ 97	$ 1,730
2.1.5	Detector Plane Prototypes	$ 26	$ 244	$ 270	$ 380	$ 213	56%	$ 19	$ 612
2.1.6	Steel Management	$ 75	$	$ 75	$ 89	$ 45	50%	$ 9	$ 142
2.2	**Scintillator Detector Fabrication**	$ 9,626	$ 3,428	$13,055	$15,887	$ 5,834	37%	$ 1,603	$23,325
2.2.1	Scintillator Strips	$ 2,540	$ 441	$ 2,981	$ 3,645	$ 1,303	36%	$ 369	$ 5,316
2.2.2	Fiber	$ 2,645	$ 163	$ 2,808	$ 3,313	$ 1,518	46%	$ 400	$ 5,231
2.2.3	Scintillator Modules	$ 1,248	$ 148	$ 1,396	$ 1,688	$ 410	24%	$ 123	$ 2,222
2.2.4	Photodetector Systems	$ 1,473	$ 170	$ 1,643	$ 1,983	$ 682	34%	$ 219	$ 2,884
2.2.5	Mux boxes and Connectors	$ 436	$ 730	$ 1,166	$ 1,515	$ 659	44%	$ 162	$ 2,336
2.2.6	Calibration Systems	$ 318	$ 171	$ 488	$ 590	$ 205	35%	$ 42	$ 837
2.2.7	Ass'y & Test Equipment	$ 586	$ 169	$ 755	$ 937	$ 337	36%	$ 53	$ 1,327
2.2.8	Factories	$ 194	$ 1,361	$ 1,556	$ 1,888	$ 668	35%	$ 212	$ 2,768
2.2.9	Scintillator Management	$ 186	$ 75	$ 261	$ 329	$ 52	16%	$ 23	$ 403
2.3	**Electronics & DAQ**	$ 1,793	$ 1,265	$ 3,058	$ 3,731	$ 1,279	34%	$ 262	$ 5,273
2.3.1	Front Ends	$ 1,071	$ 363	$ 1,433	$ 1,675	$ 561	34%	$ 145	$ 2,380
2.3.2	Hubs & Interface Crate	$ 169	$ 299	$ 468	$ 603	$ 237	39%	$ 39	$ 879
2.3.3	Central System & Trigger Farm	$ 438	$ 445	$ 883	$ 1,100	$ 326	30%	$ 63	$ 1,489
2.3.4	Data Acquisition	$ 37	$ 27	$ 64	$ 78	$ 43	55%	$ 2	$ 123
2.3.5	Database	$ 29	$ 92	$ 122	$ 165	$ 75	45%	$ 9	$ 249
2.3.6	Auxiliary Systems	$ 26	$ 39	$ 65	$ 82	$ 34	41%	$ 3	$ 119
2.3.7	Electronics Management	$ 24	$	$ 24	$ 29	$ 3	10%	$ 2	$ 33
2.4	**Far Detector Installation**	$ 259	$ 3,119	$ 3,378	$ 4,192	$ 1,945	46%	$ 554	$ 6,691
2.4.1	Infrastructure	$ 91	$ 161	$ 252	$ 297	$ 131	44%	$ 30	$ 458
2.4.2	Materials Receiving & Handling	$ 46	$ 778	$ 823	$ 1,025	$ 504	49%	$ 138	$ 1,667
2.4.3	Detector Assembly	$ 111	$ 2,141	$ 2,252	$ 2,808	$ 1,279	46%	$ 379	$ 4,466
2.4.4	Alignment and Survey	$ 11	$ 40	$ 51	$ 62	$ 31	50%	$ 7	$ 100
2.5	**Near Detector Installation**	$ 62	$ 1,188	$ 1,250	$ 1,773	$ 887	50%	$ 277	$ 2,937
2.5.1	Infrastructure	$ 51	$ 186	$ 237	$ 327	$ 160	49%	$ 45	$ 532
2.5.2	Materials Handling	$ 6	$ 344	$ 350	$ 500	$ 255	51%	$ 81	$ 835
2.5.3	Detector Assembly	$	$ 647	$ 647	$ 926	$ 462	50%	$ 148	$ 1,537
2.5.4	Alignment & Survey	$ 5	$ 10	$ 15	$ 20	$ 10	50%	$ 3	$ 34
2.6	**Project Management**	$ 40	$ 972	$ 1,012	$ 1,438	$ 14	1%	$ 94	$ 1,547
2.6.1	Salary support	$	$ 972	$ 972	$ 1,391	$	0%	$ 90	$ 1,481
2.6.2	Travel support	$ 40	$	$ 40	$ 48	$ 14	30%	$ 4	$ 66
	Sub-total	$17,626	$10,593	$28,219	$34,463	$12,541	36%	$ 3,578	$50,582
	UK Funds	$ 2,045	$ 1,414	$ 3,459	$ 4,213	$ 1,444	34%	$ 297	$ 5,954
	Total	**$15,581**	**$ 9,179**	**$24,760**	**$30,250**	**$11,096**	**37%**	**$ 3,281**	**$44,628**

Figure 13.1: Summary of MINOS detector cost estimate at WBS Level 3.

Task Name	1999				2000				2001				2002				2003
	Qtr 2	Qtr 3	Qtr 4	Qtr 1	Qtr 2	Qtr 3	Qtr 4	Qtr 1	Qtr 2	Qtr 3	Qtr 4	Qtr 1	Qtr 2	Qtr 3	Qtr 4	Qtr 1	
Detector Plane Prototypes																	
Final scint module design																	
Scint production prototyping & setup																	
Scint module production																	
Far steel procurement - 8 planes proto																	
Near steel procurement - 4 plane proto																	
Far steel procurement - 1st supermodule																	
Far steel procurement - 2nd supermodule																	
Start Soudan cavern excavation				1/4													
Soudan cavern occupancy									1/8								
1st super-module installation																	
2nd super-module installation																	
Near steel procurement																	
Start FNAL civil construction				3/29													
Near hall occupancy													10/30				
Near detector installation																	
NuMI beam commissioning																10/1	

Figure 13.2: Overall schedule for MINOS detector construction. Time is in calendar years.

Appendix A

Glossary

ACNET	Fermilab accelerator controls network
ADC	Analog to digital converter
ASIC	Application specific integrated circuit
bookend	End support for MINOS steel plane assembly
CC	Charged current neutrino interaction
CDMS	Cryogenic Dark Matter Experiment (coming to Soudan in 1999)
CKM	Cabibbo-Kobayashi-Maskawa mixing matrix which describes transitions among quark states
CL	Confidence level
CNA	Charles Nelson Associates, mining engineer consultants
cookie	Plastic fixture for positioning fibers accurately on photodetector pixels
CSP	Cost and schedule plan (both printed document and Microsoft Project and Excel files)
CVS	Concurrent Versions System software management program
DAQ	Data acquisition system
DEP	Delft Electronics Products (manufactures HPD photodetectors)
DIS	Deep inelastic scattering
DNR	Department of Natural Resources (State of Minnesota)
ears	Steel plane side extensions which support MINOS octagons
ECC	Emulsion Cloud Chamber (hybrid emulsion detector)
EDIA	Engineering, design, inspection, acceptance
EM	Electromagnetic, or electromagnetic shower
FESH	Fermilab environmental, safety and health department
FPGA	Field programmable gate array
FTE	Full-time equivalent (unit of effort)
G&A	General and administrative (indirect overhead charges)
GMINOS	GEANT-based MINOS Monte Carlo simulation program
GNuMI	Monte Carlo simulation of NuMI neutrino beam
GPS	Global Positioning Satellite (absolute time standard)

hair	Fiber optics and cabling around edges of MINOS detector planes
HPD	Hybrid photodiode (photodetector made by DEP)
HV	High voltage
HVAC	Heating, ventilation and air conditioning
K2K	KEK-to-Kamiokande Japanese long baseline neutrino experiment
kt	kiloton (1000 metric tons)
L/E	Ratio of flight path length to neutrino energy which characterizes neutrino oscillations
LCW	Low conductivity water (for magnet cooling)
LED	Light emitting diode (light source for calibration system)
LOI	Letter of intent
M&S	Materials and services
M16	Hamamatsu R5900-00-M16 16-channel multianode photomultiplier
MC	Monte Carlo
MINOS	Main Injector Neutrino Oscillation Search
MIP	Minimum ionizing particle
MIPS	Million instructions per second
multiplexing	"Optical summing" of scintillation light from several optical fibers onto a single photodetector pixel (in addition to its usual meaning)
MUX box	Multiplexing box
NBB	Narrow band beam
NC	Neutral current neutrino interaction
NEUGEN	Monte Carlo neutrino event generator software
NuMI	Neutrinos at the Main Injector (neutrino beam or Project)
OO	Object oriented program
PC	Personal computer (IBM clone)
pcb	Printed circuit board
PCI	Peripheral component interconnect (PC bus protocol)
pe	Photoelectron
PLC	Programmable logic controller
PMC	PCI mezzanine card
PMP	Project management plan
PMT	Photomultiplier tube
PSAD	Preliminary safety assessment document
QC	Quality control
QE	Quasi-elastic interaction, or quantum efficiency
Rock muon	Muon from a neutrino interaction in the rock around MINOS
RTV	Room temperature vulcanization adhesive
SAD	Fermilab safety assessment document
SAW	Submerged arc welding, used for steel plane plug welds
SuperK	SuperKamiokande water Cerenkov detector
SWF	Salary, wage and fringe benefit (effort) costs
T	Tesla (1 T = 10 kG)

task   WBS element used for categorizing costs. Tasks referred to in this document include:

        Magnet steel and coils, WBS 2.1

        Scintillator detector fabrication, WBS 2.2

        Electronics and DAQ, WBS 2.3

        Far detector installation, WBS 2.4

        Near detector installation, WBS 2.5

        MINOS R&D program, WBS 3.1

        Soudan cavern construction and outfitting, WBS 3.3

        NuMI technical components, WBS 1.1

        NuMI civil construction, WBS 1.2

TDR   Technical Design Report

ton   Metric ton (1000 kg)

TPC   Time projection chamber, total project cost

TRD   Technical Requirements Document

WBB   Wide band beam

WBS   Work breakdown structure

WLS   Wavelength shifting fiber